Dipl.-Ing. David E. Sander

A Validated Elasto-Hydrodynamic Simulation for Journal Bearings Operating Under Severe Conditions

Doctoral Thesis

to achieve the university degree of
Doktor der technischen Wissenschaften
submitted to

Graz University of Technology

Supervisor and first examiner

Ao.Univ.-Prof. Dipl.-Ing. Dr.techn. Hans-Herwig Priebsch
Institute of Internal Combustion Engines and Thermodynamics
Graz University of Technology, Austria

Second examiner

Director of Research Michel Fillon
Institut Pprime
CNRS-Université de Poitiers-ISAE-ENSMA, France

Graz, July 2016

Affidavit

I declare that I have authored this thesis independently, that I have not used other than the declared sources/resources, and that I have explicitly indicated all material which has been quoted either literally or by content from the sources used. The text document uploaded to TUGRAZonline is identical to the present doctoral thesis.

Date	Signature

Acknowledgments

This dissertation presents a key outcome of a long-term research project conducted at the Virtual Vehicle Research Center in cooperation with KS Gleitlager GmbH, AVL LIST GmbH, OMV AG and the Institute of Tribology and Energy Conversion Machinery at TU Clausthal.

In the first place, I would like to express my deepest appreciation and gratitude to my supervisor Prof. Hans-Herwig Priebsch for his continuous support and his thoughtful guidance throughout my postgraduate studies and this dissertation process in particular.

I would also like to thank Prof. Michel Fillon for his thorough review and the detailed and insightful comments that allowed me to improve the quality of this work.

I greatly appreciate the very comprehensive support of my partners at KS Gleitlager, especially Mario Witt, Athanassios Skiadas and Torsten Füllenbach and would like to thank them for their experienced and valuable input. This includes the performance of measurements on their journal bearing test-rig. I am grateful for Franz Novotny-Farkas' support, who formerly worked at OMV, for providing the lubricant and for generously contributing his knowledge in helpful ways. Moreover, I would like to acknowledge Christoph Priestner, Oliver Knaus and Heinz Flesh from AVL who always supported me during this research project with many helpful discussions and beneficial advice.

My gratitude to Ludwig Brouwer from the TU Clausthal who provided me with an invaluable insight into the field of rheology and who analyzed the properties of the lubricant.

Furthermore, I would like to thank all my colleagues at the Virtual Vehicle Research Center, especially my colleagues of the tribology team Franz, Hannes, Christoph, Stefan, Tomi, Martin, Markus, and Bernhard for the countless inspiring discussions. Very special thanks to my colleague Hannes Allmaier - his boundless support greatly helped me to realize this thesis from idea to final draft.

I would like to thank my family for their unwavering support throughout my life. Finally, my deepest gratitude goes to my partner Sarah, for her patience, her trust, her endless support and encouragement.

Abstract

A current trend in the transport sector seeks to increase vehicle efficiency and to cut fuel consumption. This trend leads to a multitude of technologies and advancements in modern and future combustion engines. Some of these technical advancements lead to highly stressed engine parts and new challenges arise, particularly for crankshaft journal bearings. The increasing thermal and mechanical load caused by downsized and turbocharged engines, friction reduction by employing low-viscosity lubricants and other emission reduction measures, for instance, by utilizing stop-start systems, put unanticipated stress on the crank shaft journal bearings. To cope with these challenges, a validated simulation method is developed in this thesis to qualitatively and quantitatively analyze journal bearing friction and wear in the early design stage.

This thesis focuses on highly stressed journal bearings which operate in boundary, mixed and pure hydrodynamic lubrication regime. Therefore, measurements on a journal bearing test-rig are performed which allow an extensive verification of the numerical investigation. For the numerical analysis of friction and wear, a mixed elasto-hydrodynamic simulation approach is developed which considers the elastic deformation of the contacting components, the complex rheological behavior of the lubricant and metal-metal contact if the lubricant is unable to separate the contacting surfaces.

The complex lubricant properties are obtained from measurements and a detailed oil model for the journal bearing simulation is derived. The importance of considering the piezo-viscous effect and the non-Newtonian behavior for friction and wear prediction under high dynamic stresses is emphasized. Furthermore, the input parameters for the contact model which is used to identify metal-metal contact, are derived from surface scans of the contacting components. The obtained contact model in combination with a constant boundary friction coefficient is able to predict friction in severe mixed lubrication regime accurately.

An iterative wear calculation is performed to investigate the running-in process of dynamically loaded journal bearings. Metal-metal contact occurs at the bearing edges which is caused by an elastic bending of the shaft. The good agreement between simulation and measurement indicates that the simple iterative approach using Archard's wear equation, is able to predict the worn surface geometry.

Finally, the starting and stopping behavior of journal bearings is analyzed in great detail. With the previously developed simulation models, the breakaway torque, the friction losses and continuous wear is studied and verified by measurements.

Kurzfassung

Der gegenwärtige Trend zur Steigerung der Effizienz und zur CO_2-Reduktion von Fahrzeugen führt zwangsläufig zu neuen Technologien und Weiterentwicklungen in modernen und zukünftigen Verbrennungsmotoren. Diese technologischen Errungenschaften führen meist zu hochbelasteten Komponenten, welche neue Herausforderungen für die einzelnen Bauteile und die geschmierten Kontakte mit sich bringen. Durch hochaufgeladene Motorenkonzepte und Downsizing steigen die thermischen und mechanischen Belastungen, insbesondere in den Gleitlagern der Kurbelwelle. Reibungsreduktion durch Verwendung niedrigviskoser Schmierstoffe sowie weitere emissionsreduzierende Maßnahmen, wie zum Beispiel der Einsatz von Start-Stopp Systemen, belasten die Lager zusätzlich. Um diese Herausforderungen zu bewältigen, wird in dieser Arbeit ein validiertes Simulationsverfahren entwickelt, welches dazu beiträgt bereits in der frühen Entwicklungsphase Gleitlagerreibung und Verschleiß aussagekräftig analysieren und beurteilen zu können.

Diese Dissertation beschäftigt sich detailliert mit hochbelasteten Gleitlagern, die im Grenzreibungsbereich, Mischreibungsbereich sowie im rein hydrodynamischen Schmierungszustand betrieben werden. Als Basis für die numerische Berechnung wird eine elastohydrodynamische Simulationsmethode angewandt und entwickelt, welche die elastische Verformung der Bauteile und die komplexen rheologischen Eigenschaften des Schmieröls berücksichtigt. Ein zusätzliches Kontaktmodell berücksichtigt Festkörperkontakt, falls der Schmierspalt zwischen den Bauteilen zu gering wird. Es werden Messungen an einem Gleitlagerprüfstand durchgeführt und anhand der Messergebnisse, wird die numerische Simulationsmethode umfangreich verifiziert.

Die komplexen Schmierstoffeigenschaften werden in Laboruntersuchungen unter hohen Drücken und bei hohen Scherraten bestimmt. Anhand von den Ergebnissen, wird ein detailliertes Ölmodell für die Simulation abgeleitet. Mittels Simulation wird gezeigt, dass der piezoviskose Effekt und das nicht-Newtonsche Verhalten für die Vorhersage von Reibung und Verschleiß unter dynamischer Belastung einen wichtigen Einfluss haben. Die Rauhigkeitsparameter für das Kontaktmodell werden durch Weißlichtinterferometrie bestimmt. Das auf realen Oberflächen basierende Kontaktmodell in Kombination mit einem konstanten Grenzreibwert ermöglicht eine genaue Vorhersage von Festkörperkontakt und der Reibungsverluste im Mischreibungsbereich.

Zur Untersuchung des Einlaufvorgangs von dynamisch belasteten Gleitlagern wird eine iterative Berechnungsmethode angewandt. Die Grundlage der iterativen Methode bildet das Verschleißmodell nach Archard. An den Lagerkanten kommt es, durch eine elastische Deformation der Welle, zu Festkörperkontakt, welcher in der Folge zu Materialabtrag führt.

Aufbauend auf den zuvor entwickelten Simulationsmodellen, wird das Start-Stopp Verhalten der Gleitlager detailliert analysiert. Die transiente Methode ermöglicht die Vorhersage des Losbrechmoments und der Reibungsverluste, sowie die Berechnung des kontinuierlichen Verschleißes.

Die Berechnungsergebnisse zeigen eine gute Übereinstimmung mit den Messergebnissen.

Contents

Chapter 1

Introduction and scope of the thesis

Journal bearings which are also commonly referred to as plain bearings or fluid film bearings, are crucial machine elements in mechanical engineering applications. This apparently basic element is typically designed for a load transmission between a rotating shaft and a bearing shell. Consequently, the contacting surfaces are separated by lubricants to ensure a high efficiency and durability.

However, in many applications journal bearings have to sustain extreme loading conditions, in particular the crankshaft bearings of internal combustion engines. Therefore, the present thesis focuses on highly stressed crankshaft bearings which operate in boundary, mixed and pure hydrodynamic lubrication regime. A detailed elasto-hydrodynamic simulation model which considers the complex rheological behavior of the lubricant as well as the roughness of the contacting surfaces is elaborated here. The simulation model is validated on the basis of extensive bearing tests and is further used to analyze the friction and wear behavior of journal bearings while operating under severe conditions.

1.1 Current challenges and state of the art

A current trend in the transport sector seeks to increase the vehicle efficiency and to cut fuel consumption. This trend yields to new technologies and advancements in modern and future combustion engines. Some of these technical developments lead to highly stressed engine parts and new challenges arise particularly for journal bearings. The increasing thermal and mechanical load caused by downsized and turbocharged engines, friction reduction by employing low-viscosity lubricants and other emission reduction measures, for instance by utilizing stop-start systems, put additional stress on the crank shaft journal bearings. The journal bearing itself is a target for efficiency optimization as it contributes significantly to the mechanical losses of internal combustion engines [40, 85]. These challenges are outlined briefly below (for further details see Sander et al. [73]):

- Modern downsized combustion engines with turbocharger(s) achieve a high power output from small volume displacements and allow for efficiency improvement with lower emissions. At the same time, high power density increases the thermal and mechanical load on the engine components. Additionally, a lightweight design of the engine further improves vehicle performance. Thus, the engine and its component dimensions become smaller too. This implies even higher stresses for the components and for the lubricated contacts. For instance the big-end bearing of the connection rod has to resist specific loads above 100 MPa and a further increase is expected for future engines [25]. As a consequence the minimum lubrication gap in the journal bearing decreases below 1 μm and metal-metal contact may occur at these operating conditions. Furthermore, the elastic deformations of the bearing shell and its surrounding parts have a major influence on bearing behavior [14].

- The increasingly strict legislation concerning the emission restrictions forces the automotive industry to further increase engine efficiency. The usage of lower viscosity lubricant is considered to be a very economic measure to reach this goal [40]. However, the current trend goes to lubricants with a drastically reduced viscosity and new standards had to be defined accordingly [22]. With the new SAE standards 16, 12, 8 and even lower classes being targeted, pure hydrodynamic lubrication conditions will increasingly decline and be replaced by mixed lubrication near the minimum friction coefficient [47].

- Modern multigrade lubricants show a complex rheological behavior. The lubricant's density and viscosity increase with high hydrodynamic pressure [6]. The increase of the viscosity is also known as piezo-viscous effect and affects the journal bearing behavior in highly loaded regions which may increase the lubrication gap. A second property of multigrade lubricants is the non-Newtonian behavior. At high shear rates which typically occur in automotive journal bearings the viscosity significantly drops below the viscosity at low shear rate [59, 87]. To assess this shear thinning behavior a viscosity at high temperature and high shear rate (HTHS-viscosity) is standardized. It was shown that the HTHS-viscosity directly affects the mechanical efficiency of the engine in fleet tests [49, 50], which demonstrates the necessity to realistically consider the non-Newtonian behavior of the lubricant in the simulation. Currently, the required lubricant data are not stated in any lubricant datasheets as such measurements are not part of common standards. Therefore, these rheological data are only sparsely available and only for specific lubricants (e.g. [6, 46]).

- Another measure to improve fuel economy, especially for urban driving, is the application of stop-start systems [10, 79]. By turning off the engine instead of operating it at idle (e.g. when waiting at a crossings) significant fuel savings can be obtained [34, 79]. Stop-start systems have quickly become widely available, but despite their apparent simplicity the repeated stopping and starting of the engine presents a big challenge for bearing manufacturers. When the engine is started, the bearing has to overcome boundary and mixed lubrication regime before a hydrodynamic film has formed which separates the two contacting surfaces completely [55]. Thus, with the increasing number of stop-start cycles bearing wear will increase.

- Fuel economy improvement and emission reduction may be achieved by a cylinder de-activation technology (CDT). The benefits are a result of reduced air pumping losses and due to an increased exhaust temperature under partial loading which yields improved after-treatment efficiency for diesel engines [88]. However, CDT affects the dynamic behavior of the shaft and topics like shaft bending and journal misalignment which are relevant for bearing design and bearing layout. The ability of the bearing shell to adapt its surface geometry and further to fit the deformed or misaligned shaft can become essential. Also the friction power losses need to be investigated to show the overall efficiency benefits. A better understanding of the necessary redesign of the power train with CDT is the target in recent bearing simulation [53, 54, 78].

On the one hand, highlighted measures to improve engine efficiency challenge the bearing manufacturer who permanently develops new bearing material and, on the other hand, the engine developer who needs reliable simulation methods to cost-effectively assess and improve the engine design and the bearing layout. A reliable simulation method which is verified for a large range of operation conditions is therefore of great value. These simulation methods must include models for the deformable components, models for the high pressure and shear-thinning properties of the lubricant, and a contact model to describe metal-metal contact.

As the current state of the art, the bearing performance of statically loaded bearings operating in hydrodynamic lubrication regime is well understood. Also dynamically loaded bearings which operate under moderate stresses are broadly discussed in literature. A large number of publications use the mobility method [17, 18] but this method does not consider any local deformations of the contacting surfaces or metal-metal contact. A full elasto-hydrodynamic simulation method which considers 3D elastic deformation of the contacting bodies was primarily presented by Oh and Huebner in 1973 [64]. Recently, a review of elasto-hydrodynamic simulation methods for journal bearings in engine application was published [19]. Many of these studies concentrate on the numerical method and show the importance of including the elastic deformation of the contacting bodies, the rheological behavior of the lubricant, or the implementation of an elastic-plastic contact model by simulation. However, there is a gap of studies which discuss the current challenges of automotive journal bearings by simulation and verify their results by measurement extensively.

This study investigates four different application examples in the result section (see section 5). In the beginning of each application example the specific topic is introduced and a review of the current state of the art is presented.

1.2 Objectives

The numerical analysis of journal bearings does not represent a novel approach. However, with the increasing requirements of current journal bearing application, a detailed understanding of the influencing parameters becomes increasingly critical. Therefore, this study seeks to extend the numerical analysis to severe operation conditions beyond current state of the art. Especially for a reliable friction and wear prediction, the simulation input parameters for the lubricant and the contact model have to be based on physical data. The simulation approach needs to be verified through measurement results. Therefore, four fundamental objectives are defined for this study:

- Identify the temperature, pressure and shear rate dependency of the tested lubricant and derive a detailed oil model for the journal bearing simulation. Investigate the impact of the piezo-viscous effect and the non-Newtonian behavior on bearing friction with the help of the detailed oil model. Verify the simulation results by measurement results.
- Derive and proof the input parameters for the contact model which is used to describe friction and wear in journal bearing simulation. Verify the simulation results by measurement results.
- Describe the formation of wear scars at the bearing edges due to bearing misalignment by simulation. Verify the simulation results by measurement results.
- Develop a simulation model to analyze the start and stop behavior of journal bearings and verify it by measurements. Investigate the formation of a wear scar due to repeated starting of the shaft.

In general, the simulation methods and simulation tools are well developed for the analysis of journal bearings operating in severe conditions. For this reason, the development of an EHD code or a contact model is not an objective of this study, rather a commercial tool is used for the analysis in combination with a well-known contact model. Another neglected goal is the analysis of the thermal behavior of the bearing.

1.3 Method and realization of the thesis

Measurements on a journal bearing test-rig were performed which allow for an extensive verification of the numerical investigation. For the numerical analysis of friction and wear a mixed elasto-hydrodynamic simulation approach is employed which considers the elastic deformation of the contacting components, the complex rheological behavior of the lubricant and metal-metal contact if the lubricant is unable to separate the contacting surfaces. Both, the rheological data and the surface roughness parameters are obtained from measurements. The current challenges are studied in four application oriented examples and the influencing parameters on a reliable friction and wear prediction are explored.

This study is part of a long term research project which was realized at the Virtual Vehicle Research Centre in Graz, Austria in cooperation with KS Gleitlager GmbH (KS Gleitlager), AVL LIST GmbH (AVL), OMV AG (OMV) and the Institute of Tribology and Energy Conversion Machinery at TU Clausthal (ITR). The different backgrounds of the project partners made this project very unique and allow a best possible analysis of the complex journal bearing behavior.

KS Gleitlager supplied the bearing shells and conducted the measurements on their journal bearing test-rig. The test results provide a solid basis for the validation of the elasto-hydrodynamic simulation method. The simulation model was set up in the commercial AVL Excite software package which was provided by AVL. Furthermore, the surfaces of the bearing shell were scanned at AVL for the analysis of the roughness parameters. The lubricant used in this study was supplied by OMV. ITR evaluated the rheological data of the lubricant under high pressure and at high shear rate.

1.4 Structure of the thesis

This thesis is divided into five sections. Section 1, the introductory section, provides an overall overview of the thesis. In the beginning, the motivation, the objectives of the thesis and state of the art are highlighted, followed by the method and realization of this study. The section ends with the summary of the research findings and an outlook for further research.

Section 2 gives a brief overview of the tribological system journal bearing. The basic terms used in this study are defined and the essential friction and wear mechanisms are described. The fundamental properties of the bearing shell and the lubricant are presented.

In section 3, the test-rig is described which is used in this study to validate the simulation method.

The basic equations for the mixed elasto-hydrodynamic simulation method are presented in section 4. Additionally, the representation of the deformable components and the lubricant properties are discussed.

Section 5 shows the results of four different application examples discussing either friction, wear or both in journal bearings. Each application example is related to the current challenges in the automotive sector and consists of a validation of the simulation method.

- The first application example (see section 5.1) describes dynamically loaded journal bearings under extreme loading conditions which lead to fluid film pressures above 200 MPa and to high shear rates. The impact and the significance of a detailed oil model is discussed and compared to simplified lubricant oil. Center of attention are friction loss and minimum oil film thickness.
- The second application example (see section 5.2) focuses on friction in mixed lubrication regime. Therefore, a static load is applied to the journal bearing and Stribeck curves are calculated. By varying the roughness parameters of the contact model the influence of surface smoothing due to running-in is discussed.
- The third application example (see section 5.3) concentrates on the running-in wear of journal bearings. Running-in wear occurs in the very beginning of journal bearing lifetime and an adaption of the bearing shell geometry occurs. After the running-in process has completed, metal-metal contact in the lubrication gap vanishes completely. An adapted surface geometry is calculated by iteratively removing material from the bearing shell.
- A transient start-stop simulation is performed in the fourth example (see section 5.4). The journal rests in the bearing in the beginning of the simulation. When the journal starts to rotate the breakaway torque has to be overcome. Afterwards the bearing operates in mixed lubrication regime until the lift off speed is reached. Minimum oil film thickness and altitude angle are discussed during the whole start-stop cycle. A wear analysis is performed additionally in this application example.

1.5 Summary of research results

The behavior of journal bearings operating under severe conditions is investigated through simulation. All simulation results are verified by results from the journal bearing test rig.

- The oil properties play an essential role for the analysis of journal bearing behavior. For this reason, the tested lubricant is experimentally analyzed under high pressure and at high shear rate. From these measurement results, an oil model is elaborated which considers a temperature, pressure and shear rate dependent viscosity as well as a temperature and pressure dependent density.
- The importance of including the detailed oil model into the bearing simulation is shown by analyzing the friction in dynamically loaded bearings (see section 5.1). The periodically acting load generates maximum specific pressures of up to 100 MPa. Therefore, oil film pressures of more than 200 MPa occur locally. At this high pressure the viscosity increases nearly sevenfold compared to the viscosity at ambient pressure. Additionally to the high pressure, high shear rates (up to $2.2\cdot10^7$ s^{-1}) are generated at shaft speeds up to 7000 rpm which cause a local viscosity drop up to 25 %.

  The calculated friction losses with the detailed oil model are compared to the measurement results on the journal bearing test-rig for a wide range of operation conditions. At all operating conditions, the calculated results are located within the measurement uncertainty. Neglecting either the non-Newtonian behavior or the piezo-viscous effect in the simulation will remarkably affect the journal bearing friction. When neglecting both effects a discrepancy up to 15 % can occur.

- For the bearing analysis in mixed lubrication regime, the parameters for the contact model are derived from surface scans of the tested bearing shell. The proof of the parameters for the contact model is performed by analyzing bearing friction in mixed lubrication regime (see section 5.2). For the simulation, a constant boundary friction coefficient is assumed and the limits of this simplification are investigated. The bearing is subjected to a static load and the friction loss is identified for different shaft speeds. The calculated bearing friction matches the measured bearing friction within the measurement uncertainty in hydrodynamic and mixed lubrication regime. Only at very low shaft speeds when the bearing operates in boundary friction regime, the friction torque is underestimated. Here, a higher boundary friction coefficient would be more applicable.

  After verifying the parameters for the contact model the impact of surface roughness on journal bearing friction is analyzed. The surface of the bearing shell is scanned again, this time at a worn bearing position and the parameters for a second contact model are derived. With the newly generated contact model the friction losses are calculated. The results show a clear friction benefit in mixed lubrication regime. The results with the worn surface predict a smaller lubrication gap, lower asperity contact pressure and a smaller contact area.

- A second test of the contact model is given by the wear analysis which is performed to study the running-in behavior of journal bearings (see section 5.3). After the tests with dynamic loading worn bearing edges were identified. Due to the high load and the consequently caused elastic deformation of the shaft, the bearing edges are exposed to metal-metal contact. After an initial running-in process the bearing adapts its surface geometry and metal-metal contact at the edges vanishes. The running-in wear process is calculated by iteratively removing material from the bearing surface until only insignificant metal-metal contact pressure occurs. The finally calculated worn bearing surface is compared to the worn bearing surface which is analyzed after the measurement at the test-rig. The maximum wear depth shows a good agreement as well does the extension of the worn region in axial and circumferential direction.

  It is found that the metal-metal contact pressure monotonically decreases during the running-in process due to the geometrical adaption of the bearing shell. Furthermore, the simulation indicates that more wear is expected at higher shaft speed. The higher bearing temperatures and high shear rates at high shaft speed cause a decrease of lubricant viscosity and hence, the lubrication gap decreases.

- The simulation method is used to analyze the start and stop behavior of journal bearings in section 5.4. Essential for this study is the starting conditions when the shaft starts to rotate. Therefore, an initialization phase is introduced when the shaft does not rotate and an external static load is applied to the bearing. As a consequence, the shaft moves towards the bearing shell and pushes oil out of the bearing. In the end of the initialization phase the bearings rests on the bearing shell and is mainly supported by metal-metal contact.

  After the initialization phase a transient start-stop cycle is calculated. The results from the simulation are compared to the measurement results from the bearing test-rig where 6000 start-stop cycles were conducted. The results show a good agreement for the evaluated start-stop cycle regarding the magnitude of the breakaway torque, the friction drop between boundary and mixed lubrication regime. Also the transition between mixed lubrication and hydrodynamic lubrication is correctly identified.

- The simulation model is furthermore used to analyze the impact of surface smoothing due to running-in on the start-stop behavior of journal bearings. One start-stop cycle is therefore calculated with the roughness parameters of a worn surface. The breakaway torque remains unchanged compared to the results with the new bearing surface because at rest the shaft is mainly supported by metal-metal contact. Hence, the breakaway torque is dominated by the boundary friction coefficient. Main differences can be found in mixed lubrication regime where the friction moment decreases drastically. Consequently, the work needed to overcome friction during the entire start-stop cycle is reduced to 50 % for the smoother bearing surface.
- Finally, the adaption of the surface geometry due to metal-metal contact is investigated by applying the iterative simulation approach which is presented to calculate the running-in behavior. Contrary to previous results, metal-metal contact occurs all along the bearing axis and metal-metal contact does not reduce due to the adaption of the bearing shell. The circumferential position of the maximum wear depth is shifted by 20° in the direction of shaft rotation.

  Results calculated with the worn bearing geometry show that the friction torque increases in mixed lubrication regime. This is mainly caused by the lower hydrodynamic pressure in the oil film which leads to a smaller lubrication gap at higher shaft speeds. Consequentially, the area of metal-metal contact increases. That means a drastic increase for the friction work during a complete start-stop cycle which is 2.3 times higher than the friction work with the initial bearing geometry.

  It is also found that the wear load increases after an initial adaption of the surface geometry. In other words, the number of starts to create a certain wear depth decreases from step to step. This reduction is also caused by the increased metal-metal contact at high shaft speed.

1.6 Outlook

Future challenges for journal bearing simulation include a precise prediction of bearing lifetime. Therefore, wear coefficients for different bearing materials need to be determined which is possible by combining measurement and simulation more intensively. Start stop conditions would be appropriate for this study. Additionally, the complex interactions between bearing surface and lubricant need to be further studied to understand the effect of additives on friction and wear in journal bearings operating under severe conditions. In this context, the consideration of polymeric sliding layers in the simulation presents a new challenge for the future.

The numerical prediction of bearing failure (e.g. seizure) needs a combined consideration of accurate metal-metal contact pressure and the thermal conditions on the bearing surface. Therefore, the thermal processes need to be considered and the predictability of temperature and heat flux must be verified by measurement.

Chapter 2

Tribosystem journal bearing

A hydrodynamic journal bearing appears as a basic machine element consisting of a shaft which rotates in a bearing shell (bushing). The contacting surfaces of the shaft and the bearing shell are typically lubricated. The main function of a journal bearing is the guidance and the transmission of a radial load between shaft and bearing shell. A hydrodynamic journal bearing can be regarded as a tribological system[1] which is sketched in figure 2.1.

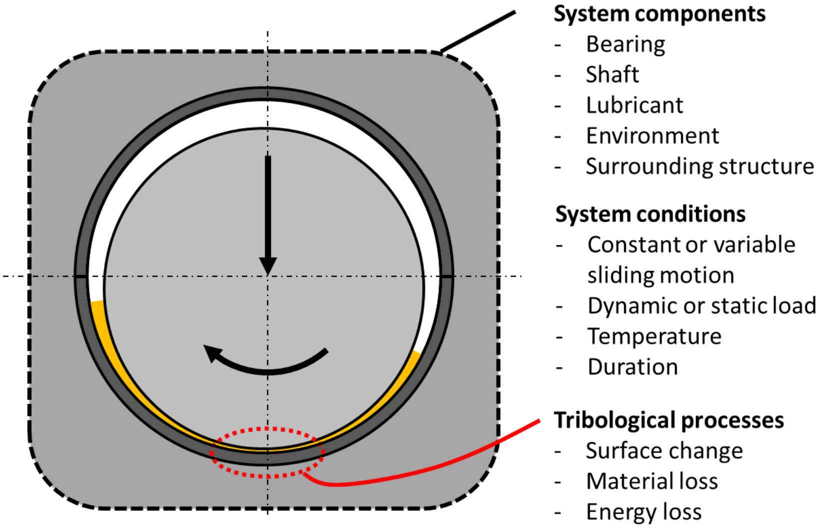

Figure 2.1: Tribological system of a journal bearing

The contacting components of a journal bearing system are the typically hardened shaft and the softer bearing shell which is in general split into two bearing shells. The surrounding components (e.g. connecting rod in a combustion engine) may deform and may therefore influence the bearing behavior. Another important component of the journal bearing system is the lubricant which separates and protects the two contacting surfaces. The lubricant is continuously supplied to the bearing via a supply bore or a

---

[1] Czichos [24] describes a tribological system or tribosystem as an entity with a structure of interacting components in relative motion to perform a technical function. The function of a tribosystem is versatile and reaches from energy transfer and guidance to forming and machining. A tribological system mainly consists of two contacting components an interfacing medium between the contacting surfaces and a surrounding medium.

supply groove. The environment or the ambient medium (e.g. air) can also affect the performance of journal bearings.

The load acting on the journal bearing and the relative velocity between shaft and bearing shell characterize the bearing condition. The bearing can either operate with a static, periodic or a transient load. Also the shaft speed can either be constant or alternating. Additionally, the duration of operation and the bearing temperature have a major impact on the bearing behavior and the tribological processes.

In the lubricated contact, tribological processes take place which are dependent on the system components and the system conditions. The loss or transport of material, the loss of energy and the modification of the surface constitute such tribological processes. Friction describes the loss of energy and wear characterizes the modification of the surface and the loss of material [28].

2.1 Tribological processes

The tribological processes describe the energy loss (friction) and material transport (wear) during the bearing operation. Tribo-chemical reactions like corrosion and the change of material properties of the contact layer are important but are beyond the scope of this study and are therefore not discussed here.

2.1.1 Friction and lubrication regimes

Friction is the force of resistance when two bodies are in contact and a relative motion between the contacting surfaces occurs [51]. The coefficient of friction μ is the relation between the friction force F_f and normal force F_n acting on the contact surface:

$$\mu = \frac{F_f}{F_n}. \tag{2.1}$$

It can be distinguished between different types of friction dependent on the relative motion of the contacting surfaces [28]. Sliding friction occurs when the two contacting surfaces show a relative motion in the contact area. Pure rolling friction occurs when one component rolls on to the other component. A mixture of rolling and sliding friction occurs in ball bearings or gears where regions of pure rolling and slip motion exist. However, in journal bearings, sliding friction is dominant.

In lubricated contacts, friction can be further classified into different lubrication regimes (or states of friction) [71]:

- Hydrodynamic lubrication regime: Full fluid film lubrication. The fluid film separates the two contacting surfaces completely.
- Elasto-hydrodynamic lubrication regime: The fluid film still separates the two contacting surfaces but the elastic deformation and the lubricant properties under high pressure get influential.
- Mixed lubrication regime: The fluid film cannot completely separate the contacting surfaces and an interaction of asperities between the two surfaces is present.
- Boundary lubrication regime: The two surfaces are in contact and the interactions of the asperities dominate the frictional behavior.

The lubrication regimes in journal bearings can be identified by the Stribeck curve (see figure 2.2). Here, the friction coefficient is plotted over the shaft speed and the bearing is loaded by a static force.

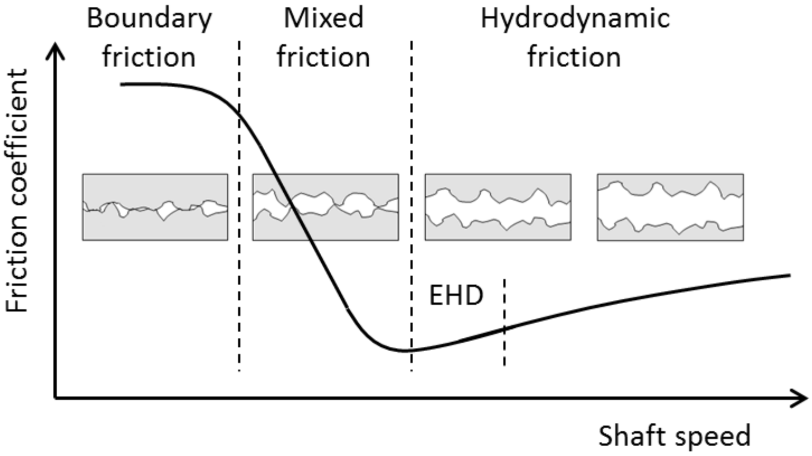

Figure 2.2: Identification of lubrication regimes by a typical Stribeck curve

At high shaft speed the contacting surfaces are completely separated by the lubricant. When the shaft speed reduces, the gap between the contacting surfaces reduces and the friction coefficient gets smaller. With a further reduction of the shaft speed single asperities of the mating surfaces interact. The friction coefficient rises with an increase of asperity contact. The maximum friction coefficient occurs in boundary lubrication regime.

Hydrodynamic friction

The resistance of relative motion in hydrodynamic lubrication regime is specified by the fluid only. The characterizing parameter is the viscosity of the lubricant. The definition of the viscosity is exemplarily described for the fluid film between two parallel plates (see figure 2.3).

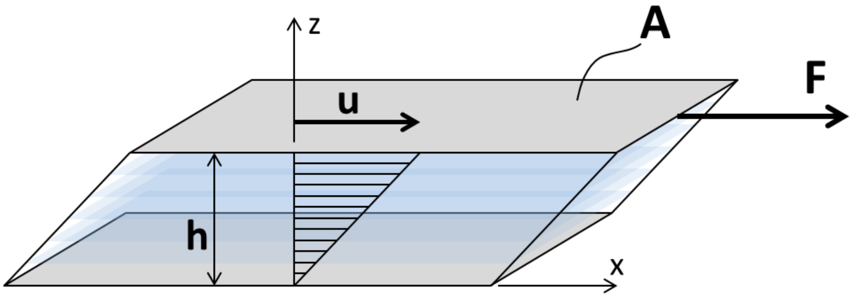

Figure 2.3: Sketch for the definition of viscosity

The upper plate moves slowly in x direction with a constant speed of u. To conquer the internal friction in the fluid a force F needs to be applied to the moving plate. The magnitude of the force is proportional to area of the plate A and the velocity. It is inversely proportional to the fluid film thickness h:

$$F = \eta \cdot A \cdot \frac{v}{h}. \tag{2.2}$$

The dynamic viscosity η is a material parameter and specifies the shear resistance of the fluid. The unit of the dynamic viscosity is $(\mathrm{N} \cdot \mathrm{s})/\mathrm{m}^2$ or $\mathrm{Pa} \cdot \mathrm{s}$. Between the two plates the velocity gradient along z direction or shear rate $\dot{\gamma} = \frac{\partial u}{\partial z}$ is constant over the film height. Therefore, previous equation can be written in a more general form which is valid for laminar flow:

$$\tau = \eta \cdot \dot{\gamma}, \tag{2.3}$$

with the shear stress $\tau = \frac{F}{A}$. This equation was first defined by Isaac Newton and is known as Newton's law of viscosity. Fluids which show a linear proportional behavior ($\eta = const$) between shear stress and shear rate are called Newtonian fluids. Many fluids have a distinct non-Newtonian behavior. Two typical characteristics for non-Newtonian fluids are shown in figure 2.4.

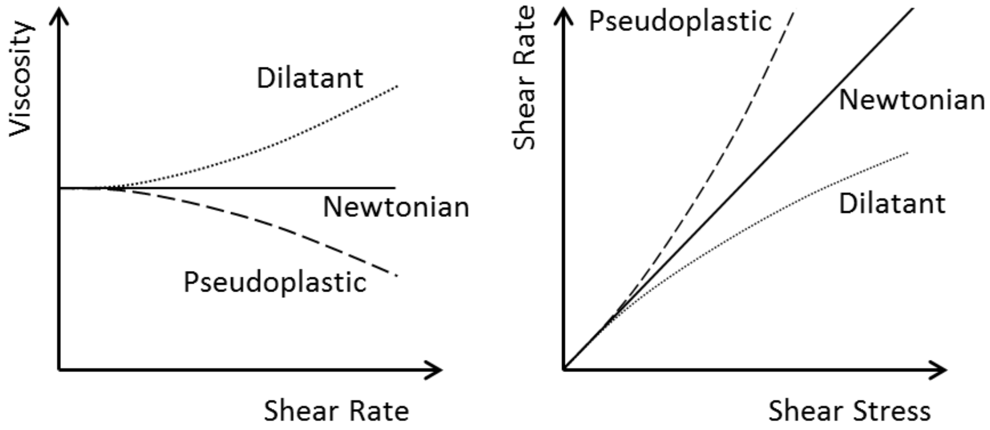

Figure 2.4: Newtonian and non-Newtonian properties of different fluids, Viscosity versus shear rate and Shear rate versus Shear stress

The pseudoplastic behavior describes the viscosity reduction of a fluid at increasing shear rate. Accordingly, this behavior is often called shear-thinning effect. At low shear rate the molecules of the fluid are randomly arranged but at high shear rate the molecules tend to align in shear direction and the effective viscosity changes [81]. A multigrade lubricant - as it is used in this study - has a distinct pseudoplastic behavior because of its complex composition (see section 2.2.3).

Contrary to the shear-thinning is the shear-thickening or dilatant behavior of a fluid. The viscosity increases with an increase of shear rate. Fluids with a high content of solid particles show this behavior. The interactions of the solid particles grow with high shear rate which causes the shear-thickening [81].

Boundary friction

Boundary friction describes the energy losses when the two sliding surfaces are in direct contact. According to Stachowiak [81] three basic mechanisms of frictional losses due to solid contact can be identified which are illustrated in figure 2.5.

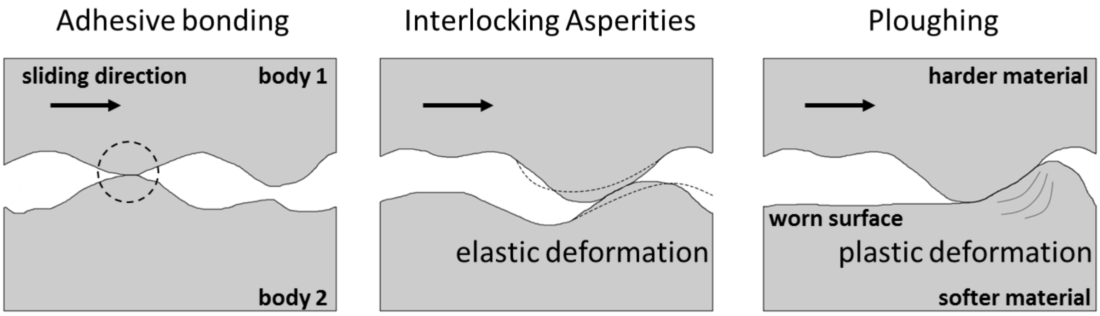

Figure 2.5: Basic mechanisms of frictional energy dissipation

- Adhesion: The interacting and deformed asperities are bonded together by interatomic forces. A force is required to overcome this bonding and to separate the two contacting bodies again. Adhesion causes high friction losses and plays an important role for unlubricated contacts. In lubricated contacts the lubricant additives build a surface layer which prevent or reduces the formation of interatomic bonding.
- Asperity interlocking: Two asperities of the opposing surfaces get into contact at their flanks due to the sliding motion. The asperities or at least one asperity must deform to maintain the sliding motion. In the case of elastic deformation the asperities recover their initial shape after the contact. The deformation causes energy losses in form of heat.
- Ploughing: A basic example of plastic deformation is ploughing which is caused when the asperity of one surface is harder than the asperity of the other surface. The harder asperity moves the softer material aside and forms a plastically deformed wave in front of the asperity. Energy is required to deform the material plastically.

While the elastic deformation of the asperities does not cause any wear, adhesion and ploughing modify the surface. Especially in the beginning of the operation the contacting surfaces adapts its surface and a change of friction occurs. The friction coefficient in lubricated contacts typically reduces during the adaption period and may develop a steady state [11].

2.1.2 Wear and wear mechanisms

Wear can be defined as the progressive loss of material from the contacting surfaces as a result of relative motion [51]. Four basic wear mechanisms for solids in contact can be distinguished between [28, 52]:

- Adhesion describes the bonding between the contacting asperities. When the adhesive connection is ruptured again material may transfer from one surface to another. Adhesive wear often forms wear particles.
- Abrasion occurs when a hard asperity or particle gets into contact with a surface

and deforms the surface plastically. Different mechanism can be identified: micro-cutting, fracture, surface fatigue due to repeated ploughing and grain pull-out [81].

- Surface fatigue is a term used for surface damage caused by a cyclic contact stress (Hertzian contact stress). Hence, surface fatigue is more relevant for roller bearings and gears which employ high contact stresses due to a non-conformal contact (point and line contact). Surface cracks, micro-pitting and delamination are examples for surface fatigue mechanisms [81].
- Tribochemical reactions are chemical reactions between the contacting surfaces, the lubricant and the environment which occurs due to the thermal and mechanical stresses. A reaction layer is formed on the contact surface which has different properties than the initial surface layer and the wear rate may increase.

The continuous wear behavior can be quantified and characterized by the progress of the wear volume. Basic trends of the wear volume over the operation time are illustrated in figure 2.6.

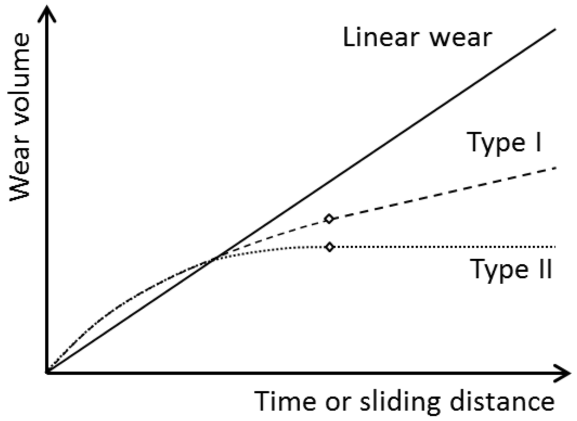

Figure 2.6: Illustration of basic wear behavior in lubricated contacts

The linear wear curve shows a constant wear progress over course of the operation time. The wear rate which is defined as the gradient of the curve is constant. Usually, at the beginning when the two contacting surfaces operate together for the first time, an adjustment process takes place and the wear rate decreases. This adjustment process is generally known as running-in process [11]. Type I and type II in figure 2.6 show a typical running-in behavior. After the running in process, type I shows a linear wear behavior which can often be found in contacts operating in boundary lubrication regime (for example, see [48, 90]). Journal bearings mainly operate in pure hydrodynamic lubrication regime and continuous wear is typically absent after an initial running-in process (type II).

The running-in process affects the geometrical conformity of the two contacting surfaces on a macro and micro scale as well as affects the mechanical and material properties [11]. Figure 2.7 illustrates the difference between macro scale adaption and the micro scale adaption of the surface.

The solid black and solid gray line show the roughness of a new and a worn contact surface. The dashed line represents the center lines of the corresponding rough surface. The transformation of the center line describes the adaption on the macro scale caused by wear. The adaption on macro scale is further called geometrical adaption of the surface.

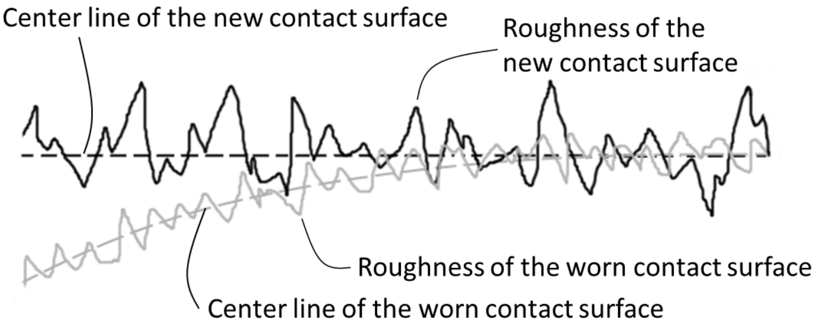

Figure 2.7: Sketch of a new and worn contact surface

The adaption on the micro scale concerns the change of the surface roughness. For journal bearings, it is typical that the roughness parameters of the softer bearing shell get smoother during the running-in process. This process is also called surface smoothing.

2.2 System components

For journal bearing application, the components which affect the tribological contact include the journal, the bearing shell with the surrounding structure, the lubricant and the environment. The surrounding structure and the environment are generally given by the situation. Therefore, the shaft, the bearing shell and the engine oil are briefly discussed in this section with a focus on the specific demands and properties for the bearing shell and the lubricant.

2.2.1 Journal

The journal is the part of the rotating shaft which slides over the bearing shell. A smooth and a hard journal surface is required to ensure a long journal bearing lifetime. In general, the shaft is therefore made of steel which is machined and heat-treated. A crankshaft is typically made of forged steel or cast steel followed by a subsequent machining and heat-treatment. This process provides a shaft with high strength, durability and great hardness. In this study, a machined and hardened shaft is utilized.

2.2.2 Bearing shell

Highest demands for bearing shells are given in automotive crank shaft bearing due to the high mechanical and thermal loads in combustion engines [25]. In this study, bearing shells which are designed for automotive application are investigated. Hence, a brief overview of the requirements on automotive journal bearings is presented and the investigated bearing materials are addressed.

Requirements and materials for journal bearings in automotive application

The requirements for crank shaft journal bearings are diverse and a wide variation of bearing shells properties are demanded. Detailed overview of requirements on bearing shells can be found in [26, 27, 52, 82]. A brief overview is provided in the following:

- Adaptability: During the running-in process the bearing shell adapts its surface to any misalignment of the shaft. The ability to adapt the bearing surface is called adaptability or conformability.

- Embeddability: Hard particles (e.g. wear debris or soot) get into the lubricated contact via the oil supply and might damage the bearing shell. To reduce the damage the hard particles are embedded into the bearing shell.
- Load capability: The bearings are excited by high dynamic loads. A high mechanical and thermal strength of the bearing shell is required to resist deformation.
- Seizure resistance: When the bearing operates in boundary lubrication regime e.g. due to a lack of lubricant the contact surfaces tend to weld together (seizure). Good emergency running behavior is required in this situation.
- Corrosion and oxidation resistance: The bearing shell is exposed to aggressive substances in the lubricant (e.g. fuel, blow-by gas or chemical products) which chemically attack the bearing material.

To cope with these increasing demands, complex materials were developed in the last decades. Sputter bearings, which were first introduced at the beginning of the 1980s [25], are suitable for extreme load conditions as they occur in connecting rod bearings in diesel engines.

Sputter or tri-metal bearings typically consist of a copper based lining material (brass or bronze) which is sintered or casted onto a steel back. On top of the lining material is a softer running layer. The sputtered running layer material typically is an alloy of aluminum, tin and copper (e.g. AlSn25Cu2.5) and has a thickness between 10 μm and 30 μm. The sputter layer is able to adapt its surface during the running-in and to embed hard particles. It also protects the bearing shell from corrosion and oxidation. The tin content reduces the risk of seizure. The brass or bronze layer is responsible for a high load capability and for a safe operation in the case the sputter layer is run through. The thickness of the lining material is between 150 μm and 500 μm. The steel back gives the mechanical strength which is required for the high mechanical loads (1.5 mm to 2.5 mm thickness).

Beside the sputter bearings aluminum composite bearings (also called bi-metal bearings) are used in this study. The aluminum composite bearing consists of an aluminum alloy with tin and copper which is metallurgically bonded on a steel back. The aluminum layer presents a good embeddability and adaptability of the bearing surface. Aluminum composite bearings bare the big advantage of the lower production costs compared to the sputter bearings. The limitation for the use of aluminum composite bearings is due to the lower mechanical strength.

2.2.3 Lubricant

This study focuses journal bearings and lubricants which are typically used in combustion engines and therefore this brief overview shall focus on automotive engine oils.

Demands and composition of lubricants

The main function of the lubricant is to separate the contacting surfaces to facilitate a smooth power transmission between the shaft and the bearing. In this process, the lubricant cools the involved components, removes dirt and debris to keep the surfaces clean, reduces friction and protects the surfaces from wear [52, 58]. To meet these challenging requirements - in particular for modern combustion engines - a complex composition of lubricants is necessary. Therefore, typical engine oil consists of a base oil (or base stock) which accounts to between 80 % and 95 % of the lubricant formulation [81] and an additive package (5 % to 20 %) which improves the chemical and physical properties of the base oil or affects the contact surfaces [8].

The base oil can be a mineral oil, synthetic oil or a mixture of both. Mineral oils are typically refined from crude oil and are most commonly used as engine oils. In recent years the demand for high performance lubricants has increased and synthetic oils have emerged on the market for engine lubricants. Hydrocarbon lubricants are the most important type of synthetic oils which are artificially produced mainly by polymerization of short-chain hydrocarbons (like ethylene) or other modified petroleum components. Polyalphaolefins (PAO) are an important example for synthetic hydrocarbons lubricants. Ester based lubricants and polyglycols are also covered in the group of synthetic hydrocarbons. Main advantages of synthetic lubricants compared to mineral oil based lubricants are a higher oxidation resistance, a low volatility and a good viscosity-temperature behavior [81]. Environmentally-friendly and biodegradable base oils were recently studied for alternatively composed lubricants [89].

The base oil is responsible for the fundamental physical properties of the lubricant. Of special interest in this study, is the lubricant's viscosity which drastically decreases with an increasing temperature. For a safe running of the bearing, the lubricant has to guarantee a sufficient high viscosity at high temperature to keep the contacting surfaces separated. The higher viscosity at low temperature raises the friction losses and lowers the efficiency. At even lower temperature, the pumpability of the lubricant must be given [84]. An arbitrary measure for the viscosity temperature relation is the viscosity index (VI). The definition of the viscosity index can be found in [81] or [84]. A preferable high viscosity index represents a lower temperature dependency of the lubricant. The viscosity behavior for two different lubricants is illustrated in figure 2.8 on the left.

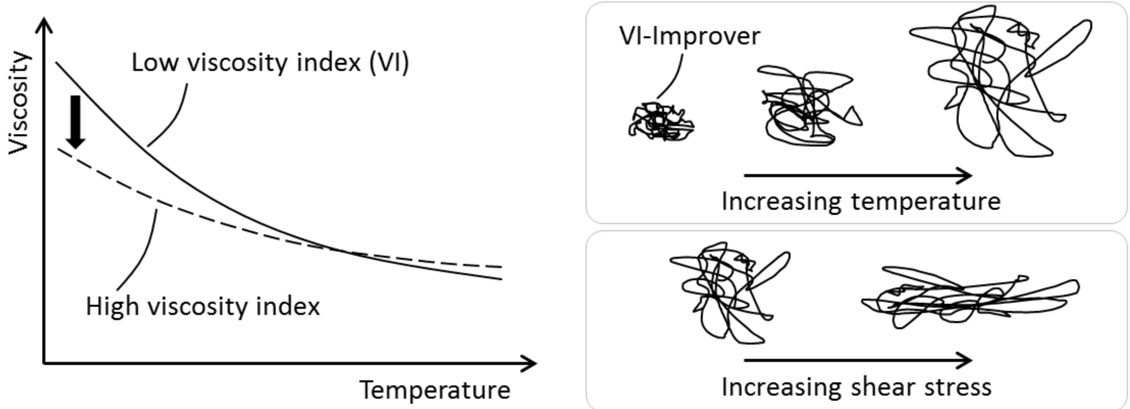

Figure 2.8: Viscosity temperature relation of lubricants with and without friction modifier, illustration of the functionality of viscosity index (VI) improver

A high viscosity index can be achieved when a viscosity index improver (VI-improver or viscosity modifier) is added to the base oil. VI-improvers are typically chain-like polymers with a high-molecular weight and are dissolved in the oil [81]. The molecules are able to change their shape with temperature. The basic mechanism of a VI-improver is illustrated in figure 2.8 on the top right. At low temperature, the VI-improvers are coiled to a spherical shape and do not affect the viscosity. With an increase of temperature, the VI-improvers uncoil due to a better solubility at high temperature. The polymers spread out and cause an increase in viscosity. The side effect of VI-improvers is a viscosity drop at high shear stress which is caused by the alignment of the high-molecular polymers in the lubrication gap (see figure 2.8 on the bottom right). This shear-thinning effect can be temporary or permanent in the case that the high shear stress breaks down the polymers. Modern multigrade engine oils are composed of low-viscosity base oil and VI-improvers and show a distinct shear-thinning behavior.

Additional additives enhance the properties of an engine oil to fulfill the demands above mentioned. These additives are briefly outlined below. A detailed description of their functionality can be found in various textbooks, e.g. in [52, 58, 67, 81].

- Detergents and dispersants keep impurities in the lubricant (e.g. debris, soot, water, acids) solubilized and prevent the formation of deposits and sludge.
- Extreme-pressure (EP) and anti-wear (AW) additives protect the contact surface and reduce friction and wear. The molecules are bonded to the surface either by physical adsorption or chemisorption which involves a chemical reaction between the additives and the contact surface. Zinc dialkyldithiophosphates (ZDDP) is an important example for the latter.
- Friction Modifiers (FM) can be fatty alcohols or amides and form thin surface layers due to physical adsorption. These surface layers reduce the boundary friction coefficient in mixed lubrication but are ineffective at high temperatures. Friction modifiers with a different functionality are e.g. molybdenum dithiocarbonate (MoDTC) which forms small plates of MoS_2.
- Rust inhibitors are polar molecules which adsorb on steel and protect the surface from corrosion.
- Oxidation inhibitors (Antioxidants) reduce oxidation of the hydrocarbon molecules and enhance the lifetime of the engine oil.
- Foam inhibitors are additives which have a lower surface tension than the oil itself. When air is entrained and mixed into the oil foam inhibitors prevent the formation of foam.
- Pour point depressants lower the temperature at which the formation of paraffin wax occurs and prevents oil thickening in the range of operation temperature.

The lubricant used in this study is a multigrade engine oil. It is composed of low-viscous hydrocarbon base oil and a complete additive package. The rheological data of the studied oil including the viscosity temperature relation as well as the viscosity behavior at high shear stress is presented in section 4.4.3.

Chapter 3

Testing

Tests are required for the comprehensive verification and validation of the journal bearing simulation approach under severe condition. Therefore, journal bearing tests are performed at a journal bearing test-rig. Measurement results are thus evaluated in comparison with the simulation results. This chapter gives a brief overview of the journal bearing test-rig which is used for this study.

3.1 Journal bearing test-rig

Various journal bearing tests are conducted at the test-rig at KS Gleitlager (referred to as ”test-rig” hereafter) is shown in figure 3.1.

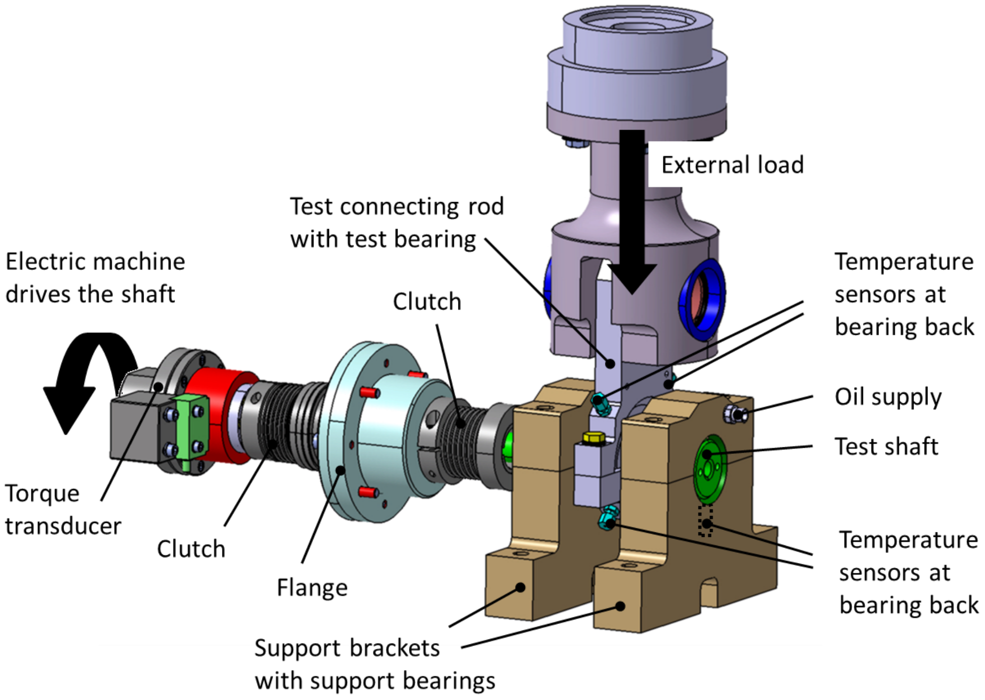

Figure 3.1: Components of the journal bearing test-rig

The test-rig enables a detailed analysis of journal bearing behavior under static and dynamic loads for constant or transient shaft speed. The test-rig consists of a straight shaft (test shaft) which rests on two support brackets. Each support bracket contains a plain journal bearing and is fixed on a base. The test connecting rod with the test bearing is placed in between the two support brackets. An external load is applied on the test connecting rod which is generated by an electromechanical high-frequency pulsator. The test shaft is driven by an elastically clutched electric motor.

The dimensions and oil supply design of the two support bearings correspond to automotive main bearings with a partial circumferential oil supply groove. The oil supply groove employs over the upper half of the bearing with a circumferential extension of 180° and has a width of 5 mm. It is located in the axial center of the bearing. The test journal bearing corresponds to a big-end bearing with an oil supply hole in the load-free (lower) shell. The bearing dimensions are listed in table 3.1.

Table 3.1: Journal bearing dimensions and properties

	support bearing	test bearing
Width [mm]	25	17.2
Diameter [mm]	54	47.8
Thickness [mm]	2.5	1.5
Diametral clearance [μm]	50	30 (23[2])
Oil supply	partial circumferential groove	1.5 mm bore

Two different bearing material types are used for the tests. The support bearings are made of a steel-aluminum composite material. The highly loaded test bearing is either a sputter bearing or a steel-aluminum composite bearing. The test bearing material is further specified in the particular result section.

The supplied oil is brought to temperature and stabilized with an external conditioning unit. Additionally, either the oil flow rate or the supply pressure can be imposed via a control unit. In this study, the supply pressure is imposed.

3.1.1 Measurement equipment

The total friction torque caused by all three journal bearings is measured by a torque transducer which is located between the motor and the clutch. The torque transducer, a Manner Sensortelemetrie 50 Nm standard sensor element, has an accuracy of ± 0.15 Nm. The rotational speed of the shaft is also measured by the torque transducer. The uncertainty of the speed measurement is evaluated with ± 42 rpm.

For the temperature measurements, PT100 elements are used which have an accuracy of ± 0.5 °C. The temperature sensors have a diameter of 2 mm. Two oil supply temperatures are recorded during each test run, one for both support bearings, and one for the test bearing. Additionally, temperatures at the back of the bearing shells are measured. Therefore, the distance from the measurement position to the lubricated gap is equal to the bearing thickness (see table 3.1). In axial direction, the temperature sensors are located in the center. Both support bearings are equipped with one sensor in the high load zone at an angle ζ of 180° as shown in figure 3.2. Four temperature sensors are applied to the test bearing and are evenly distributed along the circumferential direction at angles ζ of 45°, 135°, 225° and 315°.

---

[2] For the study of the start-stop behavior, a diametral clearance of 23 μm is identified for the test bearing (see section 5.4)

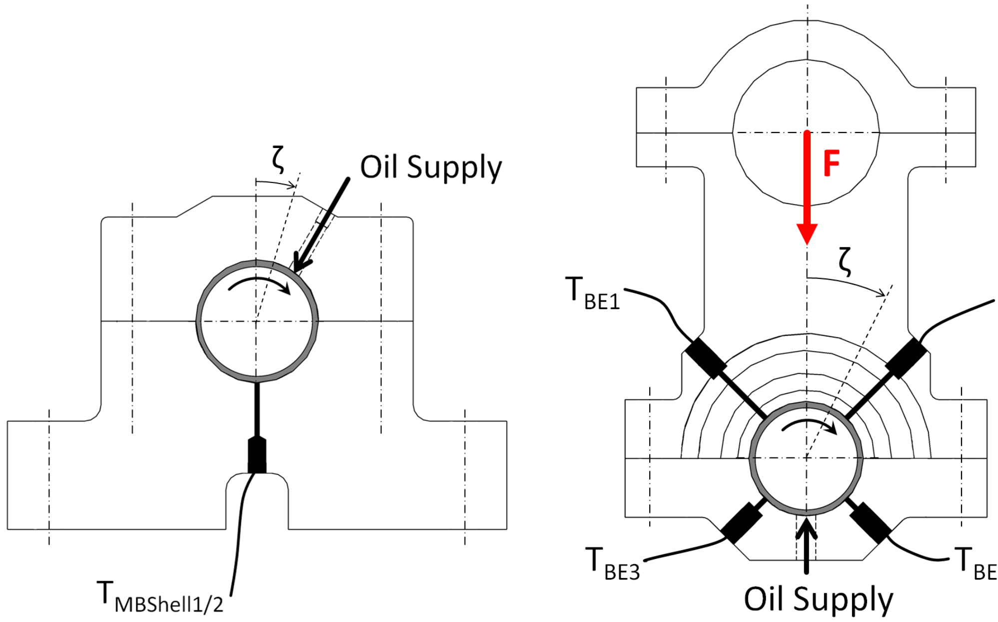

Figure 3.2: Temperature measurement positions in the support bearings (left) and the test bearing (right)

Supply pressure and oil flow are also monitored and recorded during the tests. Both are measured collectively for the two support bearings and for the test bearing separately. HBM-P3IC pressure transducers with an uncertainty of ± 0.3 MPa are used to measure the supply pressure. The oil flows are determined by gear type flow meters VC from Kracht with an uncertainty of 0.3 %. The externally applied force acts in vertical direction. The definition of the positive force direction is shown in figure 3.2 as red arrow. A force transducer from interface force measures the load with an uncertainty of ± 0.4 kN.

3.1.2 Test conditions

The load conditions and shaft speed conditions vary for the realized tests. The measurements which are performed to analyze the hydrodynamic bearing performance are conducted with high dynamic loads and constant shaft speed. Therefore, specific pressures up to 100 MPa are reached for some tests. In other tests, a static load is applied to operate the bearings mixed lubrication regime. For a static load, a lower specific pressure is sufficient to obtain noticeable metal-metal contact. For the start-stop investigation, the shaft follows a transient speed ramp. Consequently, it is reasonable to describe the detailed test conditions for each test in the corresponding application example in the result section (see section 5).

Chapter 4

Simulation

Lubricated contacts and particularly journal bearings have been the central of tribological research for the last century. In 1886, Osborne Reynolds presented the basic equations to describe lubricated contacts in his publication on the theory of lubrication [72]. These equations are still of ongoing importance in today's journal bearing analysis. Arnold Sommerfeld [80] determined the analytical solution for an infinitely long bearing. He studied the movement of the journal within the bearing and evaluated the friction coefficient for varying shaft speeds.

DuBois and Ocvirk [31] derived an analytical solution for short bearings and verified the calculated hydrodynamic pressure distribution to measurements. The analytical solutions for both, the infinitely long and the short bearing, describe the behavior for steady state conditions.

For dynamically loaded journal bearings Booker [17, 18] introduced the mobility method in 1965 and presents numerical solutions for general bearing problems. The method originally considers the short bearing approximation introduced by DuBois. The mobility method was widely used as a design tool and to assess bearing performance [71, 83, 85]. However, the mobility method doesn't consider metal-metal contact and is therefore restricted to pure hydrodynamic lubrication regime. Further, elastic deformation of the contacting bodies is not considered.

In addition to the analytical and simplified solutions, numerical methods were established which consider elastic deformation of the journal and the bearing. An early elasto-hydrodynamic bearing simulation method was presented by Oh and Huebner [64] in 1973. The authors used the finite element technique and presented an iteration scheme to calculate a three dimensional deformation of the housing and to solve the Reynolds equation simultaneously. With the increase of computational capability, the elasto-hydrodynamic bearing simulation could gain more and more attention. Booker and Boedo [19] give an overview of the achievements for elasto-hydrodynamic bearing simulation with a focus on numerical approaches.

In today's bearing applications, the elastic deformation of the contacting bodies plays a key role. Due to high specific loads (above 100 MPa for the big end bearing in internal combustion engines), the magnitude of the deformation is in the same order as the lubrication gap itself.

Further, the increasing load leads to high hydrodynamic pressures within the lubricant which necessitates that the lubricant properties at high pressure have to be considered. Multigrade engine oils behave highly non-Newtonian which further means that the shear rate dependency of the viscosity needs to be considered.

During the running-in process of journal bearings or during the starting of the shaft, the bearing operates in boundary and mixed lubrication regime. Consequently, metal-metal contact must be represented in the simulation approach.

To fulfill these requirements (including elastic deformation, lubricant properties at high pressure and high shear rate, metal-metal contact), a numerical simulation approach is necessary. This chapter describes the basic equations for the simulation approach used in this study. It starts with the basic Reynolds equation and describes in detail the consideration of cavitation region, micro-hydrodynamic and metal-metal contact. Also, the representation of the lubricant properties in the elasto-hydrodynamic simulation approach is described.

4.1 Journal bearing simulation theory

The basic equation to obtain the hydrodynamic pressure in lubricated contacts like journal bearings is the Reynolds equation, derived by Osborne Reynolds in 1886. It can be derived from the Navier Stokes equation by considering the following assumptions:

- The body forces of the fluid are neglected (e.g. gravity)
- The film thickness is (very) small compared to the other dimensions of the lubricated contact. For this reason, the pressure across the film thickness is considered constant
- The curvature of the contacting surfaces is large compared with film thickness
- There exists no slip at boundaries
- The lubricant is Newtonian and the viscosity is therefore independent on shear rate
- The lubricant shows a laminar flow
- Fluid inertia is neglected
- The lubricant viscosity is constant in film thickness direction[3]

The detailed derivation can be found in many textbooks containing information on hydrodynamic lubrication theory [13, 21, 41, 81]. Therefore, a complete derivation of the Reynolds equation is omitted here. In general, the Reynolds equation for journal bearings can be written as:

$$\begin{aligned} &\overbrace{-\frac{\partial}{\partial x}\left(\frac{h^3}{12\eta}\frac{\partial p}{\partial x}\right)-\frac{\partial}{\partial y}\left(\frac{h^3}{12\eta}\frac{\partial p}{\partial y}\right)}^{\text{Poiseuille term}}+\\ &\underbrace{+\frac{\partial}{\partial x}\left(h\frac{u_1+u_2}{2}\right)+\frac{\partial}{\partial y}\left(\frac{v_1+v_2}{2}\right)}_{\text{Couette term}}+\underbrace{\frac{\partial h}{\partial t}}_{\text{Squeeze term}}=0, \end{aligned} \tag{4.1}$$

where x, y denote the circumferential and the axial direction, respectively. p is the hydrodynamic pressure and h the oil film thickness which is dependent on x and y.

---

[3] Studies by various authors, such as [1, 12, 16], have shown that the temperature varies across the film thickness direction. Therefore, the viscosity is not constant across the film thickness direction but for simplified modeling, it can be assumed to be constant.

Further, u_1, u_2, v_1 and v_2, denote the sliding speeds in x and y direction of the two sliding surfaces '1' and '2'. $\eta = \eta(x, y, t)$ represents the oil viscosity which is dependent on location and time.

The Poiseuille term describes the fluid flow caused by a pressure gradient in the fluid film. The Couette term defines the shear flow driven by relative movement of the opposed surfaces. The squeeze term represents the time dependent hydrodynamic film thickness which will change due to a normal movement (squeeze) of the two surfaces. The normal movement creates a hydrodynamic pressure field on the bearing.

The fluid velocity in the lubrication gap is observed by superposing the Poiseuille flow and Couette flow (see figure 4.1).

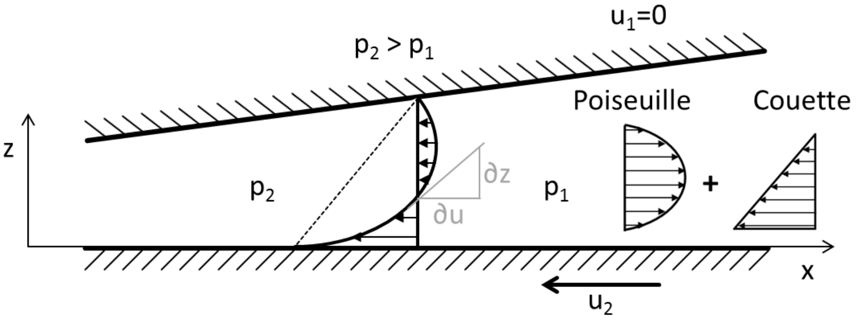

Figure 4.1: Superposition of Poiseuille and Couette flow in lubrication gap

The pressure gradient causes a parabolic fluid velocity profile along the film thickness. The shear flow produces a linear velocity profile. The effective velocity profile is a combination of shear and pressure flow.

For journal bearings the sliding speed in axial direction is zero. Therefore, the term $\frac{\partial}{\partial y}(\frac{v_1+v_2}{2})$ becomes zero.

For compressible fluids a variable density $\rho(x, y, t)$ is introduced, accordingly to the viscosity which is dependent on location and time. The Reynolds equation for journal bearings with compressible fluids can then be written as:

$$-\frac{\partial}{\partial x}\left(\theta \frac{h^3 \rho}{12\eta} \frac{\partial p}{\partial x}\right) - \frac{\partial}{\partial y}\left(\theta \frac{h^3 \rho}{12\eta} \frac{\partial p}{\partial y}\right) + \frac{\partial}{\partial x}\left(\theta h \rho \frac{u_1 + u_2}{2}\right) + \frac{\partial}{\partial t}(\theta h \rho) = 0. \tag{4.2}$$

In the region of a divergent lubrication gap, subambient pressure occurs. This subambient pressure causes a disruption of the liquid phase. In general, two forms of film rupture or cavitation are recognized [13, 30]. First, gas from the environment (air) may enter into the fluid film due to the subambient pressure in the lubrication gap. This behavior can be observed in bearings operating in steady-state conditions. Structured air cavities are typically formed. Second, the pressure in the lubrication gap drops below the vapor pressure of the fluid. As a consequence, vapor-filled bubbles are formed which collapse when they enter a region with high pressure. The bubbles appear unstructured. This form of film rupture is mainly relevant to dynamically loaded bearings.

To consider film rupture or cavitation in the simulation, a mass conserving model which is based on the Jakobsson-Floberg-Olsson (JFO) approach [43, 7] is utilized in this study. Therefore, θ is introduced to the equation (4.2) which represents the fill ratio [45, 70]. In the cavitation region (C), the hydrodynamic pressure p becomes the cavitation pressure p_c and the fill ratio is below 1. In the lubricated region (L), the fill ratio becomes 1.

$$\begin{aligned} p > p_c \wedge \theta = 1 \Leftrightarrow (x,y) \in L \\ p = p_c \wedge \theta \leq 1 \Leftrightarrow (x,y) \in C \end{aligned} \tag{4.3}$$

4.1.1 Reynolds equation for non-Newtonian fluids

To this point, the presented Reynolds equation assumes Newtonian fluids. Non-Newtonian fluids change their viscosity with respect to the shear rate ($\eta(\dot{\gamma})$). The shear rate changes in film thickness direction ($\dot{\gamma} = \frac{\partial u}{\partial z}$, compare figure 4.1). Therefore, the viscosity of non-Newtonian fluids varies in film thickness direction and the Reynolds equation can be extended by the coefficients f_1^2, f_2 and f_3 [7, 39, 45]:

$$-\frac{\partial}{\partial x}\left(\theta f_1^2 \frac{\partial p}{\partial x}\right) - \frac{\partial}{\partial y}\left(\theta f_1^2 \frac{\partial p}{\partial y}\right) + \frac{\partial}{\partial x}(\theta f_2) + \frac{\partial}{\partial t}(\theta f_3) = 0, \tag{4.4}$$

with

$$f_1^2 = \rho h^3 \int_0^1 \frac{Z}{\eta}\left(Z - \frac{\int_0^1 \frac{Z}{\eta} dZ}{\int_0^1 \frac{1}{\eta} dZ}\right) dZ, \tag{4.5}$$

$$f_2 = \rho h \left(u_2 (1 - \frac{\int_0^1 \frac{Z}{\eta} dZ}{\int_0^1 \frac{1}{\eta} dZ}) + u_1 \frac{\int_0^1 \frac{Z}{\eta} dZ}{\int_0^1 \frac{1}{\eta} dZ}\right), \tag{4.6}$$

and

$$f_3 = \rho h. \tag{4.7}$$

A major simplification for the computation of the coefficients can be achieved by introducing an averaged shear rate [39] of

$$\overline{\dot{\gamma}} = \frac{\partial u}{\partial z} \cong \left| \frac{u_2 - u_1}{h} \right|. \tag{4.8}$$

As a consequence, the viscosity is evaluated for the averaged shear rate and is therefore independent on film thickness direction. An average viscosity in film thickness direction is therefore given as

$$\overline{\eta} = \eta(T, p, \overline{\dot{\gamma}}) \quad (= \eta(x, y, t)). \tag{4.9}$$

The coefficients f_1^2 and f_2 are simplified to

$$f_1^2 = \frac{\rho h^3}{12\overline{\eta}}, \tag{4.10}$$

$$f_2 = \rho h \frac{u_2 + u_1}{2}. \tag{4.11}$$

Finally, the Reynolds equation with an average shear rate reduces to a form which is similar to equation (4.2) for Newtonian fluids

$$-\frac{\partial}{\partial x}\left(\theta \frac{h^3 \rho}{12\overline{\eta}} \frac{\partial p}{\partial x}\right) - \frac{\partial}{\partial y}\left(\theta \frac{h^3 \rho}{12\overline{\eta}} \frac{\partial p}{\partial y}\right) + \frac{\partial}{\partial x}\left(\theta h \rho \frac{u_1 + u_2}{2}\right) + \frac{\partial}{\partial t}(\theta h \rho) = 0. \tag{4.12}$$

This major simplification is reasonable for journal bearing applications for which the relative velocity between the contacting surfaces is high compared to the hydrodynamic pressure gradient. The assumption is supported by evaluating the velocity variation across the film thickness. The velocity variation is calculated according to

$$u(x,y,z) = \frac{\partial p}{\partial x} \cdot \frac{z(z - h(x,y))}{2 \cdot \eta} + \frac{u_1 + u_2}{h(x,y)}(z - h(x,y)), \tag{4.13}$$

which is presented in many textbooks (e.g. in [69, 81]). Due to the small geometry inclination between journal and bearing shell, the fluid flow is considered as flow between two parallel surfaces.

Variation of the velocity component *u* across the film thickness is calculated for the test bearing excited by dynamic loads where high pressure and further high pressure gradients occur. The results are taken from application example I (see section 5.1). The velocity variation at the axial center of the bearing is plotted in figure 4.2 for two different speeds.

The top graph shows results of the test bearing at 7000 rpm and the bottom graph at 1000 rpm, respectively. The bearing is loaded with a dynamic force which has a maximum specific pressure of 100 MPa. The figure is captured when the maximum load occurs. The solid black line represents the hydrodynamic pressure distribution. It has a maximum at the top bearing position (0°) of 200 MPa for both shaft speeds.

The shaded area represents the lubrication gap (fluid film) between the two contacting surfaces '1' and '2' (bearing shell and shaft). Due to the elastic deformation of the bearing shell which is caused by the high pressure, an almost linear lubrication gap can be identified between -60° and 45°. The minimum lubrication gap is located at around 45°. However, each line of the shaded area represents the calculated variation of the velocity component u across the film thickness direction at the corresponding circumferential location. The relative sliding velocity between surface '1' and surface '2' is calculated by $\Delta u = u_1 + u_2$. The viscosity profile appears as a straight line which indicates that the velocity in the fluid film is dominated by the Couette term (shear flow). A significant pressure flow caused by the Poiseuille term cannot be identified. The inclination of the single lines increases as the film height decreases because the relative sliding velocity is constant. At 7000 rpm the relative velocity is larger compared to 1000 rpm which can also be identified by comparing the top and bottom graph.

The results justify the simplified estimation of the averaged shear rate in journal bearings for the intended applications.

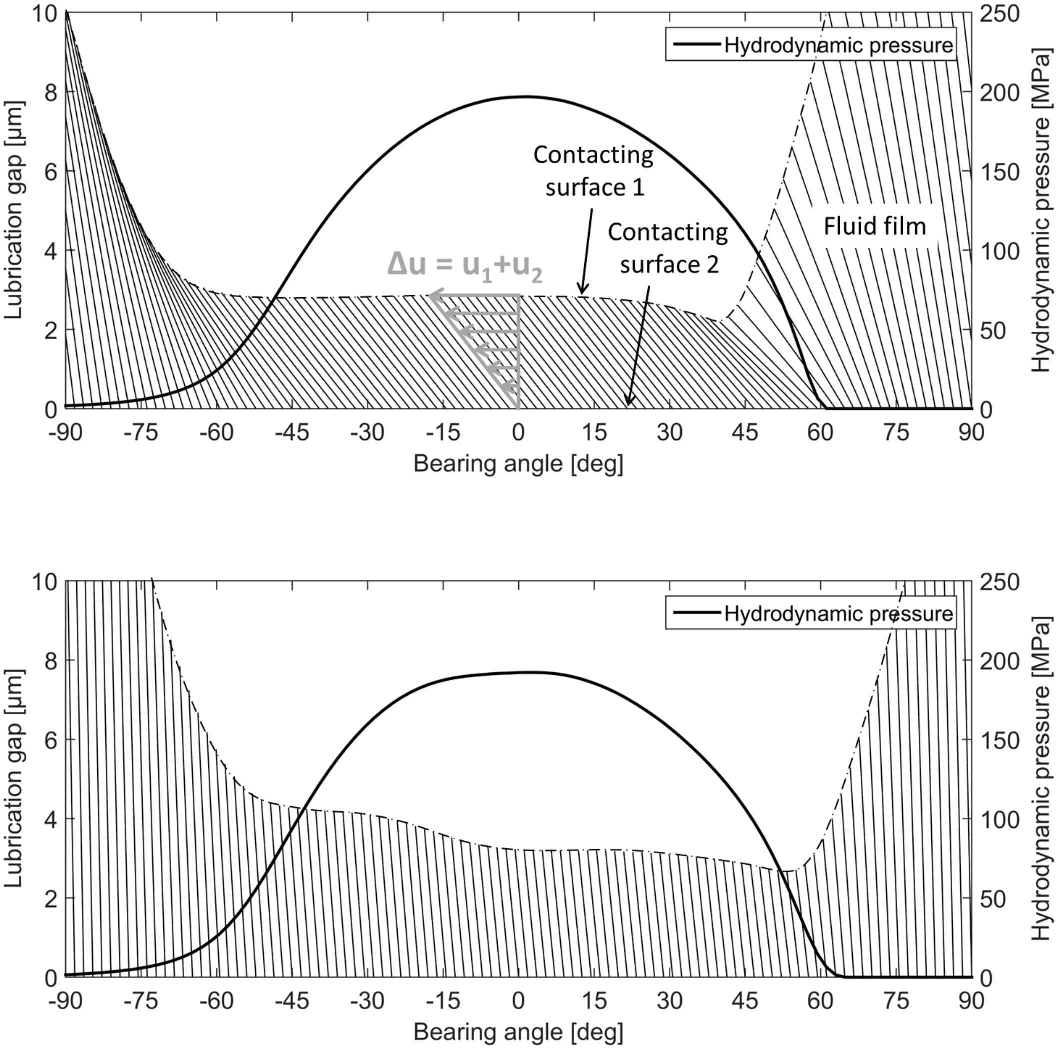

Figure 4.2: Variation of the velocity component u across the film thickness at different circumferential bearing positions at 7000 rpm (top) and 1000 rpm (bottom)

4.1.2 Averaged Reynolds equation for rough surfaces

The previously presented Reynolds equation describes the pressure distribution in a hydrodynamic journal bearing for smooth surfaces. However, if the minimum film thickness gets small, the asperities on the contacting surfaces can affect the hydrodynamic film and the oil flow. These effects are called micro-hydrodynamic effects. In simulation, these effects can either be computed by considering rough surfaces in the lubrication gap (direct method) or by using correction factors (flow factors) which are added to the Reynolds equation (indirect method) [7, 15]. In this study the indirect method is utilized. Patir and Cheng [65, 66] introduced the flow factors to the Reynolds equation:

$$
\begin{aligned}
&-\frac{\partial}{\partial x}\left(\phi_{\mathrm{x}}\theta\frac{h^3\rho}{12\overline{\eta}}\frac{\partial p}{\partial x}\right)-\frac{\partial}{\partial y}\left(\phi_{\mathrm{y}}\theta\frac{h^3\rho}{12\overline{\eta}}\frac{\partial p}{\partial y}\right)+\\
&+\frac{\partial}{\partial x}\left(\theta h\rho\frac{u_1+u_2}{2}\right)+\frac{\partial}{\partial x}\left(\phi_{\mathrm{s}}\theta\rho\frac{u_1+u_2}{2}\sigma_s\right)+\frac{\partial}{\partial t}(\theta h\rho)=0.
\end{aligned}
\tag{4.14}
$$

where ϕ_{x} and ϕ_{y} refer to the pressure flow factors in axial and circumferential direction and ϕ_{s} describes the shear flow factor. These flow factors are predetermined for varying film height and different boundary conditions. They can be interpreted as the relation of the oil flow between rough surfaces and the oil flow between smooth surfaces. In general, there exist two methods to predetermine the flow factors [7, 15]. The deterministic method uses the real surfaces to determine the flow. Calculations at various boundary conditions are performed between fractions of the real surfaces. The flow factors are determined from these calculations. The stochastic methods consider statistical roughness parameters of the surface to identify the flow factors. In this study, the stochastic method according to Patir and Cheng [65, 66] is utilized. Patir and Cheng calculated the flow factors for numerically generated surfaces with a Gaussian distribution of the asperity heights. The asperities are assumed to be rigid and oriented along the axial or circumferential direction. The standard deviation of the surface height and the asperity orientation are parameters for the stochastic method. The orientation is taken into account by the definition of Peklenik [68]:

$$
\Gamma=\frac{\lambda_{0.5x}}{\lambda_{0.5y}},
\tag{4.15}
$$

where $\lambda_{0.5x}$ and $\lambda_{0.5y}$ represent the autocorrelation length in circumferential and axial direction, respectively. If Γ is greater than one, the asperities are aligning with the circumferential direction. For Γ smaller than one, the asperities are oriented along the axial direction.

In this study, the standard deviation of the asperity heights and the asperity orientation are determined from surface scans of the bearing surface and the shaft surface. These parameters are used to calculate the flow factors according to Patir and Cheng.

4.1.3 Asperity contact: Greenwood and Tripp

When a fluid film cannot completely separate the two contacting surfaces anymore, single asperities interact and metal-metal contact occurs. To take metal-metal contact into account, a contact model is included in the simulation approach. The contact model returns the asperity contact pressure and the contact area for a specific film height. In this study, asperity contact is calculated using the Greenwood and Tripp approach [35, 36]. The theory of Greenwood and Tripp is based on the contact of two nominally flat, randomly rough surfaces. The main assumptions for the relative simple contact model are:

- The asperity heights are normally distributed (Gaussian distribution)
- All asperities have the same peak curvature (mean summit radius)
- Asperities can deform elastically, plastic deformation is not considered
- The method is based on the Hertzian contact theory for single asperities

- Neighboring asperities do not influence the deformation of single asperities

With these assumptions taken into account, the asperity contact pressure can be written as

$$p_{\mathrm{a}} = KE^{*}F_{\frac{5}{2}}(H_s), \tag{4.16}$$

with a composite elastic modulus

$$E^{*} = (\frac{1-\nu_1^2}{E_1} + \frac{1-\nu_2^2}{E_2})^{-1}, \tag{4.17}$$

where ν_1, ν_2, E_1 and E_2 are the Poisson ratio and Young's modulus of the two sliding surfaces '1' and '2'.

$F_{\frac{5}{2}}(H_s)$ is an integral of the Gaussian distribution of asperity heights. This function can only be solved by numerical methods and therefore it is more convenient to use approximation formulas in elasto-hydrodynamic simulation [44]. Greenwood and Tripp presented values for $F_{\frac{5}{2}}(H_s)$ in [35]. However, Hu et al. [42] approximated this function by fitting an efficient power-law formula to the presented values:

$$F_{\frac{5}{2}}(H_s) = \begin{cases} 4.4086 \cdot 10^{-5}(4 - H_s)^{6.804}, & \text{if } H_s < 4 \\ 0, & \text{if } H_s \geq 4 \end{cases} \tag{4.18}$$

where H_s is a dimensionless clearance parameter,

$$H_s = (h - \overline{\delta}_s)/\sigma_s), \tag{4.19}$$

with h being the nominal distance between the two contacting surfaces and $\overline{\delta}_s$ is the combined mean summit height,

$$\overline{\delta}_s = \overline{\delta}_{s,1} + \overline{\delta}_{s,2}. \tag{4.20}$$

The index '1' and '2' refer to the two mating surfaces. Figure 4.3 illustrates two contacting surfaces with a Gaussian distributed summit height.

The combined asperity summit roughness σ_s is calculated according to

$$\sigma_s = \sqrt{\sigma_{s,1}^2 + \sigma_{s,2}^2}, \tag{4.21}$$

where $\sigma_{s,1}$ and $\sigma_{s,2}$ represent the standard deviation of the summit heights of the two surfaces.

The form factor $F_{\frac{5}{2}}(H_s)$ becomes zero for a dimensionless clearance parameter beyond four, which means, that no further asperity contact occurs. Finally, the elastic factor K is defined as

$$K = \frac{16 \cdot \sqrt{2} \cdot \pi}{15} \cdot (\sigma_s \cdot \overline{\beta}_s \cdot \eta_s)^2 \cdot \sqrt{\frac{\sigma_s}{\overline{\beta}_s}}, \tag{4.22}$$

where $\overline{\beta}_s$ is the mean summit radius and η_s is the summit density.

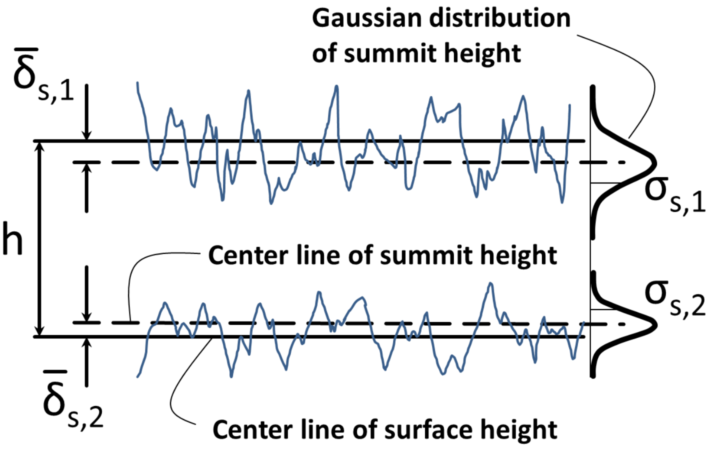

Figure 4.3: Sketch of two contacting surfaces with a Gaussian distribution of their summit heights

4.1.4 Friction in mixed lubrication

Friction losses in mixed lubrication regime consist of both: hydrodynamic losses and losses due to metal-metal contact. The friction force can be calculated by integrating the hydrodynamic shear stress τ_h and the asperity shear stress τ_a over the bearing surface as presented previously in [76]. The friction torque is further obtained by multiplying the friction force with the nominal shell radius r

$$M_{\text{Friction}} = r \iint_A (\tau_h + \tau_a)\, dxdy, \tag{4.23}$$

where A denotes the bearing surface. The hydrodynamic shear stress is calculated by

$$\tau_h = \overline{\eta} \cdot \frac{u_1 - u_2}{h} (\phi_{\text{f}} \pm \phi_{\text{fs}}) \pm \left(\phi_{\text{fp}} \frac{h}{2} \cdot \frac{\partial p}{\partial x} \right), \tag{4.24}$$

where $+$ and $-$ refer to the shell surface and the journal surface, respectively. ϕ_{f}, ϕ_{fs} and ϕ_{fp} are the shear stress factors according to Patir and Cheng. The shear stress factors modify the hydrodynamic shear stress as a result of micro-hydrodynamic effects. In this study, the values from Patir and Cheng are used for the flow factors. η is represented as a function of temperature, pressure and shear rate $\eta(T, p, \overline{\dot{\gamma}})$.

When the two surfaces are in contact, the shear stress caused by asperity interaction is calculated by

$$\tau_a = \mu_{\text{Bound}} \cdot p_a, \tag{4.25}$$

where the asperity contact pressure p_a is calculated according to equation 4.16. Asperity contact occurs if the dimensionless clearance parameter $H_s < 4$ (see equation 4.18). The boundary friction coefficient μ_{Bound} is assumed to be constant in this study. Allmaier et al. [2] defined a boundary friction coefficient of 0.02 which represents a reasonable value for a lubricated contact with fully formulated engine oils which contains friction modifying additives. Therefore, a boundary friction coefficient of 0.02 is chosen.

4.2 Wear calculation: Archard

In general, wear can occur when asperities of the sliding surfaces get into contact. One simple mathematical model to describe sliding wear was established by Archard [4]. Archard's equation is given as

$$h_w = \frac{C}{H} \cdot W \cdot L, \tag{4.26}$$

where h_w is the wear depth, C is a proportional constant which describes the probability for adhesive wear (wear coefficient), W is the normal load, L is the sliding distance and H describes the hardness of the softer contact surface.

The product of normal load and sliding distance can also be expressed by a wear load $\overline{W}_L$ multiplied by the relevant step time t_{step} [62]. Therefore the Archard's equation modifies to

$$h_w = \frac{C}{H} \cdot t_{\text{step}} \cdot \overline{W}_L. \tag{4.27}$$

The wear load is the averaged product of asperity contact pressure p_{a}, obtained from equation (4.16), and the relative sliding speed $|\Delta u|$ during the duration of one load cycle T.

$$\overline{W}_L = \frac{1}{T} \int_t^{t+T} p_{\text{a}} |\Delta u| dt. \tag{4.28}$$

The step time t_{step} represents the adaption time used to achieve a certain wear depth. In this study, instead of defining a step time, a maximum wear depth $h_{w,max}$ is introduced at the position of maximum wear load.

To calculate the wear distribution on the bearing surface, the factor $\frac{C}{H} \cdot t_{\text{step}}$ has to be evaluated. This factor is then multiplied with the local wear load and the worn surface geometry for the bearing is obtained.

With the knowledge of the surface hardness H and the wear coefficient C, an effective step time t_{step} can be calculated.

The wear volume ΔV_w can be calculated by integrating the wear depth over the bearing surface:

$$\Delta V_w = r \iint_A h_w(\varphi, z) d\varphi dz, \tag{4.29}$$

Finally, a material removal rate can be defined as:

$$R_{mr} = \frac{\Delta V_w}{t_{\text{step}}}. \tag{4.30}$$

4.2.1 Iterative surface profile generation

An iterative adaption of the bearing geometry is introduced for the investigation of the running-in process of dynamically loaded journal bearings [75] and the continuous wear process due to repeated starting of the shaft in stop-start application. The iterative generation of the worn surface profile (surface geometry) starts with the nominal bearing shape of a new bearing which is assumed to be a perfect cylinder in this study. Figure 4.4 schematically illustrates the iterative generation of the worn surface profile.

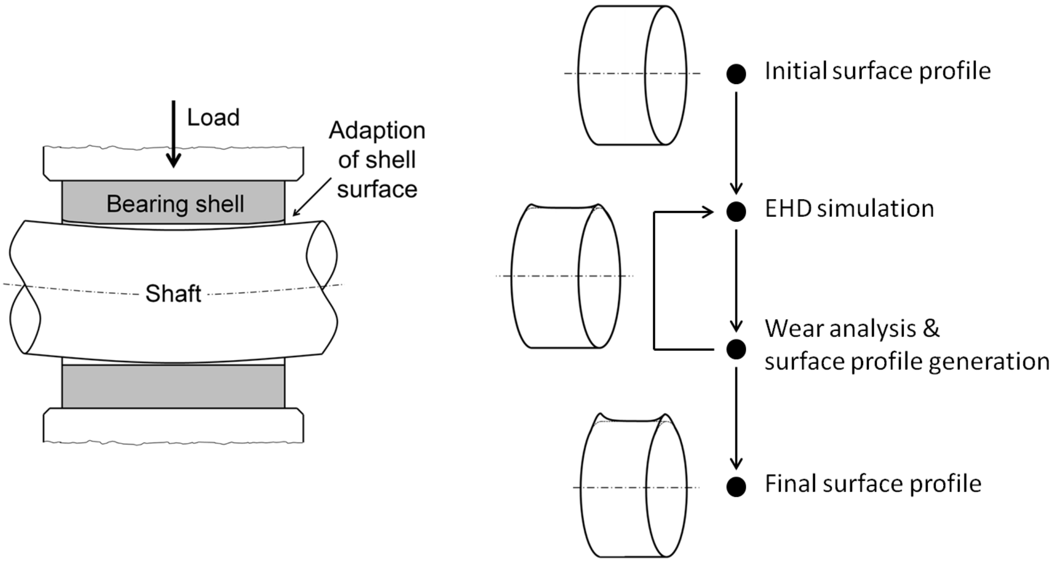

Figure 4.4: Sketch of bearing geometry adaption on the left; flow chart of the iterative surface profile generation on the right

The surface profile is then adapted step by step. One step includes the EHD simulation of a full load cycle and a subsequent evaluation of wear caused by metal-metal contact. A worn surface profile is generated at the end of one step with a defined maximum wear depth $h_{w,max}$ (see equation 4.27). This new surface profile replaces the nominal surface profile in the next step. Again, a full step is performed and the newly calculated worn surface profile replaces the previous surface profile. This stepwise profile adaption is repeated until the asperity contact pressure reaches a minimum (running-in) or a certain accumulated wear depth is reached.

For simplicity, the wear at the journal is assumed to be zero which is a reasonable approximation due to the considerably harder surface material.

4.3 Numerical approach

The non-linear model is solved in time domain by applying numerical time integration [63] and a backward differentiation formula (BDF) is applied. During a time step, the equations of motion are calculated for each body. Additionally, the contact equations in each time step are solved by applying a Newton-Raphson method. The lubricated journal bearings are computed by finite volume approach. Therefore, a discretization of the lubricated regime is performed. The elastic deformation of bearing and journal are calculated at each time step and are coupled to the hydrodynamic discretization nodes. Considering the elastic deformation, the clearance gap, the rheological properties of the fluid, the hydrodynamic and the asperity contact pressure are determined for each volume element.

4.4 Simulation model

For the simulation, the test-rig (see section 3.1 is modeled within the flexible multi-body solver AVL Excite Power Unit[4] [62, 63]. A schematic representation of the multi-body simulation model is shown in figure 4.5.

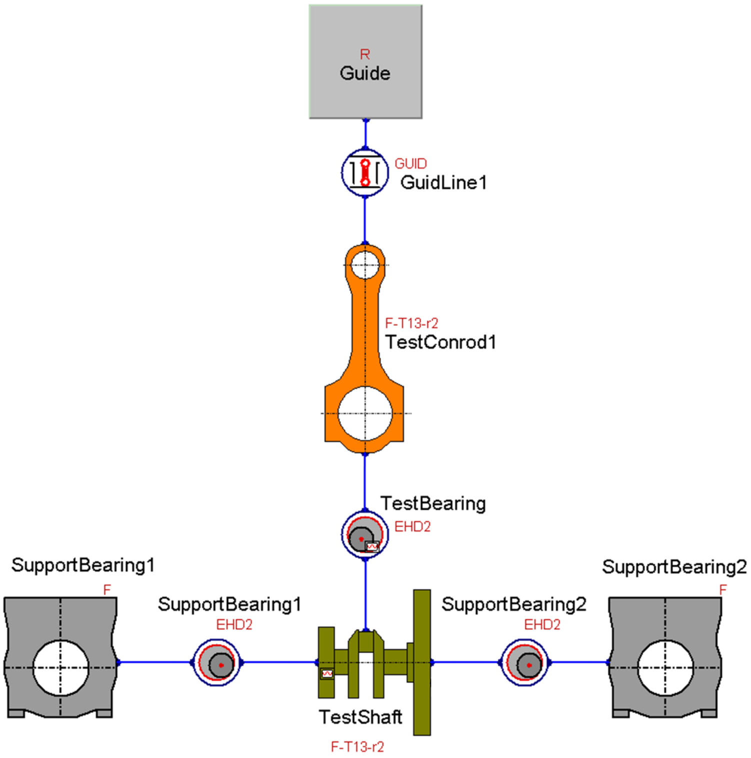

Figure 4.5: Schematic representation of the simulation model

The multi-body simulation model of the test-rig consists of flexible bodies and joints which connect the bodies. The two support brackets with the support bearings and the test connecting rod including the test bearing are represented as mathematically condensed finite element structures with reduced degrees of freedom [61]. Therefore, a pre-processing step needs to be performed to create the condensed bodies. The test shaft is also modeled as elastic body but instead of using a condensed structure a simplified beam and disc body is utilized. Finally, a rigid body is modeled which guides the connecting rod in vertical direction.

Two elasto-hydrodynamic joints are placed in between the test shaft and the two support brackets. A third joint is placed between the shaft and the test connecting rod. Finally, a spring damper element is used to connect the guide with the upper end of the test connecting rod. In what follows, the components are described in more detail.

4.4.1 Components

The pre-processing for the connecting rod and the support bearing is performed with Abaqus/standard[5]. The pre-processing consists of modeling and meshing of the components as well as the reduction of degree of freedoms (static and dynamic condensation).

---

[4] AVL List GmbH, Advanced Simulation Technology, Hans-List-Platz 1, 8020 Graz, Austria, www.avl.com

[5] Dassault Systèmes, 10 rue Marcel Dassault, 78946 Vélizy-Villacoublay Cedex France, www.3ds.com

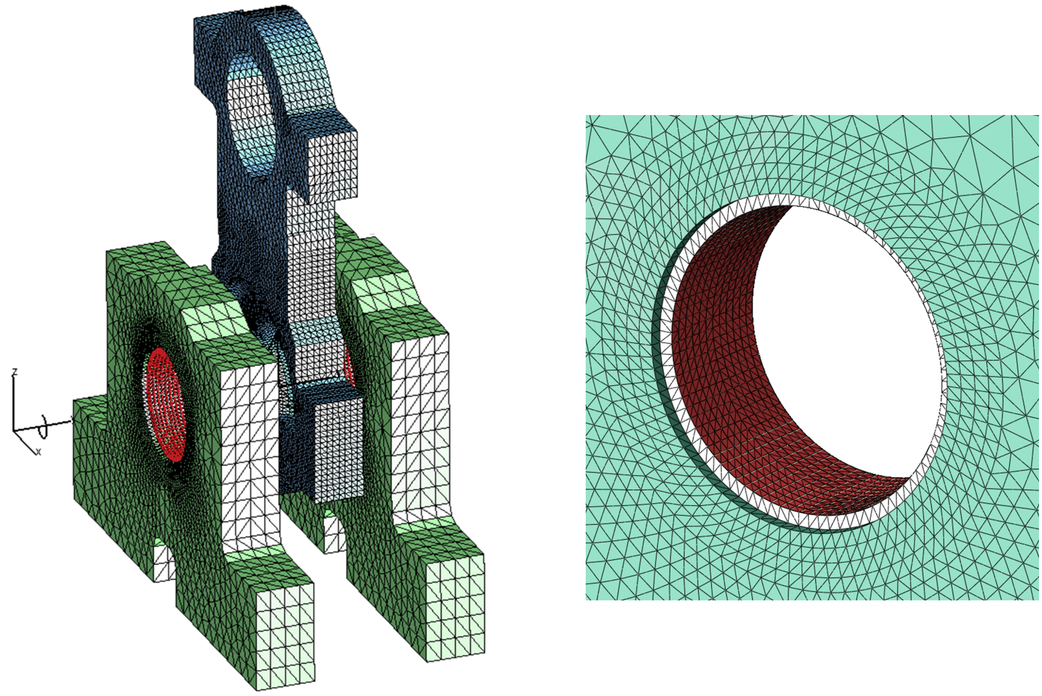

Figure 4.6: Finite element models of connecting rod and support bearing bracket on the left and, a detailed view of the finite element mesh of the bearing shell on the right

The finite element (FE) model is derived from the CAD data of the test-rig. The bodies are modeled with second order tetrahedral (tet) elements (C3D10M) which bear the advantage that complex geometries can be easily meshed. Further, second order elements increase the accuracy of the results compared to linear tet elements at the costs of increased computation time. At the bearing surface however, linear membrane elements are included which improve the contact behavior. The nodes of the membrane elements are tied to the nodes of the tet mesh. The mesh of the connecting rod and the support bearing bracket is shown in figure 4.6. The left and right support bearing brackets are identical and therefore the pre-processing is only performed once.

A detailed view of the bearing shell is also shown in figure 4.6 on the right hand side. The membrane is shown in red and the nodes of the membrane are aligned with the nodes of the surrounding tet mesh. The material properties are individually defined for the bearing bracket and the bearing shell.

Instead of including the complete FE model in the multi body simulation, the bodies are represented as condensed bodies. The condensed body is a statically and dynamically reduced body with a decreased number of degrees of freedom [5] with the benefit of a reduced calculation time. The condensed body only consists of the nodes which are in contact to other bodies. The retained nodes of the bearing brackets are the nodes on the bearing surface. For the connecting rod an additional node at the ″small end″ center is kept for the guidance of the connecting rod.

The straight test shaft is modeled as a beam body. The simplified body consists of single point masses which are connected by beam elements. The point masses represent the mass of a shaft section and the masses are distributed along the rotational axis. The stiffness of the beam elements are defined by the geometry between the point masses. For the journals of the test-rig six nodes are defined along the bearing axis. Therefore, the elastic deformation of the shaft is considered in the multi body simulation.

4.4.2 Joints

The three lubricated contacts between test shaft and support bearings as well as between the test shaft and test bearing are modeled as elasto-hydrodynamic joints (EHD2). The fluid film is calculated according to the averaged Reynolds equation which is discussed in section 4.1 in more detail. The numerical approach requires a discretization of the bearing surface. Therefore, 25 hydrodynamic (HD) nodes are defined in axial direction which are equally distributed in each bearing (support bearings and test bearing). The test bearing has 200 nodes in circumferential direction and the support bearings have 176 nodes, respectively. Every second node is directly coupled to the condensed FE model.

As a consequence of the chosen isothermal EHD approach, the bearing temperature is considered to be constant in the fluid film but the temperature is allowed to vary for different load and speed conditions (see section 4.4.5). The lubricant properties are evaluated at each HD node depending on pressure and shear rate. The representation of the lubricant properties is discussed in the next section.

4.4.3 Lubricant

The lubricant used in this study is a fully formulated low-viscous 0W20 hydrocarbon engine oil. It is a standard multigrade lubricant which is available for the automotive market. The main properties of the lubricant are summarized in table 4.1.

Table 4.1: Basic properties of the tested 0W20 lubricant

Density at 40 °C	832.5	kg/m^3
Dyn. viscosity at 40 °C	37.5	mPa·s
Dyn. viscosity at 100 °C	6.8	mPa·s
HTHS-viscosity at 150 °C and a shear rate of 10^6 1/s	2.7	mPa·s

The main lubricant properties show that the viscosity is strongly dependent on temperature. Various mathematical functions exist to consider the temperature dependency in simulation. An overview of equations which describe the viscosity temperature relation for fluids in general are provided in [77]. In this study, the effect of temperature on viscosity is specified by the Vogel equation [86],

$$\eta(T) = A_v \cdot e^{\frac{B_v}{T+C_v}}, \tag{4.31}$$

where T is the oil temperature and A_v (mPa s), B_v (°C) and C_v (°C) are constants for a given lubricant. The Vogel equation is very accurate for hydrocarbon lubricants for a wide range of temperatures.

The viscosity also increases with high pressure. The increase of viscosity can be very significant in heavily loaded contacts like roller bearings or gears [81]. However, in dynamically loaded journal bearings high pressures above 200 MPa can occur. The increase of viscosity due to high pressure can therefore be higher than the viscosity variation with temperature.

A well-known and basic mathematical relation between pressure and viscosity was established by Barus [9]:

$$\eta(T,p) = \eta(T) \cdot e^{\alpha \cdot p}, \tag{4.32}$$

where α is the piezo-viscous coefficient. More advanced approaches for these effects exist which perform even more accurately over a larger range of pressures and temperatures. However, the simple approach according to Barus is chosen for this study because its accuracy is sufficient for the appearing pressure and temperature range. A detailed overview of existing models for pressure dependency can be found in [6].

The non-Newtonian behavior of modern lubricants can be described by viscosity function depending on shear rate or shear stress. An overview of various viscosity functions is also presented in [6]. In this study, the Cross equation [23] is used to describe the lubricant's distinct shear-thinning effect

$$\eta(T,p,\dot{\gamma}) = \eta(T,p) \cdot \left(r_c + \frac{1 - r_c}{1 + (\lambda \cdot \dot{\gamma})^m} \right), \tag{4.33}$$

where r_c (-), m (-) and λ (s) are coefficients for a given lubricant. In this study, the three coefficients are assumed to be constant. The coefficient r_c is a material constant which describes the relation from the viscosity at maximum shear rate to the viscosity at zero shear rate. m represents the slope of the viscosity drop and λ is the position in terms of shear rate. The latter are dependent on temperature and pressure.

The rheological properties of the investigated lubricant have been determined experimentally for different temperatures, pressures and shear rates at an external partner institute. The parameters for Vogel, Barus and Cross equation are derived by curve fitting (method of least squares) the measurement results. The detailed derivation can be found in [74]. Table 4.2 lists the values of the parameters for the lubricant model.

Table 4.2: Parameters for Eqs. (4.31), (4.32), (4.33) derived from the experimental data [74]

A_v	0.0516	mPa·s
B_v	1127.6	°C
C_v	130.7	°C
α	0.0095	1/MPa
r_c	0.53	-
m	0.79	-
λ	7.9 e-8	s

The viscosity characteristics obtained from the derived parameters are additionally shown in figure 4.7 and figure 4.8.

Density is the second lubricant property which is dependent on temperature and pressure. The density typically decreases linearly with an increase of temperature and it rises non-linearly with increasing pressure. Several descriptive formulas for the pressure dependency of the density exist (e.g. according to Dowson and Higginson [29]).

Instead of using a descriptive function for the simulation model, the density is provided in tabular form dependent on temperature and pressure. Therefore, the measured density is directly integrated into the simulation model. Figure 4.9 shows the density behavior of the investigated lubricant.

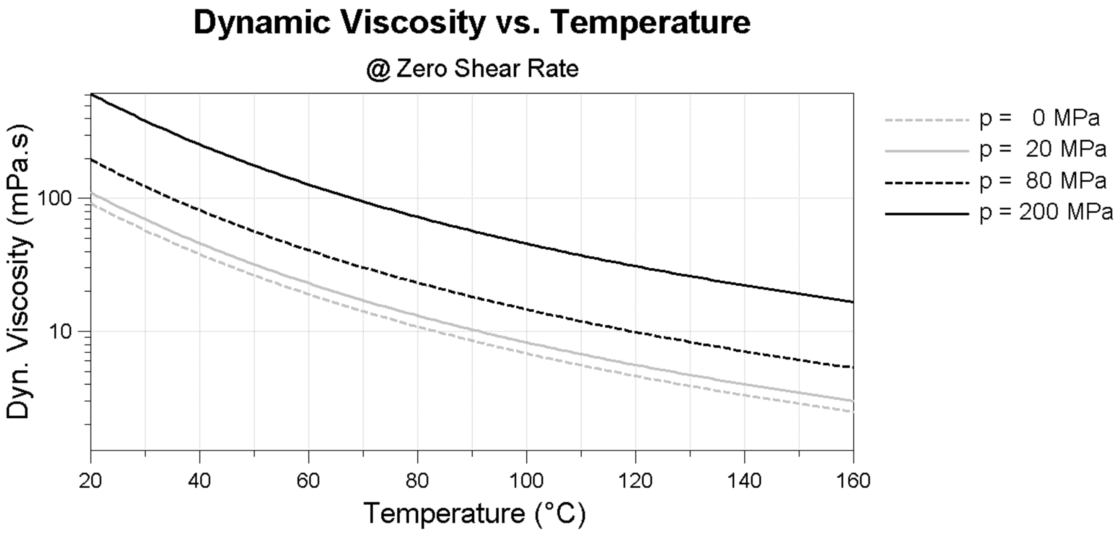

Figure 4.7: Viscosity behavior over temperature for the investigated 0W20 lubricant at different pressures

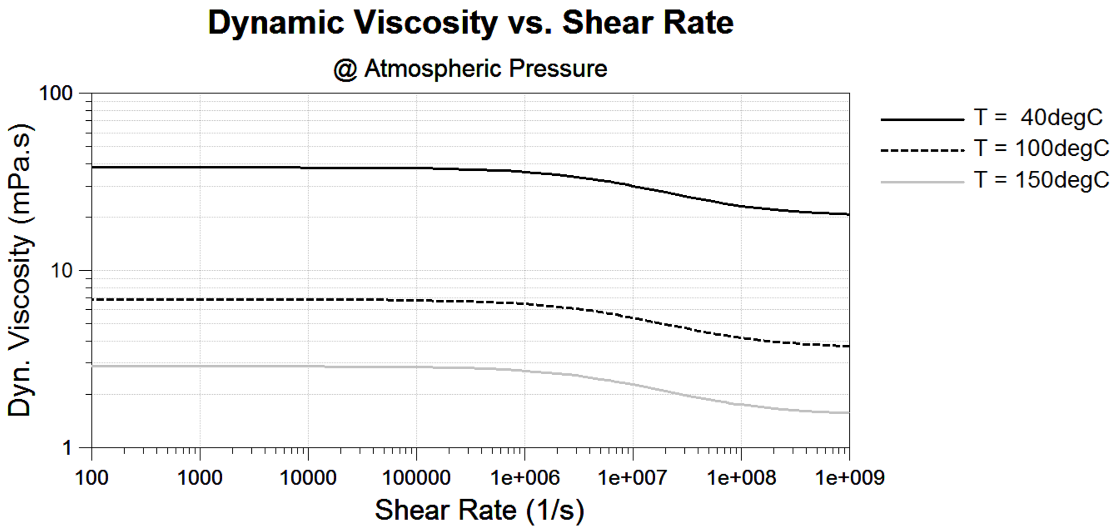

Figure 4.8: Viscosity behavior over shear rate for the investigated 0W20 lubricant at different temperatures

4.4.4 Load

The external load is applied at the ”small end” of the test connecting rod. In the tests, the force only acts in vertical direction. The bearing load is either a static or a dynamic load and is dependent on the application example. Therefore, a detailed description of the external load is omitted here. Accordingly, details can be found in each of the following application examples (see section 5).

4.4.5 Bearing temperatures

The numerical approach is simplified by assuming an isothermal bearing. This implies that the bearing temperature and the temperature of the lubricant are assumed to be constant in the lubrication gap. In many studies by various authors, it was experimentally and numerically shown that the oil film temperature varies in circumferential and axial

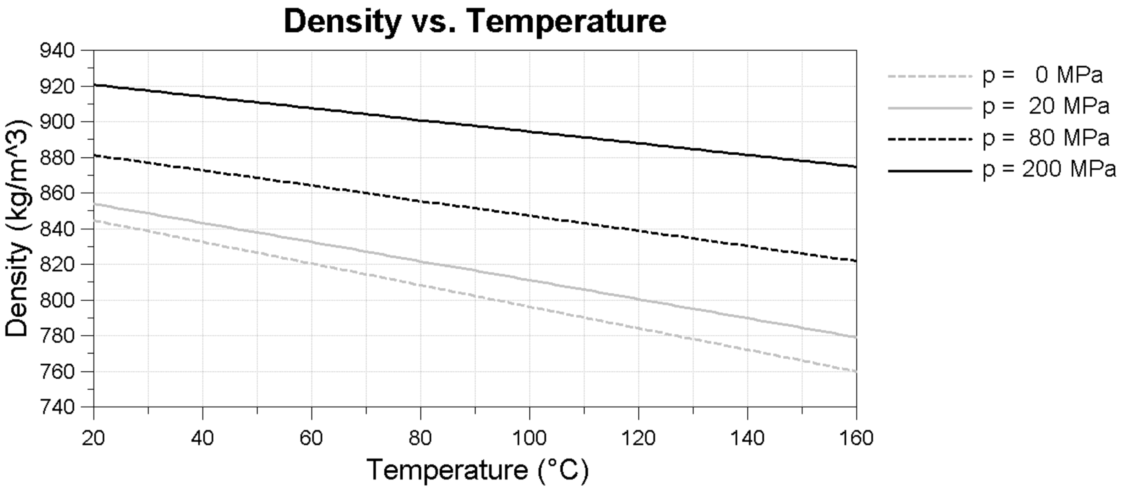

Figure 4.9: Density behavior over temperature for the investigated 0W20 lubricant at different pressures

direction as well as in film thickness direction (see, for instance, [1, 12, 16]). The temperature measurements in this study also show a varying temperature along circumferential direction. Therefore, the assumption of an isothermal bearing is a major simplification. However, suitable global temperatures need to be specified for each bearing. These global temperatures are further called equivalent temperatures.

The equivalent temperatures can either be calculated from theoretical oil flow and friction estimations or they can be derived from the measured temperatures. Beneficial for the theoretical estimation of the equivalent temperature is that no experimental data is needed. However, many effects will influence the accuracy of the estimation of oil flow and bearing friction. Such effects are for instance the deformation of bearing shell due to thermal and mechanical stress, misalignment between shaft and bearing, a highly dynamic shaft movement, or heat transfer into the surrounding structures. These effects are not considered in simplified predictive temperature estimations. For this reason, and because of the availability of the temperature measurements, the equivalent temperature is derived from measured temperatures in this study.

Allmaier et al. [1] performed a detailed thermo-elasto-hydrodynamic study of dynamically loaded journal bearings and compared the results to measured temperatures at the back of the bearing shell. Besides the precise prediction of the measured temperatures, the authors have shown that the bearing temperatures at the back of the bearing shell are representative for the temperature within the oil film especially in the highly loaded region. Furthermore, the authors introduced a representative oil temperature for the elasto-hydrodynamic analysis of bearing friction. The representative oil temperature considers the temperature measured at the back of the bearing shell and a correction factor to take the lower temperature around the partial circumferential oil supply groove into account. The authors discuss the isothermal assumption in detail and verified the results by thermo-elasto-hydrodynamic simulation and also by measurement.

In this thesis, two different bearing types are utilized. The two support bearings have a circumferential oil groove on the lower loaded bearing shell which encloses an angle of 180°. For this bearing type, the equation for the representative oil temperature elaborated by Allmaier et al. [1] is used as equivalent temperature:

$$T_{\text{Support}} = T_{\text{MB Shell}} - \left(\frac{T_{\text{MB Shell}} - T_{\text{MB Supply}}}{4} \right), \tag{4.34}$$

where $T_{\text{MB Shell}}$ and $T_{\text{MB Supply}}$ denote the bearing back temperature in the highly loaded region of the support bearings and the temperature of the supplied oil, respectively. The positions of the temperature sensors on the test-rig are sketched in section 3.1.1 (see figure 3.2).

The test bearing has a central bore in the lower loaded bearing shell to supply the oil. Therefore, a modified assumption of the equivalent temperature is used for the test bearing compared to the support bearings. Four temperatures at the back of the test bearing shell are measured during the tests. The sensors are located in the axial center and are evenly distributed in circumferential direction (see figure 3.2). The measured temperatures around the bore are higher than the oil supply temperature. Instead of using the oil supply temperature to calculate the equivalent temperature, a weighted average of the four temperature measurements at the bearing back is considered. The temperatures in the highly loaded zone are weighted with a factor two because high shear rate and further high shear stress occur in this part of the journal bearing. The equivalent temperature for the test bearing is calculated according to:

$$T_{\text{Test}} = \frac{2 \cdot (T_{\text{BE 1}} + T_{\text{BE 2}}) + T_{\text{BE 3}} + T_{\text{BE 4}}}{6}, \tag{4.35}$$

where $T_{\text{BE 1/2/3/4}}$ is the measured temperature with the index pointing to the locations shown in Fig. 3.2.

Chapter 5

Results

In this chapter, four different journal bearing application examples are discussed in four sections. Each application example deals with a distinguished challenge, discussing either friction, wear, or both in journal bearings. The investigated operation conditions of the journal bearings range from elasto-hydrodynamic lubrication regime to severe mixed lubrication regime and boundary lubrication regime. The load conditions in combination with the fully formulated low-viscous lubricant, the bearing dimensions, and bearing materials represent a typical spectrum of operating conditions for modern and future combustion engines. However, individual examples are presented in complementary fashion.

All simulation results are compared to measurement results obtained from a journal bearing test-rig (see section 3). The validation of the presented models is important to show the usability of the developed approach. Especially the application of approximated functions to describe the lubricant viscosity and statistically derived contact models need to be verified.

The first application example discusses friction in dynamically loaded journal bearings. The bearings operate in elasto-hydrodynamic lubrication regime with only minor metal-metal contact. This condition typically occurs in big-end bearings of modern combustion engines. Due to the heavy load, high maximum hydrodynamic pressures of more than 200 MPa arise in the bearings. Additionally, shear rates up to $2 \cdot 10^7$ 1/s occur. To reliably predict friction in this condition, a detailed description of the lubricant behavior under high pressure and at high shear rate becomes necessary. To achieve this, the lubricant properties are derived from measurement and the influence of high pressure and shear-thinning is discussed. Furthermore, equivalent temperatures (see section 4.4.5) for the isothermal simulation approach are defined which are derived from temperature measurement at the back of the bearing shells. These equivalent temperatures are applied in each of the subsequent examples.

The second application example examines journal bearing friction in mixed lubrication regime. In mixed lubrication regime, metal-metal contact occurs and leads to a drastic rise in friction. Mixed lubrication can be found for instance during the starting of an engine when the shaft begins to rotate. The Greenwood and Tripp contact model is used to predict friction caused by the interaction of asperities of the contacting surfaces. The surface roughness parameters for the contact model are derived from surface scans of shaft and bearing shell. In this section, mixed lubrication is realized by applying a static load to the bearing and reducing the shaft speed. Under static load, the hydrodynamic pressure is rather small; nonetheless, the detailed oil model derived in the first application example is incorporated here. After validation of the simulation approach the influence of surface smoothing due to running-in is discussed.

The third application example uses both the lubricant properties and the contact model parameters derived in previous examples to discuss running-in wear in journal bearings. The bearing shells show worn areas on the bearing edges after operation under dynamic load (first application example). The simulation results also identified metal-metal contact at the bearing edges which was reduced by considering a worn bearing surface geometry. In this section, a simulation approach to calculate the final wear depth is presented which adapts the bearing geometry iteratively using Archard's wear equation. Initial point is a perfect cylindrical bearing geometry. The final wear depth and the shape of the wear scar on both edges are compared to measurement. Additionally, the wear volume and wear rate are studied over operation time.

The fourth application example discusses the start and stop behavior of journal bearings. A static load is applied to the test bearing and 6000 start-stop cycles are performed on the test-rig. The static load has a similar magnitude as it occurs in engines during the starting. However, before the shaft begins to rotate, it rests on the bearing shell and the load is supported by metal-metal contact only. Hence, when the shaft starts to move, the bearing operates in boundary lubrication regime. With an increase of speed, the fluid film develops and the bearing operates in mixed lubrication regime until lift-off speed is reached and the surfaces are completely separated. The application example analyzes the torque which is necessary to overcome boundary friction. The contact model for this investigation is based on the approach discussed in the second application example. Additionally, the wear behavior due to several starts is examined according to the approach which is verified in the third application example.

The first three application examples are all published in detail in Tribology International [74, 76, 75]. These publications are appended to each section. Summaries are provided to introduce each publication. The fourth application example is described in detail in section 5.4.

5.1 Impact of high pressure and shear-thinning on journal bearing friction

Friction in hydrodynamic lubrication regime is dominated by the lubricant viscosity. The lubricant viscosity itself, is strongly dependent on temperature, pressure and shear rate. In this paper [74], a fully formulated low viscosity engine oil is analyzed by measurement and the viscosity properties are identified. The piezo-viscous effect is analyzed for pressures up to 300 MPa and high shear stress is generated to determine the non-Newtonian lubricant behavior. The pressure and temperature dependency of the lubricant density is also derived from measurement data.

From the lubricant analysis, parameters for a descriptive viscosity function are derived. This viscosity function presents the basis for the numerical investigation and furthermore the validation of journal bearing friction simulation.

Friction measurements with dynamically loaded journal bearings are performed on a journal bearing test-rig. With the applied dynamic load, maximum specific pressures up to 100 MPa are generated. These conditions can typically occur in a big-end bearing operating at full load. The analyzed lubricant is used for the friction tests. The bearings mainly operate in pure hydrodynamic lubrication regime, in other words, only an insignificant amount of metal-metal contact occurs, which is important as the simulation of the full film lubrication shall be tested.

The lubricant viscosity function and density properties are also included in the elasto-hydrodynamic simulation model of the test-rig. The detailed lubricant model enables an accurate calculation of the friction losses for the presented load cases. A further investigation shows the impact of neglecting the piezo-viscous and shear-thinning effect in journal bearing friction.

The details of the numerical and experimental work as well as the results are described in [74] which are presented in section 5.1.2. Prior to this, the research findings of the publication are summarized.

5.1.1 Summary of research findings

- The viscosity and density of a modern fully formulated low-viscosity engine oil is determined under high pressures up to 300 MPa.
- Measurements at high shear stresses provide the viscosity properties for the non-Newtonian lubricant.
- Parameters for the empirical viscosity function according to Vogel, Barus and Cross are derived from these measurements.
- Friction tests with the analyzed lubricant are performed on a journal bearing test-rig for a wide range of operation conditions. The shaft speed ranges from 1000 rpm to 7000 rpm and a maximum specific bearing load of 100 MPa is reached.
- Equivalent temperatures are introduced for the calculation of journal bearing friction with the isothermal simulation method.
- The calculated friction torque matches the test-rig results for a wide range of operation conditions.
- The temperature influence on friction torque is correctly identified by the simulation.

- Neglecting either the non-Newtonian behavior or the piezo-viscous effect in the simulation, will significantly affect the journal bearing friction. When neglecting both effects, a discrepancy up to 15 % can occur.

Annotation and additional reference

The simulation and measurement results presented in this section, are additionally discussed in another publication [3]. The study focuses on the temperature viscosity relation, the non-Newtonian effect and their influence on bearing behavior. The main research finding holds that the minimum lubrication gap decreases with increasing shaft speed which is contrary to initial expectations. This effect occurs due to a viscosity drop which is caused by high temperature and high shear rate. Additionally, the defined equivalent temperatures are verified in more detail.

5.1.2 Paper I [74]

Tribology International 81 (2015) 29–37

Contents lists available at ScienceDirect

Tribology International

journal homepage: www.elsevier.com/locate/triboint

Impact of high pressure and shear thinning on journal bearing friction

D.E. Sander [a,*], H. Allmaier [a], H.H. Priebsch [a], F.M. Reich [a], M. Witt [b], T. Füllenbach [b], A. Skiadas [b], L. Brouwer [c], H. Schwarze [c]

[a] Virtual Vehicle Research Center, Inffeldgasse 21A, 8010 Graz, Austria
[b] KS Gleitlager GmbH, Am Bahnhof 14, 68789 St. Leon-Rot, Germany
[c] Institute of Tribology and Energy Conversion Machinery, TU Clausthal, Leibnizstraße, 38678 Clausthal-Zellerfeld, Germany

ARTICLE INFO

Article history:
Received 25 April 2014
Received in revised form
25 June 2014
Accepted 23 July 2014
Available online 1 August 2014

Keywords:
Lubrication
Rheology
Multi-grade engine oil
Journal bearing

ABSTRACT

For the study of mixed lubrication in journal bearings, this paper employs a combined experimental and simulative approach. Extensive measurements on a journal bearing test rig with a low viscosity 0W20 multi-grade lubricant provide a solid basis which is complemented by experimental lubricant data that is measured under high pressure and high shear rates. In this paper, this data is used to investigate the impact of the piezoviscous effect and the non-Newtonian lubricant properties on the friction power losses in journal bearings over a wide range of dynamic loads and shaft speeds.

In particular, this work seeks to predict the friction power losses for journal bearings under both moderate (50 MPa peak load) and high dynamic loads (100 MPa peak load) using the recently presented accurate numerical method (Allmaier et al., 2011 [1], Allmaier et al., 2013 [2]). From the direct comparison to the experimental data a key finding is that the simulation conforms very closely to the measured data. To be more exact, the agreement lies within the measurement uncertainty.

Following this result, the influence of the often neglected piezoviscous effect and the non-Newtonian lubricant rheology is investigated. We conclude that both the piezoviscous effect and the non-Newtonian behaviour are essential to describe the lubrication with multi-grade lubricants in journal bearings. Only the consideration of both properties describes the experimental data very accurately over the entire range of operating conditions studied.

1. Introduction

Journal bearings have been the focus of research for a very long time. From simplified analytical approaches (e.g. [3]) to extensive thermoelastohydrodynamical simulations (e.g. [2,4]) a large number of works have investigated specific questions involving this seemingly simple element. Consequently, we do not reproduce an extensive lists of general references here, but refer to the extensive lists of references in the previous works [1,2,5,6].

Furthermore, it is important to note that the methods to calculate the friction power loss due to the shearing of the oil film have come a long way. Especially the scientific works comparing theoretical approaches directly to experimental data are particularly noteworthy. Early papers presented well chosen approximations and applied them to simplified conditions [7] or used basic numerical evaluations of the Reynolds equation [8]. Recent publications by the authors extended these efforts and presented a numerical technique that is able to predict the friction power loss from full film lubrication to (weak) mixed lubrication under high dynamic loads [1,2,6]. It is worthwhile to mention that this approach requires only two easily measurable temperatures and no iterative adjustments to experimental data are necessary.

Central to these works is the consideration of the complex rheological properties of the lubricant [5] and the inclusion of a physically derived contact model together with a realistic surface contour of the journal bearing [9]. The following work builds on these previous works and extends them to multi-grade lubricants with strong non-Newtonian behaviour. In addition, the methodology is generalized to journal bearings without 180° oil supply groove as they are used as e.g. big end bearings in internal combustion engines.

Besides the scientific interest, the consumer demand and the increasingly strict environmental legislation are strong motivations in the industrial and automotive sector to develop engines that are more energy efficient. About 10% of fuel energy is needed to overcome friction in conventional engines, to which friction in journal bearings contributes up to 44% [10]. One way to reduce friction in journal bearings is the application of low viscosity engine oils [10–12]. While the hydrodynamic losses are decreased by reducing the lubricant viscosity [13,14], the appearance of

---

* Corresponding author.
E-mail address: david.sander@v2c2.at (D.E. Sander).

http://dx.doi.org/10.1016/j.triboint.2014.07.021

metal–metal contact (mixed lubrication) becomes more likely and increases the risk of premature failure of the journal bearing due to seizure or wear. This poses a great challenge which is further intensified by high mechanical and thermal loads in modern internal combustion engines with ever increasing high power densities.

To explore the potential of reducing friction power losses in journal bearings and to design more efficient engines, reliable simulation methods which are proven by measurements are required.

To address this task, extensive measurements on a journal bearing test rig with controlled ambient conditions provide a solid basis. It is the aim of the present work to predict the friction power losses for journal bearings under moderate (50 MPa peak load) and under high dynamic loads (100 MPa peak load) using the recently presented generic numerical method [1,2] in direct comparison to the experimental data. Oil viscosity is the key parameter to describe lubricated contacts and is considerably sensitive to pressure [15] and shear rate [16,17]. Therefore, the influence of the often neglected piezoviscous effect and the non-Newtonian lubricant rheology are investigated.

2. Lubricant rheology

The lubricant used for this investigation is a fully formulated low-viscous 0W20 hydrocarbon engine oil. Previous works [1,2,5,6] investigated monograde lubricants that do not show a strong non-Newtonian behaviour. In this work the investigated lubricant is a multi-grade lubricant as they are commonly used in the automotive sector. The present work investigates also the influence of its strong non-Newtonian behaviour.

The main properties of the lubricant including the density and the viscosity at various conditions are given in Table 1.

The dynamic oil viscosity was measured at different temperatures as shown in Fig. 1.

For numerical reasons in practical applications it is more convenient to use empirical equations in the simulation instead of using the experimental data directly. Vogel's equation [18] is used here to describe the dependency of viscosity η from temperature in this paper:

$$\eta(T) = A \cdot e^{B/(T+C)}, \tag{1}$$

where T (°C) is the temperature, and A (mPa s), B (°C) and C (°C) are constants determined by curve fitting of the measurement results; Table 2 lists the values of these constants. Fig. 1 shows the measured viscosities at various temperatures and the corresponding curve obtained from Vogel's equation.

The lubricant viscosity under high pressure was measured using a quartz viscometer at the TU Clausthal. A piezoelectric sensor is excited to mechanical oscillation by applying an alternating voltage [19–21]. A particular benefit of this method is the minor temperature increase because the applied electric power is very low. Further, viscosities can be investigated for pressures up to 10 000 bar. The measured pressure viscosity relation of the

Table 1
Basic properties of the tested 0W20 lubricant.

Density at 40 °C	832.5 kg/m^3
Dyn. viscosity 40 °C	37.5 mPa s
Dyn. viscosity 100 °C	6.8 mPa s
HTHS-viscosity[a]	2.7 mPa s

[a] The HTHS-viscosity is defined as the viscosity at high temperature (150 °C) and high shear rate (10^6 1/s).

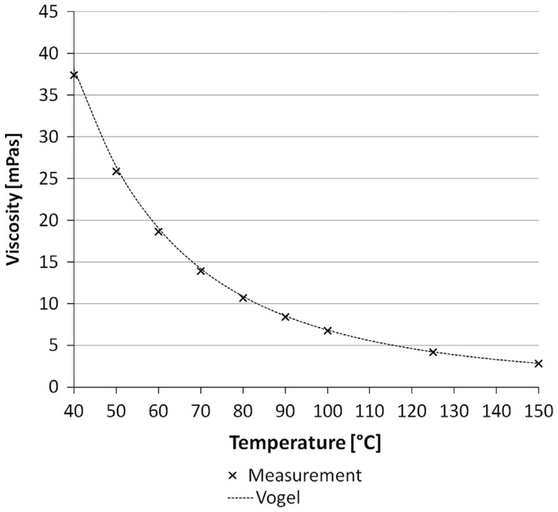

Fig. 1. Viscosity temperature dependence of the tested 0W20 lubricant at ambient pressure. The measured data are shown as crosses and the displayed curve is obtained from Vogel's equation, Eq. (1), with the parameters in Table 2.

Table 2
Parameters for Eqs. (1)–(3) derived from the experimental data.

A	0.0516 mPa s
B	1127.6 °C
C	130.7 °C
α	0.00095 1/bar
r	0.53 (–)
m	0.79 (–)
K	7.9 e–8 s

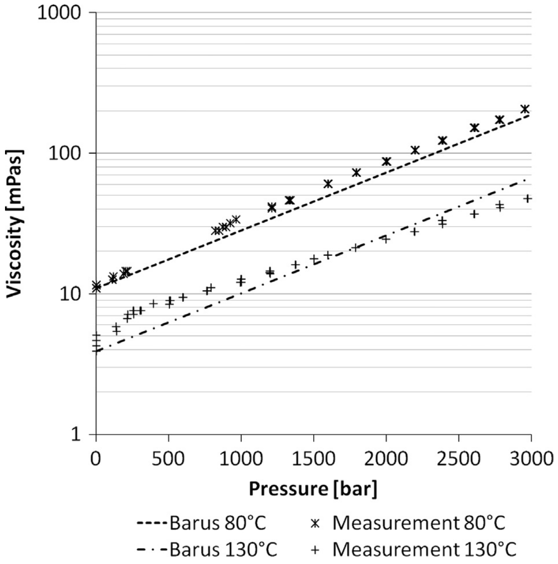

Fig. 2. Viscosity pressure dependence of the tested 0W20 lubricant. The measured data for 80 °C and 130 °C are shown as crosses and pluses, respectively. The displayed curve is obtained from Barus' equation, Eq. (2), with the parameters in Table 2.

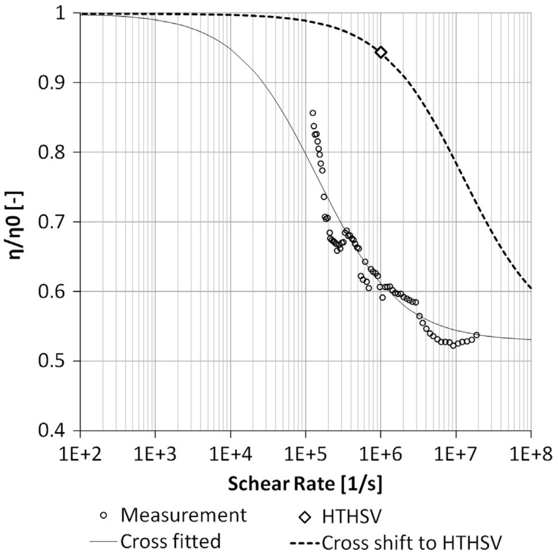

Fig. 3. Dependence of relative viscosity and shear rate of the tested 0W20 lubricant is shown at ambient pressure in relation to the viscosity at zero shear rate η_0. The measured data are shown as circles. A fit of the Cross equation, Eq. (3), to the measured data yields the solid line. To meet the measured HTHS-viscosity (marked as diamond), this curve is shifted to higher shear rates and depicted as dashed line.

tested 0W20 lubricant is shown in Fig. 2 for pressures up to 3000 bar and for a lubricant temperature of 80 °C and 130 °C.

In the following, Barus equation [22] is used to describe the experimental data

$$\eta(T,p) = \eta(T) \cdot e^{\alpha \cdot p}, \quad (2)$$

where α (1/bar) is the piezoviscous coefficient, and p (bar) denotes the pressure; Table 2 lists the used value.

While the impression might arise from Fig. 2 that a closer fit of the experimental data using more complex functions than the Barus equation might be beneficial, the authors found that the shown deviations from the experimental data have only an insignificant influence on the calculated friction power losses.

In addition the lubricant viscosity for different shear rates was measured at ambient pressure, which is shown in Fig. 3 and shows a strong dependence. In the simulation, this shear thinning effect is described using the Cross equation [23]:

$$\eta(T,p,\dot{\gamma}) = \eta(T,p) \cdot \left(r + \frac{1-r}{1+(K \cdot \dot{\gamma})^m} \right), \quad (3)$$

where $\dot{\gamma}$ (1/s) is the shear rate. r is a material constant for a given lubricant and describes the relation between viscosity at maximum shear rate and viscosity at lowest shear rate at a given temperature and pressure. m, assumed to be constant, refers to the slope of the viscosity drop and K (s) is the position in terms of shear rate.

Cross equation is fitted to the measured data points and so constants r and m are obtained. However, K is considered to depend on both temperature and pressure [24]. This might explain that in Fig. 3 the HTHS-viscosity (measured at 150 °C and 10^6 1/s) does not coincidence with the measured data.

For highly stressed journal bearings, like the investigated ones, typically shear rates between 10^5 1/s and 2×10^7 1/s occur. Therefore, to evaluate parameter K, the Cross curve is shifted to higher shear rates so that it meets the HTHS-viscosity. For completeness, Table 2 lists the used values for these constants.

Finally, Fig. 4 contains the measured lubricant densities for different pressures and temperatures.

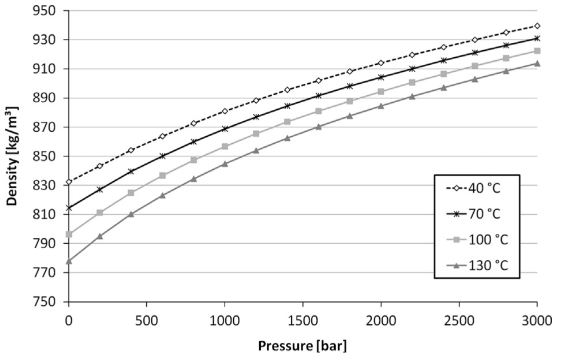

Fig. 4. Pressure and temperature dependent density of the tested 0W20 lubricant.

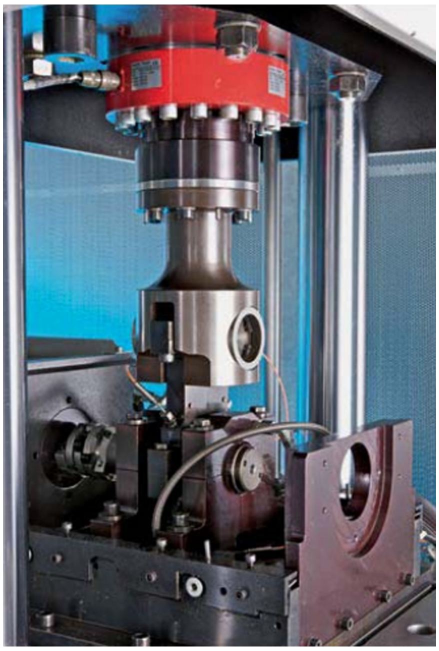

Fig. 5. Journal bearing test-rig at KS Gleitlager.

3. Test method

All tests were conducted on the journal bearing test-rig at KS Gleitlager shown in Fig. 5.

The test-rig consists of a rotating straight shaft which rests on two supporting journal bearings in support brackets. Via a test connecting rod an external load is applied onto the central test journal bearing. The dimensions and oil supply design of the journal bearings correspond to automotive main bearings with a 180° oil supply groove for the two supporting journal bearings. The test journal bearing corresponds to big-end bearings having an oil supply hole in the load-free (lower) shell. The bearing dimensions and materials are listed in Table 3.

An elastically clutched electric motor drives the shaft. The total friction torque caused by all three journal bearings is measured by a torque transducer which is located between the motor and the clutch. The torque transducer, a Manner Sensortelemetrie 50 N m standard sensor element, has an accuracy of ±0.15 N m.

The test connecting rod is dynamically excited by an electromechanical high-frequency pulsator, which is operated at 80 Hz.

Table 3
Journal bearing dimensions and materials.

Bearing properties	Support bearing	Test bearing
Width (mm)	25	17.2
Diameter (mm)	54	47.8
Clearance (μm)	50	30
Material	Steel/aluminium composite	Sputter bearing

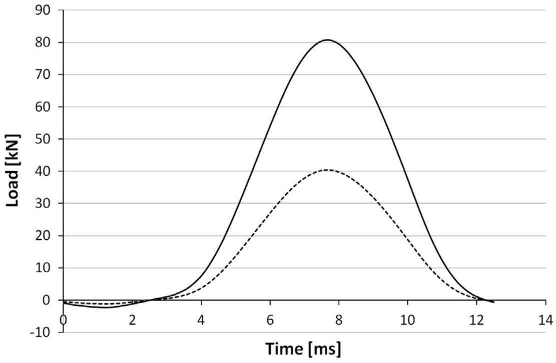

Fig. 6. Periodic load acting on the test connecting rod with a frequency of 80 Hz; the dashed line represents a specific load of maximum 50 MPa (40 kN load) on the test bearing; the solid line 100 MPa peak specific load (80 kN load).

Two load cases were investigated, one with 40 kN maximum load and one with 80 kN maximum load; the dynamic load curves are shown in Fig. 6. For comparison to other works, 40 kN corresponds to 50 MPa specific load in the test bearing and 80 kN to 100 MPa. These two different loads correspond roughly to part load and full load conditions in automotive internal combustion engines. Therefore, a wide range of operating conditions are covered by the test procedure.

The measurements were conducted separately for the two different load cases. For every load new journal bearings were used and the measurements were conducted for different journal speeds in the same run. The test procedure at one specific load was started at a shaft speed of 1000 rpm and a stepwise run-up was performed up to 7000 rpm followed by a run-down to again 1000 rpm. Each step is operated for 20 min. The measured average friction moment is then obtained by averaging over the last 10 s of the corresponding step.

For temperature measurements PT100 elements are used that have an accuracy of ± 0.5 °C.

Two oil supply temperatures were recorded during each test run, one for both support bearings, and one for the test bearing. Additionally, temperatures at the back of the bearing shells were measured. The support bearings were equipped with one sensor close to the high load zone of the lower shell as shown in Fig. 7.

Four temperature sensors were applied to the test bearing and were evenly distributed along the circumferential direction as shown in Fig. 7.

The inflow temperature varies in dependence on the flow rate and the overall test rig environment temperature. Flow rate and environment temperature depend on the revolution speed and the load case. For the 50 MPa peak load case the inflow temperature varied between 75 °C and 82 °C (see Table A2). In the case of 100 MPa peak load the set temperature was decreased to avoid thermal overload in the lubrication gap. For the latter case, the inflow temperature varied between 40 °C and 51 °C (see Table A1). The oil supply pressure was set to 5 bar for the test and support bearings, again comparable to combustion engine applications.

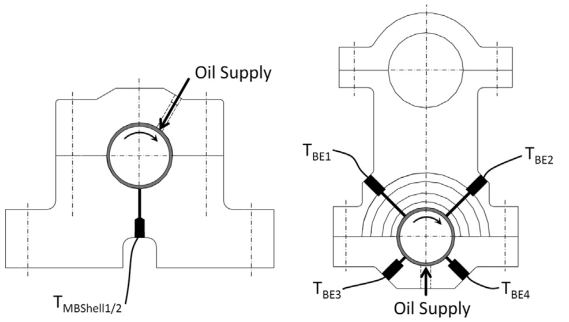

Fig. 7. Temperature measurement positions in the support bearings (left) and the test bearing (right).

4. Simulation

The KS Gleitlager test rig is modelled within an elastic multi-body dynamics solver (AVL Excite PowerUnit[1]). The simulation model consists of a test connecting rod including the test bearing, two support blocks including the support bearings and the test shaft. All bodies have mass characteristics and can deform elastically and are represented as mathematically condensed finite element structures [25].

The isothermal elastohydrodynamic description of the lubricant film in the simulation is discussed in depth in previous publications [1,5]. For completeness, a brief theoretical overview of the elastohydrodynamic journal bearing simulation is given here.

The movement of the journal within the bearing is calculated using the Reynolds equation:

$$-\frac{\partial}{\partial\varphi}\left(\frac{h^3}{12\eta}\frac{\partial p}{\partial\varphi}\right)-r^2\frac{\partial}{\partial z}\left(\frac{h^3}{12\eta}\frac{\partial p}{\partial z}\right)+r\frac{\partial}{\partial\varphi}\left(h\frac{u_1+u_2}{2}\right)+r^2\frac{\partial h}{\partial t}=0, \qquad (4)$$

where φ, z denote the azimuth angle and the axial direction, respectively. p is the hydrodynamic pressure and h the oil film thickness which is dependent on φ and z. Further, r is the nominal shell radius, u_1 and u_2 denote the sliding speeds of the contacting surfaces. η is the oil viscosity that is considered either as constant, as pressure dependent or as pressure and shear rate dependent in this paper.

The influence of surface roughness on hydrodynamic lubrication is considered in the simulation using the averaged Reynolds equation according to Patir and Cheng [26,27]. However, it was found that the influence of the pressure and shear flow factors on the friction power losses is negligible for the operating conditions studied. Therefore, these are omitted in Eqs. (4)–(6).

The friction torque acting on the bearing surface considers both, hydrodynamic losses and losses due to asperity contact. Therefore, the friction torque M_{Friction} can be calculated by integrating the shear stresses over the bearing surface:

$$M_{\text{Friction}}=r\iint_A(\tau_h+\tau_a)\,d\varphi\,dz, \qquad (5)$$

where A denotes the bearing surface. τ_h the hydrodynamic shear stress which is calculated by

$$\tau_h=\eta\cdot\frac{u_1-u_2}{h}\pm\frac{h}{2r}\cdot\frac{\partial p}{\partial\varphi}, \qquad (6)$$

where + and − refer to the shell surface and the journal surface, respectively.

---

[1] Version 2011.2, AVL List GmbH, Advanced Simulation Technology, Hans-List-Platz 1, 8020 Graz Austria, www.avl.com.

The shear stress in case of asperity contact between the shell surface and the journal surface is calculated by

$$\tau_a = \mu_{\text{Bound}} \cdot p_a, \tag{7}$$

where μ_{Bound} is the boundary friction coefficient and p_a denotes the asperity contact pressure. The contact pressure is calculated using the Greenwood and Tripp approach [28]. The theory of Greenwood and Tripp is based on the contact of two nominally flat, random rough surfaces. The asperity contact pressure can be written as

$$p_{\text{a}} = KE^{*}F_{5/2}(H_s), \tag{8}$$

where K is the elastic factor, E^{*} denotes the composite elastic modulus, $E^{*} = ((1-\nu_1^2)/E_1 + (1-\nu_2^2)/E_2)^{-1}$, where ν_i and E_i are the Poisson ratio and Young's modulus of the adjacent surfaces respectively, and $F_{5/2}(H_s)$ is the form function, which is further discussed in [1,5].

The surface roughness for a run-in part of the bearing shell was measured using a focus variation microscope of the Alicona Imaging GmbH. Hence, the asperity roughness $\sigma_{s,S} = 0.2$ μm and the mean summit height $\delta_{s,S} = 0.4$ μm of the bearing shell were obtained. For the journal an asperity roughness of $\sigma_{s,J} = 0.2$ μm and a mean summit height of $\delta_{s,J} = 0.1$ μm were used. Further, an elastic factor of $K = 0.003$ and a boundary friction coefficient of $\mu_{\text{Bound}} = 0.02$ were employed [1].

4.1. Oil temperatures in an isothermal simulation

The viscosity of engine oil is highly sensitive to temperature as can be seen in Fig. 1. Within the bearing locally different temperatures occur which are significantly higher in the highly loaded area than in the unloaded area. However, in the no-load area considerably cooler and, consequently, thicker lubricant is present that needs to be considered in the simulation of the friction power losses [2].

However, the choice of an isothermal elastohydrodynamic bearing approximation requires an equivalent global lubricant temperature that considers both the hot temperature in the highly loaded zone and the cool temperature in the no-load zone. Depending on the specific bearing oil supply design, different amounts of cool lubricant are in the bearing. This requires different relations between these two distinct temperatures and the equivalent temperature used in the simulation.

Automotive main bearings have a distinctive oil groove to supply sufficient engine oil to the contact area. For the two support bearings of the journal bearing test-rig two main bearings are used. For these, the oil supply groove is on the load-free shell and encloses an angle of 180°. The equivalent temperature for journal bearings with such a groove was introduced and validated in [2], applying the following equation:

$$T_{MB} = T_{\text{MB Shell}} - \left(\frac{T_{\text{MB Shell}} - T_{\text{MB Supply}}}{4}\right), \tag{9}$$

where $T_{\text{MB Shell}}$ and $T_{\text{MB Supply}}$ denote the temperature in the highly loaded zone and the temperature of the supplied oil, respectively.

The test bearing of the journal test-rig employs an automotive big-end bearing. This bearing uses a bore in the load free, lower shell to supply the oil. The measured temperatures around the bore ($T_{BE\,3}$ and $T_{BE\,4}$, compare Fig. 7) are higher than the oil inflow temperature. To use all available experimental temperature data, a weighted average of all four temperature measurement points is used in the simulation. The temperatures in the highly loaded zone are weighted with a factor two because high shear rates and further high shear stress occur in this part of the journal bearing,

$$T_{BE} = \frac{2 \cdot (T_{BE1} + T_{BE2}) + T_{BE3} + T_{BE4}}{6}. \tag{10}$$

Alternatively, in the spirit of Eq. (9), if only the temperature in the hottest part of the big end journal bearing and the oil supply temperature is available experimentally, the following equivalent temperature relation delivers results similar to Eq. (10):

$$T_{BE} = T_{\text{BE Shell}} - \left(\frac{T_{\text{BE Shell}} - T_{\text{BE Supply}}}{8}\right). \tag{11}$$

However, in the following Eq. (10) is used in the simulation.

4.2. Surface contour

To avoid an unrealistic calculation of the asperity contact at the bearing edges a surface contour is defined [1,9]. A simple spline contour is defined along the axial bearing direction which has a flat area in the center of the bearing. Towards the edges a parabolic characteristic raise to a maximum deviation of 5 μm at the edges.

5. Results

In the following the comparison of measurement results, obtained from the journal bearing test-rig, is shown with calculated results using the presented method for the two load cases (50 MPa and 100 MPa dynamic peak specific load).

Fig. 8 shows the measured average friction torque for different shaft speeds for the 50 MPa load case (dashed grey curve) and for the 100 MPa load case (dashed black curve). The measurement uncertainty is displayed as error bars for reference. It contains the measurement error of the torque transducer and the standard error of the mean. At 50 MPa and 2000 rpm the journal bearing test-rig showed strong resonances. Therefore, the measured torque results at 50 MPa and 2000 rpm are excluded from the figures.

The average friction torque for the 100 MPa peak load case varies between 1.5 N m at low speed and 2.9 N m at high speed. In particular, a distinct difference between run-up and run-down can be identified. This can be explained by the measured temperatures given in Table A1 in the Appendix. The measured temperatures at the run-down are about 3 °C higher compared to the run-up at the same shaft speed. Due to the higher temperature and, therefore, lower lubricant viscosity at the run-down the friction torque is lower compared to the one at run-up.

For the 50 MPa peak load case, the measured friction torque ranges from 0.7 N m at 1000 rpm to 1.9 N m at 7000 rpm and is, therefore, clearly below the friction torque at 100 MPa. For a shaft speed of 5000 rpm and above there is no significant torque

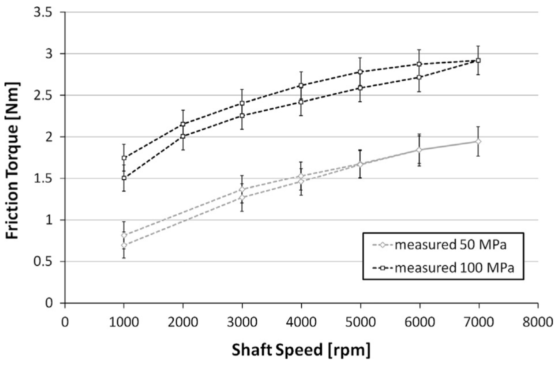

Fig. 8. Average friction torque measured on the test-rig for 50 MPa and 100 MPa specific peak load.

difference between the run-up and run-down at corresponding shaft speeds. This is because for these cases there is only a minor temperature difference (see Table A2 in the Appendix). Below 5000 rpm the temperature difference between run-up and run-down is roughly 2 °C and this is already sufficient to cause the torque difference seen in Fig. 8.

The calculated average friction torque using the basic viscosity model neglecting the piezoviscous and shear thinning effect (Eq. (1)) is shown as solid curve in Fig. 9 in comparison to the experimental data.

While the calculated friction torques at 50 MPa (solid grey curve) agree already closely to the measured curve (dashed grey curve) the calculated friction torques at 100 MPa (solid black curve) underestimate systematically the measured torques (dashed black curve). Nevertheless, the different torques at 100 MPa between run-up and run-down caused by the temperature differences are already clearly seen with this basic rheological model.

The simulation calculates peak oil film pressures of around 200 MPa in the test bearing for the 100 MPa load case independently from the shaft speed. As can be seen in Fig. 2 the pressure induced viscosity increase is significant for such high pressures. Consequently, in the journal bearing the lubricant viscosity increases locally by up to 650% compared to the viscosity at ambient pressure.

Therefore, calculations are performed that consider the piezoviscous effect (Eq. (2)) and the results are shown as solid curves in Fig. 10.

The piezoviscous effect of hydrocarbon lubricants leads to significantly higher viscosity in regions of high pressure. Therefore, the friction torque increases when considering a pressure dependent oil model.

The magnitude of the piezoviscous effect depends naturally on the applied load and is, therefore, intuitively expected to be more important for the higher loaded case of 100 MPa peak load. Indeed this can be seen in the results.

The calculated increase of the friction power losses can be seen at 50 MPa but even more so at 100 MPa. At low shaft speeds the calculated friction torque agrees closely with the measured torque results for both load cases. However, for shaft speeds above 3000 rpm the calculated torque overestimates increasingly the measured torque.

The relative sliding speed in the lubricated gap increases with higher shaft speed and higher shear rates occur. This is also shown in Fig. 11, where the calculated maximum shear rate in the test bearing during one full load cycle is depicted. Clearly, the shear rate increases quite linearly with the shaft speed.

Fig. 12 shows the calculated friction torque considering both the piezoviscous and shear thinning effect (as in Eq. (3)) in the simulation.

As the shear rates increase with the shaft speed, the influence of the shear thinning effect is very small at low shaft speeds and becomes increasingly important for higher shaft speeds.

At 1000 rpm the maximum shear rate is 2.2×10^6 1/s for both load cases, 50 MPa (grey curve) and 100 MPa (black curve). Only a small viscosity decrease of less than 10% occurs for these shear

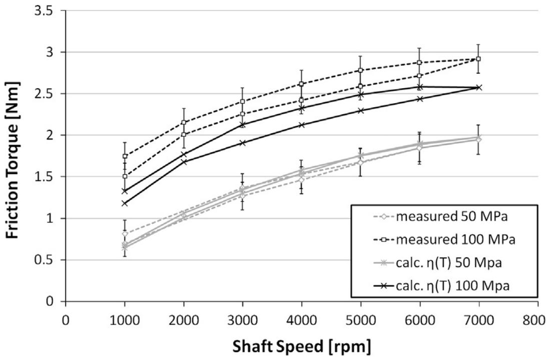

Fig. 9. Comparison of the average friction torque measured on the test-rig with the simulated mean friction torque using the basic oil model (Eq. (1) at 50 MPa and 100 MPa specific peak load.

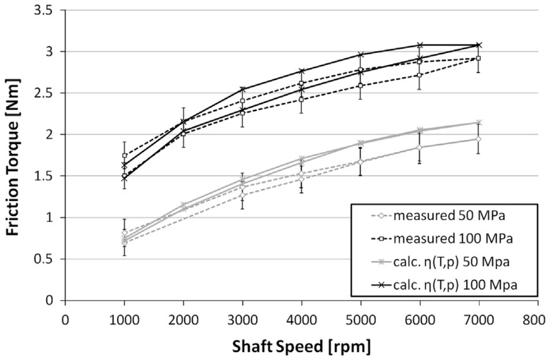

Fig. 10. Comparison of the averaged friction torque measured on test-rig with the simulated mean friction torque using the temperature and pressure dependent oil viscosity model (Eq. (2)) at 50 MPa and 100 MPa specific peak load.

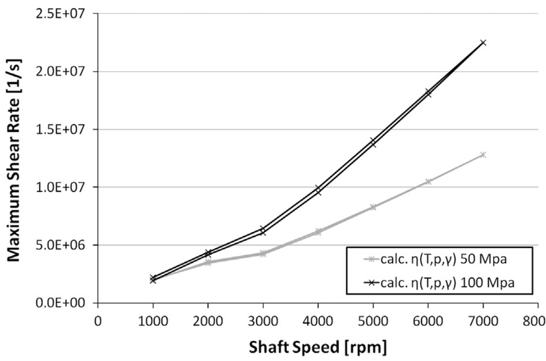

Fig. 11. Calculated maximum shear rate in test bearing at 50 MPa and 100 MPa specific peak load.

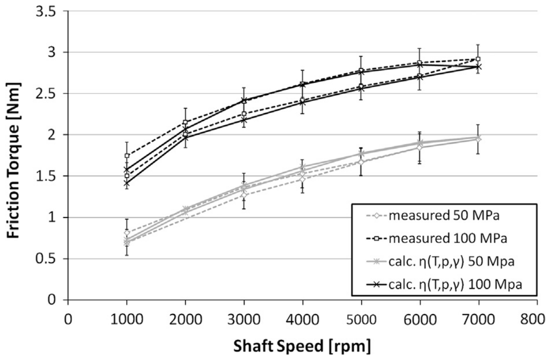

Fig. 12. Comparison of the averaged friction torque measured on test-rig with simulated mean friction torque using the temperature, pressure and shear rate dependent oil viscosity (Eq. (3)) at 50 MPa and 100 MPa specific peak load.

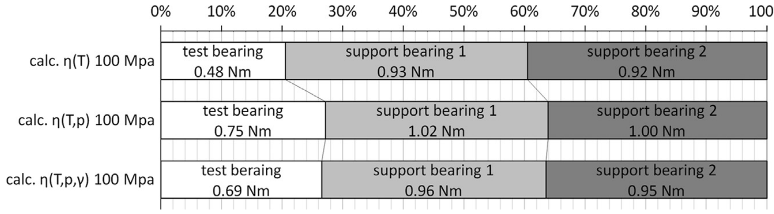

Fig. 13. Friction torque contribution of each bearing at 100 MPa load and 4000 rpm during the run-up. Comparison of different viscosity models: basic model (Eq. (1)) on top; pressure dependent model (Eq. (2)) in the middle; pressure and shear rate dependent model (Eq. (3)) on the bottom.

rates (compare Fig. 3). Also, this maximum shear rate occurs only in a small part of the journal bearing. Consequently, the influence of shear thinning on the friction torque is almost negligible for this shaft speed.

In contrast, at 7000 rpm and 100 MPa the maximum shear rate reaches a ten time higher value of 2.2×10^7 1/s. The viscosity drop is significant (about 25%) and also the area of high shear rate increases. Also at 50 MPa the shear rate increases to 1.3×10^7 1/s and the shear thinning effect becomes significant also in this case, as can be seen from a comparison of Figs. 10–12.

The effect of shear thinning in the rheological lubricant model reduces the calculated friction torque at high shaft speed considerably. Above 5000 rpm a torque difference of about 0.15 N m is determined between the two lubricant models $\eta(T,p)$ and $\eta(T,p,\dot{\gamma})$ independently of the load case.

The calculated friction torques considering temperature, pressure and shear rate dependent viscosity match the measured friction torque closely for the run-down as well as the run-up. An exception from this are the friction torques at low shaft speeds (1000 rpm and 2000 rpm) during the run-up. As mentioned earlier, new journal bearings were used for each test run. In the beginning of the new test run, the journal bearing experiences a run-in process where the edges of each bearing are exposed to wear. This run-in process takes place at the first and second step, where the measured friction torque is consequently higher compared to the calculated friction torque.

In the simulation the finished run-in process is considered by employing surface contours as discussed at the beginning of this paper. The surface contours minimize metal–metal contact and, therefore, the run-in process itself is not considered.

Finally, the contribution of each of the three bearings to the total average friction torque is discussed. Fig. 13 compares the calculated shares of each bearing for a representative load case at 100 MPa and 4000 rpm.

The top bar of Fig. 13 shows the contribution of each bearing calculated with the simple rheological model neglecting the piezoviscous and shear thinning effects. The calculated contribution is given for the individual journal bearings within the bar. Using the simplified rheological model, the test bearing accounts for 20% while each support bearing contributes 40%.

Including the piezoviscous effect – shown as middle bar – a drastic increase of the average friction torque in the test bearing from 0.48 N m to 0.75 N m results. In the support bearings where only half of the peak oil film pressure of the test bearing occurs, the friction torque increases only by less than 0.1 N m. The contribution of the test bearing increases significantly from 20% to about 27%.

Considering in addition the shear thinning effect, the friction torques of all bearings decrease (shown as bottom bar). However, the relative contributions of each bearing remain almost unchanged compared to the previous case. In comparison to the simple model neglecting both effects, the complete rheological model considering both effects shows an average friction moment of 0.69 N m in the test bearing which is an increase by 43%.

To summarize, for the study of highly loaded journal bearings with multi-grade lubricants it is essential to consider both the piezoviscous and shear thinning effects in the simulation. Both effects are needed to describe the absolute friction power losses in a journal bearing as well as the amount of mixed lubrication.

6. Conclusion

In this work a simulation methodology is presented to calculate and reliably predict friction power losses in journal bearings under moderate and high dynamic load conditions. The results from simulation are compared to measurement results obtained from a journal bearing test rig for a large variety of operating conditions.

From the result it can be concluded that a complete description of the rheological lubricant properties is essential to achieve a very close agreement with the experimental data over the entire range of the operating conditions studied.

Only considering either the piezoviscous effect or the non-Newtonian effect improves the simulation accuracy only in a limited range regarding the investigated operating conditions. The inclusion of both effects is necessary to describe the full range of studied operating conditions.

When neglecting the shear thinning effect in simulation the average friction torque is overestimated especially for high rotational shaft speeds. The strong non-Newtonian behaviour in modern low viscosity engine oil makes it even more important to consider its viscosity drop at high shear rates.

The key parameter to describe lubricated contacts is the oil viscosity, which varies strongly with temperature. To consider the temperature gradient of the physical journal bearing in the simulation, equivalent temperature relations for the simulation are introduced. In addition to the equivalent temperature for journal bearings with a 180° oil supply groove which was published previously [2], the present work introduces an equivalent temperature relation for journal bearings without such a groove. The direct comparison to the measured average friction moments shows that these simple equivalent temperature relations are well suited approximations to the real temperature gradient in the journal bearing.

For further investigation, for example, fretting which can appear at high speed and high load, the consideration of shear thinning is essential and shall be the subject of future work.

Acknowledgements

We would like to express our gratitude to our supporting industrial and scientific project partners, namely KS Gleitlager, OMV Refining & Marketing and the Institute of Tribology of the TU Clausthal. We are also grateful to Alicona Imaging GmbH for their kind support.

Table A1
Measured temperatures and simulation input temperatures at 100 MPa test conditions. T_{MB1}, T_{MB2} and T_{BE} are calculated by Eqs. (9) and (10), respectively.

Shaft speed (rpm)	$T_{\text{MB Supply}}$ (°C)	$T_{\text{MB Shell1}}$ (°C)	$T_{\text{MB Shell2}}$ (°C)	T_{BE1} (°C)	T_{BE2} (°C)	T_{BE3} (°C)	T_{BE4} (°C)	T_{MB1} (°C)	T_{MB2} (°C)	T_{BE} (°C)
1000	40.3	48.6	49.0	56.7	57.5	53.6	54.4	46.6	46.9	56.1
2000	43.9	60.7	61.6	72.6	74.2	66.0	68.7	56.5	57.2	71.4
3000	42.0	69.0	70.8	85.1	87.9	74.1	80.2	62.3	63.6	83.4
4000	41.9	77.5	81.2	99.8	103.4	83.4	93.4	68.6	71.4	97.2
5000	42.9	85.4	91.5	112.0	117.1	91.3	105.3	74.8	79.4	109.1
6000	45.3	93.0	101.0	123.0	131.0	99.5	116.9	81.1	87.1	120.7
7000	50.4	101.9	111.5	136.1	145.6	109.3	129.6	89.0	96.2	133.7
6000	51.2	95.9	102.6	123.7	132.9	103.4	119.8	84.7	89.8	122.7
5000	50.3	89.1	94.0	113.4	119.6	95.1	109.1	79.4	83.1	111.7
4000	48.9	81.7	84.8	102.0	106.5	87.1	96.6	73.5	75.8	100.1
3000	46.6	72.9	74.7	88.5	91.8	77.6	83.9	66.4	67.7	87.0
2000	44.2	63.3	64.4	75.7	77.5	68.8	71.5	58.5	59.3	74.4
1000	41.8	53.4	53.8	62.5	63.7	58.7	59.9	50.5	50.8	61.8

Table A2
Measured temperatures and simulation input temperatures at 50 MPa test conditions. T_{MB1}, T_{MB2} and T_{BE} are calculated by Eqs. (9) and (10), respectively.

Shaft speed (rpm)	$T_{\text{MB Supply}}$ (°C)	$T_{\text{MB Shell1}}$ (°C)	$T_{\text{MB Shell2}}$ (°C)	T_{BE1} (°C)	T_{BE2} (°C)	T_{BE3} (°C)	$T_{BE\ 4}$ (°C)	$T_{MB\ 1}$ (°C)	T_{MB2} (°C)	T_{BE} (°C)
1000	75.6	73.2	72.9	75.8	75.0	76.1	75.8	73.8	73.6	75.6
2000	77.2	80.5	80.4	82.6	82.8	81.1	82.3	79.7	79.6	82.4
3000	78.7	86.5	86.5	89.6	91.0	86.3	89.0	84.6	84.6	89.4
4000	79.8	92.0	92.5	97.4	100.3	91.7	97.0	88.9	89.3	97.3
5000	81.2	97.6	98.2	105.3	110.1	98.0	105.2	93.5	94.0	105.7
6000	82.5	102.8	103.8	112.4	119.0	102.8	112.6	97.7	98.4	113.0
7000	82.0	108.1	109.5	119.6	127.8	107.8	120.4	101.6	102.6	120.5
6000	80.7	102.5	103.5	112.4	119.2	103.7	113.3	97.1	97.8	113.4
5000	78.2	97.7	98.4	106.1	111.2	98.7	106.1	92.8	93.3	106.6
4000	80.0	93.2	94.0	99.1	102.1	93.6	98.9	89.9	90.5	99.2
3000	81.0	88.3	88.6	91.9	93.4	88.3	91.1	86.4	86.7	91.7
2000	80.0	82.7	82.8	85.3	85.8	83.3	84.6	82.0	82.1	85.0
1000	76.7	75.8	75.8	78.6	78.3	77.8	77.9	76.0	76.0	78.2

Furthermore, the authors would like to acknowledge the financial support of the "COMET - Competence Centers for Excellent Technologies Programme" of the Austrian Federal Ministry for Transport, Innovation and Technology (bmvit), the Austrian Federal Ministry of Science, Research and Economy (bmwfw), the Austrian Research Promotion Agency (FFG), the Province of Styria and the Styrian Business Promotion Agency (SFG).

Appendix A. Measured temperatures

See Tables A1 and A2.

References

[1] Allmaier H, Priestner C, Six C, Priebsch H, Forstner C, Novotny-Farkas F. Predicting friction reliably and accurately in journal bearings—a systematic validation of simulation results with experimental measurements. Tribol Int 2011;44(10):1151–60.
[2] Allmaier H, Priestner C, Reich F, Priebsch H, Novotny-Farkas F. Predicting friction reliably and accurately in journal bearings—extending the simulation model to TEHD. Tribol Int 2013;58:20–8.
[3] Sommerfeld A. Zur hydrodynamischen Theorie der Schmiermittelreibung. Z Math Phys 1904;50(97):155.
[4] Wang Y, Zhang C, Wang Q, Lin C. A mixed-TEHD analysis and experiment of journal bearings under severe operating conditions. Tribol Int 2002;35(6):395–407.
[5] Allmaier H, Priestner C, Reich F, Priebsch H, Forstner C, Novotny-Farkas F. Predicting friction reliably and accurately in journal bearings—the importance of extensive oil-models. Tribol Int 2012;48:93–101.
[6] Allmaier H, Priestner C, Sander D, Reich F. Friction in automotive engines. In: Pihtili H, editor. Tribology in engineering. Rijeka: Intech; 2013 ISBN: 978-953-51-1126-9, http://dx.doi.org/10.5772/51568.
[7] DuBois GB, Ocvirk FW. Analytical derivation and experimental evaluation of short-bearing approximation for full journal bearings. US Government Printing Office; 1953.
[8] Durak E, Kurbanoğlu C, Bıyıklıoğlu A, Kaleli H. Measurement of friction force and effects of oil fortifier in engine journal bearings under dynamic loading conditions. Tribol Int 2003;36(8):599–607.
[9] Priestner C, Allmaier H, Priebsch H, Forstner C. Refined simulation of friction power loss in crank shaft slider bearings considering wear in the mixed lubrication regime. Tribol Int 2012;46(1):200–7.
[10] Holmberg K, Andersson P, Erdemir A. Global energy consumption due to friction in passenger cars. Tribol Int 2012;47:221–34.
[11] Tung SC, McMillan ML. Automotive tribology overview of current advances and challenges for the future. Tribol Int 2004;37(7):517–36.
[12] Taylor R, Coy R. Improved fuel efficiency by lubricant design: a review. Proc Inst Mech Eng Part J: J Eng Tribol 2000;214(1):1–15.
[13] Kapadia R, Bovington C, Lee-Prudhoe I. A tribological investigation of lubricant effects on bearing friction and fuel economy for passenger car engines and heavy duty diesel engines. Lubr Sci 2007;19(1):11–23.
[14] Warrens C, Jefferies A, Mufti R, Lamb G, Guiducci A, Smith A. Effect of oil rheology and chemistry on journal-bearing friction and wear. Proc Inst Mech Eng Part J: J Eng Tribol 2008;222(3):441–50.
[15] Bair S. High pressure rheology for quantitative elastohydrodynamics, vol. 54. Amsterdam: Elsevier; 2007 ISBN:978-0-444-52243-6.
[16] Bair S. The shear rheology of thin compressed liquid films. Proc Inst Mech Eng Part J: J Eng Tribol 2002;216(1):1–17.
[17] Bair S. Measurements of real non-Newtonian response for liquid lubricants under moderate pressures. Proc Inst Mech Eng Part J: J Eng Tribol 2001;215(3):223–33.
[18] Vogel H. The law of the relation between the viscosity of liquids and the temperature. Physica Z 1921;22:645–6.
[19] Bode B. Entwicklung eines Quarzviskosimeters für Messungen bei hohen Drücken [Ph.D. thesis]. Technische Universität Clausthal; 1984.
[20] Bode B. Entwicklung eines Quarzviskosimeters für Messungen bei hohen Drücken. Tribologie und Schmierungstechnik 1988;35(5):256–61.
[21] Gundrum J. Entwicklung eines Quarzviskosimeters für Messungen bei hohen Temperaturen und Drücken [Ph.D. thesis]. Technische Universität Clausthal; 1991.
[22] Barus C. Isothermals, isopiestics and isometrics relative to viscosity. Am J Sci 1893(266):87–96.
[23] Cross MM. Rheology of non-Newtonian fluids: a new flow equation for pseudoplastic systems. J Colloid Sci 1965;20(5):417–37.

[24] Coy R. Practical applications of lubrication models in engines. Tribol Int 1998;31(10):563–71.
[25] Offner G. Modelling of condensed flexible bodies considering non-linear inertia effects resulting from gross motions. Proc Inst Mech Eng Part K: J Multi-body Dyn 2011;225(3):204–19.
[26] Patir N, Cheng H. An average flow model for determining effects of three-dimensional roughness on partial hydrodynamic lubrication. ASME Trans, J Lubr Technol 1978;100:12–7.
[27] Patir N, Cheng H. Application of average flow model to lubrication between rough sliding surfaces. ASME Trans, J Lubr Technol 1979;101:220–30.
[28] Greenwood J, Williamson J. Contact of nominally flat surfaces. Proc R Soc Lond Ser A Math Phys Sci 1966;295:300–19.

5.2 Simulation of journal bearing friction in severe mixed lubrication – Validation and effect of surface smoothing due to running-in

Metal-metal contact is dominant in the mixed lubrication regime which leads to a rise in friction losses. To calculate friction losses in mixed lubrication regime, a contact model is necessary which considers the surface roughness of the contacting partners. Here, the contact model according to Greenwood and Tripp [35, 36] is included to the simulation model. The contact model calculates the contact pressure and contact area when asperities are interacting. The input parameters for the contact model are derived from surface scans of the shaft and the bearing shells.

The asperities of the contacting surfaces are also influencing the oil flow when the lubrication gap becomes smaller (below 2 μm for the investigated contact pair). This effect is taken into account by the averaged Reynolds equation according to Patir and Cheng [65, 66].

To validate the simulation model in mixed lubrication regime, friction tests on the journal bearing test-rig are performed. The test bearing is loaded with a static force and the test shaft is accelerated and slowed down until it stops. Therefore, the journal bearings operate between pure hydrodynamic friction and severe mixed friction. A similar static load can occur during the starting and stopping of an automotive engine.

The lubricant which is used for the tests in mixed lubrication regime, is the same low-viscosity engine oil as that was also utilized in the previous application example 5.1. Hence, the detailed lubricant model considering high pressures and high shear rates is included in the simulation model. The assumption of the equivalent bearing temperatures for the isothermal simulation method is also adopted from the previous example.

The details of the numerical and experimental work as well as the results are described in [76] which are presented in section 5.2.2. Prior to this, the research findings of the publication are summarized.

5.2.1 Summary of research findings

- The parameters for the Greenwood and Tripp contact model are derived from surface scans of journal bearing shells.
- From the surface scans, the orientation factor of the asperities is evaluated and the flow factors according to Patir and Cheng are calculated.
- The Greenwood and Tripp contact model in combination with a constant boundary friction coefficient, leads to a close agreement with the measured friction torque from the beginning of mixed lubrication regime until severe mixed lubrication.
- The limits of using a constant boundary coefficient can be identified by entering boundary friction regime. The calculated friction torque underestimates the measured friction torque.
- A second contact model is derived from the surface roughness of a worn journal bearing. The additional ″worn″ contact model in comparison with the ″new″ contact model shows a friction benefit in mixed lubrication regime. The ″worn″ contact model predicts a smaller lubrication gap, lower asperity contact pressure

and a smaller contact area due to the reduced surface roughness of the bearing shell.

- In mixed lubrication regime, the impact of neglecting the flow factors according to Patir and Cheng is shown. Especially in mixed lubrication regime, a larger friction torque is determined (up to 20 %).

5.2.2 Paper II [76]

Tribology International 96 (2016) 173–183

Contents lists available at ScienceDirect

Tribology International

journal homepage: www.elsevier.com/locate/triboint

Simulation of journal bearing friction in severe mixed lubrication – Validation and effect of surface smoothing due to running-in

D.E. Sander [a,*], H. Allmaier [a], H.H. Priebsch [a], M. Witt [b], A. Skiadas [b]

[a] *Virtual Vehicle Research Center, Inffeldgasse 21A, 8010 Graz, Austria*
[b] *KS Gleitlager GmbH, Am Bahnhof 14, 68789 St. Leon-Rot, Germany*

ARTICLE INFO

Article history:
Received 28 September 2015
Received in revised form
14 December 2015
Accepted 18 December 2015
Available online

Keywords:
Conformal contact
Non-Newtonian lubricant
Stribeck curve
Mixed elastohydrodynamic lubrication

ABSTRACT

This paper focuses on the friction behavior of journal bearings operating from hydrodynamic to mixed lubrication regime where severe metal–metal contact occurs. Therefore, friction tests with two different static loads are carried out on the journal bearing test-rig from KS Gleitlager. The test results in the form of Stribeck curves provide a solid base to proof the isothermal elastohydrodynamic simulation approach. The simulation approach solves the averaged Reynolds equation introduced by Patir and Cheng and considers metal–metal contact by using the Greenwood and Tripp contact model. All necessary surface parameters are derived from surface scans. No less essential in this approach are the experimentally identified lubricant properties under high pressure and high shear rate.

The calculated friction torque matches the measurement results within the measurement uncertainty for a wide range of operation conditions. With the validated simulation approach the influence of surface smoothing due to metal–metal contact is discussed. Additionally, the limits of a constant boundary coefficient are identified and the effects of flow factors are presented.

1. Introduction

The mixed lubrication regime describes the transition between the pure hydrodynamic lubrication regime, where a fluid separates the contacting surfaces and the boundary lubrication regime, where metal–metal contact is leading. Characteristically for the mixed lubrication regime is that the fluid film cannot completely separate the adjacent surfaces and single asperities interact. Hence, the friction in mixed lubrication regime (mixed friction) is characterized by the co-existence of hydrodynamic and asperity friction [1]. The friction coefficient finds its minimum between the pure hydrodynamic lubrication and the mixed lubrication. In terms of friction reduction and efficiency it is beneficial to operate lubricated contacts in this condition. Unfortunately, wear occurs as asperities are in contact and durability problems can occur.

Especially in the automotive sector a trend to cut fuel consumption and emissions has been established which is driven by emission regulations and customer satisfaction. Downscaled turbocharged combustion engines with high power density are an achievement in modern engine development for performance improvement. The high power and small dimensions of engine components lead to highly loaded lubricated contacts such as journal bearings. Another efficiency benefit is pledged to friction reduction with low-viscous lubricants. These advancements lead to a decreasing oil film thickness in lubricated contacts. This means that journal bearings, which formerly mainly ran in pure hydrodynamic lubrication regime to ensure a long lifetime, may partly expose metal–metal contact during the dynamic operation [2–4].

For lubricated contacts, and particularly for journal bearings the Stribeck curve (see Fig. 1), named after Richard Stribeck [5,6], has become a common tool to assess friction benefits. A static load is applied to the journal bearing and the friction torque is measured for a wide speed range. With such a test configuration the different lubrication regimes can be identified. Bovington [7] describes the importance of the Stribeck curve in bearing design and discusses the effect of low-viscosity lubricant and oil additives. He conducted several tests with various engine oils which were formulated differently. More recently, the influence of surface dimple effects on journal bearing friction is experimentally studied [8] by evaluating the Stribeck curve. In the present study, a similar test setup is used for the measurements. The experimental results in the form of Stribeck curves provide a solid base to validate the simulation approach.

---

[*] Corresponding author.
E-mail address: david.sander@v2c2.at (D.E. Sander).

http://dx.doi.org/10.1016/j.triboint.2015.12.024
0301-679X/© 2015 Elsevier Ltd. All rights reserved.

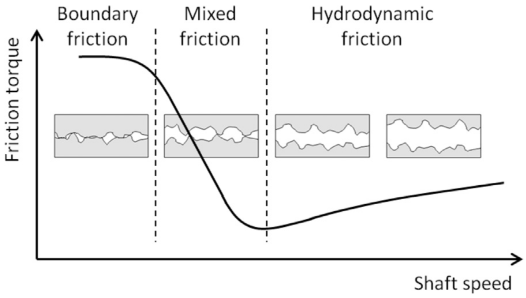

Fig. 1. Sketch of a Stribeck curve with different lubrication regimes.

Predictive simulation approaches to describe lubricated contacts in journal bearings are broadly discussed in the literature and differ in their level of detail. An overview of elastohydrodynamic lubrication analysis of conformal contacts without metal–metal contact is given by Booker et al. [9]. The extensive review focuses on the 2D Reynolds equation and discusses, among other things, bearing deformation, mass-conservative cavitation and pressure–viscosity effects. Also, the effect of surface roughness on bearing performance in elastohydrodynamic lubrication is discussed. Dobrica et al. [10] compare stochastic and deterministic models in more detail and conclude that the stochastic model correctly anticipate the trends of the deterministic models for the investigated surfaces. Both studies do not consider slip boundary conditions which is recently reviewed and discussed by Jao et al. [11]. Beyond the scope of this study is the 3D consideration of the fluid film using a computational fluid dynamics (CFD) approach [12]. Recently, Shahmohamadi et al. [13] present a thermohydrodynamic analysis using CFD approach including a vapor transport equation to consider cavitation. Both temperature and pressure distribution agree well with experimental data.

However, the interaction of single asperities between the contacting surfaces occurs in mixed lubrication regime and has an impact on journal bearing performance. Simulation approaches considering the asperity contact in journal bearings are covered in many text books, for instance [14–16]. Therefore, an extensive reference list is not replicated here.

Notably, only a minor number of publications discuss journal bearing friction in severe mixed lubrication and verify the calculated results with measurement results. Bartel et al. [17] present an analytical model considering metal–metal contact by using an energy approach. The calculated results were compared to measured Stribeck curves. The authors conclude that the viscosity–pressure behavior has a huge influence on the results and should not be neglected. Further, macro-deformation of shaft and bearing need to be considered for realistic friction prediction. Lu et al. [18] present a simple theoretical analysis for friction prediction in mixed and boundary lubrication regime and verified the analysis for different loads and temperatures. The tool is also used to investigate the effect of surface pattern and asperity orientation on Stribeck curves [19].

Wang et al. [20] present an analytical method to derive Stribeck curves and discuss the influence of roughness, elasticity, and thermoelasticity on friction. Especially the elastic deformation has a strong influence on the friction behavior. The influence of surface adaption caused by running-in wear on friction in dynamically loaded bearings is discussed by Bartel et al. [21]. Beside the change of surface roughness an adaption of the bearing geometry is calculated. A clear reduction of maximum contact pressure and friction is identified for the worn bearing. The influence of a worn geometry on journal bearing performance is also discussed by investigating misaligned bearings [22] and bearings subjected to numerous starts and stops [23]. Both papers conclude that a worn bearing geometry decreases the bearing temperatures. Sun et al. [24] calculate the effect of surface roughness change on misaligned journal bearings and highlight the importance of elastically deformation of the contacting bodies. However, no contact model is implemented to discuss friction due to asperity interaction.

The present study focuses on friction losses in journal bearings operating in severe mixed lubrication regime. The analytical investigation uses an isothermal mixed elastohydrodynamic simulation approach which considers the elastic deformation of shaft and bearing structure. Although the temperature is assumed to be constant within the bearing, the variation between different loads and shaft speeds is considered with introducing an equivalent bearing temperature. The equivalent bearing temperature is derived from temperature measurements at the back of the bearing shells. Additionally, the piezoviscous and non-Newtonian behavior of the lubricant are included in the approach. The equation describing the lubricant viscosity is dependent on temperature, pressure and shear rate and was previously derived by measurement. The detailed derivation of the viscosity equation was published in [25] and validated for dynamically loaded journal bearings operating in mainly hydrodynamic regime.

The influence of asperities on hydrodynamic friction is included by using the flow factors according to Patir and Cheng [26,27]. Friction due to metal–metal contact is considered by the Greenwood and Tripp contact model [28]. To derive the parameters for both, flow factors and contact model, bearing shell surface and shaft surface were scanned by white light interferometry. From the surface scans roughness parameters and asperity orientation are established. The boundary friction coefficient is the remaining unknown parameter which is chosen to be constant in this work.

Primary aim of this study is the validation of the simulation approach to calculate journal bearing friction in severe mixed lubrication regime. Further, the practicability and limits of the simple elastic Greenwood–Tripp contact model in combination with a constant boundary friction coefficient is discussed.

For a secondary aim, the influence of surface smoothing due to running-in on friction in mixed lubrication is discussed. Therefore, a ran-in journal bearing surface is analyzed and a second contact model is derived. The influence on metal–metal contact pressure, minimum radial clearance and friction is analyzed.

Further, the exclusion of the flow factors from the simulation and its effect on journal bearing friction is discussed.

Moreover, the presented study complements previous research by the authors which focused on journal bearing friction excited by dynamic loads. Allmaier et al. [29,30] presented a simulation approach using an isothermal bearing assumption. He included the viscosity–pressure relation for different single-grade lubricants and validated the friction losses over a wide range of operation conditions. Metal–metal contact was identified by simulation and also by measuring the contact voltage [31]. Later, the isothermal model was extended to a thermo-elastohydrodynamic model [32] which is able to predict the measured temperatures at the bearing shell. The results also justified the usage of an isothermal simulation approach in terms of friction prediction. Sander et al. [25] included the non-Newtonian behavior of modern multi-grade engine oils into the isothermal simulation approach. Again, the simulation results were validated for a variety of shaft speeds and dynamic loads up to 100 MPa specific load in the test bearing. After the test procedure worn areas on the bearing surface were identified which was caused by metal–metal contact. Metal–metal contact was also identified by simulation. As a consequence research on the running in process of journal bearings was conducted [33,34]. Complementary, the presented results are obtained from the same simulation approach yet discuss friction in severe mixed lubrication regime.

2. Lubricant properties

The lubricant's viscosity is directly related to the friction in hydrodynamic lubrication regime. In mixed lubrication regime the lubrication additives modifies the frictional behavior of the contacting surfaces. It is thus important to explicitly describe the lubricant.

In this work a fully formulated low viscous 0W20 hydrocarbon engine oil is used as it is available on the automotive market. The main properties of the modern lubricant including the density and the viscosity at various conditions are given in Table 1.

Additionally to the temperature dependency of the rheological properties, the viscosity is strongly dependent on pressure and shear rate. Therefore, the piezoviscous and the non-Newtonian behavior of the lubricant were analyzed. In previous publication by the authors [25] the parameters (see Table 2) for the empirical viscosity equation according to Vogel [35], Barus [36] and Cross [37] were derived from experimental data:

$$\eta(T,p,\dot{\gamma})=A\cdot e^{B/(T+C)+\alpha\cdot p}\cdot\left(r+\frac{1-r}{1+(K\cdot\dot{\gamma})^{m}}\right) \qquad (1)$$

In the simulation the viscosity is represented by Eq. (1). The corresponding values are listed in Table 2.

3. Testing

The journal bearing test-rig at KS Gleitlager was used to perform the experimental friction measurement. The test-rig is sketched in Fig. 2.

It consists of a rotating straight shaft which rests on two supporting journal bearings in support brackets. The shaft is driven by an elastically clutched electric motor. A test connecting rod is placed in between the two support brackets. An external load is applied onto the test connecting rod and on to the test journal bearing. The test journal bearing has a diameter of 47.8 mm and a width of 17.2 mm and corresponds to a typical big-end bearing used in modern combustion engine. The preconditioned oil is supplied through a hole in the lower bearing shell which. Both support journal bearings have a diameter of 54 mm and a width of 25 mm. It has an 180° oil supply grove all along the top shell. All three bearings are made of a steel–aluminum composite material.

The test rig is equipped with a torque transducer, a Manner Sensortelemetrie 50 N m with an accuracy of ±0.15 N m. The transducer is placed between the electric motor and the shaft to measure the friction torque generated by all three bearings. The bearing temperatures were monitored during the test. Therefore, PT100 elements were placed at the back of the bearing shells. The elements have an accuracy of ±0.5 °C.

3.1. Test conditions

For the investigation of friction in mixed lubrication regime a static load is applied to the test connecting rod. Hence, only the top shell of the test bearing and the bottom shell of the support bearings are stressed. Further the oil is supplied via the unloaded bearing shells. Two load cases are investigated, the first with 8 kN load and the second with a 4 kN load which correspond to 10 MPa specific load in the test bearing and 5 MPa, respectively. In the beginning of each test new bearing shells are placed into the test connecting rod and the support brackets. One test run consists of a constant speed-up to 6000 rpm followed by a constant speed-down until the shaft stops to rotate. One test run lasts for 12 min. The second half in other words, the speed-down is recorded and evaluated. The shaft speed during the speed-down is plotted in Fig. 3 over time (dashed black line).

Table 1
Basic properties of the tested 0W20 lubricant.

Density at 40 °C	832.5	kg/m^3
Dyn. viscosity 40 °C	37.5	mPa s
Dyn. viscosity 100 °C	6.8	mPa s
HTHS-viscosity[a]	2.7	mPa s

[a] The HTHS-viscosity is defined as the viscosity at high temperature (150 °C) and high shear rate (10^6 1/s).

Table 2
Parameters for Eqs. (1) derived from experimental data [25].

A	0.0516	mPa s
B	1127.6	° C
C	130.7	° C
α	0.00095	1/bar
r	0.53	–
m	0.79	–
K	7.9 e−8	s

The lubricant which is supplied to all three bearings is preconditioned during the entire test procedure. Hence, the lubricant supply temperature stays stable between 91 °C and 92 °C during the test run and is similar for both load cases. The black solid curve in Fig. 3 shows the supply temperature for 10 MPa load and the grey solid curve represents the supply temperature for 5 MPa load.

3.2. Test results

The measured overall friction torque is shown in Fig. 4 over the shaft speed for both load cases.

The black curve represents the measured friction torque under the specific static load of 10 MPa. At a shaft speed of 6000 rpm the friction torque is 1.6 N m. By reducing the shaft speed the friction moment decreases to a minimum of 0.5 N m at around 400 rpm. Below 400 rpm the friction moment abruptly increases. At high speed the bearing operates in hydrodynamic lubrication regime. The rise of the friction torque below 400 rpm is attributed to metal–metal contact between the shaft and bearing shell. The grey curve shows the friction torque measured with an applied load of 5 MPa. Compared to the 10 MPa load case, a lower friction torque can be identified all over the investigated speed range. In the hydrodynamic regime the friction torque is reduced by around 15 %.

4. Simulation

For the simulation the KS Gleitlager test rig is modeled within the flexible multi-body solver AVL Excite Power Unit[1] [38,39]. The test shaft, the test connecting rod and the two support brackets are represented as mathematical condensed finite element structures which can deform elastically [40]. The lubricated journal bearings which connect the components are calculated by solving the Reynolds equation by finite volume approach [38]. The discretization points of the lubrication regime are equally distributed along the axial and circumferential direction. In the presented model 25 points in axial direction are chosen for all bearings. In circumferential direction the test bearing has 200 points and the support bearing has 176 points. Every second point is directly coupled to a point on the solid structure. The displacement of the

---

[1] Version 2014.1, AVL List GmbH, Advanced Simulation Technology, Hans-List-Platz 1, 8020 Graz Austria, www.avl.com

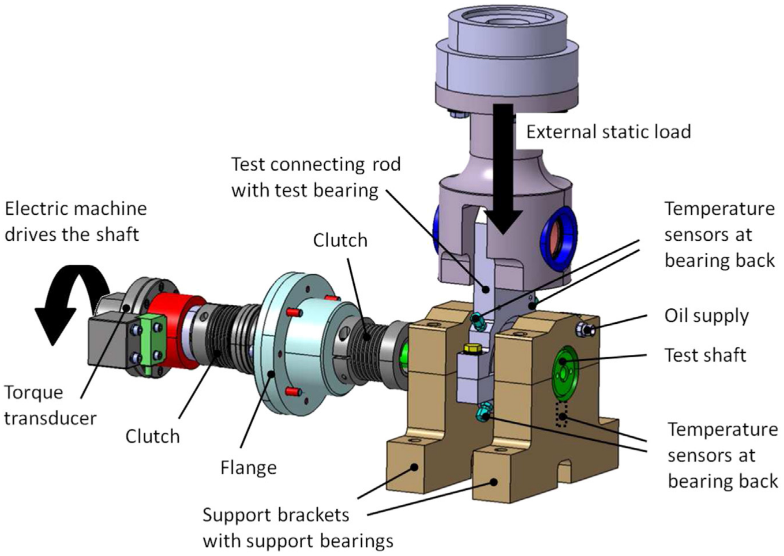

Fig. 2. Journal bearing test-rig at KS Gleitlager.

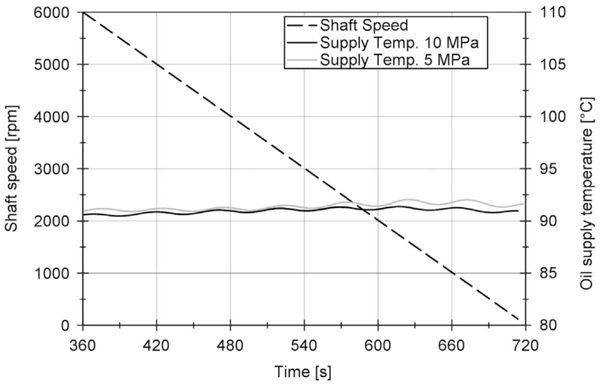

Fig. 3. Shaft speed (black dashed curve) and oil supply temperature (black and grey solid curve) over time.

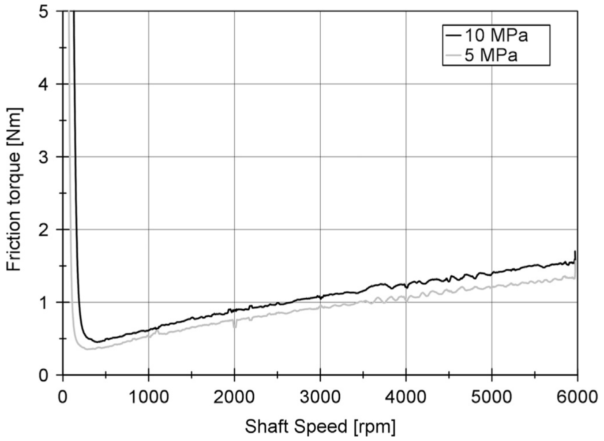

Fig. 4. Friction torque over shaft speed for 10 MPa static load (black) and 5 MPa static load (grey).

points in between are interpolated. The coupling method is described in [41]. When the distance between the facing surfaces decreases their surface roughness will affect the oil flow. Patir and Cheng [26,27] introduced flow factors to the Reynolds equation taking this influence into account:

$$-\frac{\partial}{\partial x}\left(\phi_x\frac{h^3}{12\eta}\frac{\partial p}{\partial x}\right)-\frac{\partial}{\partial y}\left(\phi_y\frac{h^3}{12\eta}\frac{\partial p}{\partial y}\right)+\frac{\partial}{\partial x}\left(h\frac{u_1+u_2}{2}\right)+\frac{\partial}{\partial x}\left(\phi_s\frac{u_1+u_2}{2}\sigma_s\right)+\frac{\partial h}{\partial t}=0, \qquad (2)$$

where x, y denote the circumferential and the axial direction, respectively. p is the hydrodynamic pressure and h the oil film thickness which is dependent on x and y. Further, u_1 and u_2 denote the sliding speeds of the facing surfaces. The influence of surface roughness is considered by the pressure flow factors ϕ_x, ϕ_y and the shear flow factor ϕ_s. The oil viscosity η is considered temperature, pressure and shear rate dependent in this paper (see Eq. (1)).

The consideration of the asperity contact itself is described below (see Section 4.2). The cavitation model is based on the JFO approach [42,41]. However, the non-linear model is solved in time domain. Therefore, each simulation runs until a stable quasi-static condition is achieved.

4.1. Friction moment

The friction torque acting on the bearing surface considers both hydrodynamic losses and losses due to asperity contact. Therefore, the friction torque M_{Friction} can be calculated by integrating the shear stresses over the bearing surface:

$$M_{\text{Friction}} = r \int \int_A (\tau_h + \tau_a)\, dx\, dy, \tag{3}$$

where A denotes the bearing surface and r is the nominal shell radius. τ_h is the hydrodynamic shear stress. It is calculated by

$$\tau_h = \eta \cdot \frac{u_1 - u_2}{h} (\phi_{\text{f}} \pm \phi_{\text{fs}}) \pm \phi_{\text{fp}} \frac{h}{2} \cdot \frac{\partial p}{\partial x}, \tag{4}$$

where $+$ and $-$ refer to the shell surface and the journal surface, respectively. ϕ_{f}, ϕ_{fs} and ϕ_{fp} are the shear stress factors according to Patir and Cheng.

The shear stress in case of asperity contact τ_a between the shell surface and the journal surface is calculated by

$$\tau_a = \mu_{\text{Bound}} \cdot p_a, \tag{5}$$

where μ_{Bound} is the boundary friction coefficient and p_a denotes the asperity contact pressure.

4.2. *Asperity contact pressure*

The asperity contact pressure is calculated using the Greenwood and Tripp approach [43,28]. The theory of Greenwood and Tripp is based on the contact of two nominally flat, random rough surfaces. The asperity contact pressure can be written as

$$p_{\text{a}} = KE^* F_{5/2}(H_s), \tag{6}$$

where E^* is the composite elastic modulus, $E^* = \left(\frac{1-\nu_1^2}{E_1} + \frac{1-\nu_2^2}{E_2}\right)^{-1}$, where ν_i and E_i are the Poisson ratio and Young's modulus of the adjacent surfaces, and $F_{5/2}(H_s)$ is the form function, which is defined as

$$F_{5/2}(H_s) = \begin{cases} 4.4086 \cdot 10^{-5} (4 - H_s)^{6.804}, & \text{if } H_s < 4 \\ 0, & \text{if } H_s \geq 4 \end{cases} \tag{7}$$

H_s is a dimensionless clearance parameter, defined as $H_s = (h - \overline{\delta}_s)/\sigma_s)$, with σ_s being the combined asperity summit roughness, which is calculated according to

$$\sigma_s = \sqrt{\sigma_{sJ}^2 + \sigma_{s,S}^2} \tag{8}$$

and $\overline{\delta}_s$ being the combined mean summit height, $\overline{\delta}_s = \overline{\delta}_{sJ} + \overline{\delta}_{s,S}$. The form factor $F_{\frac{5}{2}}(H_s)$ becomes zero for a dimensionless clearance parameter beyond four which further means no asperity contact occurs. Finally, the elastic factor K is defined as

$$K = \frac{16 \cdot \sqrt{2} \cdot \pi}{15} \cdot (\sigma_s \cdot \overline{\beta}_s \cdot \eta_s)^2 \cdot \sqrt{\frac{\sigma_s}{\overline{\beta}_s}}, \tag{9}$$

where $\overline{\beta}_s$ is the mean summit radius and η_s is the summit density.

4.3. *Bearing temperatures*

The lubricant temperature within the journal bearing varies according to the local position. For the simulation, an equivalent bearing temperature is introduced to consider the temperature as constant in the lubrication gap. For each speed the equivalent temperature is calculated from the measured bearing back temperatures. The approach is described in [25]. For completeness the equivalent temperatures are listed in Table 3 for a specific load of 10 MPa and in Table 4 for 5 MPa, respectively.

Table 3
Equivalent bearing temperatures at 10 MPa load.

Speed (rpm)	150	200	250	300	400	500	1000	3000
T_{TB} (°C)	101.0	101.0	101.1	101.2	101.4	101.6	102.8	108.0
T_{SB1} (°C)	102.4	102.5	102.5	102.6	102.8	103.0	104.3	108.0
T_{SB2} (°C)	102.7	102.8	102.9	103.0	103.2	103.3	104.5	108.2

Table 4
Equivalent bearing temperatures at 5 MPa load.

Speed (rpm)	150	200	250	300	400	500	1000	3000
T_{TB} (°C)	99.1	99.2	99.2	99.3	99.4	99.6	100.6	105.6
T_{SB1} (°C)	101.1	101.1	101.2	101.2	101.3	101.4	102.3	105.6
T_{SB2} (°C)	101.4	101.4	101.5	101.5	101.6	101.6	102.5	106.1

Table 5
Surface roughness and simulation input parameters for the test bearing shell and the shaft.

Contact pair	New		Worn	
Surface	Shell	Shaft	Shell	Shaft
R_a (μm)	0.27	0.14	0.22	0.14
R_q (μm)	0.34	0.20	0.26	0.20
σ (μm)	0.28	0.13	0.23	0.13
δ (μm)	0.39	0.21	0.19	0.21
K (−)	0.001		0.002	
E^* (GPa)	53.3		53.3	
μ_{Bound} (−)	0.02		0.02	
Γ (−)	12	4	12	4

T_{TB} represents the equivalent temperature of the test bearing. T_{SB1} and T_{SB2} is the temperature for the support bearings. The maximum temperature difference between the test bearing and the two support bearings is around 2 °C. At 3000 rpm a maximum temperature of 108 °C for 10 MPa specific load is reached. At shaft speeds below 500 rpm the temperature remains similar within 0.6 °C for each bearing. Hence, an extensive heating due to asperity contact was not observed.

4.4. *Surface roughness and contact pairs*

The surfaces of bearing shell and shaft were scanned by a white light interferometer to determine the flow factors and the surface parameters for the contact pairs. Therefore measurement spots of a size of 1 mm by 1 mm were analyzed. The bearing shell was measured before the test run and for comparison a worn bearing shell was scanned. In combination with the shaft surface two contact pairs are generated (see Table 5). The “new” contact pair combines the new bearing shell surface with the shaft surface. The “worn” contact pair represents the worn bearing shell surface. The hardened steel shaft is not subjected to any surface changes during the test. Therefore, the shaft surface parameters remain unchanged. The arithmetic average R_a of the bearing shell surface drops from 0.27 μm to 0.22 μm. The root mean square R_q decreases from 0.34 μm to 0.26 μm. Table 5 summarizes the parameters of the “new” and “worn” contact pair.

Specified are the arithmetic average of the surface profile R_a, the root mean square of the profile R_q as well as the asperity summit roughness (root mean squared) σ and the mean summit height δ which both are relevant for the contact model in the simulation. The combined Young's modulus E^* and the elastic factor K are calculated according to Section 4.2. A boundary friction coefficient μ_{Bound} of 0.02 is defined. Γ identifies the orientation of the asperities for each surface by the definition from Peklenik [44] which is used by Patir and Cheng:

$$\Gamma = \frac{\lambda_{0.5x}}{\lambda_{0.5y}}, \tag{10}$$

where $\lambda_{0.5x}$ and $\lambda_{0.5y}$ represents the autocorrelation length in circumferential and axial direction, respectively. If Γ is greater than

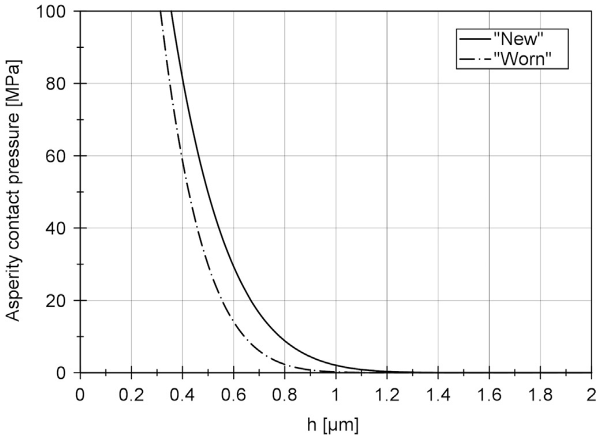

Fig. 5. Calculated contact pressure according to Eq. (6) over oil film thickness for both contact pairs.

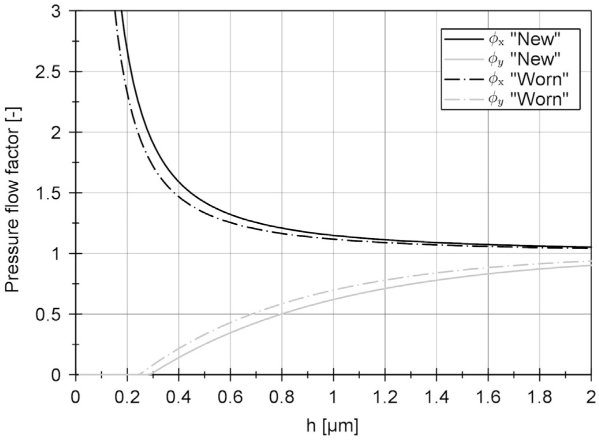

Fig. 6. Pressure flow factors according to Patir and Cheng over oil film thickness for both contact pairs.

one, as in the present case, the asperities are align with the circumferential direction.

Fig. 5 shows the asperity contact pressure over the oil film thickness. The solid line represents the "new" contact pair which shows no contact until a lubrication gap below 1.2 µm. The contact pressure strongly increases with a further reduction of oil film thickness. The "worn" contact pair is shown as dash-dotted line. First asperity contact pressure can be identified around 1 µm. The increase of contact pressure is slightly steeper compared to the "new" contact pair because of the higher elastic factor *K*.

The pressure flow factors in circumferential (x) and axial (z) direction for the two contact pairs are shown in Fig. 6. Both curves show an equal characteristics as the asperity orientation of the surfaces does not change but the curve of the "new" contact pair is slightly shifted to a higher lubrication gap h compared to the "worn" contact pair. The characteristic curves of the shear flow factor ϕ_s and the shear stress factors ϕ_f, ϕ_{fs} and ϕ_{fp} are shown in Appendix A.

5. Simulation results and validation

This section starts with a comparison between measurement and simulation and continues with a detailed discussion of the simulation results.

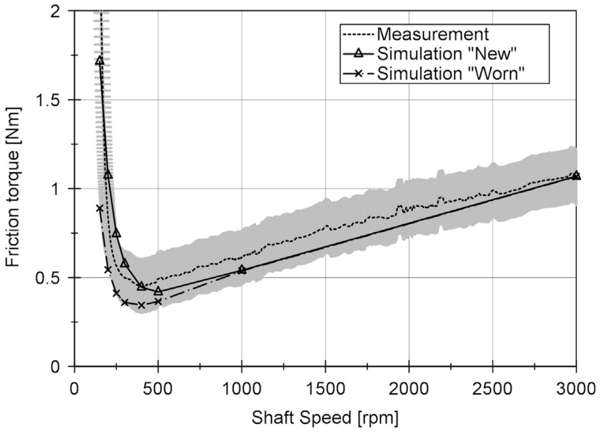

Fig. 7. Comparison between calculated friction torque and measured friction torque over shaft speed at a load of 10 MPa.

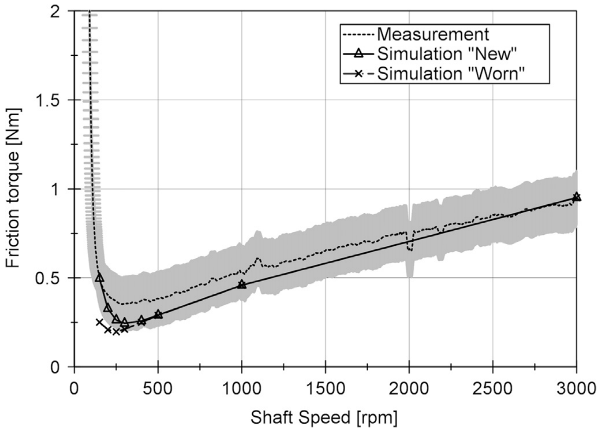

Fig. 8. Comparison between calculated friction torque and measured friction torque over shaft speed at a load of 5 MPa.

The dashed black curve in Fig. 7 shows the friction torque obtained from the measurement with a static load of 10 MPa. The grey area represents the uncertainty band of the torque and speed measurement. The other black lines represent the calculated friction torque, where the solid line refers to the "new" contact pair and the dash-dotted line to the "worn" contact pair. For both contact pairs the calculated friction torque at 1000 rpm and 3000 rpm are equal where all three bearings mainly operate in hydrodynamic regime. At 500 rpm and below, a higher friction torque is calculated for the "new" contact pair. However, both calculated friction curves lie within the measurement uncertainty. Regarding the position of minimum friction torque, the "worn" contact pair shows a good match to the measurement. The minimum friction torque occurs at 400 rpm.

Fig. 8 shows the comparison between measurement and simulation similarly to previous the figure yet for a static load of 5 MPa. The beginning of pure hydrodynamic lubrication is shifted to a lower shaft speed at around 500 rpm. Again, the calculated friction torque is equal for both contact pairs in the hydrodynamic regime and matches the measured torque. As asperity contact occurs below 500 rpm the calculated friction torque differs between the two contact pairs. Obviously, the rougher "new" contact pair shows a higher friction torque compared to the "worn" contact pair. While the calculation results with the "new"

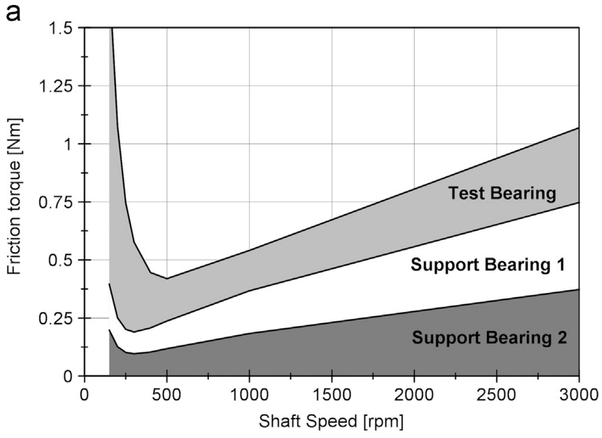

”New” contact pair

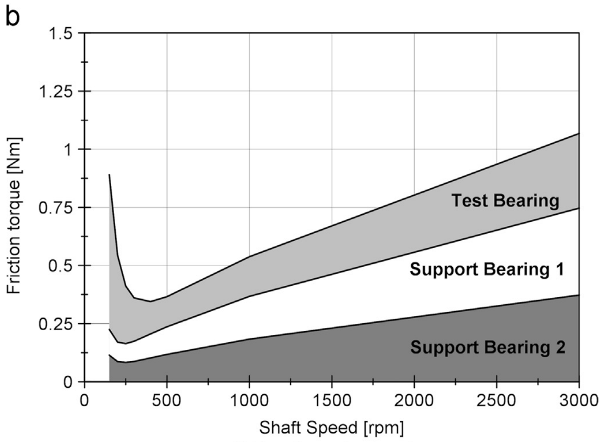

”Worn” contact pair

Fig. 9. Calculated friction contribution of each bearing at 10 MPa load.

contact pair lie within the measurement uncertainty for all speeds, the friction torque is slightly underestimated with the “worn” contact pair at low speed.

The calculated friction torque agrees with the measured friction torque for 5 MPa and 10 MPa over a wide range of operation. Hence, it can be concluded that the presented method is suitable for lubricated journal bearings operating with intense asperity contact. Subsequently, the calculated results are further analyzed to discuss the influence of surface roughness on asperity contact pressure and friction losses. The case with a static load of 10 MPa is therefore exemplified.

First, the contributions of each bearing to the overall friction torque are of interest. Fig. 9(a) shows the friction shares with the “new” contact pair applied. Correspondingly, Fig. 9(b) shows the results calculated with the “worn” contact pair. In the pure hydrodynamic lubrication regime, between 1000 rpm and 3000 rpm, the overall friction torque is equally distributed between all three bearings. By reducing the shaft speed, it can be identified, that asperity contact occurs primarily at the test bearing followed by the two support bearings. The bearing load per projected area is roughly three times higher at test bearing compared to the support bearings. As a result, the increase of friction moment with reducing shaft speed is mainly credited by the test bearing. Hence, the test bearing is mainly responsible for the sharp increase of the overall friction losses at lower speed.

By regarding the results of the two contact pairs it can be seen that the roughness influence is most notable at the higher stressed test bearing. Thus, the test bearing is further analyzed (see Fig. 10).

Fig. 10 (a) and (b) show the share of hydrodynamic friction torque and friction torque caused by asperity contact for the “new” and “worn” contact pair. The hydrodynamic friction torque decreases monotonically with decreasing shaft speed and is similar for both cases. Hence, the torque difference at shaft speeds at 500 rpm and below can be traced back to the friction caused by asperity contact only. The “new” contact pair shows a notable asperity friction torque at 500 rpm while it almost completely vanished for the “worn” contact pair. With a further speed reduction the torque caused by asperity contact steeply rises up to 1.25 Nm for the “new” contact pair at 150 rpm. In comparison the calculated maximum asperity friction torque for the “worn” contact pair reaches 0.6 Nm.

Additionally, the maximum hydrodynamic pressure and maximum asperity contact pressure which occurs in the lubrication gap are displayed as grey lines. The solid grey line represents the maximum hydrodynamic pressure. It nearly stays constant over the engine speed except at very low speed when it drops drastically, but first asperity contact pressure already occurs at higher shaft speed before the hydrodynamic pressure decreases. Therefore, the hydrodynamic pressure drop is not directly dependent to the occurrence of asperity contact. The maximum asperity contact pressure itself raises potentially with decreasing shaft speed. The deviation of maximum asperity contact pressure between the “new” and “worn” contact pair at the same speed is roughly 5 MPa. This deviation stays constant over the shaft speed.

The increase of friction moment in mixed lubrication is also dependent on the size of the area where asperity contact occurs. Fig. 10(c) and (d) shows the formation of asperity contact area for the “new” and “worn” contact pairs at three different shaft speeds. At 500 rpm (bottom figure) the asperity contact concentrates on the bearing edges only. This edge loading is caused by the elastic bending of the shaft for the presented case. However, a smaller size of contact area can be identified for the “worn” contact pair. The results of the “new” contact pair at 250 rpm show a contact area which spreads all along the bearing width. At the same speed, the contact area calculated with the “worn” contact model is still concentrated on the edges. At 150 rpm both contact pairs show asperity contact all along the bearing width.

Regarding to the above discussed maximum hydrodynamic pressure, the beginning of the pressure drop correlates to the speed where asperity contact pressure spreads over the whole bearing width for the first time. This is the case for both contact pairs.

The maximum asperity contact pressure remains at the bearing edge regardless of the shaft speed. It can also be identified that the circumferential position of the maximum asperity pressure moves towards the top position of the bearing with lower shaft speed. This behavior is best visible in Fig. 11 which shows the minimum radial distance between shaft and bearing shell and its corresponding circumferential position.

At a shaft speed of 3000 rpm the minimum radial displacement between shaft and bearing shell is 2 μm. The minimum distance occurs at 30° from the top position in other words, the shaft is shifted in circumferential direction with reference to the bearing shell. The minimum radial distance decreases with a drop in shaft speed. With Fig. 5 in mind asperity contact begins at around

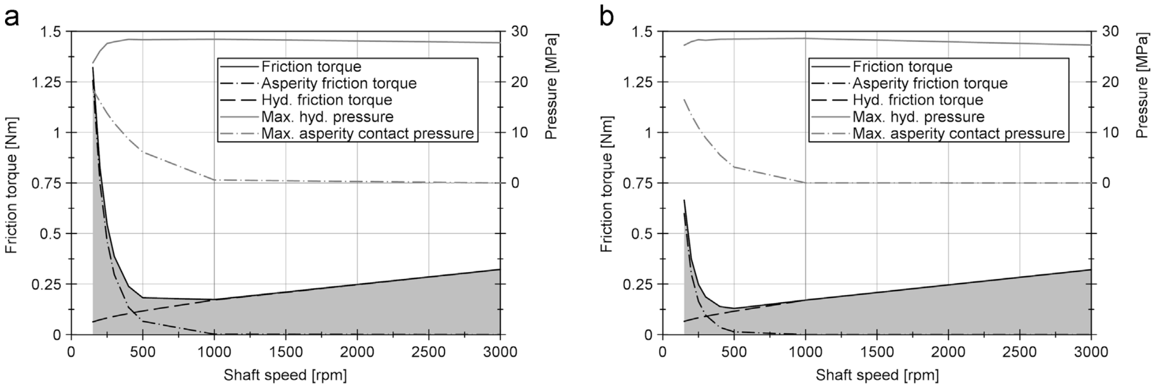

“New” contact pair, friction contribution and maximum pressure

“Worn” contact pair, friction contribution and maximum pressure

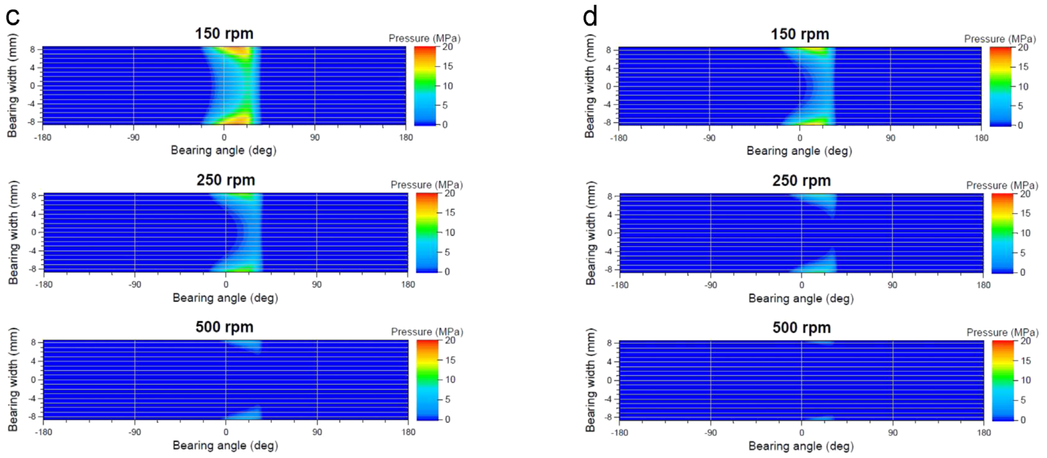

“New” contact pair, asperity contact pressure distribution at different shaft speeds

“Worn” contact pair, asperity contact pressure distribution at different shaft speeds

Fig. 10. Specific analysis of the test bearing simulation results, 10 MPa load.

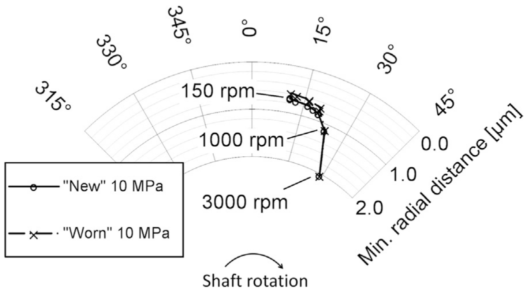

Fig. 11. Minimum radial distance between shaft and bearing shell and its circumferential position.

1.2 µm for the “new” contact pair and 1.0 µm for the “worn” contact pair, respectively. The minimum radial distance as well as its circumferential position is exactly the same, as long as the bearing operates in hydrodynamic lubrication regime. Below 1 µm the radial distance distinguishes for the two contact pairs but the circumferential position remains similar. At 150 rpm the minimum radial distance, calculated with the “new” contact pair, is 0.7 µm. Using the “worn” contact pair results to a minimum radial distance of 0.6 µm. At 150 rpm the shaft has moved towards the top position of the bearing and stays at 10°.

6. Discussion

The simulation results match the measured Stribeck curve for the presented load cases. Especially at a specific load of 10 MPa, the results calculated with both contact pairs lie within the measurement uncertainty. Although the calculated results with the “worn” contact pair show a clearly reduced friction torque in the mixed lubrication regime compared to the “new” contact pair. The detailed bearing results from previous section additionally estimate a reduced contact pressure, reduced size of contact area and a reduced minimum distance between shaft and bearing shell. Also the transition between hydrodynamic and mixed lubrication regime moves to a lower speed.

Regarding the transition speed, the “worn” contact pair appears to be more suitable at a specific load of 10 MPa. At 5 MPa the results with the “new” contact pair match the transition speed. It can be expected that an adaption of the surface roughness occur in the beginning of bearing operation. In the presented measurement procedure a speed up was performed before the Stribeck curve was determined. During the speed up metal–metal contact already occurs and a smoothing of the surface takes place. At higher specific load obviously higher metal–metal contact pressure develops and a quicker adaption of surface roughness can be expected. The quicker adaption at 10 MPa load eventually explains the good match of measurement and simulation with the "worn" surface roughness.

Nevertheless, the calculated friction benefit in mixed lubrication regime only considers the adaption of surface roughness due to running in. Beside the change of surface roughness, an adaption of the surface geometry occurs and effects the load carrying capacity of the fluid film. Additionally, a decrease in boundary friction coefficient with the running in progress can be expected which will further increase the friction benefit [45].

6.1. *Boundary friction coefficient*

A constant boundary friction coefficient μ_{Bound} is chosen for this model, although more complex models with a variable boundary friction coefficient exist [39]. The simplification bears the advantage that only a single variable has to be defined for a specific combination of bearing/shaft material and lubricant. The comparison between measurement and simulation shows that the constant friction coefficient is suitable to predict friction in mixed lubrication regime where metal–metal contact is dominant in the high loaded region of the bearing. The results show a maximum asperity contact pressure of up to 20 MPa. Disadvantage of a single friction coefficient is the restriction to the mixed lubrication regime. In boundary lubrication regime, for instance the shaft starts to rotate, the friction torque is underestimated.

A change of μ_{Bound} does neither affect the friction losses in hydrodynamic regime nor impact the magnitude of asperity contact pressure. In fact it amplifies or reduces the friction torque caused by asperity contact (see Eq. (5)). The transition speed between hydrodynamic and mixed lubrication stays exactly the same.

Nevertheless, friction in mixed lubrication is strongly dependent on film forming additives (friction modifier) added to the lubricant. The focus in the present work does not lie on the specification of lubricant additives but their influence should be mentioned as further research in this field is of interest. Spikes [46] identified three separate mechanisms in which lubricant additives can influence friction in mixed lubrication: (a) formation of a layer to reduce boundary friction at asperity contacts, (b) formation of a thin film of high viscosity on the surface and (c) a change (reduction or increase) of effective surface roughness. Hence, for the friction prediction with different formulated engine oil an exclusively change of μ_{Bound} will may not provide satisfying result. Film forming additives in journal bearing application also enable a shift of the transition between hydrodynamic and mixed lubrication.

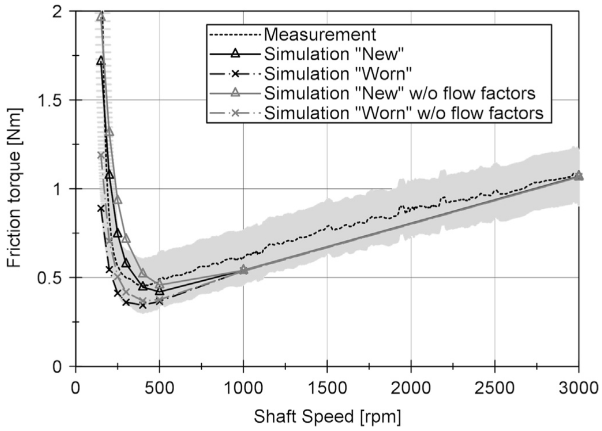

Fig. 12. Influence of flow factors on friction prediction at 10 MPa load.

6.2. *Influence of flow factors on friction torque*

The presented results in previous section are calculated using the averaged Reynolds equation which considers the flow factors according to Patir and Cheng (see Eq. (2)). The influence of neglecting the flow factors on the calculated friction torque is shown in Fig. 12.

The grey lines correspond to the calculated friction torque without considering the flow factors. The black lines include the flow factors in the calculation. The friction torque in pure hydrodynamic lubrication regime, above 1000 rpm, is not affected by the flow factors. By lowering the shaft speed and hence reducing the lubrication gap two changes when neglecting the flow factors can be identified. First the calculated friction torque in mixed lubrication regime increases notable without taking the flow factors into account. Second the transition between hydrodynamic and mixed lubrication moves slightly to a higher speed. However, the simulation results with the "worn" contact pair and without flow factors match the measurement over the observed speed range. The "new" contact pair overestimates the friction torque at low shaft speed.

7. Conclusion

This paper discusses journal bearing friction in mixed lubrication regime. For discussion purposes, measurements on a journal bearing test rig at KS Gleitlager were performed with two different static loads acting on the bearings. The measurement results provide a sound basis to validate the presented simulation approach. A detailed viscosity specification of the lubricant, dependent on temperature, pressure and shear rate, is included in the simulation model. The oil model has previously been validated for dynamic loads and a wide range of operation conditions [25]. The surface texture of the journal bearings has a major influence on friction in mixed lubrication regime. Hence, the surface of the state-of-the-art journal bearings is scanned and furthermore the flow factors, introduced by Patir and Cheng and parameters for the Greenwood and Tripp contact model, are established.

The comparison of the friction torque between measurement and simulation shows a good agreement in the hydrodynamic and mixed lubrication regime. Hence, the presented input data are suitable for the friction prediction in journal bearings operation under severe conditions. The chosen constant boundary friction coefficient of $\mu_{\mathrm{Bound}} = 0.02$ is appropriate for the presented combination of lubricant and bearing/shaft material. Both lubricant and material are current state of the art components used in modern combustion engines.

Furthermore, the simulation results are analyzed to discuss the influence of surface roughness on asperity contact and friction moment. A run-in surface roughness shows a lower maximum contact pressure and a reduced area of asperity contact compared to the roughness of a new bearing shell. A lower transition speed between hydrodynamic and mixed lubrication is identified. The run-in surface also predicts a smaller minimum distance between shaft and bearing shell.

Acknowledgments

We would like to express our gratitude to our supporting industrial and scientific project partners, namely KS Gleitlager, AVL and the Institute of Tribology of the TU Clausthal.

The authors would like to acknowledge the financial support of the "COMET – Competence Centers for Excellent Technologies Programme" of the Austrian Federal Ministry for Transport, Innovation and Technology (bmvit), the Austrian Federal Ministry of Science, Research and Economy (bmwfw), the Austrian Research Promotion Agency (FFG), the Province of Styria and the Styrian Business Promotion Agency (SFG).

Furthermore, we acknowledge the partial financial support of the Austrian Science Fund (FWF): P27806-N30.

Appendix A. Shear flow factor and shear stress factors

The shear flow factor ϕ_s and the shear stress factors ϕ_f, ϕ_{fs} and ϕ_{fp} are shown in Figs. A.1, A.2 and A.3. Each diagram compares the "new" and the "worn" contact model.

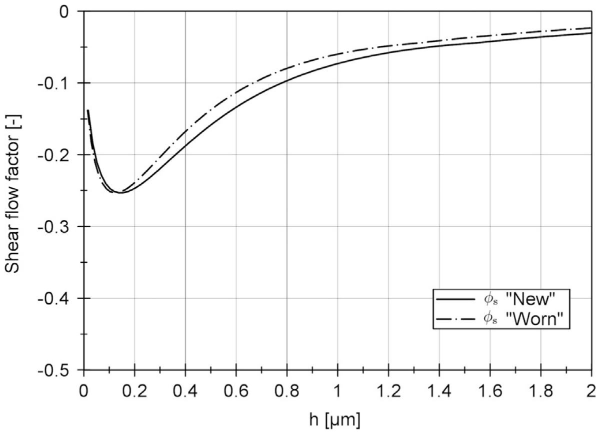

Fig. A1. Shear flow factor according to Patir and Cheng over oil film thickness for both contact pairs.

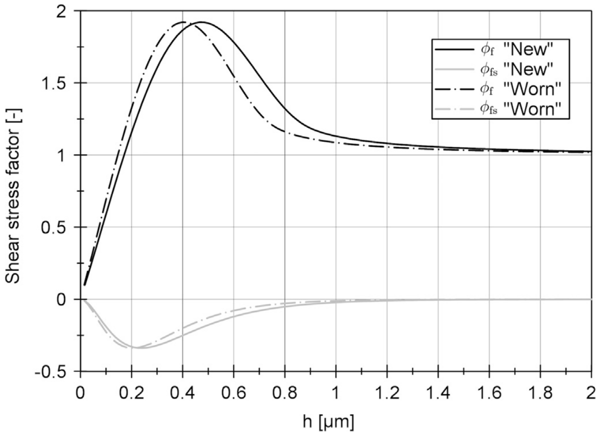

Fig. A2. Shear stress factor according to Patir and Cheng over oil film thickness for both contact pairs.

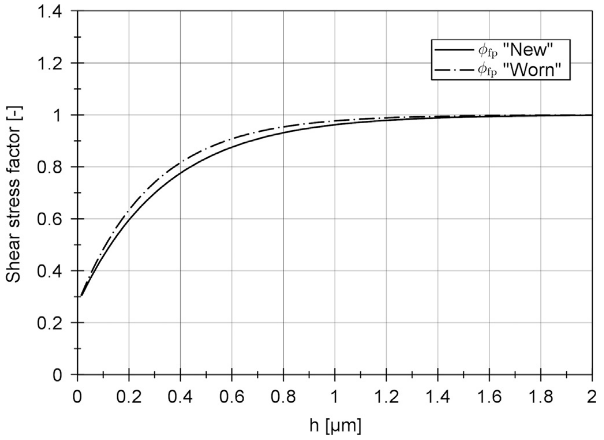

Fig. A3. Shear stress factor according to Patir and Cheng over oil film thickness for both contact pairs.

References

[1] Spikes H. Mixed lubrication—an overview. Lubric Sci 1997;9(3):221–53.
[2] Taylor C. Automobile engine tribology-design considerations for efficiency and durability. Wear 1998;221(1):1–8.
[3] Priest M, Taylor C. Automobile engine tribology-approaching the surface. Wear 2000;241(2):193–203.
[4] Tung SC, McMillan ML. Automotive tribology overview of current advances and challenges for the future. Tribol Int 2004;37(7):517–36.
[5] Jacobson B. The stribeck memorial lecture. Tribol Int 2003;36(11):781–9.
[6] Woydt M, Wäsche R. The history of the stribeck curve and ball bearing steels: the role of Adolf martens. Wear 2010;268(11):1542–6.
[7] Bovington C, Korcek S, Sorab J. The importance of the stribeck curve in the minimisation of engine friction. Tribol Ser 1999;36:205–14.
[8] Lu X, Khonsari M. An experimental investigation of dimple effect on the stribeck curve of journal bearings. Tribol Lett 2007;27(2):169–76.
[9] Booker J, Boedo S, Bonneau D. Conformal elastohydrodynamic lubrication analysis for engine bearing design: a brief review. Proc Inst Mech Eng—Part C: J Mech Eng Sci 2010;224(12):2648.
[10] Dobrica MB, Fillon M, Maspeyrot P. Mixed elastohydrodynamic lubrication in a partial journal bearing-comparison between deterministic and stochastic models. J Tribol 2006;128(4):778–88.
[11] Jao H-C, Chang K-M, Chu L-M, Li W-L. A modified average Reynolds equation for rough bearings with anisotropic slip. J Tribol 2016;138(1):011702.
[12] Tucker P, Keogh P, A generalized computational fluid dynamics approach for journal bearing performance prediction. Proc Inst Mech Eng—Part J: J Eng Tribol 1995;209(2):99–108.
[13] Shahmohamadi H, Rahmani R, Rahnejat H, Garner CP, Dowson D. Big end bearing losses with thermal cavitation flow under cylinder deactivation. Tribol Lett 2015;57(2):1–17.
[14] Bartel D. Simulation von Tribosystemen, 2010, Vieweg, Wiesbaden.
[15] Stachowiak G, Batchelor AW. Engineering tribology. Oxford: Butterworth-Heinemann; 2013.
[16] Bonneau D, Fatu A, Souchet D. Mixed lubrication in hydrodynamic bearings. New York: John Wiley & Sons; 2014.
[17] Bartel D, Deters L. Calculation of a stribeck curve of a journal bearing. Tribol Ser 1999;36:231–40.
[18] Lu X, Khonsari M, Gelinck E. The stribeck curve: experimental results and theoretical prediction. J Tribol 2006;128(4):789–94.
[19] Akbarzadeh S, Khonsari M. Effect of surface pattern on stribeck curve. Tribol Lett 2010;37(2):477–86.
[20] Wang Y, Wang QJ, Lin C, Shi F. Development of a set of stribeck curves for conformal contacts of rough surfaces. Tribol Trans 2006;49(4):526–35.
[21] Bartel D, Bobach L, Illner T, Deters L. Simulating transient wear characteristics of journal bearings subjected to mixed friction. Proc Inst Mech Eng—Part J: J Eng Tribol 2012;1350650112454510.
[22] Fillon M, Bouyer J. Thermohydrodynamic analysis of a worn plain journal bearing. Tribol Int 2004;37(2):129–36.
[23] Bouyer J, Fillon M, Pierre-Danos I. Influence of wear on the behavior of a two-lobe hydrodynamic journal bearing subjected to numerous startups and stops. J Tribol 2007;129(1):205–8.
[24] Sun J, Zhu X, Zhang L, Wang X, Wang C, Wang H, et al. Effect of surface roughness, viscosity–pressure relationship and elastic deformation on lubrication performance of misaligned journal bearings. Ind Lubric Tribol 2014;66(3):337–45.
[25] Sander D, Allmaier H, Priebsch H, Reich F, Witt M, Füllenbach T, et al. Impact of high pressure and shear thinning on journal bearing friction. Tribol Int 2015;81:29–37.

[26] Patir N, Cheng H. An average flow model for determining effects of three-dimensional roughness on partial hydrodynamic lubrication. ASME, Trans J Lubric Technol 1978;100:12–7.
[27] Patir N, Cheng H. Application of average flow model to lubrication between rough sliding surfaces. ASME, Trans J Lubric Technol 1979;101:220–30.
[28] Greenwood J, Tripp J. The contact of two nominally flat rough surfaces, Proceedings of the institution of mechanical engineers 185 (1) (1970) 625–633.
[29] Allmaier H, Priestner C, Six C, Priebsch H, Forstner C, Novotny-Farkas F. Predicting friction reliably and accurately in journal bearings—a systematic validation of simulation results with experimental measurements. Tribol Int 2011;44(10):1151–60.
[30] Allmaier H, Priestner C, Reich F, Priebsch H, Forstner C, Novotny-Farkas F. Predicting friction reliably and accurately in journal bearings—the importance of extensive oil-models. Tribol Int 2012;48:93–101.
[31] Priestner C, Allmaier H, Priebsch H, Forstner C. Refined simulation of friction power loss in crank shaft slider bearings considering wear in the mixed lubrication regime. Tribol Int 2012;46(1):200–7.
[32] Allmaier H, Priestner C, Reich F, Priebsch H, Novotny-Farkas F. Predicting friction reliably and accurately in journal bearings - extending the simulation model to TEHD. Tribol Int 2013;58:20–8.
[33] Sander DE, Allmaier H, Priebsch H, Reich F, Witt M, Skiadas A, et al. Edge loading and running-in wear in dynamically loaded journal bearings. Tribol Int 2015;92:395–403.
[34] Allmaier H, Sander D, Priebsch H, Witt M, Füllenbach T, Skiadas A. Non-newtonian and running-in wear effects in journal bearings operating under mixed lubrication. Proc Inst Mech Eng—Part J: J Eng Tribol 2015;1350650115594191.
[35] Vogel H. The law of the relation between the viscosity of liquids and the temperature. Physik Z 1921;22:645–6.
[36] Barus C. Isothermals, isopiestics and isometrics relative to viscosity. Am J Sci 1893;266:87–96.
[37] Cross MM. Rheology of non-Newtonian fluids: a new flow equation for pseudoplastic systems. J Colloid Sci 1965;20(5):417–37.
[38] Offner G. Friction power loss simulation of internal combustion engines considering mixed lubricated radial slider, axial slider and piston to liner contacts. Tribol Trans 2013;56(3):503–15.
[39] Offner G, Knaus O. A generic friction model for radial slider bearing simulation considering elastic and plastic deformation. Lubricants 2015;3(3):522–38.
[40] Offner G. Modelling of condensed flexible bodies considering non-linear inertia effects resulting from gross motions. Proc Inst Mech Eng—Part K: J Multi-body Dynamics 2011;225(3):204–19.
[41] Krasser J. Thermoelastohydrodynamische Analyse dynamisch belasteter Radialgleitlager [PhD thesis]. Technische Universität Graz; 1996.
[42] Jakobsson B, Floberg L. The finite journal bearing considering vaporization. Trans Chalmers Univ Technol 1957.
[43] Greenwood J, Williamson J. Contact of nominally flat surfaces. Proc R Soc Lond Ser A: Math Phys Sci 1966;295:300–319.
[44] Peklenik J. Paper 24: new developments in surface characterization and measurements by means of random process analysis. In: Proceedings of the Institution of Mechanical Engineers, Conference Proceedings, vol. 182. London: SAGE Publications; 1967. p. 108–26.
[45] Blau PJ. On the nature of running-in. Tribol Int 2006;38(11):1007–12.
[46] Spikes H. Film-forming additives-direct and indirect ways to reduce friction. Lubric Sci 2002;14(2):147–67.

5.3 Edge loading and running-in wear in dynamically loaded journal bearings

After the friction tests with the dynamic load (see section 5.1), the bearing shells were analyzed and a worn region was identified at the bearing edges. The simulation results also identified metal-metal contact at the bearing edges which is caused by the elastic bending of the shaft. In section 5.1, the worn regions are considered in the simulation right from the start instead of a perfect cylindrical bearing surface. In this application example, such ″worn″ surface geometry is generated by iteratively removing material from the initial bearing shell.

The presented simulation approach uses the Archard wear equation to calculate the wear distribution on the bearing surface. According to Archard, wear occurs when asperities are in contact. Asperity contact is identified by Greenwood and Tripp contact model. The parameters for the contact model are derived from surface scans of bearing shell and shaft. Similar to previous examples, the detailed lubricant data is also included in the simulation approach.

The computed worn surface geometry is compared to the real surface geometry of the test bearing following the test procedure. The good agreement between simulation and measurement enables further investigations in order to discuss the influence of shaft speed on bearing wear. Additionally, the effect of surface smoothing due to running-in on contact pressure and wear is discussed.

The details of the numerical and experimental work as well as the results are described in [75] and can be found in section 5.3.2. Prior to this, the research findings of the publication are summarized.

5.3.1 Summary of research findings

- Metal-metal contact at the bearing edges is identified by simulation. Cause for the metal-metal contact is the elastic bending of the shaft.
- The simulation approach of the iterative adaption of the bearing geometry is presented. The stepwise adaption is performed until only minor metal-metal contact is left. From the simulation results can be concluded that the maximum metal-metal contact pressure monotonically decreases with the stepwise adaption of the bearing geometry.
- The calculated maximum wear depth matches the measured wear depth at the bearing edges. The worn region in circumferential direction of the tested bearing also agrees to the calculated bearing geometry. Hence, the simple analytical approach is suitable to predict the run-in surface geometry for the presented case.
- By comparing maximum contact pressure and wear rate over time, it can be seen that the running-in process concentrates on the beginning phase of the bearing life time.
- Against expectations, the simulation results predict higher metal-metal contact pressure at high shaft speeds. The high bearing temperatures and high shear rates cause a decrease of lubricant viscosity in the lubrication gap. Hence, the oil film thickness decreases with higher speed.
- The stepwise adaption of the bearing geometry is performed with the surface parameter of a new bearing shell. When considering surface smoothing, which

is realized by adjusting the parameter of the contact model, a further reduction of metal-metal contact pressure can be identified. The results show that with the final bearing geometry a steady state of operation is achieved and further wear is unlikely to occur.

5.3.2 Paper III [75]

Tribology International 92 (2015) 395–403

Contents lists available at ScienceDirect

Tribology International

journal homepage: www.elsevier.com/locate/triboint

Edge loading and running-in wear in dynamically loaded journal bearings

David E. Sander [a,*], H. Allmaier [a], H.H. Priebsch [a], F.M. Reich [a], M. Witt [b], A. Skiadas [b], O. Knaus [c]

[a] Virtual Vehicle Research Center, Inffeldgasse 21A, 8010 Graz, Austria
[b] KS Gleitlager GmbH, Am Bahnhof 14, 68789 St. Leon-Rot, Germany
[c] AVL List GmbH, Hans-List-Platz 1, 8020 Graz, Austria

ARTICLE INFO

Article history:
Received 24 March 2015
Received in revised form
17 June 2015
Accepted 17 July 2015
Available online 29 July 2015

Keywords:
Mixed lubrication
Non-Newtonian lubricant
Simulation
Measurement

ABSTRACT

This paper focuses on the beginning phase of hydrodynamic journal bearing life time when the first adaption of the contacting surfaces occurs. Generally, this effect is known as running-in.

Experimental data from a journal bearing test rig using a low viscosity 0W20 multi-grade automotive lubricant provide the solid basis for the simulative study of the running-in process. From these measurements and a subsequent determination of the surface roughness, parameters for the mixed lubrication contact model are derived. This analysis combined with the experimentally identified lubricant properties under high pressure and high shear rate enables the evaluation of an iterative simulation approach. In this iterative approach the bearing surface geometry is adapted stepwise until a steady state of operation is achieved.

Results show worn regions at the edge of the highly loaded bearing shell. This wear is caused by metal–metal contact due to the elastic bending of the shaft. The calculated wear depth at the edge and the expansion of the worn area in axial and circumferential direction matches the measured profile. This agreement indicates that the simple iterative approach using the Greenwood and Tripp contact model and Archard's wear equation is suitable to predict the worn surface geometry after the running-in process is completed.

Furthermore, the simulation shows that the maximum asperity contact pressure in mixed lubrication decreases with the stepwise adaption of the surface geometry, until only an insignificant metal–metal contact remains. With this adapted surface geometry, the influence of shaft speed, temperature and surface roughness is also discussed.

1. Introduction

When two contacting elements operate together for the first time, adjustments of the adjacent surfaces take place, regardless if the contact is lubricated or not. This adjustment concerns the geometrical conformity on macro and micro scale as well as changes of the mechanical and material properties [1]. Such an adjustment process occurs in the early stage of operation and is commonly called running-in.

In hydrodynamic journal bearings the softer shell generally adapts its surface to fit the harder journal during the running-in. In highly loaded regions of the bearing, abrasive wear and plastic deformation occur. These impacts affect the surface shape, the radial clearance and surface roughness. Older publications on this topic [2–5] highlighted through experiments that the shell roughness gets smoother during the running-in process especially in the very beginning. Another result implied that the final shell roughness of the worn region was similar to the harder journal roughness. The experiments were conducted on journal bearing test rigs with a static load. These test conditions lead to an extensive metal–metal contact and wear along the entire bearing width. In a more recent publication [6], a similar test rig setup was used to study the effect of lubricant additives on the friction and wear behaviour of journal bearings during several starts and stops of the journal.

However, in most technical applications, such as turbines or combustion engines, journal bearings are designed for a long life time. Thus, journal bearings mainly operate in a pure hydrodynamic lubrication regime. Usually, dynamic loads (e.g. due to eccentric masses or combustion) act on the shaft and bend it

---

[*] Corresponding author.
E-mail address: david.sander@v2c2.at (D.E. Sander).

http://dx.doi.org/10.1016/j.triboint.2015.07.022
0301-679X/© 2015 Elsevier Ltd. All rights reserved.

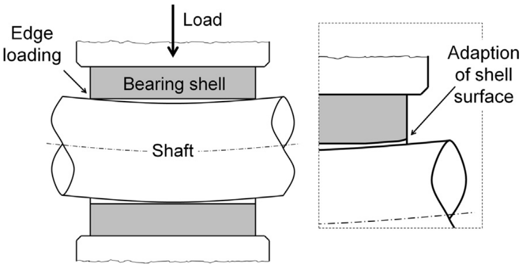

Fig. 1. Sketch of elastically deformed shaft due to external load.

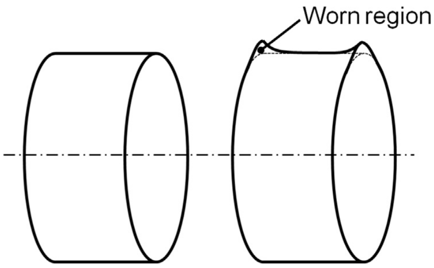

Fig. 2. Sketched surface profile of a new bearing (left) and a worn bearing after the running-in process (right).

elastically. This elastic deformation causes an unconformity of journal and shell and can lead to metal–metal contact mainly at the bearing edges (see Fig. 1). Another source for unconformity and edge loading is any minor misalignment between journal and bearing as a result of production tolerances, assembly deformation or thermal deviation.

Previous publications discuss minimum oil film thickness, pressure distribution and thermal behaviour of misaligned journal bearings either experimentally [7] or by simulation [8,9]. Sun et al. [10] experimentally investigated the behaviour of misaligned journal bearings due to elastic shaft deformation. At a specific amount of rotational load he identified an increase of bearing temperature and a reduction of the maximum hydrodynamic pressure caused by metal–metal contact at the bearing edge. Priestner et al. [11] studied the frictional losses in journal bearings using an elasto-hydrodynamic simulation tool and identified high metal–metal contact pressures at the bearing edges due to shaft bending. The high metal–metal contact pressure led to overestimated friction losses. Consequently, the author adapted the geometry of the bearing shell by superposing a worn surface profile to its nominal cylindrical shape. As a result of this measure, the metal–metal contact pressure was reduced to a minimum and the predicted friction torque correlates with the measurement for a wide range of operating conditions [12].

The present study focuses on the adaption of the bearing shell profile due to severe metal–metal contact at the bearing edge (see Fig. 1). A long-term test on a journal bearing test rig was conducted with high dynamic loads. Initially, the test was performed to validate elasto-hydrodynamic simulation models with a detailed description of the oil viscosity. The impact of temperature, pressure and shear rate on journal bearing friction was presented in [13] for a wide range of operation conditions. Although, the bearing operated mainly in pure hydrodynamic conditions, the edges of the bearing shell were worn at the end of the test. The subsequent measurements of the surface geometry and surface roughness provide a solid basis for the verification of a numerical investigation of the running-in process.

The primary aim of this study is to verify an iterative approach to calculate the worn surface profile of journal bearings using the approach published by Offner [14]. Starting with the initial cylindrical shape of the bearing shell (see Fig. 2), an elasto-hydrodynamic (EHD) simulation is performed and metal–metal contact on the bearing surface is evaluated. Using Archard's equation, a worn surface profile is generated by calculating the local amount of wear. In a following step, the worn surface profile of the first step is included into the EHD simulation and the wear calculation is performed once again. This process is repeated until metal–metal contact becomes insignificant and the surface profile allows a steady state of operation. In order to successfully verify the method, both, the input data for the contact model and the complex rheological properties of the lubricant are derived from measurements.

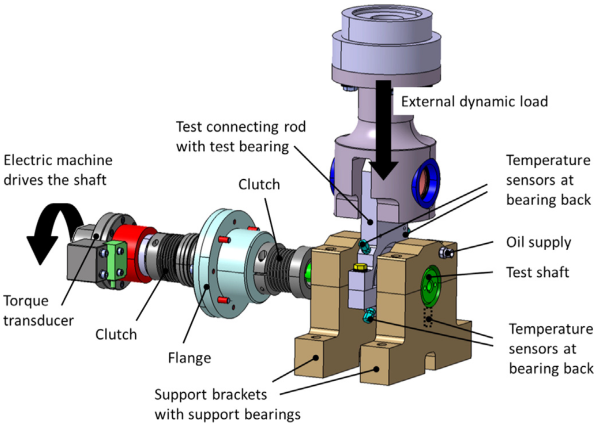

Fig. 3. Journal bearing test-rig at KS Gleitlager.

For a secondary aim, the study seeks to analyse under which operating condition more wear occurs due to edge loading.

Furthermore, the study seeks to support the use of simplified shell profiles in elasto-hydrodynamic journal bearing simulation to minimize metal–metal contact. Previous publications by the authors of this study have already shown that the inclusion of a simplified shell profile allows for a realistic estimation of metal–metal contact [12,15,16].

2. Test method

The test was conducted on the journal bearing test-rig at KS Gleitlager. The test-rig is shown in Fig. 3.

The test-rig consists of a rotating straight shaft which rests on two supporting journal bearings in support brackets. Via a test connecting rod an external load is applied onto the central test journal bearing. The dimensions and oil supply design of the journal bearings correspond to automotive main bearings with a 180° oil supply groove for the two supporting journal bearings. The test journal bearing corresponds to big-end bearings having an oil supply hole in the load-free (lower) shell. The bearing dimensions and materials are listed in Table 1.

An elastically clutched electric motor drives the shaft. The test connecting rod is dynamically excited by an electromechanical high-frequency pulsator, which is operated at 80 Hz. One load case is investigated with 80 kN maximum load which correspond to 100 MPa specific load in the test bearing; the dynamic load curve is shown in Fig. 4.

The test procedure started at a shaft speed of 1000 rpm and a stepwise run-up was performed up to 7000 rpm followed by a run-down to again 1000 rpm. Each step is operated for 20 min. A torque transducer, a Manner Sensortelemetrie 50 Nm with an accuracy of ±0.15 Nm, was placed between the electric motor and the shaft to measure the friction torque generated by all three bearings.

Table 1
Journal bearing dimensions and materials.

Bearing properties	Support bearing	Test bearing
Width (mm)	25	17.2
Diameter (mm)	54	47.8
Clearance (μm)	50	30
Material	Steel/aluminum	Sputter

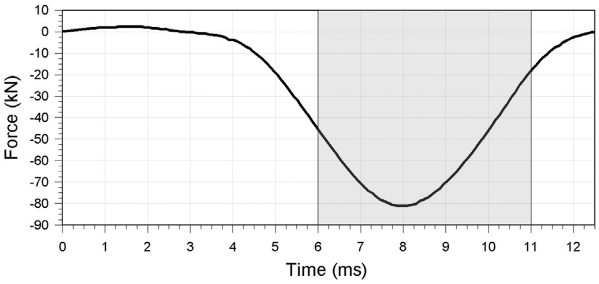

Fig. 4. External periodic load acting on the test connecting rod with a frequency of 80 Hz. The grey area marks the occurrence of wear due to the load.

Table 2
Basic properties of the tested 0W20 lubricant.

Density at 40 °C	832.5	kg/m^3
Dyn. viscosity 40 °C	37.5	m Pa s
Dyn. viscosity 100 °C	6.8	m Pa s
HTHS-viscosity[a]	2.7	m Pa s

[a] The HTHS-viscosity is defined as the viscosity at high temperature (150 °C) and high shear rate (10^6 1/s).

Table 3
Parameters for Eqs. (1) derived from experimental data [13].

A	0.0516	m Pa s
B	1127.6	°C
C	130.7	°C
α	0.00095	1/bar
r	0.53	–
m	0.79	–
K	7.9 e – 8	s

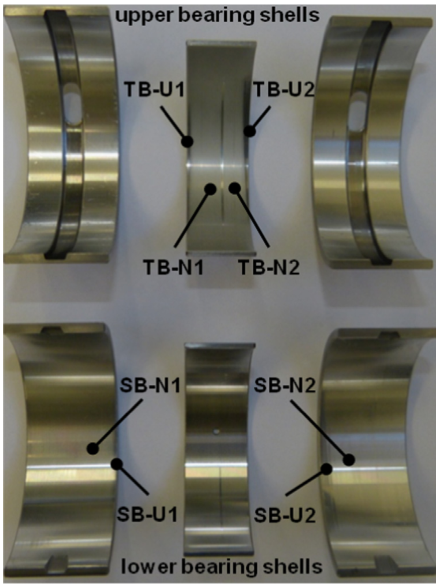

Fig. 5. Bearing shells after the test run, with the support bearings on the left and right, the test bearing is placed in the centre. The row on top show the upper bearing shells, the bottom row show the lower bearing shells.

Additionally, temperatures at the back of the bearing shells were measured by PT100 elements with an accuracy of ±0.5 °C. The detailed temperature and friction data were presented in [13].

3. Lubricant rheology

The lubricant used for this investigation is a fully formulated low-viscous 0W20 hydrocarbon engine oil as they are commonly used in the automotive sector. The rheological properties of these modern lubricants are strongly dependent on temperature, pressure and shear rate. The present work therefore considers the viscosity increase due to high pressure and also the influence of its strong non-Newtonian behaviour. The main properties of the lubricant including the density and the viscosity at various conditions are given in Table 2.

In the simulation model the viscosity of the lubricant is described as a function of temperature, pressure and shear rate. Therefore equation according to Vogel [17], Barus [18] and Cross [19] is used:

$$\eta(T,p,\dot{\gamma}) = A \cdot e^{B/(T+C)+\alpha \cdot p} \cdot \left(r + \frac{1-r}{1+(K \cdot \dot{\gamma})^m} \right) \tag{1}$$

The parameters for the viscosity equation were obtained from rheological measurement and were discussed in detail in [13]. The corresponding values are listed in Table 3.

4. Bearing analysis after test

Before the test procedure is started, new bearings were built in the test rig. After the test run the bearing shells showed worn areas. Hence, the shells were analyzed visually and by the measurement of surface geometry and surface roughness.

Fig. 5 shows all bearing shells after the test procedure. The test bearing in the middle shows a worn surface at the edges on the upper shell, which is the higher loaded shell during the test. Additionally, a wear scar in the centre of the test bearing can be identified which was most probably caused by a particle. The particle flushed out of the contact during the operation as it is not embedded into the shell surface. The lower test bearing shell does not show wear at the edges. The support bearings are loaded on the lower shell. Therefore, the running-in wear takes place at the lower shells. The affected edge is the edge towards the test bearing. No running-in wear can be seen at the upper support bearing shells.

4.1. Surface roughness

The surface roughness of the tested bearing shells were measured by a white light interferometer. Altogether eight measurement spots were evaluated. The positions are shown in Fig. 5. Each measurement spot has a size of 1 mm by 1 mm. Fig. 6 shows a measurement spot of the bearing shell on top and the shaft below.

Tables 4–6 show statistical parameters to characterise the bearing shell surface and the shaft surface. Specified are the arithmetic average of the surface profile R_a, the root mean square

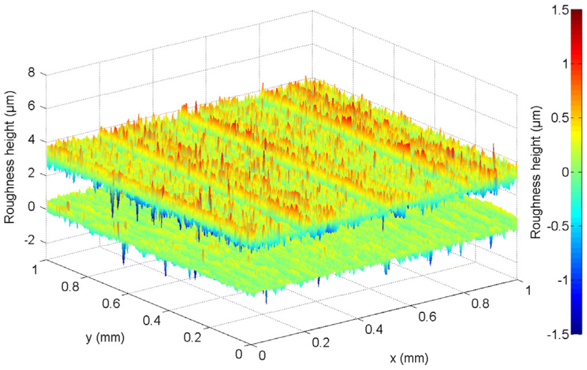

Fig. 6. Surface roughness of the bearing shell on top and the shaft below, *x* axis denotes the axial direction, *y* denotes the circumferential direction.

Table 4
Surface roughness for test bearing at four different positions.

Roughness parameter	TB-N1	TB-N2	TB-U1	TB-U2
R_a (μm)	0.23	0.23	0.13	0.07
R_q (μm)	0.29	0.29	0.18	0.13
σ (μm)	0.24	0.25	0.17	0.13
δ (μm)	0.36	0.36	0.21	0.10

Table 5
Surface roughness for support bearings at four different positions.

Roughness parameter	SB-N1	SB-N2	SB-U1	SB-U2
R_a (μm)	0.21	0.24	0.16	0.05
R_q (μm)	0.28	0.31	0.22	0.07
σ (μm)	0.25	0.30	0.22	0.11
δ (μm)	0.33	0.35	0.26	0.07

Table 6
Surface roughness for the shaft at three different positions.

Roughness parameter	Shaft-1	Shaft-2	Shaft-3
R_a (μm)	0.13	0.14	0.15
R_q (μm)	0.18	0.20	0.20
σ (μm)	0.13	0.13	0.14
δ (μm)	0.19	0.22	0.23

of the profile R_q as well as the asperity summit roughness (root mean squared) σ and the mean summit height δ which both are relevant for the contact model in the simulation.

The surface roughness of the test bearing is given in Table 4. The two test spots in the centre of the shell (TB-N1 and TB-N2) which do not show a surface adaption visually represent a “new” surface roughness. Both spots show equal surface characteristics with a R_a of 0.23 μm and a R_q of 0.29 μm. The roughness of the measurement spots on the bearing edge, marked as “used”, show a smoother surface. During the running-in the surface gets polished. A variation between the measurement spots TB-U1 and TB-U2 can be clearly identified.

The support bearings show similar characteristics to the test bearing (see Table 5). The “new” surface roughness (spots SB-N1 and SB-N2) are in same magnitude like TB-N1 and TB-N2. Again, polishing and a clearly roughness decrease can be seen around the bearing edges.

Additionally the surface roughness of a shaft, which is similar to the shaft used in the test, is given in three different surface spots (see Table 6).

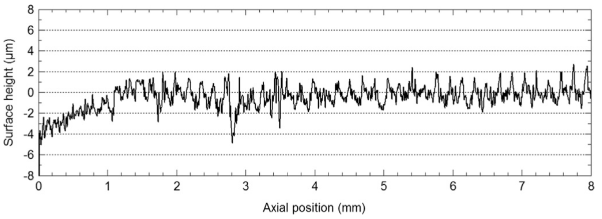

Fig. 7. Test bearing surface profile after the test run.

The shaft has an arithmetic average of the surface profile R_a of 0.14. However, the steel shaft is hardened and does not show any running-in process on the surface.

4.2. Surface profile

The axial surface profile of the worn test bearing was further measured by an optical 3D profilometer. The profile in Fig. 7 shows the highly loaded bearing shell from the left edge to the centre of the bearing.

At the edge a wear depth of 3 μm to 4 μm can be identified. The wear depth decreases to a minimum level at around 1.5 mm from the bearing edge. Again, a smoother surface can be seen at the worn edges compared to the roughness in the centre.

5. Simulation

The KS Gleitlager test rig is modelled within an elastic multibody dynamics solver (AVL Excite Power Unit).[1] The simulation model consists of a test connecting rod including the test bearing, two support blocks including the support bearings and the test shaft. All bodies have mass characteristics and can deform elastically and are represented as mathematically condensed finite element structures [20].

The isothermal elastohydrodynamic description of the lubricant film in the simulation is discussed in depth in previous publications [12,15]. For completeness, a brief theoretical overview of the elastohydrodynamic journal bearing simulation is given here.

The movement of the journal within the bearing is calculated using the Reynolds equation:

$$-\frac{\partial}{\partial\varphi}\left(\frac{h^3}{12\eta}\frac{\partial p}{\partial\varphi}\right)-r^2\frac{\partial}{\partial z}\left(\frac{h^3}{12\eta}\frac{\partial p}{\partial z}\right)+r\frac{\partial}{\partial\varphi}\left(h\frac{u_1+u_2}{2}\right)+r^2\frac{\partial h}{\partial t}=0, \qquad (2)$$

where φ, z denote the azimuth angle and the axial direction, respectively. p is the hydrodynamic pressure and h the oil film thickness which is dependent on φ and z. Further, r is the nominal shell radius, u_1 and u_2 denote the sliding speeds of the contacting surfaces. η is the oil viscosity that is considered pressure and shear rate dependent in this paper.

The influence of surface roughness on hydrodynamic lubrication is considered in the simulation using the averaged Reynolds equation according to Patir and Cheng [21,22]. The orientation factors, which are necessary for the evaluation of pressure and shear flow factors were obtained from the surface roughness measurement. The averaged orientation factor for the shell is $\Gamma_S = 1.5$ and $\Gamma_J = 4$ for the journal, respectively. However, it was found that the influence of the pressure and shear flow factors on the asperity contact pressure is negligible for the operating conditions studied. Therefore, these are omitted in Eq. (2).

---

[1] Version 2011.2, AVL List GmbH, Advanced Simulation Technology, Hans-List-Platz 1, 8020 Graz Austria, www.avl.com

5.1. Asperity contact pressure

The asperity contact pressure is calculated using the Greenwood and Tripp approach [23,24]. The theory of Greenwood and Tripp is based on the contact of two nominally flat, random rough surfaces. The asperity contact pressure can be written as

$$p_a = KE^* F_{5/2}(H_s), \tag{3}$$

where E^* is the composite elastic modulus, $E^* = ((1-\nu_1^2/E_1)+(1-\nu_2^2/E_2))^{-1}$, where ν_i and E_i are the Poisson ratio and Young's modulus of the adjacent surfaces, and $F_{5/2}(H_s)$ is the form function, which is defined as

$$F_{5/2}(H_s) = \begin{cases} 4.4086 \cdot 10^{-5}(4-H_s)^{6.804} & \text{if } H_s < 4 \\ 0, & \text{if } H_s \geq 4 \end{cases} \tag{4}$$

H_s is a dimensionless clearance parameter, defined as $H_s = (h-\overline{\delta}_s)/\sigma_s)$, with σ_s being the combined asperity summit roughness, which is calculated according to

$$\sigma_s = \sqrt{\sigma_{s,J}^2 + \sigma_{s,S}^2} \tag{5}$$

and $\overline{\delta}_s$ being the combined mean summit height, $\overline{\delta}_s = \overline{\delta}_{s,J} + \overline{\delta}_{s,S}$. The form factor $F_{5/2}(H_s)$ becomes zero for a dimensionless clearance parameter beyond four which further means no asperity contact occurs. Finally, the elastic factor K is defined as

$$K = \frac{16 \cdot \sqrt{2} \cdot \pi}{15} \cdot (\sigma_s \cdot \overline{\beta}_s \cdot \eta_s)^2 \cdot \sqrt{\frac{\sigma_s}{\overline{\beta}_s}}, \tag{6}$$

where $\overline{\beta}_s$ is the mean summit radius and η_s is the summit density. From the surface measurement spots, the elastic factor was identified to be K=0.001.

5.2. Wear calculation

In general, wear can occur when asperities of the sliding surfaces get into contact. One simple mathematical model to describe sliding wear was established by Archard [25]. Archard's equation is given as

$$h_w = \frac{C}{H} \cdot W \cdot L = \frac{C}{H} \cdot t_{\text{step}} \cdot \overline{W}_L, \tag{7}$$

where h_w is the wear depth, C is a proportional constant which describes the probability for adhesive wear (wear coefficient), W is the normal load, L is the sliding distance and H describes the hardness of the softer contact surface. The product of normal load and X expressed by a wear load $\overline{W}_L$ multiplied by the relevant step time t_{step} [14].

$$\overline{W}_L = \frac{1}{T}\int_t^{t+T} p_a |\Delta u| \, dt, \tag{8}$$

The wear load is the averaged product of asperity contact pressure p_a, obtained from Eq. (3), and the relative sliding speed $|\Delta u|$ during the duration of one load cycle T. The step time represents the adaption time used to achieve a certain wear depth. Here, instead of defining an step time, a maximum wear depth $h_{w,max}$ is introduced at the position of maximum wear load. Hence, the factor $C/H \cdot t_{\text{step}}$ can be calculated and a surface profile can be generated according to the local wear load.

With the knowledge of the surface hardness and the wear coefficient the effective step time t_{step} can be calculated. However, the wear coefficient can only be determined by measurement and was not yet available for the investigated combination of material and lubrication. For a relative comparison, the wear coefficient was assumed to be $C = 10^{-6}$. Yang [26] presented wear coefficients with a similar order of magnitude. The surface hardness was identified to be H=1470 MPa.

The wear volume ΔV_w can be calculated by integrating the wear depth over the bearing surface:

$$\Delta V_w = r \iint_A h_w(\varphi, z)\, d\varphi\, dz, \tag{9}$$

and a material removal rate is defined as

$$R_{mr} = \frac{\Delta V_w}{t_{\text{step}}}. \tag{10}$$

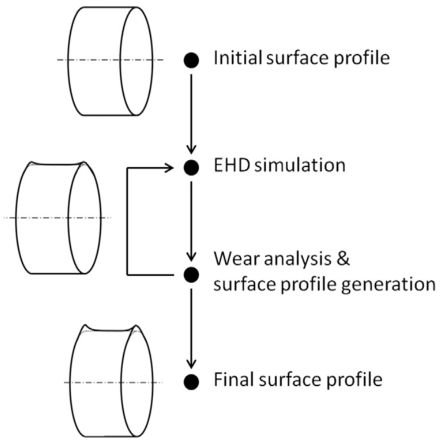

Fig. 8. Flow chart of the iterative surface profile generation.

5.3. Iterative surface profile generation

The iterative generation of the worn surface profile starts with the nominal bearing shape of a new bearing, in this work it was represented as a cylindrical shape (see Fig. 8).

The surface profile is then adapted step by step. One iterative step includes the EHD simulation of a full load cycle and the following evaluation of wear caused by metal–metal contact. A worn surface profile is generated in the end of one step with a maximum wear depth $h_{w,max} = 0.1$ μm. This worn surface profile replaces the nominal surface profile in the next iterative step. Again, a full iterative step was performed and the newly calculated worn surface profile replaces the previous surface profile. This stepwise profile adaption is repeated until the asperity contact pressure reaches a certain limit.

The value of the maximum wear depth in one iterative step was chosen for numerical and practical reason. In the case $h_{w,max}$ is chosen too large, numerical problems due to discontinuities on the surface profile could lead to immense metal–metal contact pressure. If $h_{w,max}$ is chosen too small, more iterative cycles must be calculated which increases the overall simulation time.

The total time t and wear volume V_w is the accumulated step time t_{step} and the accumulated wear volume per iterative step ΔV_w, respectively.

For simplicity, the wear at the journal was assumed to be zero because of the much harder surface material.

5.4. Bearing discretization

AVL Excite solves the Reynolds equation by finite volume method [27,28]. Therefore, a discretization of the lubrication domain is arranged. The discretization points are equally distributed along the axial and circumferential direction. In the presented model 25 points in axial direction are chosen for all bearings. In circumferential direction the test bearing has 200 points and the support bearing has 176 points. Every second point is directly coupled to a point on the solid structure. The displacement of the

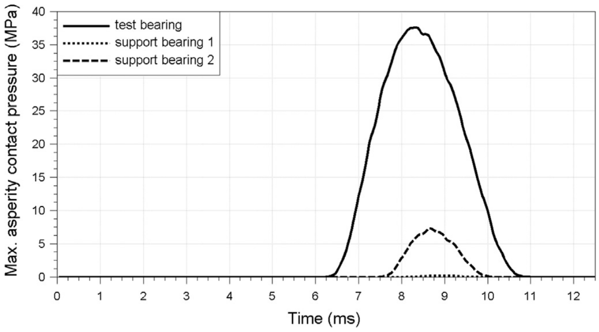

Fig. 9. Maximum asperity contact pressure during one load cycle, solid line shows the test bearing, dashed lines are the support bearings.

points in between are interpolated. The coupling method is described in [28].

5.5. Bearing temperatures

The temperature in the elasto-hydrodynamic bearing simulation is considered to be constant. An equivalent bearing temperature was introduced and described in detail by the authors in [13] which take the measured temperatures at different positions on the back of the bearing shell into account. The temperature variation caused by different shaft speed can therefore be considered in the simulation.

6. Simulation results

The running-in process is calculated for a shaft speed of 4000 rpm and maximum specific load of 100 MPa, related to the test bearing. The first iteration step is conducted with cylindrical surface profiles for all bearing shells. One full load cycle is computed and the wear analysis is performed.

Fig. 9 shows the maximum asperity contact pressure during one full load cycle for all three bearings. The solid line represents the test bearing. Asperity contact occurs between 6 ms and 11 ms when the external load becomes a maximum (compare Fig. 4). The maximum asperity contact pressure reaches a value of 38 MPa. Additionally, the two support bearings are shown with dashed lines. There is almost no asperity contact at the support bearing 1, which is closer to the electric motor. The support bearing 2, located at free end of the shaft, has a maximum asperity contact pressure of 7 MPa. These diverging results originate from the asymmetric setup of the test rig, moreover the asymmetric bending of the shaft. Typically for this test rig, the support bearing 2 shows more running-in wear than support bearing 1 (see Fig. 5). The simulation results confirm the unequal behaviour of the support bearings due to the shaft bending.

The following result discussion will focus on the test bearing because of the higher edge loading resulting in more wear.

Fig. 10 shows the asperity contact pressure occurring in the first iteration step at 8.3 ms when the maximum asperity contact pressure was identified. The asperity contact pressure develops exclusively at the edges of the bearing shell and spread from -35° to 35° around the top. The maximum asperity contact pressure occurs on the top position of the bearing. The asperity contact is symmetrically distributed on both edges.

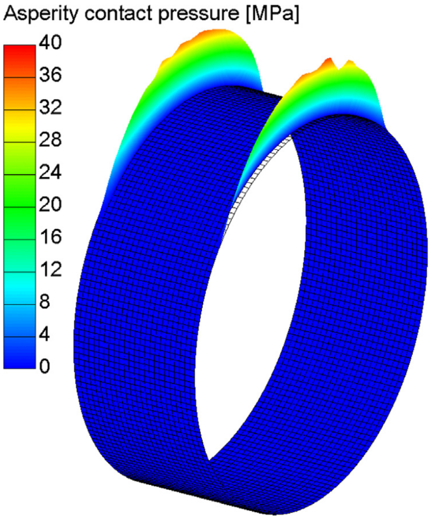

Fig. 10. Distribution of asperity contact pressure during the first iterative step at maximum load (8.3 ms).

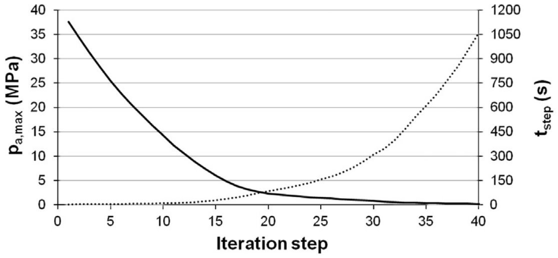

Fig. 11. Decrease of max. asperity contact pressure with the number of iterative step (solid line), and increase of adaption time used each iterative step (dashed line).

The worn surface profile is established according to Eq. (7) after the first iterative step as discussed. It shows a wear depth of 0.1 μm at the top position of the bearing edges. The generated profile is then used as surface profile in the new simulation step. Due to the adapted surface profile, the occurrence of asperity contact decreases. Hence, the maximum asperity contact pressure is reduced in the second step. This procedure is repeated 40 times and a gradually reduction of asperity contact pressure can be identified from step to step (compare solid line in Fig. 11).

After 16 simulation steps the peak asperity contact pressure is reduced below 5 MPa, after 30 steps a peak asperity contact pressure below 1 MPa is reached. Additionally, the adaption time to achieve the defined wear depth of 0.1 μm is shown for each iterative step. Due to the fact that the asperity contact pressure is reduced, the adaption time increases from step to step. The adaption time monotonically increases from 2.5 s to 1050 s.

Fig. 12 shows the development of the three-dimensional surface profile of the test bearing.

The surface profile on the top left shows the estimated wear depth after 10 iterative steps. Wear is only identified on the high loaded upper shell and is nearly symmetric. The surface adaption concentrates on the edges only, because of the high asperity contact pressure at the edges. The symmetry of the wear depth can be clearly seen in Fig. 13 which shows the axial cut through the most worn area of the surface profile.

After 10 iterative steps a maximum wear depth of 1 μm can be seen at the edges. After 20 steps (top right in Fig. 12) the wear depth at the edges increases and the length and width of the worn area expands. Wear concentrates on the edges only but migrates towards the centre of the bearing and also expands in circumferential direction from step to step. The maximum wear depth increases to 2 μm after 20 steps and 3 μm after 30 steps. After 40

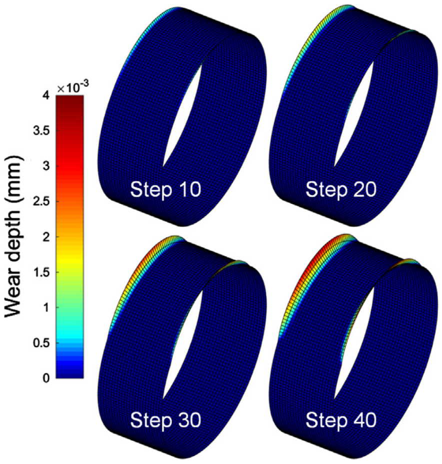

Fig. 12. Surface profile during the iterative running-in process.

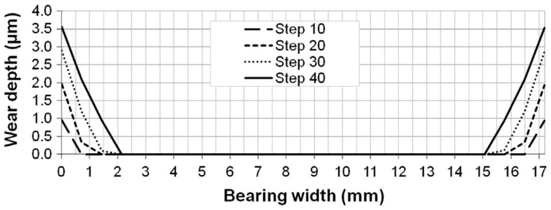

Fig. 13. Section view of the surface profile during the iterative running-in process at the position of max. wear depth.

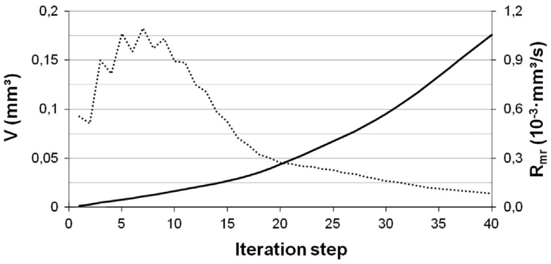

Fig. 14. Increase of total wear volume (solid line), and progress of the material removal rate (dashed line) with the number of iterative step.

steps a maximum wear depth of 3.6 μm can be identified, and thus the wear load maximum moves towards the centre as well. The area below the curves in Fig. 13 clearly indicate that the wear volume increases with the number of steps. Therefore, the accumulated wear volume is examined for each step during the iterative surface profile generation. After 40 steps (bottom right) a maximum wear depth of 3.6 μm is reached and the worn surface profile is nearly symmetric.

The solid line in Fig. 14 shows the accumulated wear volume over the iteration steps. In the beginning, the wear volume shows a nearly linear progression up to step 15. Afterwards the wear volume grows quadratically. The overall wear volume after 40 steps reaches 0.18 mm^3. With the consideration of the adaption time the material removal rate is evaluated according to Eq. (10) and shown as dashed line. During the first seven iterative steps the material removal rate increases to $1.1 \cdot 10^{-3}$ mm^3/s, followed by a drop to $0.4 \cdot 10^{-3}$ mm/s after 15 steps. From step 15 on the material removal rate decreases linearly to its minimum at step 40.

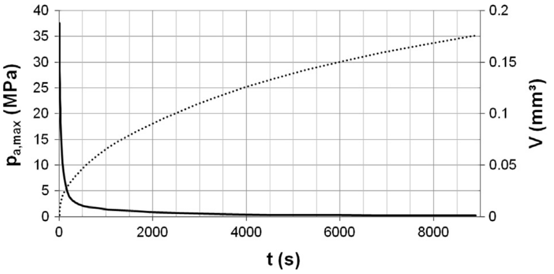

Fig. 15. Asperity contact pressure drop (solid line) and wear volume (dashed line) over time.

Finally, the maximum asperity contact pressure (solid line) and the wear volume (dashed line) are plotted over the total time in Fig. 15. Within the first 200 s of operation the maximum asperity contact pressure drops severely below 5 MPa. From there on the maximum asperity contact pressure steadily decreases to a minimum in the end. The wear volume increases strongly in the beginning and flattens out over time.[2] A steady state of wear was not identified during the investigated time, as the wear volume does not change linearly with time or sliding distance [26]. Rather a steady state of operation is achieved without continuing wear (see discussion in Section 7.2).

7. Discussion

The comparison of the obtained simulated surface profile (see Fig. 13) and the measured surface profile (see Fig. 7) shows a good correlation. Wear develops exclusively at the higher loaded bearing shell. The test bearing shows a worn area at the edges of the top bearing shell. The worn area spreads from −45° to 45° around the top which is also identified by simulation. The maximum wear depth for both measurement and simulation were obtained at the edges and reached a value of about 3.5 μm. The measured wear width in axial direction reaches 1.5 mm from the edge. The calculated wear width is slightly higher with 2 mm after 40 iterative steps. Again, it should be pointed out that the surface roughness used in the simulation is not changed between the iterative steps. Hence, the asperity contact pressure is overestimated for the worn bearing regions as will be discussed later.

In the simulation a symmetrical wear profile is developed, but the bearing shells in Fig. 5 do not show this symmetric behaviour. The right edge of the test bearing shows a greater polished area than the left edge. This asymmetric behaviour was possibly caused by an axial misalignment of the support bearing 2 and the test bearings, which was not included to the simulation model.

7.1. Comparison of different load cases

A further investigation focuses on the question at which shaft speed more asperity contact and wear occurs. It is expected that the lubrication gap should increase with speed, but the answer is not straight forward because the temperature and the high shear rate influence the lubricant viscosity. As mentioned earlier the iterative calculation of the surface profile was conducted at 4000 rpm. Now, the shell profile from step 30 and step 40 are included to the simulation model and calculations are conducted at 1000 rpm and 7000 rpm.

---

[2] The total time is calculated on the assumption of a constant wear coefficient. The wear coefficient is likely to decrease during the running-in process when the contact pressure drops. Therefore, it can be presumed that wear volume curve will flatten out even more.

Table 7
Peak asperity contact pressure and equivalent temperature during one load cycle for different shaft speeds, “new” surface roughness.

Shaft speed (rpm)	1000	4000	7000
Equivalent temperature (°C)	56.1	97.2	133.7
p_a (MPa), profile step 30	0.2	0.8	9.4
p_a (MPa), profile step 40	0	0.2	4.7

Table 8
Peak asperity contact pressure and equivalent temperature during one load cycle for different shaft speeds, “used” surface roughness.

Shaft speed (rpm)	1000	4000	7000
Equivalent temperature (°C)	56.1	97.2	133.7
p_a (MPa), profile step 30	0	0	1.9
p_a (MPa), profile step 40	0	0	0.3

The simulation parameters and results are summarized in Table 7. The measured temperatures show a vast difference between the investigated operation conditions. At 1000 rpm the equivalent bearing temperature is 56.1 °C. An increase of speed to 4000 rpm and 7000 rpm elevates the bearing temperature to 97.2 °C and 133.7 °C, respectively. Generally, it can be stated that a temperature difference of 20 °C halves the lubricant viscosity. Therefore the temperature influence is significant in this investigation. Additionally, the higher shaft speeds cause higher shear rates, and hence a further viscosity decrease occurs [13].

The maximum asperity contact pressure calculated with the surface profile from step 30 has its minimum with 0.2 MPa at low shaft speed and its maximum of 9.4 MPa at high shaft speed. Using the surface profile from the iterative step 40 a reduction of asperity contact occurs for all three load cases, but still the load case with 7000 rpm shows more asperity contact. Hence, it is concluded that higher wear occurs at higher shaft speed.

7.2. Comparison of different surface roughness

As mentioned earlier, the surface roughness is not changed during the simulative investigation. All steps are conducted with the properties of a “new” surface. Now, the contact model is updated to the measured surface roughness of the “used” region and again calculations are performed at 1000 rpm, 4000 rpm and 7000 rpm.

Table 8 shows the results from the simulations using the “used” surface roughness. At 1000 rpm and 4000 rpm the asperity contact pressure disappears completely. The maximum asperity contact pressure reduces to 0.3 MPa at 7000 rpm with the profile generated in step 40. Compared to the “new” surface roughness, the “used” surface roughness shows a clear reduction in asperity contact pressure, from 4.7 MPa to 0.3 MPa. Therefore, when using a “new” or initial surface roughness, the asperity contact pressure is overestimated past the first iterative steps. It can also be concluded, that the running-in process ends before the asperity contact becomes zero. Therefore, a threshold of maximum asperity contact pressure can be defined at which an adaption of surface profile ends.

8. Conclusion

In this work, a simple iterative approach to calculate the worn surface profile of dynamically loaded journal bearing is evaluated. The results from the simulation are compared to results obtained from a journal bearing test rig. For reference, the surface profile and surface roughness of the tested bearing are analyzed after the test run and their physical properties are included to the simulation model.

The calculated maximum wear depth at the bearing edge shows an excellent match with the measured wear depth. The worn area in axial and circumferential direction obtained from the simulation suits the polished surface of the test bearing after the test run. The beneficial correlation between simulation and measurement indicates that the simple iterative approach, using Greenwood and Tripp contact model and Archard's wear equation, is able to predict the worn surface profile after the running-in process in highly stressed journal bearings.

From the simulation it can be concluded that the maximum asperity contact pressure monotonically decreases with the stepwise adaption of the surface profile. By evaluating the maximum asperity contact pressure and the wear volume over time, it can be seen, that the adaption of the bearing surface occurs mainly during the beginning of the operation.

When reducing the surface roughness after the running-in process, only minor asperity contact pressures (below 1 MPa) are identified. Therefore, it is expected that no further adaption of the worn surface profile occur and a steady state of operation is maintained.

Against initial expectation, more wear occurs at high shaft speed. Crucial, in this wear process, is the influence of high temperature and high shear rate on lubricant viscosity, which leads to more asperity contact at higher shaft speeds. Hence, a detailed description of the lubricant viscosity, including the piezoviscous effect and shear-thinning is essential.

According to the results, we recommend the use of a worn surface profile for friction prediction in journal bearings. Without a surface profile the asperity contact is overestimated and the friction prediction is not accurate.

Acknowledgment

We would like to express our gratitude to our supporting industrial and scientific project partners, namely KS Gleitlager, AVL and the Institute of Tribology of the TU Clausthal.

Furthermore, the authors would like to acknowledge the financial support of the “COMET – Competence Centers for Excellent Technologies Programme” of the Austrian Federal Ministry for Transport, Innovation and Technology (bmvit), the Austrian Federal Ministry of Science, Research and Economy (bmwfw), the Austrian Research Promotion Agency (FFG), the Province of Styria and the Styrian Business Promotion Agency (SFG).

Appendix A. Impact of oil models on the prediction of minimum oil film thickness

The influence of high pressure and shear thinning on journal bearing friction was discussed in an earlier publication [13]. This work focuses on mixed lubrication, and therefore the influence of these two properties on the minimum oil film thickness are appended here. Three oil models with a different level of detail are compared. The basic model only considers the temperature dependency of the oil viscosity, $\eta(T)$, according to Vogel's equation. The second model additionally includes the piezoviscous effect, $\eta(T,p)$, according to

Table A1
Minimum oil film thickness (MOFT) at different shaft speeds for different oil models.

Shaft speed (rpm)	1000	4000	7000
Equivalent temperature (°C)	56.1	97.2	133.7
MOFT, $\eta(T)$	1.12	0.97	0.74
MOFT, $\eta(T,p)$	1.30	1.25	0.93
MOFT, $\eta(T,p,\dot{\gamma})$	1.32	1.15	0.84

Barus equation. A third model, which is used in the present work, is completed with the shear thinning effect of modern multigrade engine oils, $\eta(T, p, \dot{\gamma})$, according to Cross Table A1 shows the minimum oil film thickness (MOFT) at different shaft speeds calculated with the three different oil models.

The results show that with increasing speed the MOFT decreases independent on the oil model. Responsible for this effect mainly is the temperature increase. For the $\eta(T)$ model a MOFT decrease of 0.38 μm is obtained from 1000 rpm to 7000 rpm. The $\eta(T, p)$ model shows a higher MOFT at all shaft speeds compared to the $\eta(T)$ model, due to the viscosity increase in the high loaded bearing area. The MOFT difference between 1000 rpm and 7000 rpm stays similar to the $\eta(T)$. The viscosity decrease due to shear thinning affects the MOFT mainly at high speeds. Hence, the MOFT difference between the 1000 rpm and 7000 rpm increases to 0.48 μm.

To predict friction and wear reliable in mixed lubrication a detailed oil model becomes necessary, which considers the piezo-viscous effect and shear thinning of modern engine oils.

References

[1] Blau PJ. On the nature of running-in. Tribol Int 2006;38(11):1007–12.

[2] Rowe G, Kaliszer H, Trmal G, Cotter A. Running-in of plain bearings. Wear 1975;34(1):1–14.

[3] Mokhtar M, Howarth R, Davies P. Wear characteristics of plain hydrodynamic journal bearings during repeated starting and stopping. ASLE Trans 1977;20 (3):191–4.

[4] Masouros G, Dimarogonas A, Lefas K. A model for wear and surface roughness transients during the running-in of bearings. Wear 1977;45(3):375–82.

[5] Roy Chowdhury S, Kaliszer H, Rowe G. An analysis of changes in surface topography during running-in of plain bearings. Wear 1979;57(2):331–43.

[6] Durak E, Adatepe H, Biyiklioglu A. Experimental study of the effect of additive on the tribological properties journal bearing under running-in and start-up or shut-down stages. Ind Lubr Tribol 2008;60(3):138–46.

[7] Bouyer J, Fillon M. An experimental analysis of misalignment effects on hydrodynamic plain journal bearing performances. J Tribol 2002;124 (2):313–9.

[8] Boedo S, Booker J. Classical bearing misalignment and edge loading: a numerical study of limiting cases. J Tribol 2004;126(3):535–41.

[9] Sun J, Changlin G. Hydrodynamic lubrication analysis of journal bearing considering misalignment caused by shaft deformation. Tribol Int 2004;37 (10):841–8.

[10] Sun J, Gui C, Li Z. An experimental study of journal bearing lubrication effected by journal misalignment as a result of shaft deformation under load. J Tribol 2005;127(4):813–9.

[11] Priestner C, Allmaier H, Priebsch H, Forstner C. Refined simulation of friction power loss in crank shaft slider bearings considering wear in the mixed lubrication regime. Tribol Int 2012;46(1):200–7.

[12] Allmaier H, Priestner C, Six C, Priebsch H, Forstner C, Novotny-Farkas F. Predicting friction reliably and accurately in journal bearings—a systematic validation of simulation results with experimental measurements. Tribol Int 2011;44(10):1151–60.

[13] Sander D, Allmaier H, Priebsch H, Reich F, Witt M, Füllenbach T, et al. Impact of high pressure and shear thinning on journal bearing friction. Tribol Int 2015;81:29–37.

[14] Offner G. Friction power loss simulation of internal combustion engines considering mixed lubricated radial slider, axial slider and piston to liner contacts. Tribol Trans 2013;56(3):503–15.

[15] Allmaier H, Priestner C, Reich F, Priebsch H, Forstner C, Novotny-Farkas F. Predicting friction reliably and accurately in journal bearings—the importance of extensive oil-models. Tribol Int 2012;48:93–101.

[16] Allmaier H, Priestner C, Reich F, Priebsch H, Novotny-Farkas F. Predicting friction reliably and accurately in journal bearings—extending the simulation model to TEHD. Tribol Int 2013;58:20–8.

[17] Vogel H. The law of the relation between the viscosity of liquids and the temperature. Phys Z 1921;22:645–6.

[18] Barus C. Isothermals, isopiestics and isometrics relative to viscosity. Am J Sci 1893;266:87–96.

[19] Cross MM. Rheology of non-Newtonian fluids: a new flow equation for pseudoplastic systems. J Colloid Sci 1965;20(5):417–37.

[20] Offner G. Modelling of condensed flexible bodies considering non-linear inertia effects resulting from gross motions. Proc Inst Mech Eng Part K: J Multi-body Dyn 2011;225(3):204–19.

[21] Patir N, Cheng H. An average flow model for determining effects of three-dimensional roughness on partial hydrodynamic lubrication. ASME, Trans, J Lubr Technol 1978;100:12–7.

[22] Patir N, Cheng H. Application of average flow model to lubrication between rough sliding surfaces. ASME, Trans, J Lubr Technol 1979;101:220–30.

[23] Greenwood J, Williamson J. Contact of nominally flat surfaces. Proc R Soc Lond Ser A, Math Phys Sci 1966;295:300–19.

[24] Greenwood J, Tripp J. The contact of two nominally flat rough surfaces. Proc Inst Mech Eng 1970;185(1):625–33.

[25] Archard J. Contact and rubbing of flat surfaces. J Appl Phys 1953;24(8):981–8.

[26] Yang L. Wear coefficient equation for aluminium-based matrix composites against steel disc. Wear 2003;255(1):579–92.

[27] Herbst H. Theoretical modeling of the cylinder lubrication in internal combustion engines and its influence on piston slap induced noise, friction and wear [Ph.D. thesis]. Technische Universität Graz, 2007.

[28] Krasser J. Thermoelastohydrodynamische Analyse dynamisch belasteter Radialgleitlager [Ph.D. thesis]. Technische Universität Graz, 1996.

5.4 Friction and wear analysis of journal bearings exposed to repeated start and stop cycles

Journal bearings are typically designed to operate in pure hydrodynamic lubrication regime to ensure its lifetime. However, upon, for example, the starting of an engine or turbine, the bearing has to overcome boundary and mixed lubrication regime before a hydrodynamic film has established which may completely separate the two contacting surfaces. This application example deals with the start and stop behavior of journal bearings. Therefore, a large number of starts and stops are performed on the test-rig with the same fully formulated engine oil as in all previous examples. Once again, these measurement results are used to verify the presented simulation approach.

The simulation model from the previous examples is used to analyze the start-stop behavior. Before the shaft starts to rotate, a quasi-static condition needs to be established. Therefore, an initialization phase is included where a static load is applied to the bearing and the shaft moves towards the bearing shell until it reaches its resting position. The shaft is then accelerated and decelerated again until the shaft stops to rotate. The simulation approach incorporates the contact model which is derived in section 5.3.

After verifying the simulation approach on the basis of the measurement, the calculated results are analyzed in more detail. A main focus concerns the development of hydrodynamic and asperity contact pressure as well as the journal loci.

Due to the repeated starting of the shaft and the according occurrence of metal-metal contact, the bearing shell is exposed to wear. Similar to the third application example (see section 5.3), a stepwise adaption of the bearing geometry is calculated. In contrast to the previous example, where a final worn geometry is generated, wear continuously proceeds because metal-metal contact always exists when the shaft rests. However, the wear calculation begins with the start of the shaft rotation and ends when maximum speed is reached. It is repeated until a distinct wear scar is reached.

The influence of running-in on journal bearing behavior and friction losses is evaluated for two effects separately. First, the effect of surface smoothing due to running-in is analyzed and second, the effect of geometry adaption is investigated.

In line with the previous section of the result chapter, the research findings of the fourth application example are summarized at the beginning. Afterwards, an introduction for the study of the start and stop behavior of journal bearings is provided which is followed by a detailed description of the test and simulation results. A detailed conclusion is presented at the end of the chapter.

5.4.1 Summary of research findings

- 6000 start-stop cycles under static load are performed on the journal bearing test-rig. The shaft rests at the beginning of the test, accelerates to a maximum speed of 260 rpm and slows down until it completely stops again. The measurement results are analyzed for various start-stop cycles to identify a change over the number of start-stop cycles.
- The breakaway torque to overcome static friction decreases with the number of start-stop cycles.
- A simulation approach to calculate a complete start-stop cycle is presented. The importance of the initial phase when the external load is applied and the shaft

moves towards the bearing is highlighted. The start conditions are presented. TWhen the shaft rests, the static load is mainly supported by metal-metal contact.

- A full start-stop cycle is calculated with the presented approach and compared to the measured friction torque. The results show a good agreement for the evaluated start-stop cycle regarding the magnitude of the breakaway torque, the friction characteristics and the transitions between the lubrication regimes.
- The simulation results present more detailed information about the journal behavior during the start-stop cycle. Immediately after the shaft starts to rotate, the hydrodynamic pressure rises and a significant drop of asperity contact pressure can be seen. Due to the asymmetric hydrodynamic pressure distribution, the shaft is also pushed in horizontal direction.
- The influence of surface smoothing due to running-in of the bearing shell on the journal bearing behavior and friction is discussed. A smoother surface reduces the asperity contact in mixed lubrication regime and decreases the frictional losses. The numerical results predict a reduction of friction work by the factor of two for the smoother surface during a start-stop cycle.
- A wear analysis is performed for the journal bearings by an iterative adaption of the surface geometry. The worn area (wear scar) develops all along the bearing axis with a maximum wear depth at the bearing edges. The wear scar after 9000 equivalent starts spreads from -35° to 70° in circumferential direction.
- The simulation results show that the maximum hydrodynamic pressure as well as the maximum asperity contact pressure decrease with a worn bearing geometry. The contact area increases and therefore, the wear area increases for an adapted bearing geometry.
- Finally, the influence of a worn bearing geometry on friction is discussed. Because of a smaller gradient in the lubrication gap (shaft radius and wear scar radius become similar) the hydrodynamic pressure cannot fully develop compared to a perfect cylindrical bearing shell. As a consequence, the contact area increases which leads to higher friction torque in mixed lubrication regime.

5.4.2 Introduction

When the shaft rests in a journal bearing, it is completely supported by metal-metal contact. By applying a torque to the shaft, static friction has to be overcome before the shaft starts to rotate. This maximum torque is also called breakaway torque. After a short sliding, a hydrodynamic pressure establishes and lifts the shaft. The bearing operates in mixed lubrication regime until the contacting surfaces are completely separated. This behavior of journal bearings has been experimentally observed by Mokhtar et al. [55]. The authors analyzed the movement of the journal during starting and stopping on a journal bearing test-rig. During the starting, a hydrodynamic film was rapidly formed and after reaching a final running speed, the journal found its steady state operating condition. Before the shaft was completely separated from the bearing shell, a sliding motion in circumferential direction was observed with little or no initial rolling. The authors also analyzed the stopping behavior of the shaft. The shaft operates in hydrodynamic lubrication regime until the shaft stops to rotate. After stopping the shaft follows a squeeze film trajectory to a resting position.

In a second publication, Mokhtar et al. [56] investigated the wear behavior of journal bearings exposed to repeated starting and stopping of the shaft. The authors found that the surface roughness of the bearing shell got smoother especially during the first 1000 cycles. The final surface roughness of the bearing shell approached the roughness of the hardened shaft. They also analyzed the circumferential extent of the wear scar. The location of the wear scar was shifted in the direction of shaft rotation. The authors observed that no significant wear took place during stopping of the shaft.

Bouyer and Fillon [20] measured the friction torque during start-up for different specific pressures, various radial clearance and different bearing length. The authors found a linear relation of the maximum torque in the beginning (breakaway torque) with specific pressure. The friction torque further increases with increasing roughness and is also influenced by temperature and oil feeding.

The influence of lubricant additives on journal bearing performance during start-up and shut-down is experimentally analyzed by Durak et al. [32]. The authors evaluated the average friction during several start-stop cycles and present wear characteristics for differently formulated oils.

An analytical model to investigate friction during the transient start-up of hydrodynamic journal bearings was presented by Harnoy [37]. At low start-up acceleration, the results showed extensive slip-stick behavior. At higher acceleration, slip-stick disappeared. The author further concluded that it is possible to decrease wear by applying high start-up acceleration.

Monmousseau and Fillon [57] studied the transient thermo-elasto-hydrodynamic behavior of a tilting-pad journal bearing during start-up. Their main objective is to estimate operation condition which ensures a safe running without seizure during the start-up. The influence of parameters like bearing clearance, feeding temperature and acceleration is analyzed.

Journal bearings which are exposed to repeated start-ups, show a wear scar at the highly loaded bearing region. The influence of such a worn bearing geometry on journal bearing behavior is of interest in several publications. They have in common that the bearing operation considers a steady shaft rotation. Hashimoto et al. [38] created a worn bearing geometry with a maximum wear depth in load direction. The authors analyzed the pressure distribution, eccentricity ratio and attitude angle under steady state condition.

Further, Fillon and Bouyer [33] analyzed the thermal behavior of a worn journal bearing. Similar to Hashimoto et al. a worn geometry was assumed. The authors concluded that wear defect could improve the thermo-hydrodynamic performance of a bearing. In particular, a lower maximum temperature was identified with increasing wear defect.

A friction analysis was performed by Nikolakopoulos and Papadopoulos [60] in worn journal bearings. The authors concluded that the friction coefficient increases with increasing wear depth. Additionally, the misalignment of the journal is studied. An increase of misalignment leads to higher power loss.

The present study focuses on the transient behavior of the journal bearing during starting and stopping of the shaft. A mixed elasto-hydrodynamic simulation model is presented which considers the elastic deformation of bearing and shaft (see section 4). The bearing is considered to be isothermal in the simulation, see section 4.4.5.

Primary aim is to describe the dynamic behavior of the journal bearing and the friction losses during a complete start-stop cycle. After an initial resting of the shaft, the shaft starts to rotate and operates in boundary, mixed or hydrodynamic lubrication regime. The simulation results are compared to results obtained from the journal bearing test-rig (see section 3).

Further, a wear analysis is performed which allows an iterative adaption of the bearing shell, see section 4.2 and 4.2.1. The simulation approach is described in Sander et al. [75]. A wear load is calculated during the start-up and a worn geometry is created according to Archard's wear equation.

Finally, the influence of surface smoothing and worn geometry on journal bearing performance is investigated.

5.4.3 Test conditions and test results

The start-stop tests are performed on the journal bearing test-rig described in chapter 3. A static load of 2.5 kN is applied to the test connecting rod. The resting test shaft is constantly accelerated to a maximum speed of approximately 260 rpm. The duration of the speed-up is 3 s. Subsequently, the shaft is constantly decelerated over 3 s until the shaft stops. This start-stop cycle is repeated 6000 times. In between each cycle, a recovery phase of 3 s is defined to ensure that lubricant flows out of the bearing contact zone. Hence, the reaction force in the resting bearing is dominantly supported by metal-metal contact.

Measurement results are recorded for individual cycles for a period of 6 s. Starting from cycle 100 every 100^{th} cycle is recorded until cycle 1000. Afterwards, every 1000^{th} cycle is evaluated. Hence, data is available for 15 cycles. The measurement period starts 0.5 s before the shaft starts to rotate. Therefore, the actual stopping of the shaft as well as the resting phase is not available in the results.

For the highly loaded test bearing, a sputter bearing is used. The two support bearings are steel/aluminum composite bearings. The clearance of the test bearing was determined before the tests were performed at room temperature. A diametral clearance of 23 μm was identified. Therefore, the clearance of the test bearing differs from results discussed previously (see section 5.1, 5.2 and 5.3) when the test bearing had a diametral clearance of 30 μm. The support bearings have a diametral clearance of 50 μm like in previous result sections.

The oil supply temperature for all bearings is recorded during the 6000 cycles. The supply temperature increases slightly during the first 1000 cycles because of the heating up of the test-rig components. Subsequently, the supply temperature remains stable (± 1 °C). The supply temperature of the test bearing increases from 88 °C in the beginning of the test to 93 °C after 6000 cycles. For the two support bearings, a supply temperature of 100 °C in the beginning and 107 °C in the end of the test is observed.

Figure 5.1 shows the shaft speed (dashed black curve) over time for one start-stop cycle. At the beginning, the shaft is at rest and after 0.5 s the shaft begins to rotate. The shaft speed reaches its maximum after 3.5 s and the deceleration starts.

The solid black curve represents the measured overall friction torque induced by all three bearings during the 100^{th} cycle. At rest (0 s), the shaft is in a pre-stressed condition and shows a constant torque. Shortly before the shaft begins to rotate, the torque abruptly increases to a maximum. The maximum friction torque is further called breakaway torque which indicates the transition between static and sliding friction. Once in motion, the bearing enters mixed lubrication regime and the torque decreases quickly. After 1.2 s, the torque becomes a minimum as the hydrodynamic lubrication regime begins. The shaft speed at the transition between mixed and hydrodynamic lubrication regime is around 100 rpm. After 5.5 s, the torque starts to rise again because the bearing enters mixed lubrication regime during the stop phase again. The measured signal shows

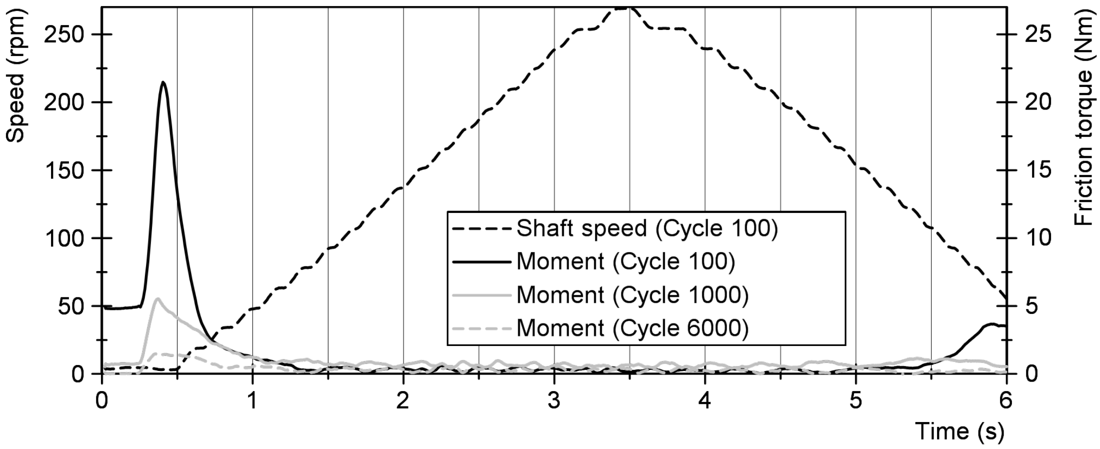

Figure 5.1: Measured shaft speed and measured overall friction torque (sum of all three bearings) for three start-stop cycles

strong fluctuations which are caused by the dynamic behavior of the test-rig. It can be expected that the impulse at the breakaway cause such strong fluctuations.

The curve in gray shows the measured overall friction torque for the 1000th cycle. The breakaway torque decreased from 20 Nm at cycle 100 to 5 Nm but the transition between mixed and hydrodynamic lubrication regime remains at 1.2 s. Because of the fluctuations of the torque signal, a difference with other cycles cannot be recognized in the hydrodynamic lubrication regime. The strong torque increase at the end of the cycle doesn't appear until 6 s. The measured overall friction torque of the 6000th cycle is shown as dashed gray curve. The breakaway torque furthermore decreases to 2 Nm.

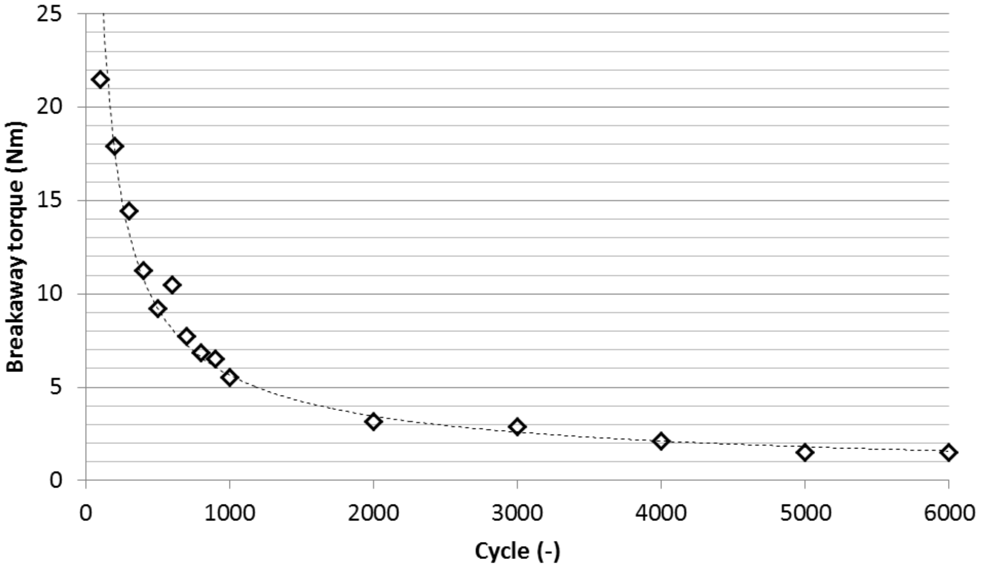

Figure 5.2: Measured breakaway torque over the number of start-stop cycles

The development of the breakaway torque during the test procedure is shown in figure 5.2. The maximum breakaway torque is identified at the first start-stop cycles. During the first 1000 cycles, the breakaway torque strongly decreases and the curve flattens out from

2000 cycles onwards. The curve follows a power law of $T_{\text{Breakaway}} \approx 760 \cdot n_{\text{Cycle}}^{-0,7}$.

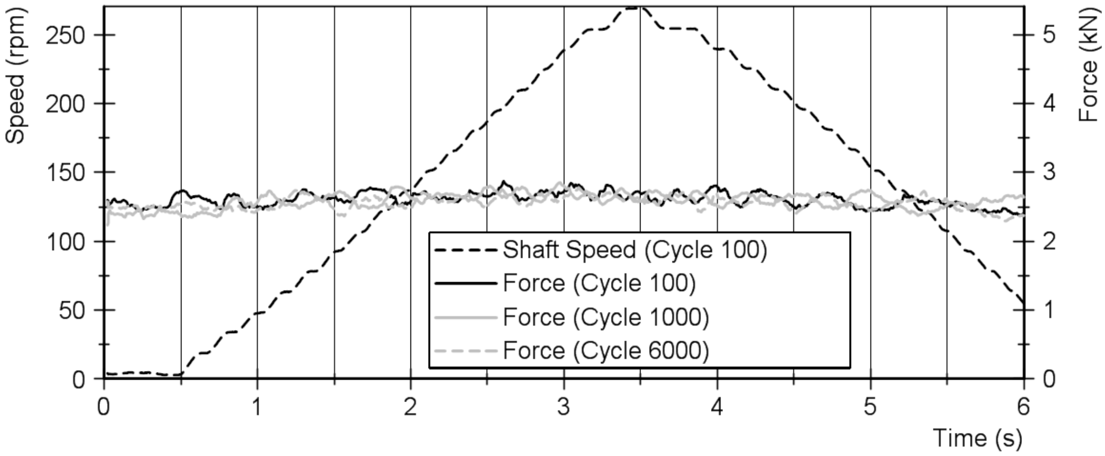

Figure 5.3: Measured shaft speed and measured force for three start-stop cycles

The magnitude of the applied load is set to 2.5 kN. However, it is also measured during the start-stop cycles. The measurement results for three start-stop cycles are shown in figure 5.3. The solid black curve shows the force during cycle 100, the solid and dashed gray curve for cycle 1000 and 6000, respectively. The measured force has an average of 2.5 kN and shows fluctuations during the cycle of ± 0.25 kN (± 10 %). The fluctuations are also caused by the dynamic behavior of the test-rig. Especially after the shaft starts to rotate, the fluctuations increase. Hence, a connection to the impulse at breakaway can be expected.

An equivalent friction coefficient μ_{eq} is calculated to compensate the influence of the load fluctuations on the friction torque. For simplicity, it is assumed that all bearings have the same equivalent friction coefficient. Hence, the overall friction torque can be written as:

$$M = \mu_{\text{eq}} F_{\text{start-stop}} r_{\text{TB}} + 2 \cdot \left(\mu_{\text{eq}} \frac{F_{\text{start-stop}}}{2} r_{\text{SB}} \right), \tag{5.1}$$

with the external load during the start-stop cycle $F_{\text{start-stop}}$, the test bearing radius r_{TB} and the support bearing radius r_{SB}. The equivalent friction coefficient can therefore be calculated by:

$$\mu_{\text{eq}} = \frac{M}{(r_{\text{TB}} + r_{\text{SB}}) F_{\text{start-stop}}}. \tag{5.2}$$

Figure 5.4 shows the equivalent friction coefficient for three start-stop cycles. The static friction coefficient can be identified when the shaft begins to rotate. For cycle 100, the static friction coefficient has a value of 0.15. After 1000 cycles, the static friction coefficient drops to 0.04 and further decreases below 0.02 after 6000 start-stop cycles. In the hydrodynamic lubrication regime, an equivalent friction coefficient of around 0.01 can be seen.

The trend of the static friction coefficient over the cycle number is also shown in figure 5.5. Similar to the measured breakaway torque, a clear decrease of static friction coefficient can be identified in the beginning of operation. After 2000 cycles, the change of static friction coefficient over decreases. The minimum is reached at the end of the test procedure.

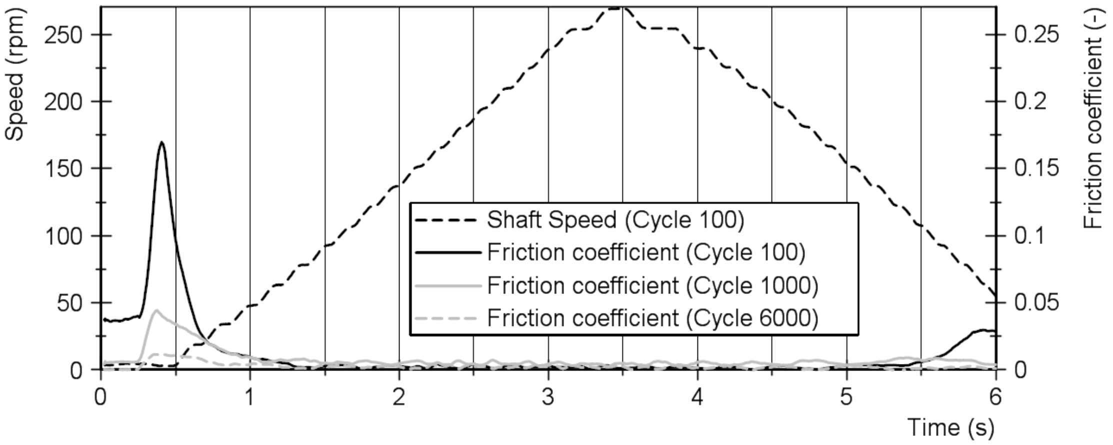

Figure 5.4: Measured shaft speed and calculated equivalent friction coefficient for three start-stop cycles

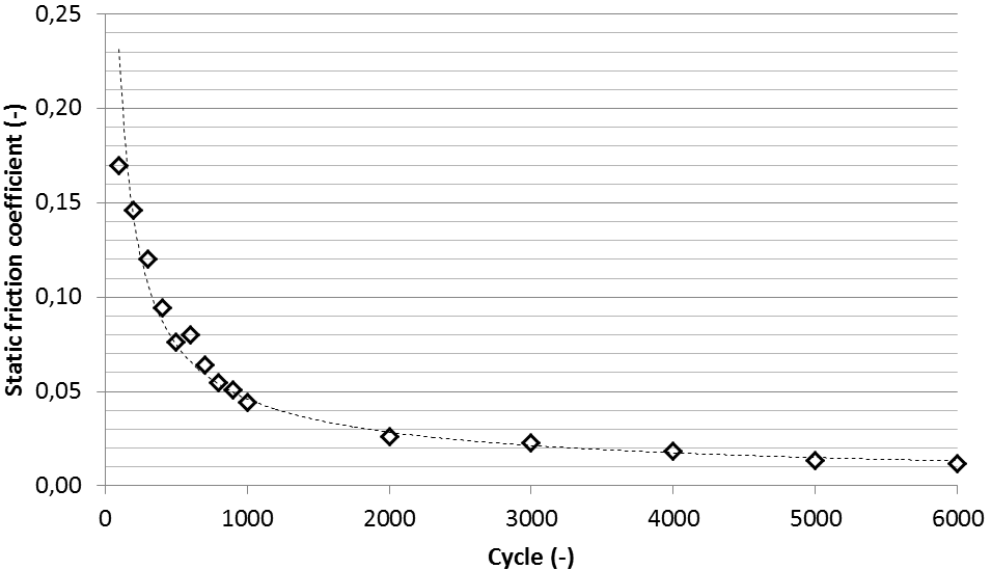

Figure 5.5: Static friction coefficient over the number of start-stop cycles

The equivalent test bearing temperature (see equation 4.35) is shown in figure 5.6. The temperature stays constant during one start-stop cycle. Therefore, the equivalent temperature is plotted over the start-stop cycles. At the 100^{th} start-stop cycle, a temperature of 94 °C is identified. During the first 1000 start-stop cycles, the equivalent bearing temperature rises to 106 °C. After 1000 cycles, the temperature varies only slightly between 105 °C and 107 °C.

Figure 5.6 additionally shows the measured oil flows in the test bearing as black crosses. Again, an average of the oil flow is calculated as the oil flow is steady during one start-stop cycle. At the beginning of the test, the oil flow increases from 0.27 l/min to 0.41 l/min after 1000 cycles. After 1000 cycles, the oil flow stays similar.

Both, equivalent bearing temperature and averaged oil flow show an identical trend. This indicates that the oil temperature with a consequential change of oil viscosity has a major influence on oil flow. An increase of oil flow due to wear cannot be determined.

After the start-stop tests, the wear scar was analyzed. A maximum wear depth occurred

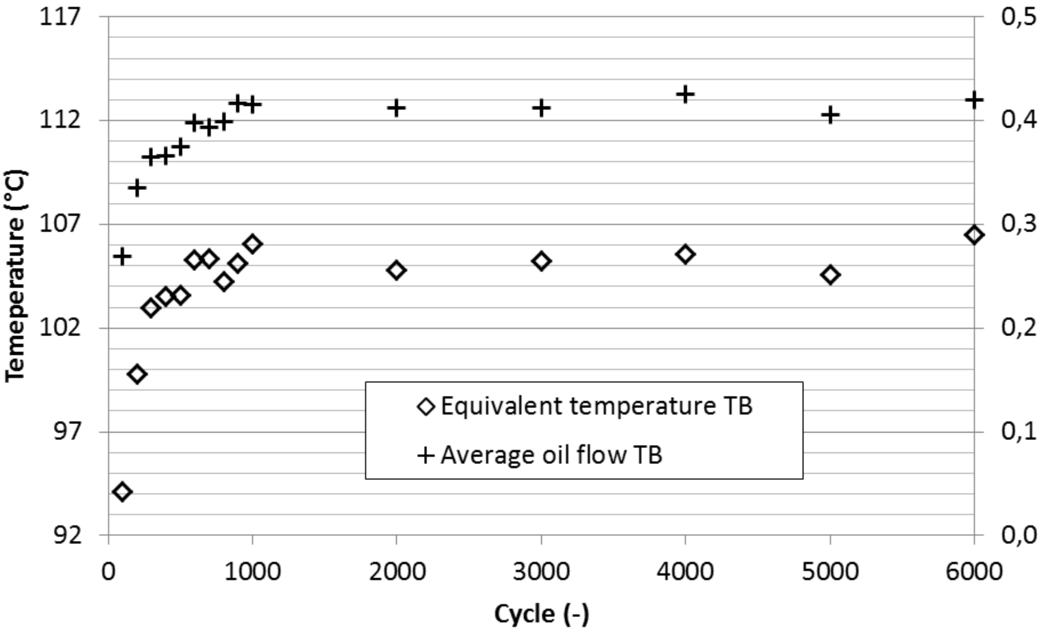

Figure 5.6: Equivalent test bearing temperature and measured test bearing oil flow over the number of start-stop cycles, TB denotes the test bearing

at the bearing edge with a magnitude of 13 μm. At the circumferential position of the maximum wear depth an average wear depth along the axial direction was identified with 7 μm.

5.4.4 Simulation model and simulation results

The initial point of the start-stop simulation model is the test-rig model used for previous examples which is described in section 4 in more detail.

The surface parameters that are necessary for the contact model, are derived from surface scans of a sputter bearing shell. This data was discussed in section 5.3. However, they are listed in table 5.1 for completeness.

Table 5.1: Surface roughness and simulation input parameters for the test bearing shell and the shaft

Surface	Shell	Shaft
σ [μm]	0.25	0.13
δ [μm]	0.36	0.22
K [-]	0.001	
E^* [GPa]	53.3	
μ_{Bound} [-]	0.02	
Γ [-]	1.5	4

Specified are the asperity summit roughness (root mean squared) σ, the mean summit height δ, the combined Young's modulus E^* and the elastic factor K. A boundary friction coefficient μ_{Bound} of 0.02 is defined. Γ identifies the orientation of the asperities.

The equivalent bearing temperatures (see section 4.4.5) are calculated from the measurement results of the 3000th load cycle. The 3000th cycle is chosen because the bearing has already been exposed to an initial run-in and because the temperature has reached a steady state, compare figure 5.6. Hence, the test bearing temperature is 105.2 °C, the support bearing temperatures 99.7 °C and 102.5 °C, respectively.

In contradiction to previous examples where a constant shaft speed was applied to a single load cases, the shaft rests, accelerates, decelerates and stops again. Due to the standstill of the shaft an angle-based simulation is not possible anymore and the problem is solved in time domain. The variable shaft speed is provided by a reference body, namely the speed controller, which is a rigid body with an infinite mass. The speed controller has a single rotational degree of freedom and is connected to the test shaft via a rotational spring damper element. The properties of the spring damper element are selected, so that the test shaft follows the rotation of the speed controller. Therefore, a very high torsional stiffness (100 kN m/rad) and damping coefficient (10 N m s/rad) are used.

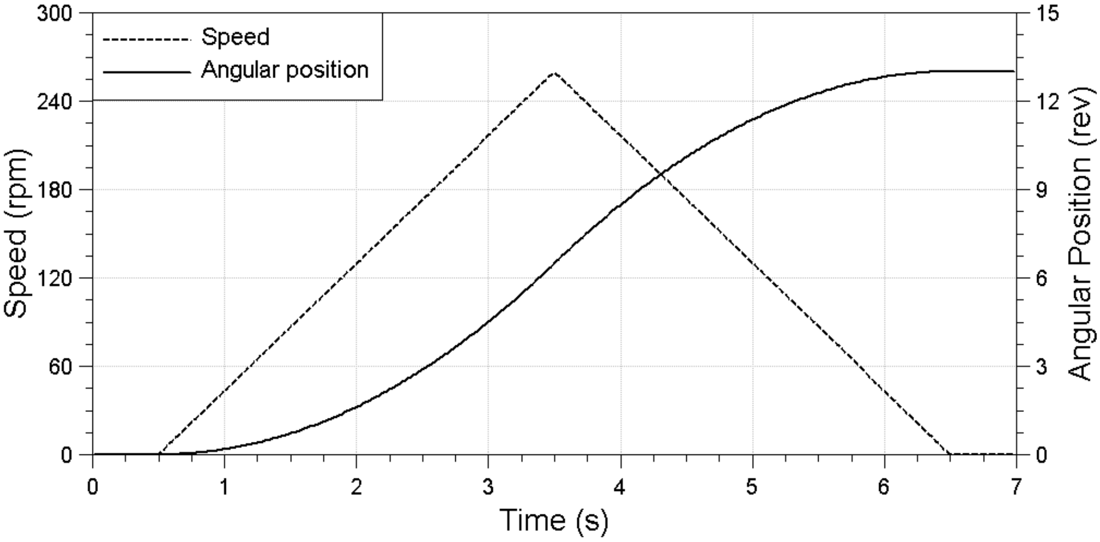

Figure 5.7: Angular position and angular velocity of the speed controller

The pre-defined motion of the speed controller is shown in figure 5.7. The solid black curve displays the angular position of the shaft in revolutions and the dashed black curve represents the angular velocity (shaft speed). For the first 0.5 s, the test shaft doesn't rotate and rests on the support bearing. The shaft starts to rotate at 0.5 s and it is constantly accelerated to a maximum speed of 260 rpm after 3.5 s. After reaching the maximum speed the shaft is constantly slowed down. At 6.5 s the shaft stops to rotate. The entire simulation duration is set to 7 s. Instead of calculating the 9 s of the measurement cycle, the simulation duration is reduced because a final resting position is achieved after 7 s. This will reduce the calculation time. Slightly more than 13 revolutions are performed during one start-stop cycle.

Initialization phase to reach a static start condition

Before the shaft starts to rotate, it is in contact with the bearing shell. To find this starting position and the distribution of contact pressure, an initialization phase is defined. During this initialization phase, which lasts for 0.5 s, the external load is applied and a static equilibrium between external load and contact pressure is numerically found by solving equation 4.14 in time domain.

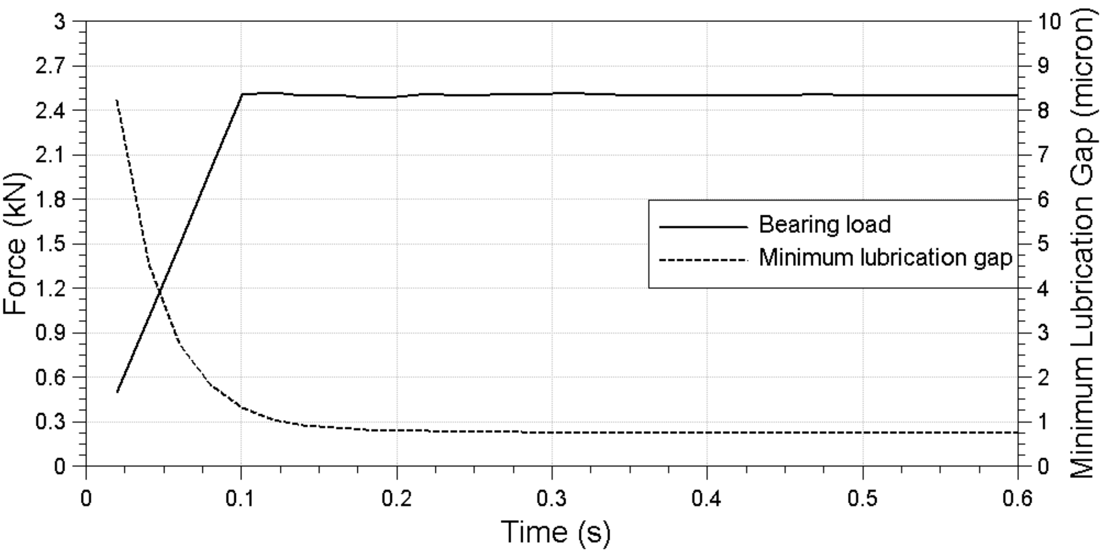

Figure 5.8: Test bearing load and corresponding minimum lubrication gap during the initialization phase of the start-stop cycle simulation

Figure 5.8 shows the initialization phase for the start-stop simulation. The solid black curve shows the load acting vertically on the test bearing. During the first 0.1 s, the static load is constantly increased until the 2.5 kN are reached. At the start of the initialization phase, it is assumed that the shaft is located in the center of the bearing. Furthermore, it is assumed that the bearing is completely filled with oil at the beginning of the initialization phase. The test bearing has a clearance of 23 μm which makes an initial distance between shaft and bearing of 11.5 μm. As the load increases the shaft subsides within the bearing and the minimum radial distance between shaft and bearing shell decreases during the load initialization. The dashed curve shows the minimum lubrication gap. After 0.1 s the minimum distance reduces to 1.3 μm. After 0.3 s, the minimal lubrication gap is reached.

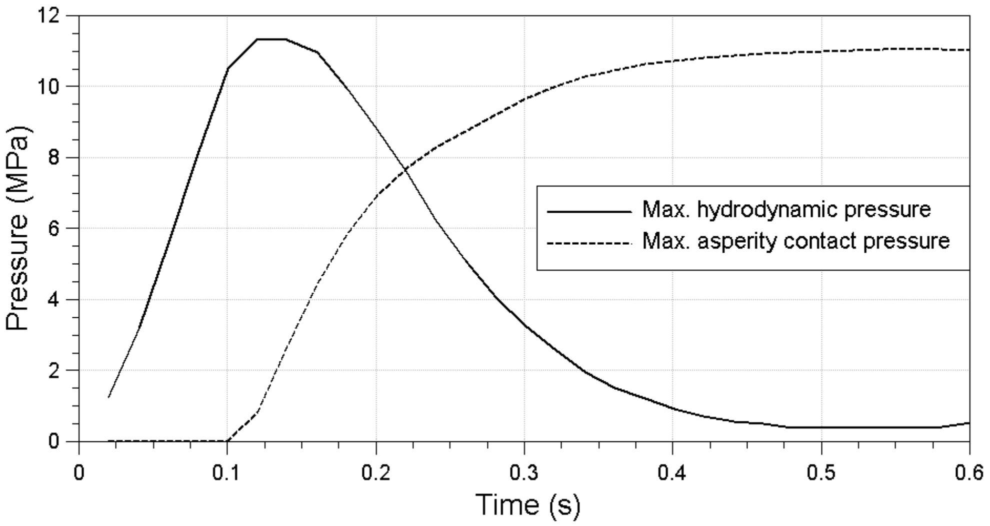

Figure 5.9: Maximum hydrodynamic and maximum asperity contact pressure during the initial phase of the start-stop cycle simulation

Figure 5.9 shows the maximum hydrodynamic pressure as solid curve and the maximum asperity contact pressure as a dashed curve during the first 0.6 s. At the beginning of the simulation, the bearing is completely filled with lubricant. When the load is applied to the bearing, the hydrodynamic pressure in the lubricant rises. At the same time, the lubricant is pushed out of the highly loaded bearing region due to the hydrodynamic pressure gradient. See figure 5.10 which shows the hydrodynamic pressure distribution at 0.12 s.

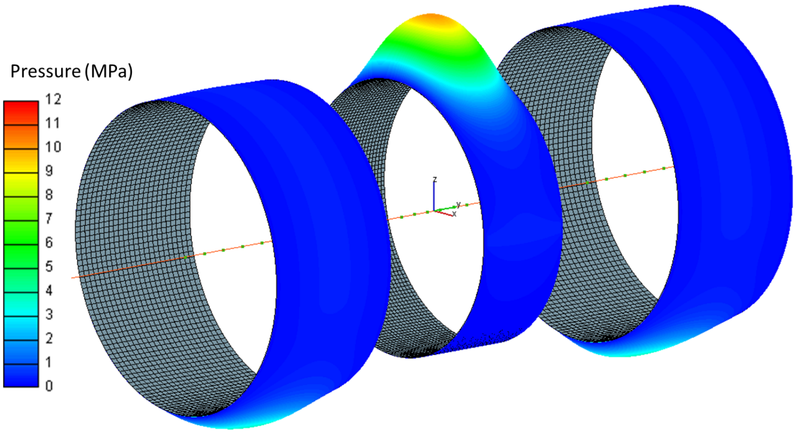

Figure 5.10: Calculated hydrodynamic pressure distribution in test bearing and the two support bearings at 0.12 s

At 0.12 s, the maximum hydrodynamic pressure is reached during the initialization phase. At the same time, asperity contact starts to develop and it increases while the minimum clearance between shaft and bearing further decreases. Shortly before the shaft starts to rotate, the hydrodynamic pressure reaches its minimum. The minimum hydrodynamic pressure is equal to the oil supply pressure of 0.4 MPa. At 0.5 s, the final quasi-static position is reached and there is no relative normal movement between shaft and bearing anymore. Hence, the shaft is mainly supported by asperity contact. The maximum asperity contact pressure occurs in the transition when the shaft begins to rotate.

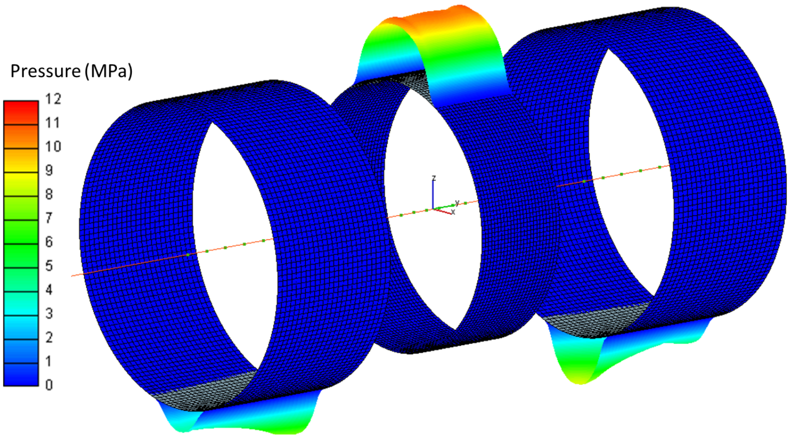

Figure 5.11: Calculated asperity contact pressure distribution in test bearing and the two support bearings at 0.5 s

Figure 5.11 and figure 5.12 show the asperity contact pressure distribution and the

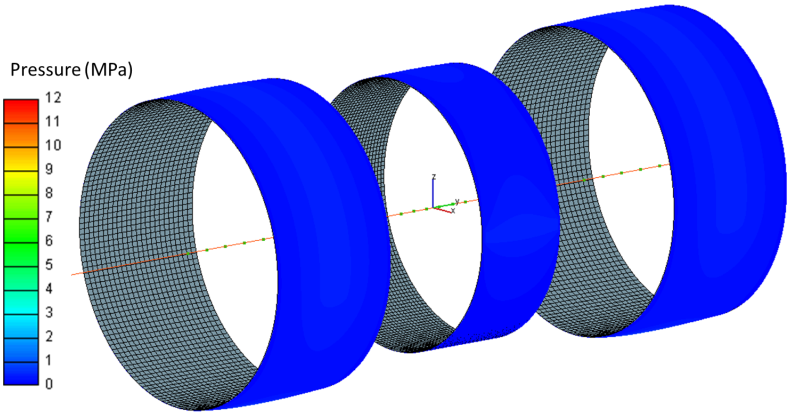

Figure 5.12: Calculated hydrodynamic pressure distribution in test bearing and the two support bearings at 0.5 s

hydrodynamic pressure distribution for all three bearings at 0.5 s. The hydrodynamic pressure in the entire lubrication gap is equal to the oil supply pressure because there is no relative motion between shaft and bearing. Only at the bearing edges, the pressure drops to the ambient pressure of 0.1 MPa.

The highest asperity contact pressure occurs at the top position of the test bearing. The contact pressure decreases in both circumferential direction by moving away from the top position and disappears completely beyond an angle of 25°. In axial direction, the contact pressure stays nearly constant.

The maximum contact pressure in the support bearing is smaller than in the test bearing. However, the two support bearings do not show a constant pressure distribution along the axial direction. The maximum contact pressure occurs at the bearing edge which is located closer to the test bearing and decreases along the bearing width. The asymmetric contact pressure distribution is caused by the elastic deformation of the test shaft due to the static load (deflection curve).

Simulation of a full start-stop cycle

The initialization phase ensures that the bearing is mainly supported by asperity contact when the shaft starts to rotate. The behavior of the bearing during the starting and stopping of the shaft can then be analyzed. First, the hydrodynamic and asperity contact pressure will be discussed.

Figure 5.13 shows the maximum hydrodynamic pressure (solid black curve) and the maximum asperity contact pressure (dashed black curve) for the entire start-stop cycle. After the breakaway, the shaft constantly accelerates and a relative motion between shaft and bearing is obtained. The hydrodynamic pressure develops due to the relative motion and rises with an increasing rotational speed. The shaft is lifted from the bearing which can also be identified in figure 5.14 where the minimum distance between shaft and bearing is plotted as solid curve over time. However, the hydrodynamic pressure strongly rises within 1.5 s from the breakaway and stabilizes afterwards. The hydrodynamic pressure has a maximum of 11.5 MPa at a shaft speed above 150 rpm. At the same time when the hydrodynamic pressure builds up, a decrease of asperity contact pressure occurs. At the maximum shaft speed of 260 rpm, asperity contact is still present but it is below 0.5 MPa. The asperity contact pressure increases immediately as the angular velocity of the shaft is reduced again. The hydrodynamic pressure rapidly drops after

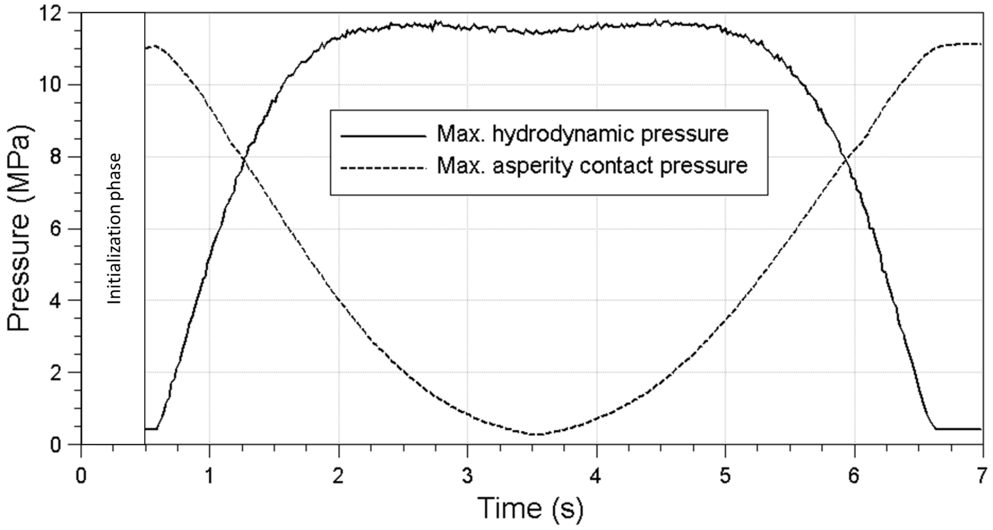

Figure 5.13: Maximum hydrodynamic and maximum asperity contact pressure during the start-stop cycle simulation

5.5 s. A static condition at the end of the cycle is reached which is identical to the condition at the breakaway.

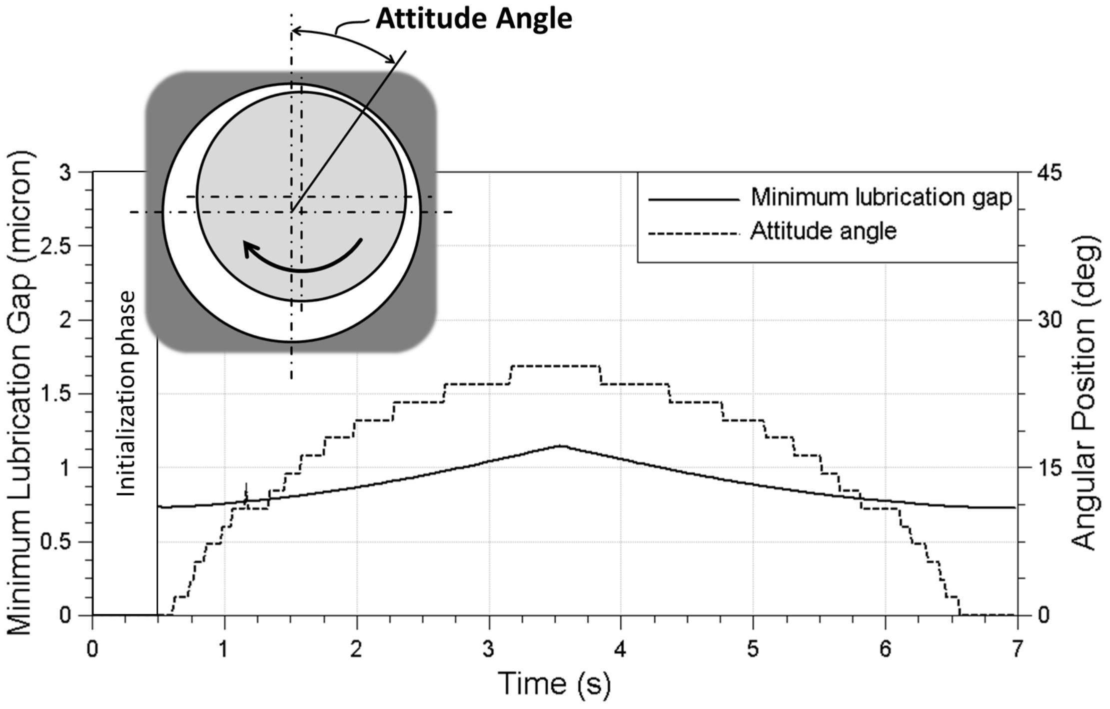

Figure 5.14: Minimum lubrication gap and angular position of the minimum lubrication gap during the start-stop cycle simulation

The minimum lubrication gap and its angular position (attitude angle) are shown in figure 5.14. The position of the minimum lubrication gap corresponds to the position of the maximum asperity contact pressure. However, the minimum lubrication gap occurs at the breakaway and at the end of the load cycle. With an increase of speed, the shaft is lifted from its resting position and the lubrication gap increases. The minimum lubrication gap reaches its maximum of 1.1 μm at maximum shaft speed. At the end of the load cycle, the resting position is reached again.

The dashed curve shows the attitude angle of the shaft. At the beginning of the cycle, the minimum distance between shaft and bearing is located at the top bearing position (0°) because the applied load acts vertically on the bearing. Shortly after the shaft starts to rotate, the attitude angle moves in the rotational direction of the shaft. This is caused by the development of an asymmetrical hydrodynamic pressure distribution as soon as the shaft starts to rotate. This asymmetric pressure distribution pushes the shaft in direction of rotation. This behavior will be discussed in detail in a subsequent section. However, the attitude angle rises with an increase of speed and reaches a maximum of 25° at 260 rpm. When the shaft decelerates again, the attitude angle moves back towards the top bearing position. The shaft stops to rotate at exactly 6.5 s but the final attitude angle is reached with a short delay. The stepped character of the curve appears because the minimum distance is only evaluated at the discretized grid nodes.

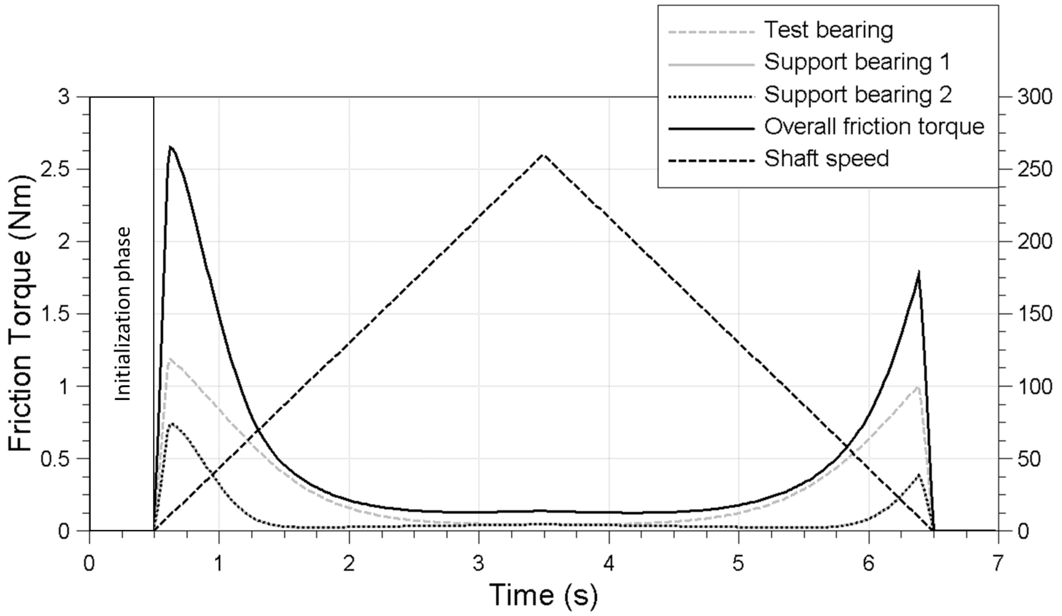

Figure 5.15: Overall friction torque, individual bearing friction torque and shaft speed during the start-stop cycle simulation

Finally, figure 5.15 shows the calculated overall friction torque (solid black curve) and the calculated friction torques of the individual bearings during the entire start-stop cycle. The friction torque for the two support bearings are almost identical and the curves lie on top of each other (black dotted and gray solid curve). Additionally, the shaft speed is shown as dashed black curve. During the initialization phase, no friction torque occurs because the shaft does not rotate. Immediately as the shaft begins to rotate, the friction torque abruptly rises to its maximum. Regarding the overall torque, a maximum torque or breakaway torque of 2.7 Nm is reached. After overcoming static friction, all bearings operate in the mixed lubrication regime and the friction torque decreases. The two support bearings have a minimum friction torque at around 1.5 s. Afterwards, they operate in hydrodynamic regime and the friction torque increases slightly. The test bearing shows the minimum friction torque at the maximum speed when asperity contact is still present (compare figure 5.13). During the deceleration, an inverse behavior can be seen but the maximum friction torque at the end of the cycle is below the breakaway torque. However, the test bearing contributes the major friction torque to the overall torque especially in the mixed and boundary lubrication regime.

5.4.5 Comparison between measurement and simulation

The temperature parameters for the simulation model are based on the 3000th start-stop cycle because constant temperatures are established at the test-rig. Therefore, the measured torque of the 3000th cycle is compared to the simulated friction torque results.

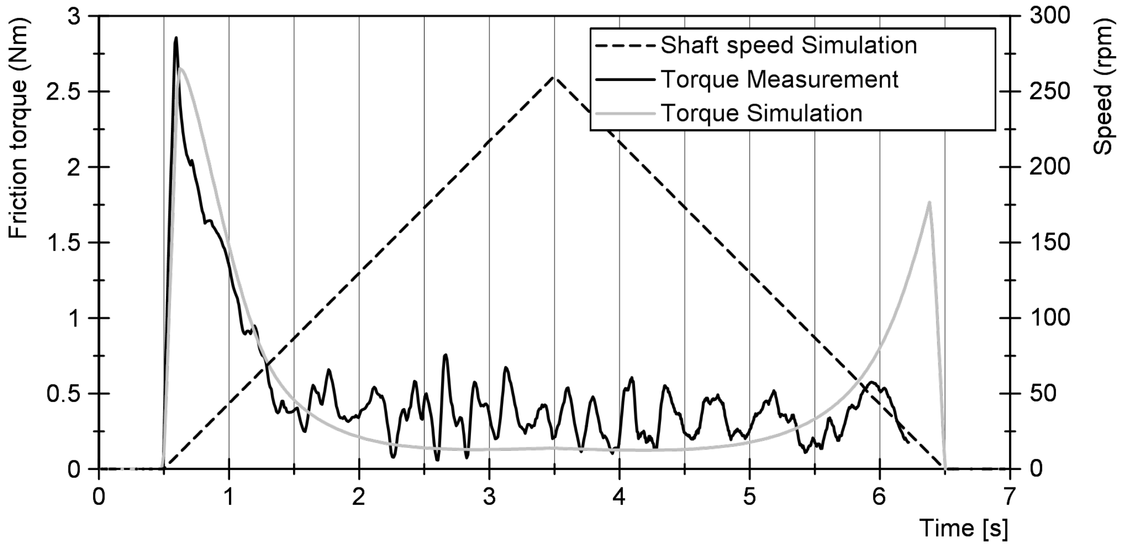

Figure 5.16: Measured and calculated friction torque during the start-stop cycle

The black curve in figure 5.16 represents the measured torque from the test-rig. The gray curve shows the calculated friction torque as a sum of all three bearings. The two curves show an identical trend up to the breakaway torque. The calculated breakaway torque is 2.65 Nm and the measured breakaway torque is 2.86 Nm. With increasing speed, both curves drop parallel as they reach mixed lubrication regime. From the measurement result, the transition between mixed and hydrodynamic lubrication regime is hard to identify because of high fluctuation in the torque signal. However, in the end of the start-stop cycle, the simulation predicts an increase of friction torque before the shaft completely stops to rotate. The measured friction torque does not show any increase until 6 s. It can be expected that the roughness of the bearing surface will smoothen during the test because the bearing operates in mixed lubrication regime. Therefore, the results calculated with a new bearing surface probably overestimate the friction torque during the starting and the stopping. The influence of surface smoothing is investigated in the upcoming section 5.4.6.

The test shaft rests at the breakaway point and the load is mainly supported by metal-metal contact. Only an insignificant amount is still supported by the hydrodynamic pressure within the bearing. Therefore, the integral of the asperity contact pressure over the bearing surface is nearly equal to the applied load. Hence, the breakaway torque can be estimated by the basic static equilibrium:

$$M = \mu_{\text{Bound}} F_{\text{start-stop}} r_{\text{TB}} + 2 \cdot \left(\mu_{\text{Bound}} \frac{F_{\text{start-stop}}}{2} r_{\text{SB}} \right), \tag{5.3}$$

with the applied load $F_{\text{start-stop}}$, the boundary friction coefficient μ_{Bound}, the test bearing radius r_{TB} and the support bearing radius r_{SB}. With a boundary friction coefficient of $\mu_{\text{Bound}} = 0.02$ and a static load of $F_{\text{static}} = 2.5$ kN the breakaway torque is calculated to 2.55 Nm. This estimation implies that the breakaway torque only depends on the friction coefficient and is independent on the surface roughness. The surface roughness may affect the friction coefficient. However, the surface roughness will influence the friction in mixed lubrication regime as it is shown in the following section.

5.4.6 Effect of surface smoothing due to running-in on friction

So far, the results are calculated with the surface parameters of a new bearing shell. During the operation, the bearing surface will smoothen because of the interaction of the asperities of the contacting surfaces. For the evaluation of the impact of surface smoothing due to running-in of the bearing surface, a contact model with a ″worn″ bearing surface is established. Therefore, the surface of a worn bearing shell is scanned. The results of the surface analysis are already described in section 5.3. For convenience, the main surface roughness parameters are shown in table 5.2.

Table 5.2: Surface roughness and simulation input parameters for the test bearing shell and the shaft of the ″New″ and ″Worn″ contact pair

Contact pair	New		Worn	
Surface	Shell	Shaft	Shell	Shaft
σ [μm]	0.25	0.13	0.15	0.13
δ [μm]	0.36	0.22	0.15	0.22
K [-]	0.001		0.001	
E^* [GPa]	53.3		53.3	
μ_{Bound} [-]	0.02		0.02	
Γ [-]	1.5	4	1.5	4

The asperity summit roughness σ of the bearing shell changed from 0.25 μm to 0.15 μm due to the surface adaption. The mean summit height δ drops from 0.36 μm to 0.15 μm. The combined Young's modulus E^*, the elastic factor K and the asperity orientation Γ remain unchanged. The boundary friction coefficient μ_{Bound} remains unchanged too to point out the influence of roughness change only.

Figure 5.17 shows the friction torque calculated with the ″worn″ bearing surface (gray curve). The simulation results taken from the ″new″ bearing surface discussed previously, are added to the figure to display the difference caused by the different surfaces. Regarding the breakaway torque, both contact models produce the same result as expected. When the shaft starts to rotate, the friction torque calculated with the ″worn″ bearing surface shows a clear reduction of friction torque compared to the ″new″ bearing surface. It also shows an earlier transition point between mixed and hydrodynamic lubrication regime. At maximum speed (at 3.5 s), both models indicate an identical friction torque due to dominant hydrodynamic lubrication. A major difference can be seen in the behavior during the slowdown and stopping of the shaft. The ″worn″ bearing surface shows a distinct reduction of maximum friction torque of 1.2 Nm.

The main differences are obtained for the test bearing. Therefore, detailed simulation results for the test bearing are shown in figure 5.18. The black curves represent the simulation results calculated with the ″new″ bearing surface and the gray curves with the ″worn″ bearing surface. The maximum hydrodynamic pressure is shown as solid curve and the maximum asperity contact pressure is shown as dashed curve. At the breakaway

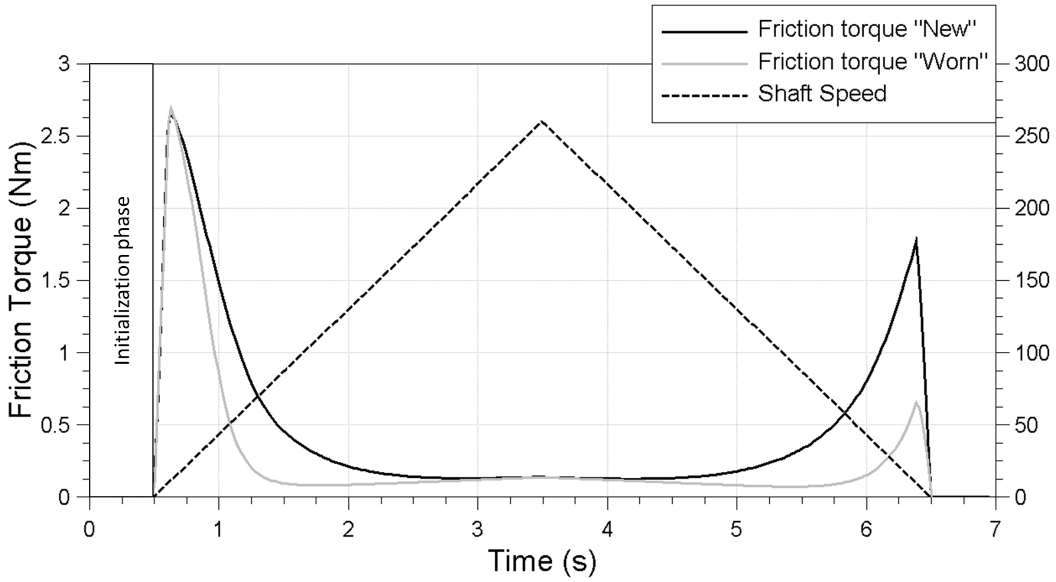

Figure 5.17: Calculated overall friction torque during the start-stop cycle for the "new" and "worn" contact model

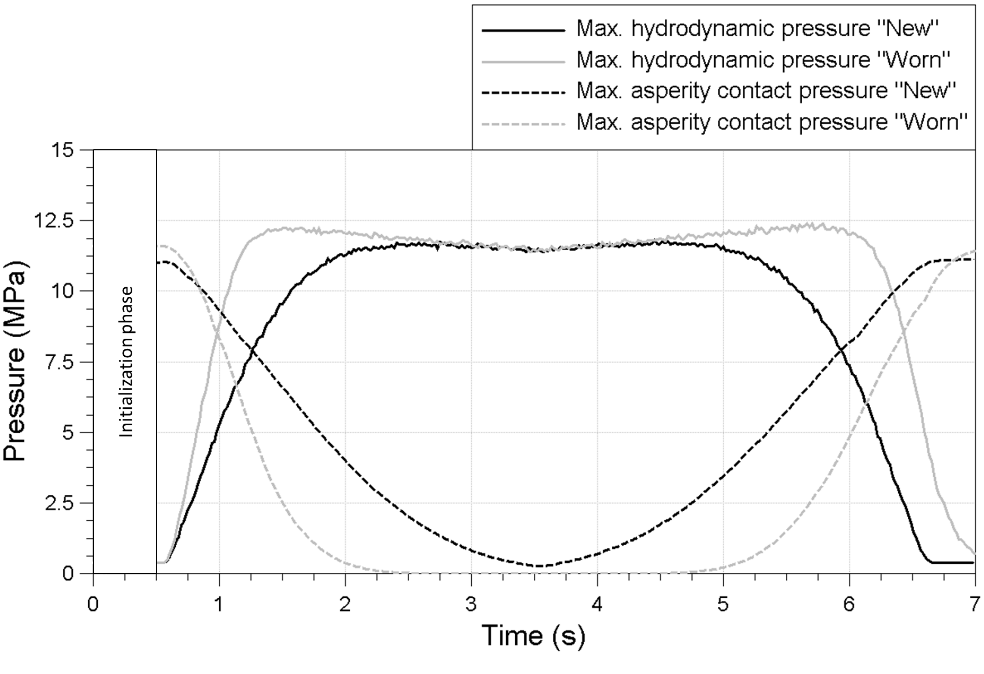

Figure 5.18: Maximum hydrodynamic and maximum asperity contact pressure during the start-stop cycle for the "new" and "worn" bearing surface, modified initialization phase for "worn" bearing surface

point, both contact models show a maximum hydrodynamic pressure of the oil supply pressure (0.4 MPa). The asperity contact pressure finds its maximum at the breakaway point. For the "worn" bearing surface, the maximum asperity contact pressure is slightly higher but when the shaft starts to rotate the contact pressure drops quicker compared to the "new" bearing surface. Accordingly to the drop of asperity contact pressure, the hydrodynamic pressure increases with increasing shaft speed. After 2 s the bearing with the "worn" bearing surface operates mainly in hydrodynamic lubrication regime. At maximum speed (at 3.5 s), both contact models predict similar hydrodynamic pressures.

The shaft stops to rotate after 6.5 s. While the maximum hydrodynamic pressure calculated with the "new" bearing surface almost reaches its minimum, there is still a noticeable hydrodynamic pressure with the "worn" bearing surface. Hence, the shaft stops to rotate before the hydrodynamic pressure completely dissolves. Furthermore, the shaft moves towards the bearing shell after it stops to rotate and pushes the lubricant out of the bearing.

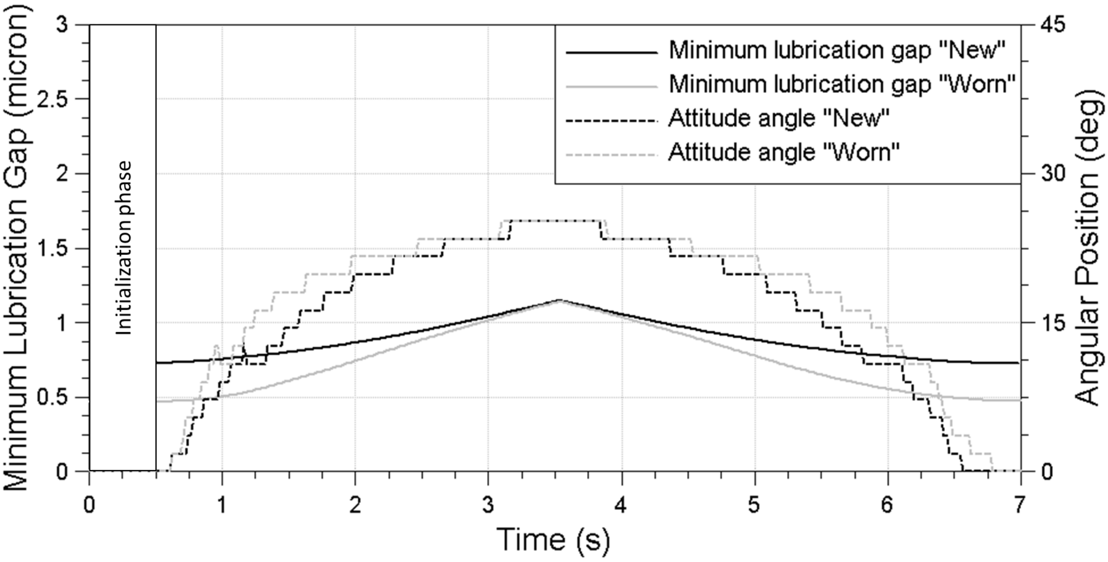

Figure 5.19: Minimum lubrication gap and angular position of the minimum lubrication gap during the start-stop cycle for the "new" and "worn" bearing surface, modified initialization phase for "worn" bearing surface

The minimum lubrication gap between shaft and test bearing shell and its angular position are shown in figure 5.19 as solid curve and dashed curve. In boundary and mixed lubrication regime, a clear reduction in minimum lubrication gap can be identified for the "worn" bearing surface. With increasing speed, the minimum lubrication gap rises. At 3.5 s when both contact models identify mainly hydrodynamic lubrication, the lubrication gap becomes identical. Entering mixed lubrication, the "worn" bearing surface calculates a smaller lubrication gap.

The position of the minimum lubrication gap (attitude angle) differs slightly during the run-up and the slow-down. The "worn" bearing surface shows a larger attitude angle than the "new" bearing surface. However, a different attitude angle is notable when the shaft stops to rotate. While the stop position for the "new" bearing surface is close to the top bearing position, the "worn" bearing surface still shows an attitude angle of 6°. After the shaft stops to rotate, it moves down to its resting position which is the top bearing position.

Friction power loss and friction work is shown in figure 5.20 to evaluate efficiency benefits. The solid curve shows the friction power loss as a sum of all three bearings. As long as there is no relative speed between shaft and bearing, the friction power loss is equal to zero. The friction power loss increases quickly to its maximum when the shaft begins to rotate. The maximum occurs in the mixed lubrication regime and is clearly higher for the "new" bearing surface. It is also shifted to a higher shaft speed. With increasing speed, the asperity contact pressure reduces and the friction power loss drops to a local minimum. While the bearing operates in hydrodynamic lubrication regime, the power

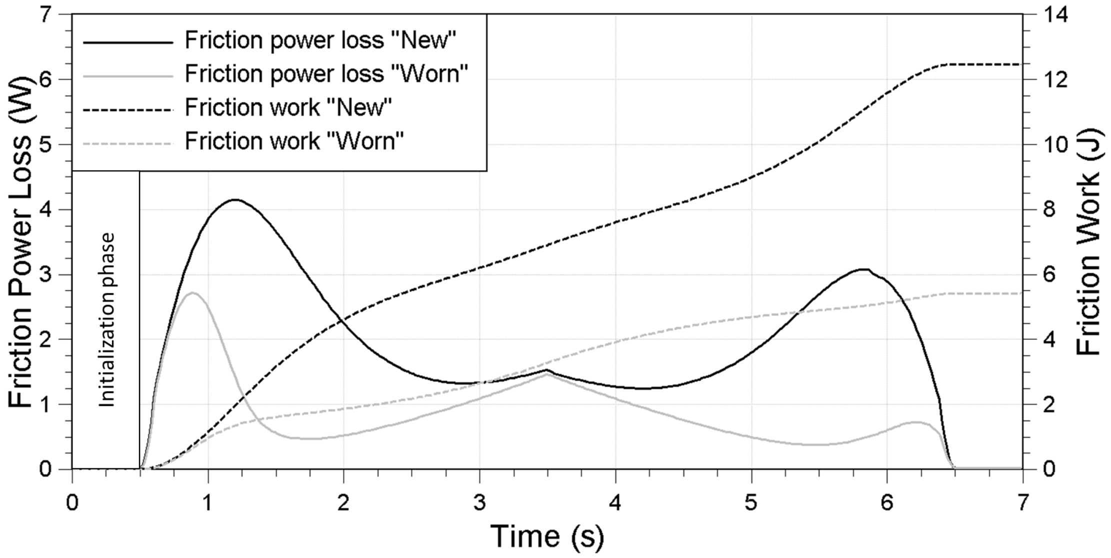

Figure 5.20: Friction power loss and friction work during the start-stop cycle for the "new" and "worn" bearing surface

loss increases with the shaft speed. A major difference can again be identified in the end of the start-stop cycle. The "worn" bearing surface does not show a distinct rise of power loss before the shaft stops to rotate.

The friction work which is done during one start-stop cycle is shown as dashed curve. The "worn" bearing surface shows a reduction from 20 J to 11 J compared to the "new" bearing surface. Hence, it can be concluded that the surface smoothing due to running-in of the bearing surface is beneficial in terms of friction reduction.

5.4.7 Wear due to repeated starting of the shaft

The wear process due to repeated starting of the shaft is performed for the start-stop model presented in section 5.4.4. The calculation of the wear load (see equation 4.28) begins when the shaft starts to rotate and ends at the maximum speed. The iterative adaption of the surface geometry (surface profile) starts with a cylindrical shape for all three bearings. The evidence and applicability of this approach was discussed in section 5.3 for dynamic loads and constant shaft rotation. In contrast, this analysis considers a constant load in combination with an accelerating shaft.

The temperature conditions are not modified to previous section. Therefore, the bearing temperatures correspond to the 3000th start-stop cycle performed on the test-rig. The surface parameter are taken from the "new" bearing surface. Temperature and contact model are not changed during the stepwise geometry adaption. The maximum wear depth $h_{w,max}$ (see equation 4.27) for one stepwise adaption is set to 0.2 μm. The sensitivity of the chosen maximum wear depth is discussed in the end of this section. The analysis is performed for all three bearings. However, the presented results focus on the test bearing because it is exposed to more wear compared to the support bearings.

The duration of the initialization phase is set to two seconds to ensure a static resting position when the shaft starts to rotate. The following results show that the shaft requires more time to reach the resting position when a worn geometry develops.

Maximum metal-metal contact pressure occurs when the shaft rests as it was shown in previous section 5.4.4 (see figure 5.13). For the test bearing, the contact pressure has its maximum on the top position and it is nearly constant in axial direction (compare 5.11). However, wear only occurs when the two contact surfaces have a relative velocity. Hence, wear develops when the shaft rotates. The maximum asperity contact pressure decreases with higher shaft speed. According to this, the maximum wear load occurs when product of sliding velocity and asperity contact pressure becomes a maximum.

The position of the maximum asperity contact pressure moves in circumferential direction as soon as the hydrodynamic pressure forms. The asymmetric hydrodynamic pressure distribution pushes the shaft in the direction of the shaft rotation. For this reason, maximum wear is expected to occur aside the top bearing position.

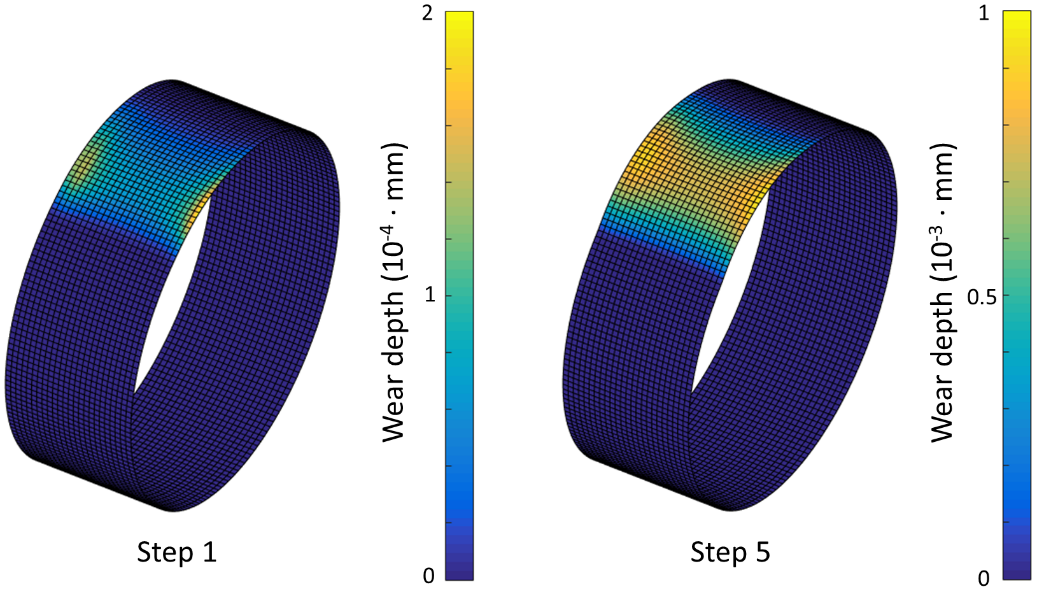

Figure 5.21: Surface geometry after the first and fifth step, the wear scar is multiplied by factor 1000 for a better illustration, mind the different color scale

Figure 5.21 shows the surface geometry after the first step on the left and after five steps on the right. The wear depth is proportional to the wear load according to Archard's wear equation. After the first step, the maximum wear depth develops at the bearing edges. The wear depth slightly reduces in axial direction towards the center of the bearing. On the one hand, this is caused by the elastic bending of the shaft which causes edge loading. On the other hand, a higher hydrodynamic pressure develops in the center of the bearing which increases the oil film thickness.

After five steps, the maximum wear depth accumulates to 1 μm at the bearing edges. At the center line of the bearing, the maximum wear is slightly lower with a maximum of 0.8 μm. However, the maximum wear depth at the center as well as at the bearing edge occurs at the same circumferential position. The circumferential position of the maximum wear depth can be seen in figure 5.22 which shows the development of the wear scar in circumferential direction for various steps.

The results clearly indicate that the maximum wear depth does not appear at the top position of the bearing but is shifted in circumferential direction. More specifically, it is shifted in the direction of the shaft rotation according to the circumferential shift of maximum asperity contact pressure and minimum lubrication gap. When the shaft

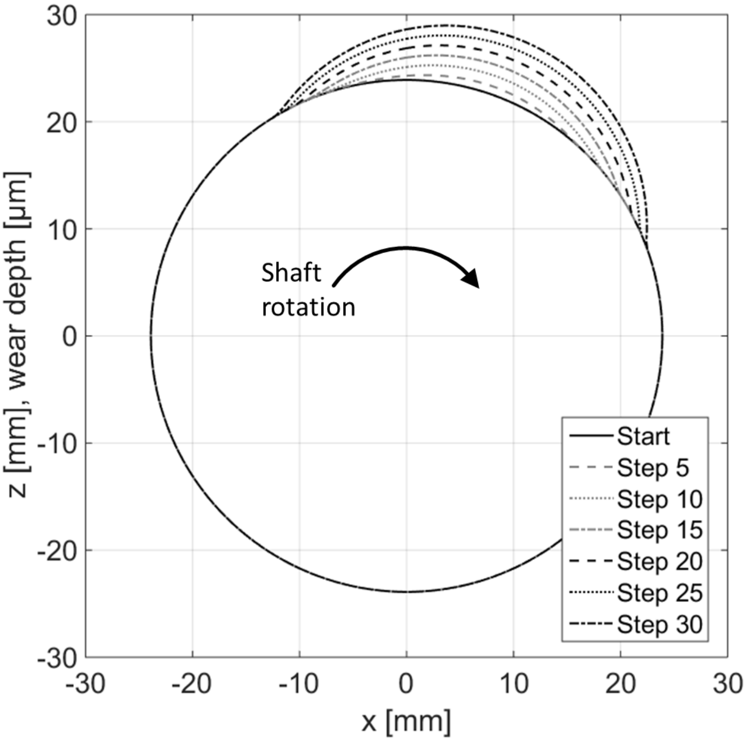

Figure 5.22: Surface contour during the wear process, the wear scar is multiplied by factor 1000 for a better illustration

begins to rotate, a lubrication wedge develops and hydrodynamic forces lift the shaft from the bearing shell. The hydrodynamic forces also push the shaft in circumferential direction due to an asymmetric pressure distribution. At maximum wear load, when the product of velocity and contact pressure becomes a maximum, the shaft has already an attitude angle. Hence, the maximum wear depth can be found at an angular position of 20° from the top position.

The results also indicate that the wear volume increases from step to step as the cross section of the wear scar increases. In other words, due to the adapted bearing geometry, more material needs to be removed from step to step to reach the defined maximum wear depth of 0.2 μm. Therefore, the wear volume which is removed during one step is calculated and shown as solid black curve in figure 5.23.

As expected, the wear volume per step has its minimum in the beginning of the wear calculation. Afterwards, the wear volume monotonically increases and becomes a maximum at the last step. The inclination of the curve increases from step to step. The steady increase is caused by the improved geometrical fit between shaft and bearing shell due to the adaption.

Not only the wear volume, but also the time to reach the defined maximum wear depth per step t_{step} (see section 4.2) changes from step to step. Therefore, the step time is calculated. Instead of evaluating the time, the number of equivalent starts is obtained by dividing t_{step} by the duration of one start phase (3 s). The black diamonds in figure 5.23 represent the number of equivalent starts which are necessary to obtain a maximum wear depth of 0.2 μm.

The lowest number of equivalent starts to reach a maximum wear depth of 0.2 μm is necessary in the beginning of the wear process because the wear load concentrates

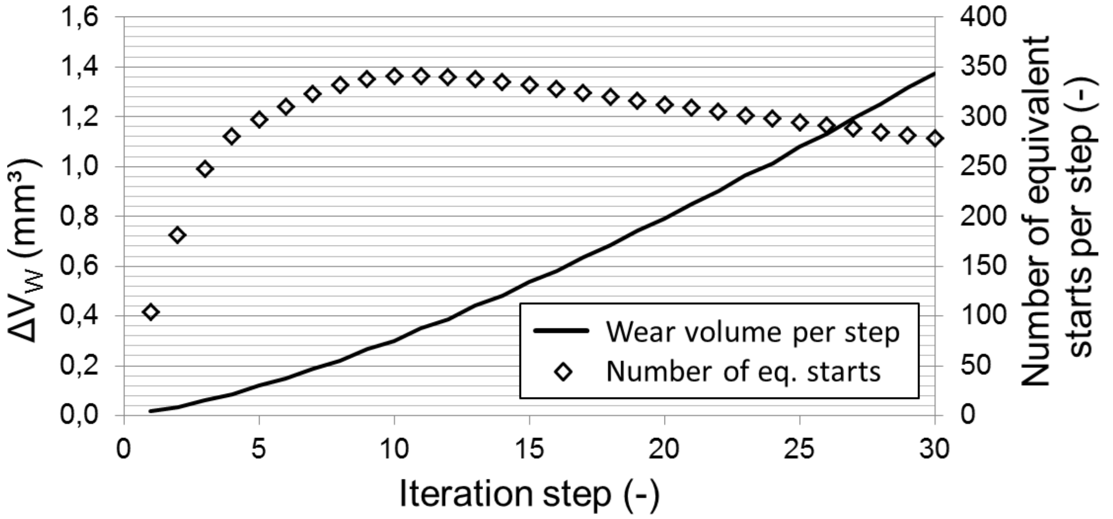

Figure 5.23: Wear volume per step and equivalent number of starts per step

on the bearing edges. Hence, the adaption takes place predominantly on the bearing edges (compare 5.21). Because of the better fit between shaft and bearing shell and the associated reduction of asperity contact pressure, the number of equivalent starts rise rapidly to a maximum after 10 iteration steps. Afterwards, the equivalent number of starts decreases constantly until the simulation process ends. This behavior is investigated in more detail below.

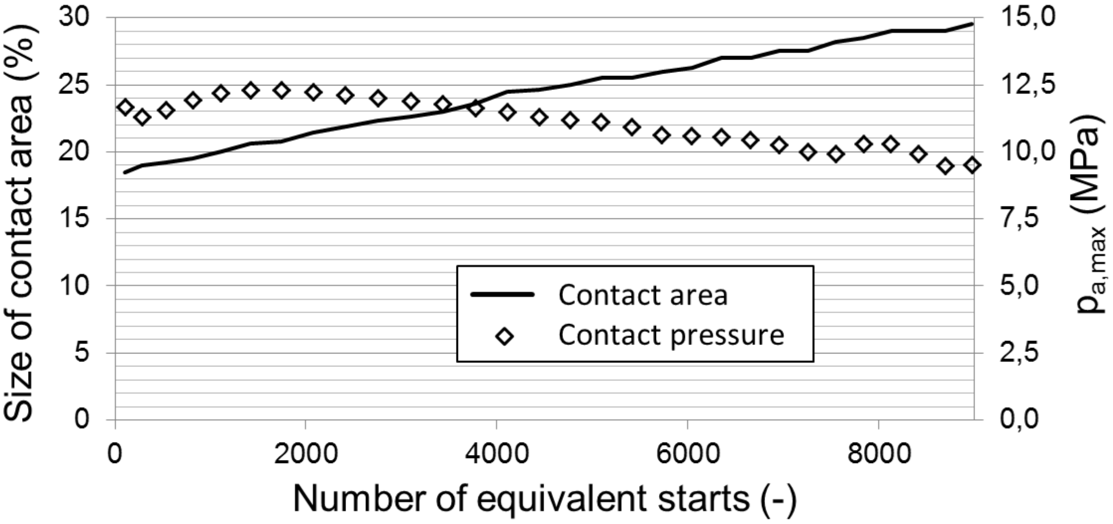

Figure 5.24: Contact area in percentage of the bearing surface and maximum asperity contact pressure both at resting position before the shaft starts to rotate

The contact area and contact pressure while the shaft is at rest, changes with the stepwise adaption of the bearing geometry. The solid black curve in figure 5.24 shows the size of the contact area related to the overall bearing surface when the shaft rests. The curve is now plotted over the number of equivalent steps. It can be seen that the contact area increases with an adaption of the shell surface geometry and reaches almost 30 % after 9000 equivalent starts. Additionally, the maximum asperity contact pressure at the resting position is presented as black diamonds. The maximum contact pressure increases slightly in the beginning and lowers after 2000 starts when the geometry adaption advances.

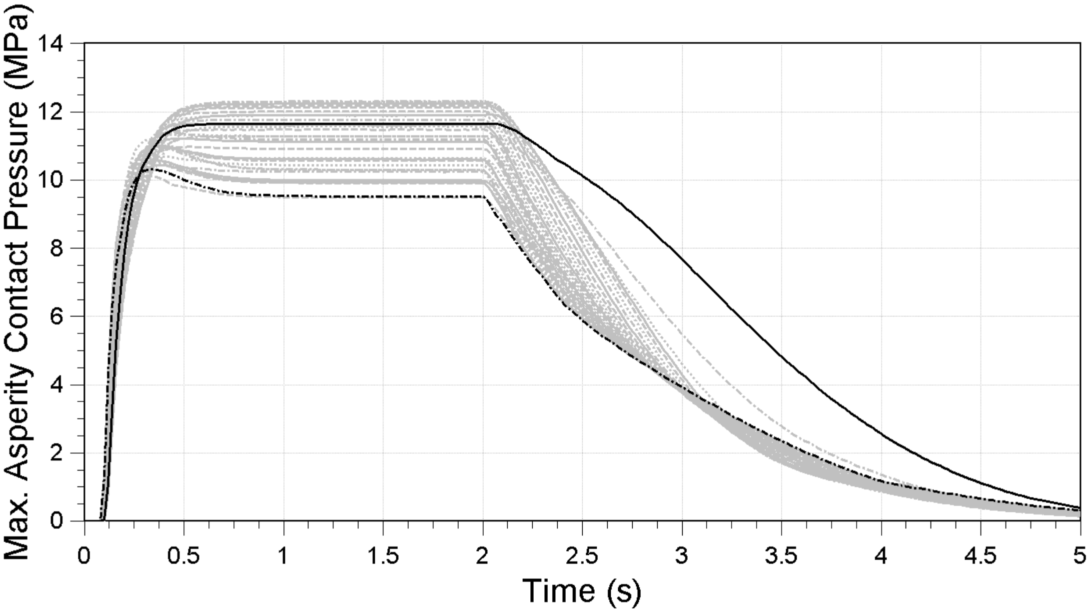

Figure 5.25: Maximum asperity contact pressure during one start cycle including the initializations time of 2 s

The maximum asperity contact pressure is also shown in figure 5.25 yet for the full start cycle. The solid black curve shows the contact pressure during the first step when the shell geometry is cylindrical. The dash-dotted black curve shows the contact pressure for the last step (step 30). The gray curves show the results of the steps in-between. The external static load is steadily increased in the first 0.1 s. The contact pressure increases with the increase of static load. A stable condition is found during the initialization phase of 2 s. After 2 s, the shaft starts to rotate and the bearing operates in mixed lubrication regime. In the first step a clearly higher maximum contact pressure occurs compared with the contact pressure calculated in the last step. This is caused by the bearing shell adaption. With the adaption of the bearing shell, the contact pressure is more equally distributed and the contact area increases. The distribution of the asperity contact pressure at resting position can be seen on the left in figure 5.26.

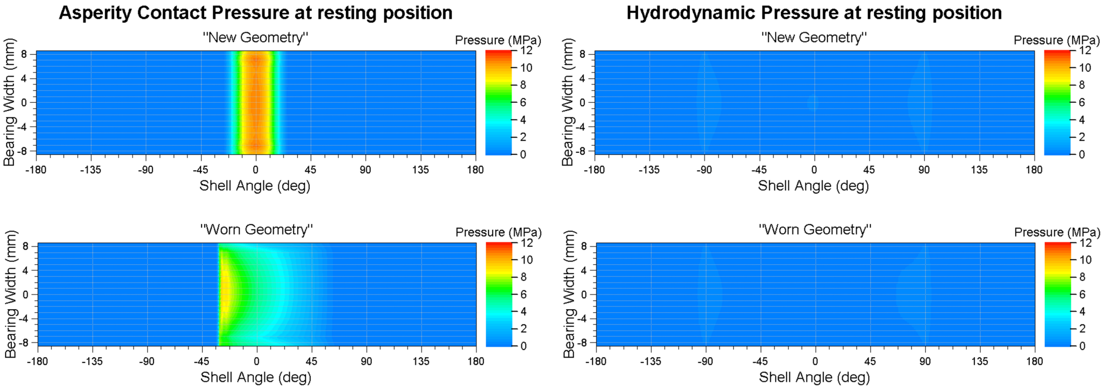

Figure 5.26: Asperity contact and hydrodynamic pressure distribution in the test bearing at 2 s for the "new" and "worn" bearing geometry

The upper figure shows the contact pressure for the ”new” bearing geometry (step 1). The maximum asperity contact pressure arises at the top position of the bearing all along the axial direction. The contact area spreads from -23° to 23°. The figure below, shows the asperity contact pressure for the last step. The magnitude of the maximum asperity contact pressure has reduced but the contact area has increased. The maximum occurs at the edge of the wear scar which is located at -35°. The contact area spreads to 65°. On the right, the hydrodynamic pressure is illustrated. A hydrodynamic pressure cannot develop because there is no relative movement between shaft and shell occurs at resting position.

After the initialization phase which lasts for two seconds, the shaft starts to rotate and the bearing enters mixed lubrication regime. The asperity contact pressure immediately drops (see figure 5.25). However, two different characteristics can be found in mixed lubrication regime. Focusing on the first second after the shaft starts to rotate (between 2 s and 3 s), the maximum asperity contact pressure reduces from step to step. In the last two seconds of the cycle, the maximum asperity contact pressure drops during the first five steps but it subsequently increases again. The reason for the first characteristic can be found in the more equally distributed contact pressure and larger contact area. Therefore, the maximum asperity contact pressure decreases. The opposed behavior in the second part is caused by a lower hydrodynamic pressure in the oil film. Figure 5.27 therefore shows the maximum hydrodynamic pressure during the start cycles.

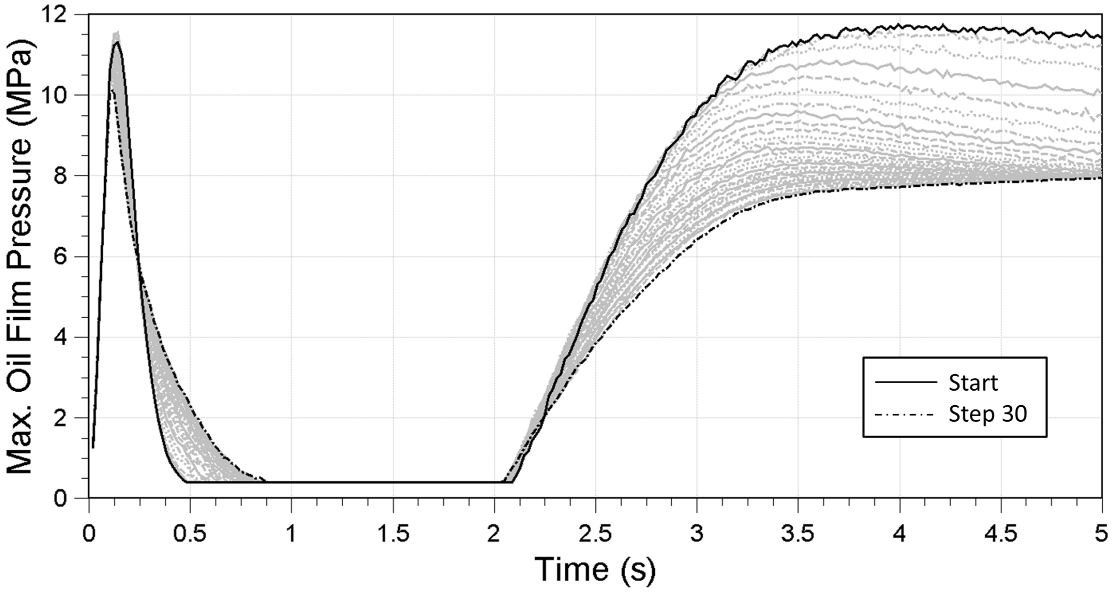

Figure 5.27: Maximum hydrodynamic pressure in the oil film during one start cycle including the initialization time of 2 s

Again, the solid and dash-dotted black curves correspond to the result of the first and last step. During the initialization phase, the hydrodynamic pressure becomes a peak when the static load is applied. After the shaft has sunken towards the bearing shell, the hydrodynamic pressure reduces to its minimum. The duration until the hydrodynamic pressure becomes a minimum, extends from step to step. However, at the end of the initialization phase, the hydrodynamic pressure is equal to the supply and ambient pressure. When the shaft starts to rotate, the hydrodynamic pressure starts to rise. The maximum hydrodynamic pressure increases within 1.5 s to its maximum. For the first step, a higher hydrodynamic pressure develops compared to the last one. The higher hydrodynamic pressure in the lubrication gap is caused by the larger geometrical gradient when the bearing has a cylindrical shape. With the adaption of the bearing surface, the geometrical gradient decreases and the geometrically caused pressure buildup is reduced. Due to the lower hydrodynamic pressure, the minimum lubrication gap between shaft and bearing is smaller. The minimum lubrication gap is shown in figure 5.28.

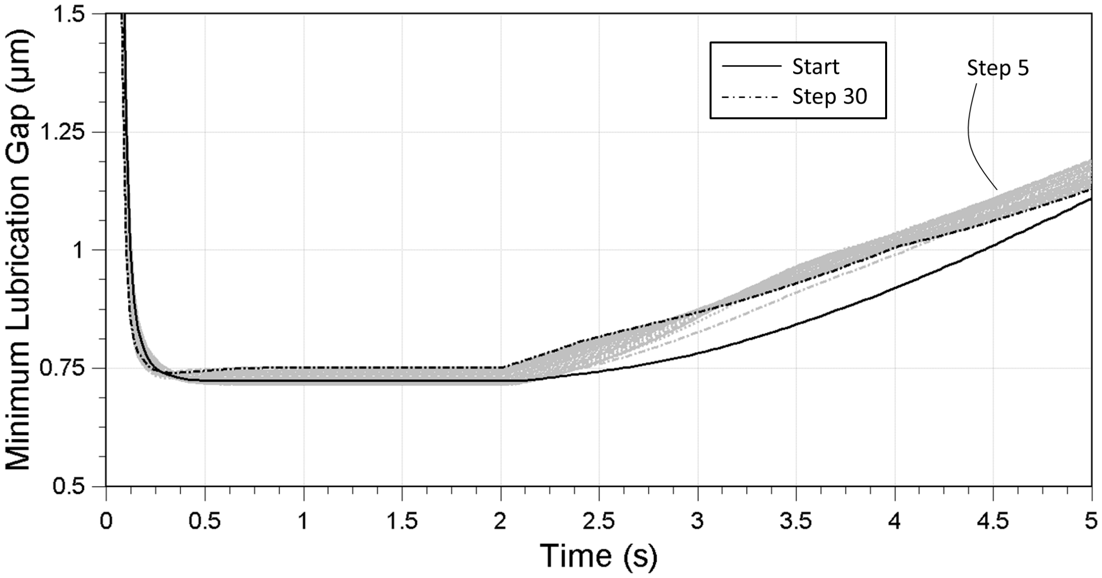

Figure 5.28: Minimum lubrication gap during one start cycle including the initialization time of 2 s

The minimum lubrication gap is reached immediately after the static load is applied to the test bearing. The different height of the lubrication gap in the resting phase is caused by the decreasing contact pressure and increasing contact area with an adaption of the bearing geometry. More interesting is the behavior in mixed lubrication regime. The solid black curve shows the minimum lubrication gap for the "new" bearing geometry. In mixed lubrication regime, it has the smallest minimum oil film thickness during the entire start cycle. The minimum lubrication gap occurs at the bearing edges and originates from shaft bending which causes edge loading. After five steps, the bearing edges are adapted (compare figure 5.21). At the fifth step, the largest minimum lubrication gap is reached in the period from 3 s to 5 s. After the fifth step, the minimum oil film thickness in the same period decreases again.

Previously in this section, the number of equivalent starts to reach the defined wear depth per step was discussed and shown in figure 5.23. The edge loading due to the elastic bending of the shaft is responsible for the increase of the number of equivalent starts during the first steps. After five to ten steps, the adapted surface particularly reduces the edge loading. From there on, the number of equivalent starts constantly decreases again. This reduction is caused by the asperity contact between 3 s and 5 s. The increasing contact pressure and contact area in mixed lubrication regime in combination with the high relative velocity between the two contacting surfaces at this condition increases the wear load.

So far, only the maxima of hydrodynamic and asperity contact pressure were discussed when the bearing operated in mixed lubrication regime. More detailed information can be obtained from the pressure distribution in the bearing at a specific time.

Figure 5.29 shows the pressure distribution in the test bearing at 3.3 s. The asperity

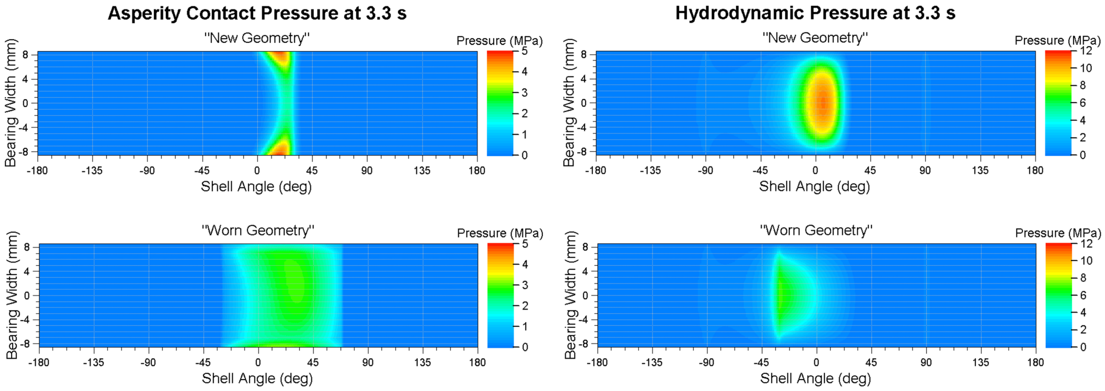

Figure 5.29: Asperity contact and hydrodynamic pressure distribution in the test bearing at 3.3 s for the "new" and "worn" bearing geometry

contact pressure is shown on the left and the hydrodynamic pressure on the right. The top graph shows the results calculated with the "new" bearing geometry. The maximum asperity contact pressure with 5 MPa develops at the bearing edges. This is caused by the elastic bending of the shaft. Towards the center of the bearing, the contact pressure decreases to 2 MPa. The asperity contact pressure appears as a line contact which spreads between 0° and 35° from the top position. The hydrodynamic pressure has a maximum of 12 MPa which occurs in the center of the bearing.

The results calculated with the "worn" bearing geometry show a different behavior. The maximum asperity contact pressure has a magnitude of 3 MPa. But the asperity contact pressure is equally distributed on a large area of the bearing. The contact area reaches from -35° to 70°. It can also be seen that the hydrodynamic pressure is much lower compared to the results calculated with the "new" bearing geometry. The hydrodynamic pressure is formed by the geometrical gradient of the lubrication gap. This gradient is lower for the adapted "worn" bearing geometry.

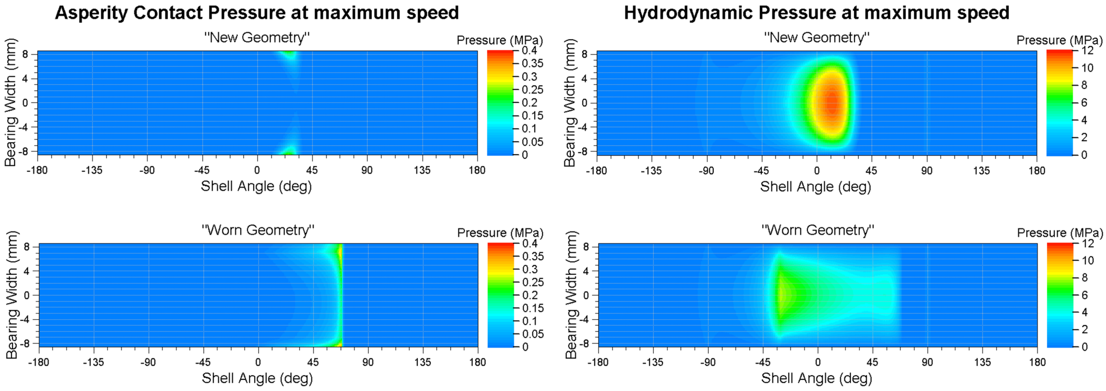

Figure 5.30: Asperity contact and hydrodynamic pressure distribution in the test bearing at maximum speed (5 s) for the "new" and "worn" bearing geometry

At 5 s, the maximum speed of 260 rpm is reached. At this speed, the static load is mainly carried by the hydrodynamic pressure in the oil film. Due to the adapted bearing geometry, a different hydrodynamic pressure distribution can be identified (see figure 5.30). The hydrodynamic pressure distribution with the "new" bearing geometry concentrates on the top position of the bearing and reaches a maximum of 12 MPa. The hydrodynamic pressure distribution with the "worn" bearing geometry is more evenly distributed and has a lower maximum of 8 MPa. Again, this is caused by the lower geometrical gradient in the lubrication gap.

At maximum speed, the asperity contact pressure reduces to a maximum of 0.4 MPa. For the "new" bearing geometry, the asperity contact dominantly occurs at the bearing edges. The asperity contact pressure with the "worn" geometry occurs along the axial direction at the edge of the wear scar and appears as a line contact.

Orbital path of the shaft center in the journal bearing

Beside the hydrodynamic and asperity contact pressure, the movement of the shaft in journal bearing is of interest. The orbital path of the journal (shaft) is therefore shown in figure 5.31.

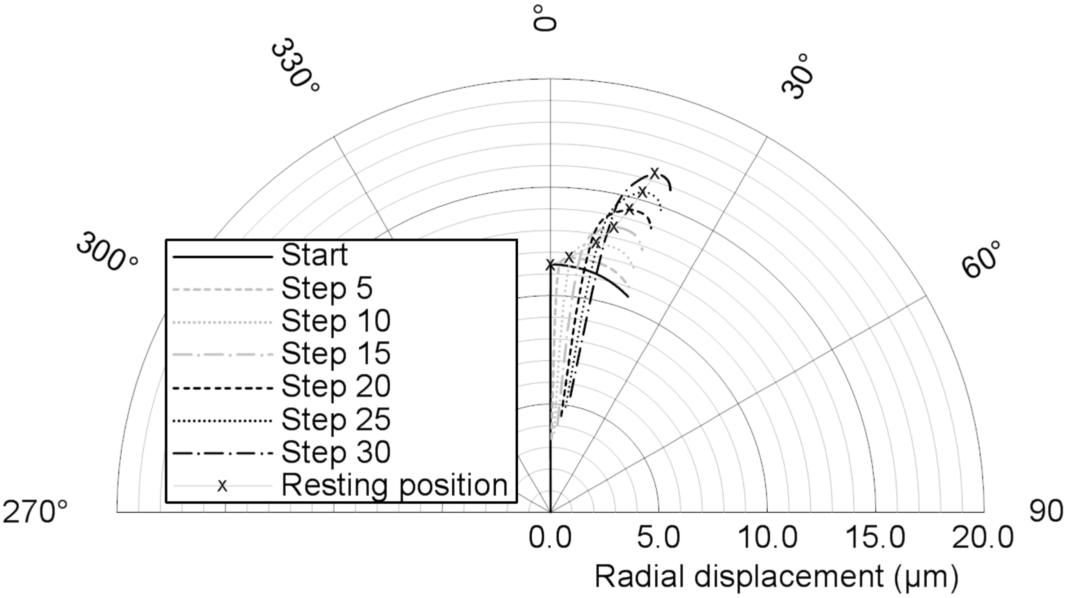

Figure 5.31: Orbital path of the shaft center in the bearing during the start cycle

The solid black curve shows the journal movement in the bearing shell with a perfect cylindrical shape. The journal moves towards the top bearing position during the initialization phase when the static load is steadily increased. The resting position of the shaft is marked with a black X. The radial displacement of the shaft is exactly 11.5 μm which corresponds to radial clearance of the bearing. When the shaft starts to rotate, the hydrodynamic pressure develops and lifts the journal. Hence, the radial displacement decreases. The hydrodynamic pressure additionally pushes the bearing in the direction of shaft rotation (horizontal). The maximum attitude angle occurs at maximum speed.

The dashed gray curve (step 5) represents the loci of the journal in a "worn" bearing shell. The maximum wear depth is about 1 μm (5 steps multiplied with the defined maximum wear depth of 0.2 μm) and occurs at the bearing edges. During the initialization phase, the shaft is pushed against the bearing shell. The pressure distribution which is caused by the squeezing motion is not symmetrically anymore because of the wear scar. Therefore, the journal is pushed in horizontal direction. When the journal gets in contact with bearing shell, an additional force caused by metal-metal pushes the journal away from the bearing top position. The resting position of the journal is again marked with a black X. The shaft starts to rotate and is again lifted and pushed in direction of shaft rotation. The maximum attitude angle is similar to the attitude angle calculated with the initial bearing geometry.

Further curves represent the orbital path of the journal for various wear calculation steps. It can be seen that the resting position of the shaft moves to a larger attitude angle. After 30 steps (9000 equivalent starts), the attitude angle of the resting position is about 16° from the top position. After the breakaway, the radial displacement of the shaft increases and seems to move towards the bearing shell. The reason for this behavior is that the maximum wear depth occurs at an angular position of 20°. Hence, the lubrication gap automatically increases when the shaft starts to rotate as it is pushed in the direction of shaft rotation. The hydrodynamic pressure has not fully separated the contact surfaces. Hence, the shaft moves towards the bearing shell and the radial displacement increases. However, the attitude angle at maximum speed remains unchanged during the surface geometry adaption.

Friction torque during the iterative wear process

The different behavior of the hydrodynamic journal bearing during the wear process affects the journal bearing friction. For this reason, the friction torque is plotted during the start cycle in figure 5.32.

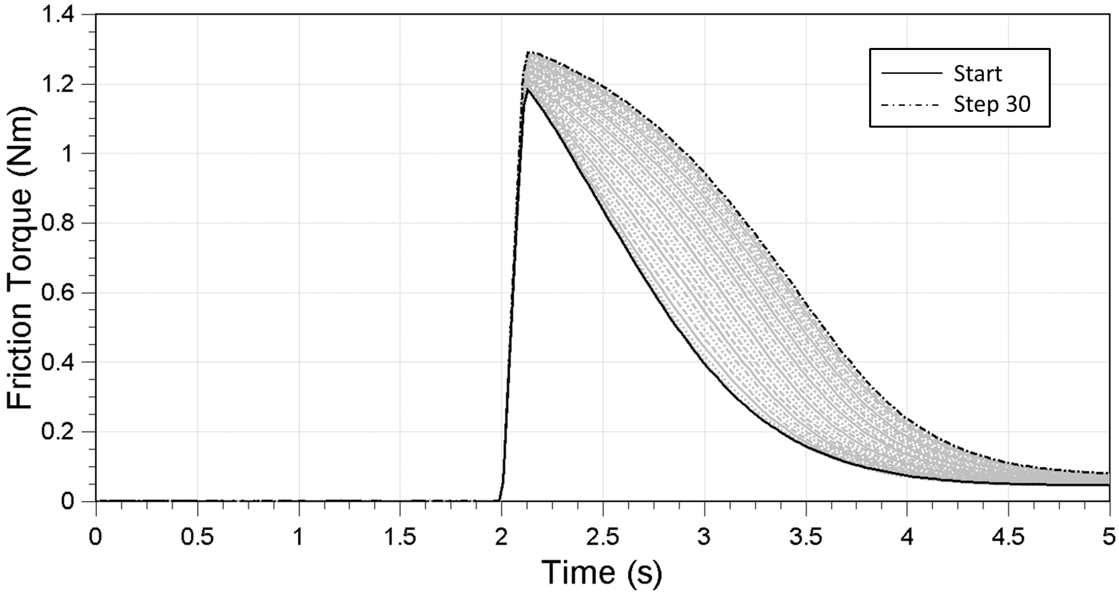

Figure 5.32: Friction torque in the test bearing during one start cycle including the initialization time of 2 s

The solid black curve shows the friction torque in the test bearing for a "new" bearing geometry. The dash-dotted curve represents the friction torque calculated with the "worn" bearing geometry after 30 steps. The gray curves correspond to the steps in between. The breakaway torque increases from 1.2 Nm to 1.3 Nm from the first to the last step. This behavior is caused by the quicker buildup of the hydrodynamic pressure for a new journal bearing because of the geometrical gradient in the lubrication gap. However, the main difference can be identified in mixed lubrication regime. The friction torque increases from step to step and also the transition to pure hydrodynamic lubrication is shifted to higher shaft speed. The increased contact area and the increased asperity contact pressure (between 3 s and 5 s) are responsible for the rise of friction losses. In summary, the adaption of the bearing geometry increases the friction torque.

Final wear scar for all three journal bearings

So far, only the test bearing behavior was analyzed during the wear process. However, the wear calculation is performed for all three bearings. The final wear scar after 9000 equivalent starts of the shaft is shown in figure 5.33.

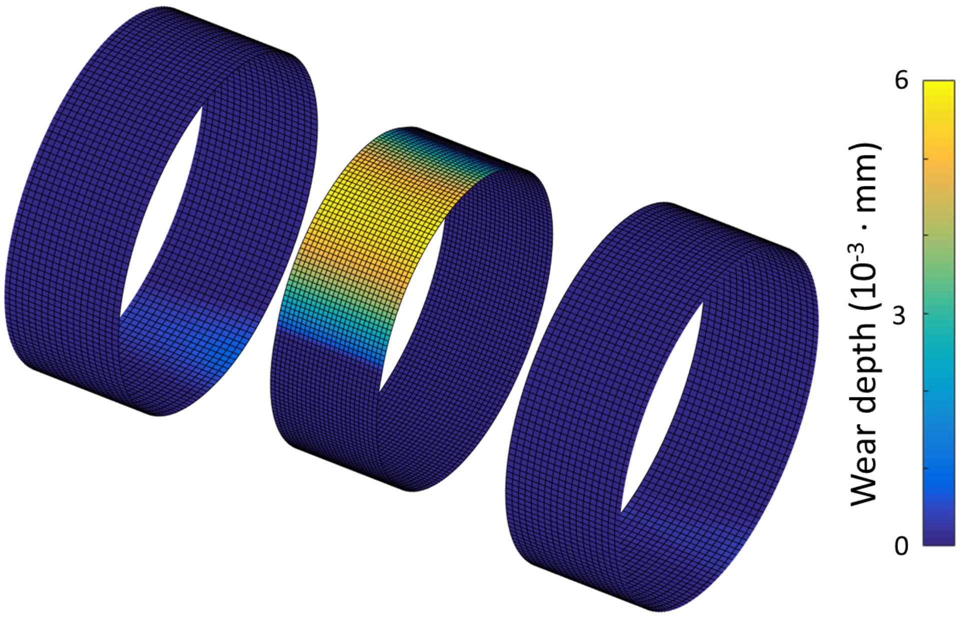

Figure 5.33: Surface profile at the end of the wear process after 9000 equivalent starts, the wear scar is multiplied by a factor of 200 for a better illustration

First of all, it can be clearly identified that the central test bearing shows more wear than the two support bearings. Due to the symmetrical setup of the test-rig and the corresponding simulation model, the static load is equally distributed onto the two support bearings and is therefore only half the load of the test bearing. Additionally, the dimensions of the support bearings are larger compared to the dimensions of test bearing which leads to a lower specific bearing load.

The test bearing shows a maximum wear depth of 5.8 μm at both bearing edges. The wear depth at the center of the test bearing is only 0.1 μm below the maximum wear depth. The support bearing one and the support bearing two have a maximum wear depth of 1.5 μm and 0.9 μm.

Variation of maximum wear depth per step size

The maximum wear depth per step $h_{\mathrm{w,max}}$ is set to 0.2 μm as mentioned in the beginning of section 5.4.7. The maximum wear depth is chosen from practical and numerical reason. First, if the step size is smaller, a larger number of steps are needed to achieve a final result. A larger number of calculations consequently increase the calculation time. Second, if the maximum wear depth is selected too great, it is possible that the wear profile contains sharp edges. These sharp edges may produce an abrupt local increase of asperity contact pressure. This will then also lead to a high local wear load and to sharp edges in the worn geometry. Hence, the numerical stability is not guaranteed anymore.

To prove the use of the chosen maximum wear depth, an additional wear calculation is performed with a smaller maximum wear depth. Therefore, the maximum wear depth is set to 0.1 μm. Instead of calculating 60 steps, two steps are executed which also results in an accumulated maximum wear depth of 0.2 μm. This newly calculated surface geometry is then compared and verified with the surface geometry from previous results.

The basis for the investigation is the "worn" surface geometry from the fifth step which was calculated previously. Two steps are now calculated with the reduced maximum wear depth and the results are compared to the sixth step from the previous results. The results are summarized in figure 5.34 which shows the relative wear depth over the bearing angle related to the fifth step.

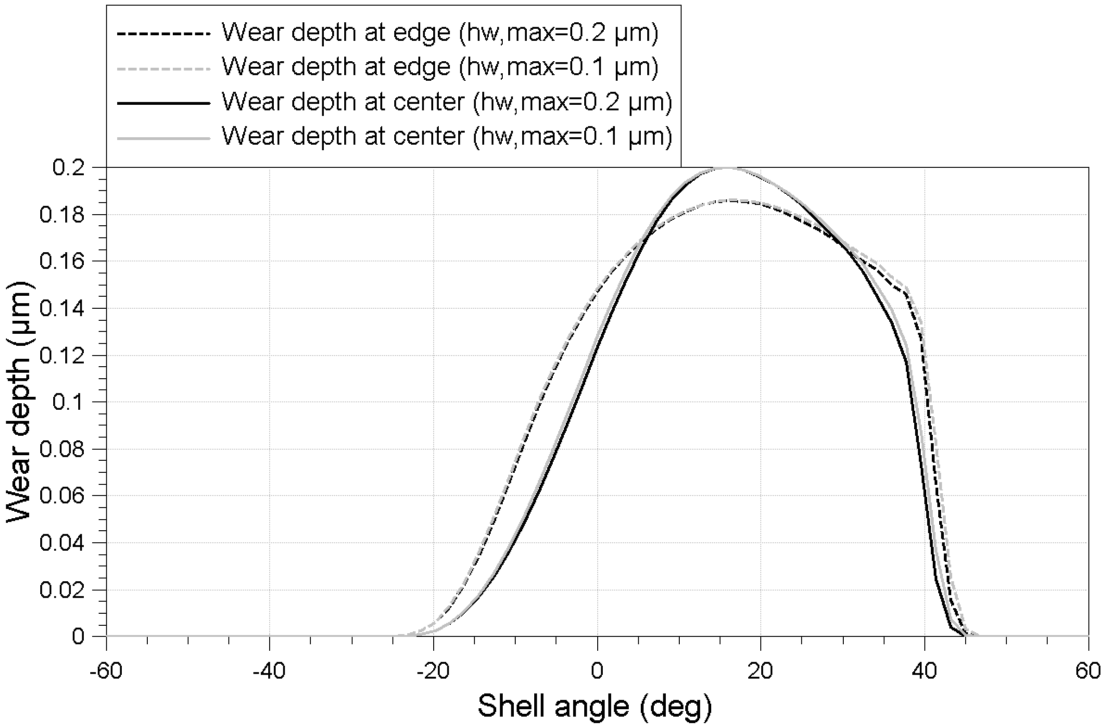

Figure 5.34: Relative wear depth over the bearing angle. The calculated bearing geometry after five steps represents the reference

The black curves represent the relative wear calculated with a defined maximum wear depth of 0.2 μm. The gray curves show the accumulated relative wear for the reduced maximum wear depth. At the center of the bearing (solid curve) and at the bearing edge (dashed curve), both curves show identical characteristics. Both wear depths have the same wear peak of 0.2 μm at the center of the bearing. A minimal difference can be identified at the end of the wear scar between 35° and 45°. The maximum variation in this region between the two curves is below 5 %. Therefore, it can be concluded that the maximum wear depth during one step is chosen appropriately.

5.4.8 Effect of shell geometry adaption due to wear on friction

The simulation results of the ″new″ and the ″worn″ bearing geometry for the entire start-stop cycle are compared to each other in this section. The ″new″ bearing geometry considers a cylindrical shape of the bearing shell, while the ″worn″ bearing geometry includes the wear profile which was calculated in section 5.4.7. The geometry of the ″worn″ bearing geometry is shown in figure 5.33. The parameters of the contact model remain unchanged and represent a ″new″ bearing surface (see section 5.4.6). The evaluation focuses on the behavior of the bearing during starting and stopping and on the friction losses.

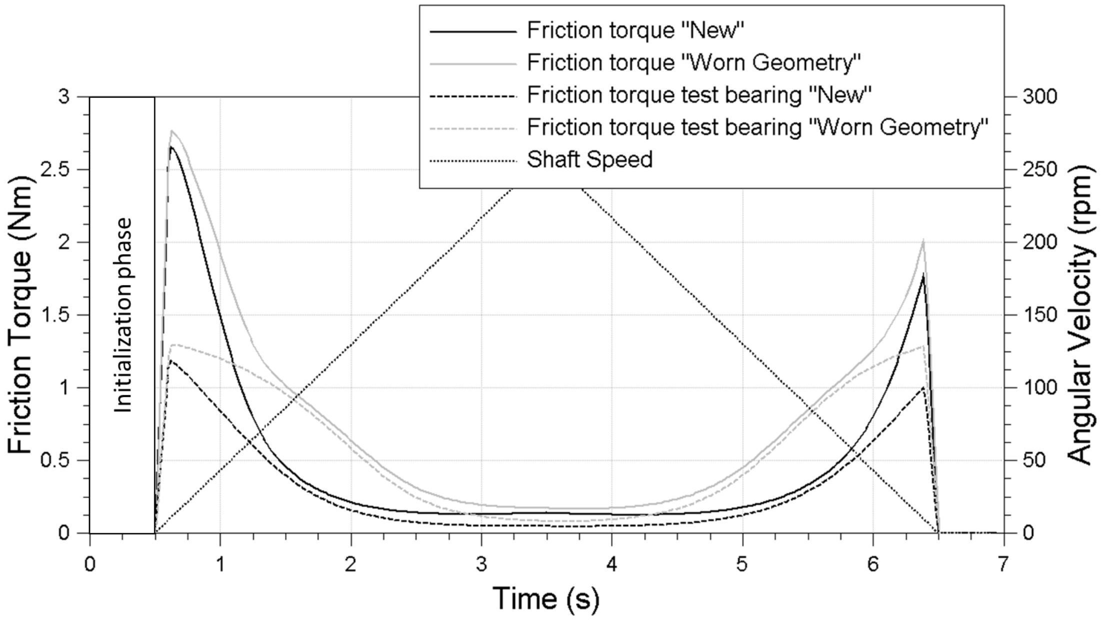

Figure 5.35: Calculated overall friction torque during the start-stop cycle for the ″new″ and ″worn″ bearing geometry

Figure 5.35 shows the calculated friction torque during one start-stop cycle. The solid black curve represents the ″new″ bearing geometry and the solid gray curve the ″worn″ bearing geometry. The dotted black curve shows the angular velocity of the shaft. The torque abruptly rises when the shaft starts to rotate. The magnitude of the breakaway torque is similar for the ″new″ and ″worn″ bearing geometry. At this time, the load is mainly supported by asperity contact pressure.

In mixed lubrication regime, the friction torque calculated with the ″worn″ bearing geometry is clearly higher compared to the ″new″ bearing geometry. This change is primarily caused by the test bearing which is shown as dashed curve for both geometries. The results of the test bearing are described in detail in section 5.4.7. However, at maximum speed, after 3.5 s, the friction torque has its minimum and is slightly higher for the ″worn″ bearing geometry. The behavior when the shaft decelerates is similar to the behavior during the run-up. Again, the ″worn″ bearing geometry shows a higher friction torque in mixed lubrication regime. At the end of the start-stop cycle, the friction torque strongly increases but the stopping torque is below the breakaway torque. This is caused by a remaining hydrodynamic pressure due to squeezing effect when the shaft moves towards the bearing shell.

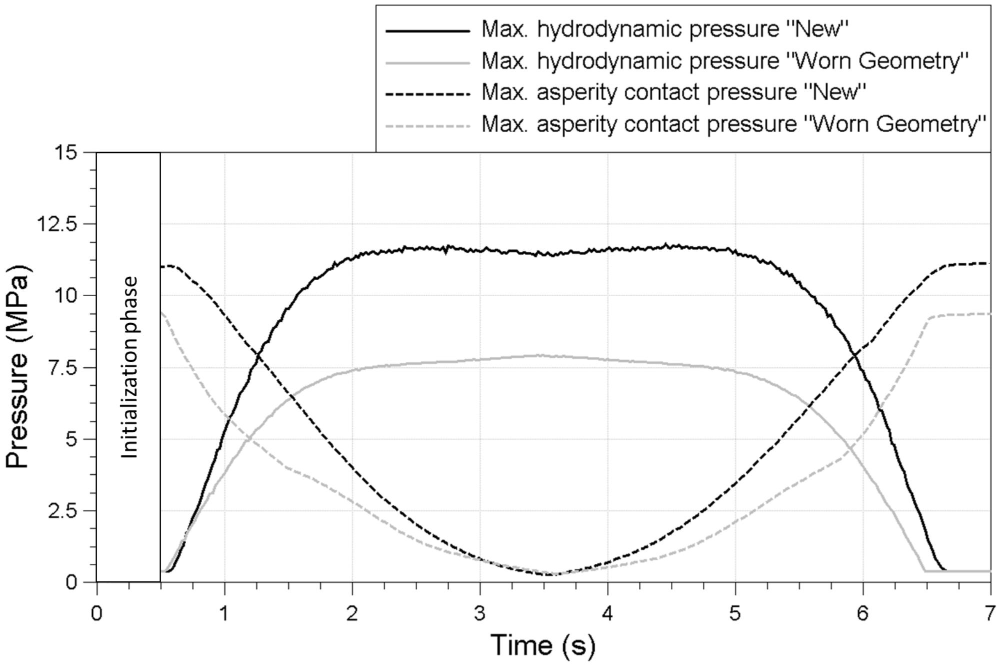

Figure 5.36: Maximum hydrodynamic and maximum asperity contact pressure in the test bearing during the start-stop cycle for the "new" and "worn" bearing geometry, modified initialization phase for "worn" bearing geometry

The maximum hydrodynamic pressure which occurs in the test bearing during one start-stop cycle, is shown as solid black curve and solid gray curve in figure 5.36. The corresponding maximum asperity contact pressure is shown as dashed curves. The maximum asperity contact pressure has its maximum at the beginning and at the end of the start-stop cycle. After the shaft starts to rotate, the asperity contact pressure drops until it reaches its minimum at 3.5 s. During the stopping of the shaft, an opposing behavior can be seen. The most significant difference between the two models can be identified at the resting position and in mixed lubrication regime. The maximum asperity contact pressure is lower for the "worn" bearing geometry. At maximum speed, both models show a similar maximum contact pressure.

The hydrodynamic pressure has its minimum when the shaft rests. It increases as soon as the shaft starts to rotate. After two seconds, an almost constant maximum hydrodynamic pressure develops. The hydrodynamic pressure drops again when the shaft slows down. There still exists a hydrodynamic pressure when the shaft stops to rotate. This is caused by the squeezing effect.

Finally, figure 5.37 presents the friction power loss during one start-stop cycle for the "new" (solid black curve) and "worn" (solid gray curve) bearing geometry. The friction power loss reaches a maximum, when the product of friction torque and shaft speed also becomes a maximum. Hence, the maximum friction power loss occurs in mixed lubrication regime. As the friction torque is higher for the "worn" bearing geometry, a higher friction power loss occurs. The maximum friction power loss is slightly shifted to a higher shaft speed compared to the "new" bearing geometry. The behavior during the slowdown is similar to the starting of the shaft.

The friction work which has to be overcome during one start-stop cycle can be evaluated by integrating the friction power loss over time. The "worn" bearing geometry shows a friction work of 28 J which is 2.3 times higher than the friction work with a "new"

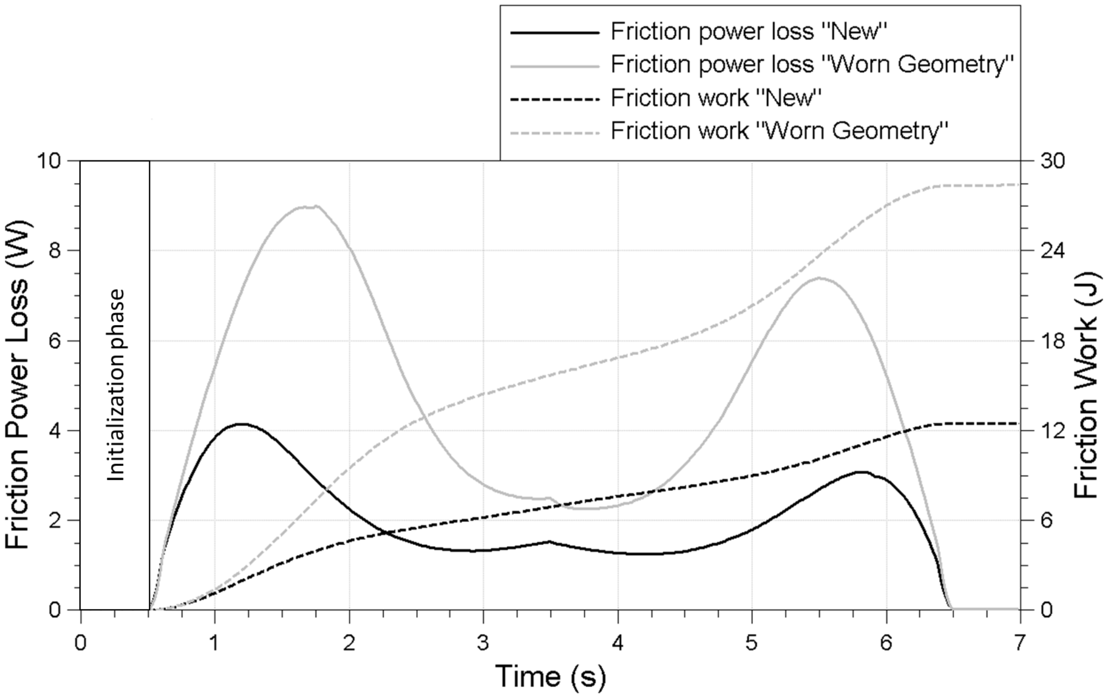

Figure 5.37: Friction power loss and friction work during the start-stop cycle for the "new" and "worn" bearing geometry

bearing geometry. It can be concluded that the friction losses during the start-stop cycle increase when the bearing shell adapts its geometry.

5.4.9 Conclusion

This section focuses on journal bearing behavior during starting and stopping of the shaft. Bearing tests under static loading are performed on the journal bearing test-rig. 6000 start-stop cycles are carried out. Each test cycle contains a starting, a stopping and a resting phase. The test duration of each phase is 3 seconds. Therefore a complete cycle last for 9 seconds.

Furthermore, a simulation model is set up in accordance with the journal bearing tests which allows the shaft to rest, accelerate and decelerate again until the shaft stops. The simulation focuses on the starting and stopping behavior of the bearing and therefore, the resting phase is omitted from the calculation as soon as a static position is reached. Therefore, the complete simulation cycle last for 7 seconds instead of 9 seconds. The journal bearing simulation is computed in time domain.

Bearing temperature, oil flow and friction torque are evaluated from the experimental results. Both, temperature and oil flow increase during the first 1000 start-stop cycles and stay constant during further cycles. The friction torque shows a peak when the shaft starts to rotate (breakaway torque). Immediately afterwards, the bearings enter mixed lubrication regime and the friction torque drops. At maximum speed, the bearings operate in hydrodynamic lubrication regime. Therefore, all lubrication regimes are examined in this study. Additionally, the trend of the breakaway torque over the number of start-stop cycles is analyzed. The breakaway torque shows a continuously decreasing magnitude. It drops from 21.5 Nm below 2 Nm after 6000 cycles.

The existing simulation model of the test-rig which is described in section 4.4 is modified to analyze the start-stop behavior. An essential part of the modification is the initialization phase. During the first period, the shaft does not rotate and the external static load is applied to the bearing. As a consequence, the shaft moves towards the bearing shell and comes to rest before the shaft starts to rotate. The initialization phase enables a start behavior in which the shaft is mainly supported by metal-metal contact.

With the simulation approach, a complete start-stop cycle is performed and the results are further compared to the measurement results. The calculated torque shows an analog behavior to the measured friction torque. The breakaway torque shows a good agreement as well as the friction drop in mixed lubrication regime. The simulation allows a further breakdown of the overall friction torque into the friction torque of the individual bearings. The largest share of friction is assigned to the test bearing because it operates in mixed lubrication regime over a longer period. Additionally, the shaft movement in the bearing is investigated.

The simulation model is further used to analyze the influence of surface smoothing due to running-in on the start-stop behavior of journal bearings. Therefore, a worn bearing surface is scanned and the parameters for the contact model are evaluated. A full start-stop cycle is simulated. The result show an identical breakaway torque compared to the new bearing surface but friction in mixed lubrication regime clearly decreases. A major difference can be identified at the end of the stop cycle when the shaft stops to rotate. The stopping friction torque reduces to one third compared to the new bearing surface. The work needed to overcome friction during the start-stop cycle is reduced to 50 % for the smoother bearing surface.

All three bearings operate in boundary and mixed lubrication regime. Hence, wear occurs and the bearing geometry changes. An iterative wear analysis is performed to obtain a worn bearing geometry. Altogether, an equivalent number of 9000 starts are calculated and a final wear geometry with a maximum wear depth of 5.8 μm is generated for the test bearing. The circumferential position of the maximum wear depth is shifted by 20° in the direction of shaft rotation. The final wear scar in the test bearing appears all along the bearing width and reaches from -35° to 70° in circumferential direction from the bearing top position.

Results calculated with the worn bearing geometry show that the friction torque increases in mixed lubrication regime. This is mainly caused by the lower hydrodynamic pressure in the oil film which leads to a smaller lubrication gap at higher shaft speeds. Consequently, the area of metal-metal contact increases and a drastic increase for the friction work during a complete start-stop cycle occurs. The friction work is 2.3 times higher than the friction work with the initial bearing geometry.

The shaft movement in the bearing is analyzed during the iterative wear calculation. It is found that the shaft resting position before the shaft starts to rotate, moves in circumferential direction. It moves into the direction of the shaft rotation. The asymmetric wear scar is responsible for this behavior.

Furthermore, the wear load increases after an initial adaption of the surface geometry. In other words, the number of starts to create certain wear depth decreases from step to step. This reduction is also caused by the increased metal-metal contact at high shaft speed.

Finally, the numerical stability of the stepwise adaption of the shell geometry is evidenced by changing the maximum wear depth per step. The sensitivity of this parameter is small and therefore, it can be concluded that the maximum wear depth is chosen appropriately.

Bibliography

[1] Allmaier, H., Priestner, C., Reich, F. M., Priebsch, H. H., and Novotny-Farkas, F. Predicting friction reliably and accurately in journal bearings—Extending the ehd simulation model to tehd. *Tribology International 58* (2013), 20–28.

[2] Allmaier, H., Priestner, C., Six, C., Priebsch, H. H., Forstner, C., and Novotny-Farkas, F. Predicting friction reliably and accurately in journal bearings—A systematic validation of simulation results with experimental measurements. *Tribology International 44*, 10 (2011), 1151–1160.

[3] Allmaier, H., Sander, D. E., Priebsch, H. H., Witt, M., Füllenbach, T., and Skiadas, A. Non-Newtonian and running-in wear effects in journal bearings operating under mixed lubrication. *Proceedings of the Institution of Mechanical Engineers, Part J: Journal of Engineering Tribology 230*, 2 (2016), 135–142.

[4] Archard, J. Contact and rubbing of flat surfaces. *Journal of Applied Physics 24*, 8 (1953), 981–988.

[5] AVL List GmbH. *Excite Power Unit v2014 - Theory*. AVL, Graz, 2014.

[6] Bair, S. S. *High Pressure Rheology for Quantitative Elastohydrodynamics*. Elsevier, Amsterdam, 2007.

[7] Bartel, D. *Simulation von Tribosystemen*. Vieweg+Teubner, Wiesbaden, 2010.

[8] Bartels, T., Bock, W., Braun, J., Busch, C., Buss, W., Dresel, W., Freiler, C., Harperscheid, M., Heckler, R.-P., Hörner, D., et al. Lubricants and Lubrication. *Ullmann's Encyclopedia of Industrial Chemistry* (2005).

[9] Barus, C. Isothermals, isopiestics and isometrics relative to viscosity. *American Journal of Science*, 266 (1893), 87–96.

[10] Bishop, J., Nedungadi, A., Ostrowski, G., Surampudi, B., Armiroli, P., and Taspinar, E. An engine start/stop system for improved fuel economy. *SAE Technical Paper* (2007).

[11] Blau, P. J. On the nature of running-in. *Tribology International 38*, 11 (2006), 1007–1012.

[12] Boncompain, R., Fillon, M., and Frene, J. Analysis of thermal effects in hydrodynamic bearings. *Journal of Tribology 108*, 2 (1986), 219–224.

[13] Bonneau, D., Fatu, A., and Souchet, D. *Hydrodynamic Bearings*. ISTE, London and John Wiley & Sons, New York, 2014.

[14] Bonneau, D., Fatu, A., and Souchet, D. *Internal Combustion Engine Bearings Lubrication in Hydrodynamic Bearings*. ISTE, London and John Wiley & Sons, New York, 2014.

[15] Bonneau, D., Fatu, A., and Souchet, D. *Mixed Lubrication in Hydrodynamic Bearings*. ISTE, London and John Wiley & Sons, New York, 2014.

[16] Bonneau, D., Fatu, A., and Souchet, D. *Thermo-hydrodynamic Lubrication in Hydrodynamic Bearings*. ISTE, London and John Wiley & Sons, New York, 2014.

[17] Booker, J. Dynamically loaded journal bearings: mobility method of solution. *Journal of Basic Engineering 87*, 3 (1965), 537–546.

[18] Booker, J. Dynamically loaded journal bearings: numerical application of the mobility method. *Journal of Lubrication Technology 93*, 1 (1971), 168–174.

[19] Booker, J., Boedo, S., and Bonneau, D. Conformal elastohydrodynamic lubrication analysis for engine bearing design: a brief review. *Proceedings of the Institution of Mechanical Engineers-Part C: Journal of Mechanical Engineering Science 224*, 12 (2010), 2648.

[20] Bouyer, J., and Fillon, M. Experimental measurement of the friction torque on hydrodynamic plain journal bearings during start-up. *Tribology International 44*, 7 (2011), 772–781.

[21] Cameron, A., and Mc Ettles, C. *Basic Lubrication Theory*. Ellis Horwood Ltd., Chichester, 1976.

[22] Covitch, M. J., Brown, M., May, C., Selby, T., Goldmints, I., and George, D. Extending SAE J300 to viscosity grades below SAE 20. *SAE Technical Paper* (2010).

[23] Cross, M. M. Rheology of non-Newtonian fluids: a new flow equation for pseudoplastic systems. *Journal of Colloid Science 20*, 5 (1965), 417–437.

[24] Czichos, H. Tribosystems. In *Encyclopedia of Lubricants and Lubrication*. Springer, 2014, pp. 2178–2183.

[25] Damm, K., Pucher, K., Skiadas, A., and Witt, M. Sputter bearings for highly charged diesel engines. *MTZ worldwide 76*, 5 (2015), 26–30.

[26] Decker, K.-H. *Decker Maschinenelemente: Funktion, Gestaltung und Berechnung*. Carl Hanser Verlag GmbH Co KG, München, Wien, 2014.

[27] Deters, L. Plain bearings. In *Encyclopedia of Lubricants and Lubrication*. Springer, 2014, pp. 1331–1356.

[28] Deters, L., Fischer, A., Santner, E., and Stolz, U. Tribologie - Verschleiß, Reibung. *GfT Arbeitsblatt 7 7* (2003).

[29] Dowson, D., Higginson, G., and Whitaker, A. Elasto-hydrodynamic lubrication: A survey of isothermal solutions. *Journal of Mechanical Engineering Science 4*, 2 (1962), 121–126.

[30] Dowson, D., and Taylor, C. Cavitation in bearings. *Annual Review of Fluid Mechanics 11*, 1 (1979), 35–65.

[31] DuBois, G. B., and Ocvirk, F. W. Analytical derivation and experimental evaluation of short-bearing approximation for full journal bearing. *NACA report 1157* (1953).

[32] Durak, E., Adatepe, H., and Biyiklioglu, A. Experimental study of the effect of additive on the tribological properties journal bearing under running-in and start-up or shut-down stages. *Industrial Lubrication and Tribology 60*, 3 (2008), 138–146.

[33] Fillon, M., and Bouyer, J. Thermohydrodynamic analysis of a worn plain journal bearing. *Tribology International 37*, 2 (2004), 129–136.

[34] Fonseca, N., Casanova, J., and Valdés, M. Influence of the stop/start system on CO2 emissions of a diesel vehicle in urban traffic. *Transportation Research Part D: Transport and Environment 16*, 2 (2011), 194–200.

[35] Greenwood, J., and Tripp, J. The contact of two nominally flat rough surfaces. *Proceedings of the Institution of Mechanical Engineers 185*, 1 (1970), 625–633.

[36] Greenwood, J., and Williamson, J. Contact of nominally flat surfaces. *Proceedings of the Royal Society of London. Series A, Mathematical and Physical Sciences 295* (1966), 300–319.

[37] Harnoy, A. Model-based investigation of friction during start-up of hydrodynamic journal bearings. *Journal of Tribology 117*, 4 (1995), 667–673.

[38] Hashimoto, H., Wada, S., and Nojima, K. Performance characteristics of worn journal bearings in both laminar and turbulent regimes. Part I: steady-state characteristics. *ASLE Transactions 29*, 4 (1986), 565–571.

[39] Herbst, H. *Theoretical modeling of the cylinder lubrication in internal combustion engines and its influence on piston slap induced noise, friction and wear*. PhD thesis, Technische Universität Graz, 2007.

[40] Holmberg, K., Andersson, P., and Erdemir, A. Global energy consumption due to friction in passenger cars. *Tribology International 47* (2012), 221–234.

[41] Hori, Y. *Hydrodynamic Lubrication*. Springer, Berlin, 2006.

[42] Hu, Y., Cheng, H. S., Arai, T., Kobayashi, Y., and Aoyama, S. Numerical simulation of piston ring in mixed lubrication—a nonaxisymmetrical analysis. *Journal of Tribology 116*, 3 (1994), 470–478.

[43] Jakobsson, B., and Floberg, L. *The finite journal bearing considering vaporization*. Transactions of Chalmers University of Technology, 1957.

[44] Jedynak, R., and Gilewicz, J. Approximation of the integrals of the gaussian distribution of asperity heights in the greenwood-tripp contact model of two rough surfaces revisited. *Journal of Applied Mathematics 459280* (2013).

[45] Krasser, J. *Thermoelastohydrodynamische Analyse dynamisch belasteter Radialgleitlager*. PhD thesis, Technische Universität Graz, 1996.

[46] Larsson, R., Larsson, P., Eriksson, E., Sjöberg, M., and Höglund, E. Lubricant properties for input to hydrodynamic and elastohydrodynamic lubrication analyses. *Proceedings of the Institution of Mechanical Engineers, Part J: Journal of Engineering Tribology 214*, 1 (2000), 17–27.

[47] Ligier, J.-L., and Noel, B. Friction reduction and reliability for engines bearings. *Lubricants 3*, 3 (2015), 569–596.

[48] Loomis, W. R., and Jones Jr, W. R. Steady-state wear and friction in boundary lubrication studies. *NASA Technical Paper 1658* (1980).

[49] Macián, V., Tormos, B., Bermúdez, V., and Ramírez, L. Assessment of the effect of low viscosity oils usage on a light duty diesel engine fuel consumption in stationary and transient conditions. *Tribology International 79* (2014), 132–139.

[50] Macián, V., Tormos, B., Ruiz, S., and Miró, G. Low viscosity engine oils: Study of wear effects and oil key parameters in a heavy duty engine fleet test. *Tribology International 94* (2016), 240–248.

[51] Mang, T. *Encyclopedia of Lubricants and Lubrication*. Springer, Berlin, 2014.

[52] Mang, T., Bobzin, K., and Bartels, T. *Industrial Tribology: Tribosystems, Friction, Wear and Surface Engineering, Lubrication*. John Wiley & Sons, 2011.

[53] Mohammadpour, M., Rahmani, R., and Rahnejat, H. The effect of cylinder de-activation on thermo-friction characteristics of the connecting rod bearing in the new european drive cycle (NEDC). *SAE Technical Paper* (2014).

[54] Mohammadpour, M., Rahmani, R., and Rahnejat, H. Effect of cylinder deactivation on the tribo-dynamics and acoustic emission of overlay big end bearings. *Proceedings of the Institution of Mechanical Engineers, Part K: Journal of Multi-body Dynamics* (2014), 1464419313519085.

[55] Mokhtar, M., Howarth, R., and Davies, P. The behavior of plain hydrodynamic journal bearings during starting and stopping. *ASLE Transactions 20*, 3 (1977), 183–190.

[56] Mokhtar, M., Howarth, R., and Davies, P. Wear characteristics of plain hydrodynamic journal bearings during repeated starting and stopping. *ASLE Transactions 20*, 3 (1977), 191–194.

[57] Monmousseau, P., and Fillon, M. Transient thermoelastohydrodynamic analysis for safe operating conditions of a tilting-pad journal bearing during start-up. *Tribology International 33*, 3 (2000), 225–231.

[58] Mortier, R. M., Orszulik, S. T., and Fox, M. F. *Chemistry and Technology of Lubricants*, third ed. Springer, Dordrecht, 2010.

[59] Mufti, R., and Priest, M. Theoretical and experimental evaluation of engine bearing performance. *Proceedings of the Institution of Mechanical Engineers, Part J: Journal of Engineering Tribology 223*, 4 (2009), 629–644.

[60] Nikolakopoulos, P. G., and Papadopoulos, C. A. A study of friction in worn misaligned journal bearings under severe hydrodynamic lubrication. *Tribology International 41*, 6 (2008), 461–472.

[61] Offner, G. Modelling of condensed flexible bodies considering non-linear inertia effects resulting from gross motions. *Proceedings of the Institution of Mechanical Engineers, Part K: Journal of Multi-body Dynamics 225*, 3 (2011), 204–219.

[62] Offner, G. Friction power loss simulation of internal combustion engines considering mixed lubricated radial slider, axial slider and piston to liner contacts. *Tribology Transactions 56*, 3 (2013), 503–515.

[63] Offner, G., and Knaus, O. A generic friction model for radial slider bearing simulation considering elastic and plastic deformation. *Lubricants 3*, 3 (2015), 522–538.

[64] Oh, K., and Huebner, K. Solution of the elastohydrodynamic finite journal bearing problem. *Journal of Lubrication Technology 95*, 3 (1973), 342–351.

[65] Patir, N., and Cheng, H. An average flow model for determining effects of three-dimensional roughness on partial hydrodynamic lubrication. *ASME, Transactions, Journal of Lubrication Technology 100* (1978), 12–17.

[66] Patir, N., and Cheng, H. Application of average flow model to lubrication between rough sliding surfaces. *ASME, Transactions, Journal of Lubrication Technology 101* (1979), 220–230.

[67] Pawlak, Z. *Tribochemistry of Lubricating Oils*, vol. 45. Elsevier, Amsterdam, 2003.

[68] Peklenik, J. Paper 24: New developments in surface characterization and measurements by means of random process analysis. *Proceedings of the Institution of Mechanical Engineers, Conference Proceedings 182*, 11 (1967), 108–126.

[69] Popov, V. *Kontaktmechanik und Reibung: von der Nanotribologie bis zur Erdbebendynamik*. Springer, Berlin, 2009.

[70] Priebsch, H. H., and Krasser, J. Simulation of the oil film behaviour in elastic engine bearings considering pressure and temperature dependent oil viscosity. *Tribology Series 32* (1997), 651–659.

[71] Priest, M., and Taylor, C. Automobile engine tribology—approaching the surface. *Wear 241*, 2 (2000), 193–203.

[72] Reynolds, O. On the Theory of Lubrication and Its Application to Mr. Beauchamp Tower's Experiments, Including an Experimental Determination of the Viscosity of Olive Oil. *Proceedings of the Royal Society of London 40*, 242-245 (1886), 191–203.

[73] Sander, D. E., Allmaier, H., and Priebsch, H. H. Friction and wear in automotive journal bearings operating in today's severe conditions. In *Tribology*. 2016, p. to be published.

[74] Sander, D. E., Allmaier, H., Priebsch, H. H., Reich, F. M., Witt, M., Füllenbach, T., Skiadas, A., Brouwer, L., and Schwarze, H. Impact of high pressure and shear thinning on journal bearing friction. *Tribology International 81* (2015), 29–37.

[75] Sander, D. E., Allmaier, H., Priebsch, H. H., Reich, F. M., Witt, M., Skiadas, A., and Knaus, O. Edge loading and running-in wear in dynamically loaded journal bearings. *Tribology International 92* (2015), 395–403.

[76] Sander, D. E., Allmaier, H., Priebsch, H. H., Witt, M., and Skiadas, A. Simulation of journal bearing friction in severe mixed lubrication–validation and effect of surface smoothing due to running-in. *Tribology International 96* (2016), 173–183.

[77] Seeton, C. J. Viscosity–temperature correlation for liquids. *Tribology Letters 22*, 1 (2006), 67–78.

[78] Shahmohamadi, H., Rahmani, R., Rahnejat, H., Garner, C. P., and Dowson, D. Big end bearing losses with thermal cavitation flow under cylinder deactivation. *Tribology Letters 57*, 1 (2015), 1–17.

[79] Silva, C., Ross, M., and Farias, T. Analysis and simulation of "low-cost" strategies to reduce fuel consumption and emissions in conventional gasoline light-duty vehicles. *Energy Conversion and Management 50*, 2 (2009), 215–222.

[80] Sommerfeld, A. Zur Theorie der Schmiermittelreibung. *Electrical Engineering (Archiv fur Elektrotechnik) 3*, 1 (1914), 1–5.

[81] Stachowiak, G., and Batchelor, A. W. *Engineering Tribology*. Butterworth-Heinemann, Oxford, 2013.

[82] Sturk, R. K., and Whitney, W. J. Fluid film bearing materials. In *Encyclopedia of Tribology*. Springer, 2013, pp. 1200–1216.

[83] Taylor, C. Automobile engine tribology—design considerations for efficiency and durability. *Wear 221*, 1 (1998), 1–8.

[84] Thong, D., Hutchinson, P. A., Wincierz, C., and Schimmel, T. Viscosity modifiers. In *Encyclopedia of Lubricants and Lubrication*. Springer, 2014, pp. 2292–2316.

[85] Tung, S. C., and McMillan, M. L. Automotive tribology overview of current advances and challenges for the future. *Tribology International 37*, 7 (2004), 517–536.

[86] Vogel, H. The law of the relation between the viscosity of liquids and the temperature. *Physikalische Zeitschrift 22* (1921), 645–646.

[87] Warrens, C., Jefferies, A., Mufti, R., Lamb, G., Guiducci, A., and Smith, A. Effect of oil rheology and chemistry on journal-bearing friction and wear. *Proceedings of the Institution of Mechanical Engineers, Part J: Journal of Engineering Tribology 222*, 3 (2008), 441–450.

[88] Wilcutts, M., Switkes, J., Shost, M., and Tripathi, A. Design and benefits of dynamic skip fire strategies for cylinder deactivated engines. *SAE International Journal of Engines 6*, 1 (2013), 278–288.

[89] Wong, V. W., and Tung, S. C. Overview of automotive engine friction and reduction trends–effects of surface, material, and lubricant-additive technologies. *Friction 4*, 1 (2016), 1–28.

[90] Yang, L. Wear coefficient equation for aluminium-based matrix composites against steel disc. *Wear 255*, 1 (2003), 579–592.

List of Figures

List of Tables